

ABSTRACT

Title of Dissertation: **NONEQUILIBRIUM STATISTICAL PHYSICS
OF FEEDBACK-CONTROLLED AND AUTONOMOUS
INFORMATION-THERMODYNAMIC SYSTEMS**

Debankur Bhattacharyya
Doctor of Philosophy, 2024

Dissertation Directed by: Professor Christopher Jarzynski,
Department of Chemistry and Biochemistry,
Institute for Physical Science and Technology,
Department of Physics.

This thesis investigates the nonequilibrium dynamics of a variety of systems evolving under control protocols. A control protocol can involve feedback based on measurements performed by an external agent, or it can be a predefined protocol that does not rely on explicit measurements of the system's state. In the context of information thermodynamics, the former setup belongs to the paradigm of non-autonomous or feedback-controlled Maxwell's demons, and the latter to the paradigm of autonomous demons.

The thesis begins with a framework for analyzing non-autonomous feedback control, when the control protocol is applied by an agent making continuous measurements on the system. A multiple-timescales perturbation theory, applicable when there exists an appropriate separation of timescales, is developed. This framework is applied to a classical two-state toy model of an information engine – a device that uses feedback control of thermal fluctuations to convert heat

into work. Additionally, quantum trajectory simulations are used to study a feedback-controlled model of Maxwell's demon in a double quantum dot system.

Next, a modeling scheme for converting feedback-controlled Maxwell's demons to autonomous (non-feedback) systems is developed. This scheme explicitly accounts for the thermodynamic costs of information processing, by incorporating an information reservoir, modeled as a sequence of bits. This modeling scheme is then applied for converting the classical analogue of the non-autonomous double quantum dot Maxwell's demon, discussed previously, to an autonomous model. Using analytical, semi-analytical and stochastic simulation-based approaches, it is shown that the obtained model can act either as an information engine, or as a “Landauer eraser”, and then the phase diagrams that identify these regimes of behavior are constructed.

Finally, fast-forward shortcuts to adiabaticity for classical Floquet-Hamiltonian systems is developed, and applied to a periodically driven asymmetric double well (without feedback control). Tools from dynamical systems theory are then used to characterize the system's angle-variable dynamics.

NONEQUILIBRIUM STATISTICAL PHYSICS OF
FEEDBACK-CONTROLLED AND AUTONOMOUS
INFORMATION-THERMODYNAMIC SYSTEMS

by

Debankur Bhattacharyya

Dissertation submitted to the Faculty of the Graduate School of the
University of Maryland, College Park in partial fulfillment
of the requirements for the degree of
Doctor of Philosophy
2024

Advisory Committee:

Professor Christopher Jarzynski, Chair/Advisor
Professor Victor M. Yakovenko, Dean's Representative
Professor Nicole Yunger Halpern
Professor Pratyush Tiwary
Professor Daniel P. Lathrop

© Copyright by
Debankur Bhattacharyya
2024

Dedication

*Dedicated to my family,
and all my friends from
St. Xavier's College,
IIT Kharagpur,
and University of Maryland.*

Acknowledgments

First and foremost, I want to thank my advisor, Prof. Christopher Jarzynski, for his constant support and guidance. It is a great pleasure to be taught and advised by Chris. Throughout the six years of this PhD journey, Chris has always supported my research interests and considered my well-being. After every chat with him, I felt I was learning something new. I am thankful for all the academic and career advice I received from him and grateful for the sense of belonging that I felt in his research group.

Next, I would like to thank all the current and past Jarzynski group members, long-term visitors, and attendees of our group meetings with whom I had the chance to interact and discuss physics over the last six years. Thanks to Guilherme De Sousa, Long Him Cheung, Greeshma Oruganti, Joshua Chiel, Anthony Munson, Saipriya Satyajit, Sangyun Lee, Wade Hodson, Carlos Floyd, Andrew Smith, Kanu Sinha, Roi Holtzman, Iwan Setiawan, Patrick Kelly, Twesh Upadhyaya, Sarathchandran Jayachandran for the fruitful discussions. Thanks to Guilherme and Long Him for all the joint research work. Friday informal seminars and group lunches are something that I always looked forward to, and I will miss them greatly. I especially thank Guilherme, Long Him, Greeshma, Sangyun, and Wade for their constant support through the ups and downs of the PhD and countless hours of informal discussions. It has been a great pleasure to know you all. I could not have asked for a better research group.

A significant part of this thesis and my PhD journey is related to the FQxi Information as

Fuel (IaF) project. Thanks to the IaF theory team: Björn Annby-Andersson, Guilherme De Sousa, Daniel Holst, Pharnam Bakhshinezhad, Patrick P. Potts, Peter Samuelsson, and Chris Jarzynski, for this exciting collaboration. I want to thank the experimental teams: Klaus Ensslin's and Ville Maisi's research groups, for our exciting discussions during joint group meetings. Thanks to Peter and Patrick for hosting me during my research visit at Lund University and the University of Basel. It was a great pleasure to meet your research groups. I want to thank Björn for all our exciting discussions and joint research work and for making my visit to Lund enjoyable. Thanks to all the attendees of the Information as Fuel Meeting at Universitätszentrum Obergurgl in 2023 for many fruitful discussions.

Thanks to my PhD dissertation committee members for their valuable feedback and comments on my thesis. I thank the University of Maryland's statistical physics and quantum thermodynamics community for many exciting discussions over the last few years. Thanks to the IPST chemical physics PhD program, which has allowed me to pursue research in an interdisciplinary area between chemistry and physics. Thanks to our program coordinators, Debbie, Souad, and Jessica, for their help with administrative things along the way. Thanks to the excellent professors at the University of Maryland who taught me different exciting courses during this PhD program. I also acknowledge the University of Maryland supercomputing resources made available for conducting the research reported in this thesis.

I acknowledge funding from the Foundational Questions Institute (FQxi), John Templeton Foundation, National Science Foundation (NSF), Alexander Family Fellowship, and University of Maryland Dean's Fellowship for the research during my PhD.

Thanks to Santa Fe Institute - Complex Systems Summer School 2022 participants for inspiring me to continue interdisciplinary research, for many interesting discussions, and for

helping me learn more about complex systems sciences.

During this PhD journey, my friends supported me constantly, and I could not have finished the PhD without them. I am grateful for all my friends at the University of Maryland who have accompanied me on this journey. Thanks to my current and former housemates, classmates, concert-going team, fencing club members, and all other friends for making these six years memorable.

I am grateful to my friends from St. Xavier's College and IIT Kharagpur for their unwavering support during my PhD. Thanks for being friends through different stages of my life over the last eight years and more.

I want to thank all the musicians, artists, and writers whose works inspired and helped me through difficult times, especially during the pandemic.

Finally, I want to thank my father, mother, and sister for their constant support and encouragement. I love you all.

Table of Contents

Dedication	ii
Acknowledgements	iii
Table of Contents	vi
List of Publications	x
List of Tables	xi
List of Figures	xii
List of Abbreviations	xvii
Chapter 1: Introduction and background	1
1.1 Chapter overview	1
1.2 Historical overview of Maxwell's demon	1
1.2.1 Maxwell's thought experiment and Szilard's engine	1
1.2.2 Landauer's principle and Bennett's exorcism	6
1.2.3 Information as a thermodynamic resource	10
1.2.4 A physical picture of information reservoirs	11
1.2.5 Autonomous and non-autonomous models of Maxwell's demons	15
1.2.6 Information thermodynamics - a transdisciplinary field	16
1.3 Organization and thematic overview of the thesis	17
1.3.1 From feedback-controlled systems to non-feedback systems	17
1.3.2 Information as fuel in a double quantum dot	18
1.3.3 Modelling frameworks and theoretical tools	19
1.4 Summary of chapters	20
Chapter 2: Unified perspective on non-autonomous feedback performed on continuously measured systems	23
2.1 Chapter overview	23
2.2 Review of classical continuous measurement formalism	24
2.2.1 Evolution without measurement	25
2.2.2 Evolution with a single purely Bayesian measurement	27
2.2.3 Evolution with repeated frequent measurements	29
2.2.4 Gaussian measurement model and continuous measurement equation	32

2.3	Master equation for continuously monitored feedback-controlled diffusive flows	36
2.3.1	Filtering equation for the measurement signal	36
2.3.2	Derivation of master equation	38
2.3.3	Effective coupled Langevin equations for the system-detector dynamics	42
2.4	Separation of timescales using multiple-timescale perturbation (MTSP) approach	43
2.4.1	General formal solution	43
2.4.2	0th and 1st order terms	50
2.4.3	Effective master equation for system state under fast feedback	51
2.4.4	Connection to linear response theory	52
2.5	Comparison with feedback-control equation for quantum and discrete stochastic systems	54
2.5.1	Comparison with quantum Fokker-Planck master equation (QFPME)	54
2.5.2	Comparison with feedback-control master equation for classical discrete-state stochastic dynamics	58
 Chapter 3: A classical two-state toy model of feedback-controlled information engine		61
3.1	Chapter overview	61
3.2	Physical setup and stochastic modelling	63
3.2.1	Stochastic modelling	64
3.2.2	Idealized feedback protocol	66
3.2.3	Imperfect feedback protocol: the feedback-resolved model	68
3.3	Analytical treatment of the model	71
3.3.1	Steady state power calculation	71
3.3.2	Thermodynamic operation modes: dissipator vs. information engine	74
3.3.3	Criteria for information engine mode in fast feedback limit ($\epsilon \approx 0$)	75
3.3.4	Steady state power in strong measurement ($\lambda \gg \gamma$) but lagging controller ($\epsilon \neq 0$)	77
3.4	Appendix: MTSP solution for steady states	78
3.5	Appendix: Evaluation of the dimensionless parameters (m, z, k) arising in first order perturbation scheme	80
3.5.1	Eigenspectrum of Fokker-Planck operator for Ornstein–Uhlenbeck (OU) process	80
3.5.2	Evaluating integrals containing Drazin inverses	82
3.5.3	Series expansion expressions for m, z and k	83
3.5.4	Limiting value of k for accurate measurements	87
 Chapter 4: Feedback controlled Maxwell’s demon in a double quantum dot (DQD) - quantum trajectory analysis		89
4.1	Chapter overview	89
4.2	Physical Setup and modelling	91
4.2.1	Idealized classical protocol	91
4.2.2	The feedback-resolved model: quantum model with weak measurement and finite-bandwidth feedback	93
4.3	Theory and methods	97
4.3.1	Evolution map of the quantum state	97

4.3.2	Trajectory and ensemble level equations of motion	100
4.4	Qualitative features from trajectory simulations	102
4.4.1	Delayed feedback effect	102
4.4.2	Quantum Zeno effect	104
4.4.3	Phase damping effect due to random feedback	105
4.4.4	Quantum to classical transition	106
4.5	Appendix: Quantum evolution map to the stochastic master equation	107
4.6	Appendix: Ideal charge detection assumption	110
4.7	Appendix: Monte Carlo wave function simulation scheme with feedback control	112
Chapter 5:	From the feedback-controlled DQD demon to autonomous information ratchet	117
5.1	Chapter overview	117
5.2	Memory-tape model of Maxwell's demon in DQD system	122
5.2.1	DQD demon with thermal feedback control	122
5.2.2	Conversion to autonomous demon: bit-coupling strategy	125
5.2.3	Details of the memory-tape model	126
5.2.4	Summary of the modelling strategy	129
5.3	Analysis and results	132
5.3.1	Methods	132
5.3.2	Thermodynamics of the memory-tape model	134
5.3.3	Analytical results for $\tau \rightarrow \infty$	138
5.3.4	Semi-analytical results for finite τ	143
5.3.5	Stochastic simulation	145
5.4	Discussion	147
5.5	Appendix: Transition rates and the detailed balance relations	148
5.6	Appendix: Rate matrix and unique stationary state for \mathcal{G}_f	150
5.7	Appendix: Details of stochastic simulation scheme	153
5.7.1	Poisson jumps	153
5.7.2	Virtual jumps	153
Chapter 6:	Fast-forward shortcuts to adiabaticity in classical Floquet-Hamiltonian systems - angle variable dynamics	155
6.1	Chapter overview	155
6.2	Background: classical flow-field based methods for shortcuts to adiabaticity (STA)	156
6.3	Theory and methods: dynamical maps and transfer operator	161
6.3.1	Hamiltonian maps for fast-forward shortcuts to adiabaticity in Floquet systems	161
6.3.2	One-dimensional angle map ($\Theta_{T,[I_0]}^{FF}$) for dynamics on preserved energy shell	164
6.3.3	Transfer operators for the evolution of the angle variable distribution	166
6.3.4	Transition probability matrix and evolution of probability distributions on the energy shell	171
6.4	Toy model system	172
6.4.1	Setup: periodically driven asymmetric double well	175

6.4.2	Discussion: preserved energy shell as a heteroclinic connection and invariant distributions	178
6.5	Appendix: Calculation of the adiabatic energy	180
6.6	Appendix: Calculation of the flow fields	181
6.7	Appendix: Numerical construction of the angle map $\Theta_{T,[I_0]}^{FF}$	183
Chapter 7:	Future directions	185
7.1	Stochastic, quantum and information thermodynamics	185
7.2	Chemical physics, biological physics and complex systems science	187

List of Publications

Paper [1]: B. Annby-Andersson, F. Bakhshinezhad, **D. Bhattacharyya**, G. De Sousa, C. Jarzynski, P. Samuelsson, and P. P. Potts, Quantum Fokker-Planck master equation for continuous feedback control, Phys. Rev. Lett. 129, 050401 (2022).

Paper [2]: **D. Bhattacharyya** and C. Jarzynski, From a feedback-controlled demon to an information ratchet in a double quantum dot, Phys. Rev. E 106, 064101 (2022).

Paper [3]: B. Annby-Andersson, **D. Bhattacharyya**, P. Bakhshinezhad, D. Holst, G. De Sousa, C. Jarzynski, P. Samuelsson and P. P. Potts, Maxwell's demon across the quantum-to-classical transition, arXiv:2405.09376 [quant-ph] (2024)

List of Tables

- 5.1 Transition rates for jumps of the variable y in \mathcal{G}_f . $R_{y_i y_j}$ denotes the transition rate from y_j to y_i . Here we have taken $r = e^{-\beta\epsilon}$ with $\epsilon = (\epsilon_u - \epsilon_0) = (\epsilon_0 - \epsilon_l)$. These rates are used construct the matrix \mathbf{R} which is shown in Eq. (5.34) in Appendix 5.6 131

List of Figures

1.1	A schematic depiction of the original Maxwell's demon thought experiment. Initially both subsystems A and B are in thermal equilibrium. The demon creates a temperature difference between the subsystem by observing the system and providing feedback accordingly.	2
1.2	The figure above shows a schematic depiction of the Szilard's engine and the figure below shows its operation protocol. Depending on the result of the measurement the demon provides two different feedback protocols to extract work out of the system.	4
1.3	A schematic depiction of Bennett's analysis of the operation cycle of Szilard's engine with the memory register. Possible combined states of the engine and demon memory are shown in the table in the right upper corner. The first letter of the two letter description of the state denotes the state of the particle in gas container $\{A, B\}$ and the second letter shows the state of the demon memory $\{S, L, R\}$. The state of the register in each step is shown in a circle above the container pictures. The description of the statistical state of the overall system is depicted by shading state diagrams. Shaded boxes correspond to the possible state of the overall system. Note that another additional erasure step is required to take the full system to its initial condition.	8
1.4	A schematic diagram of information engine that illustrates how empty information reservoir can act as a thermodynamic resource. Here the system extracts heat from a bath and directly converts it work, at the cost of randomizing the information reservoir which is depicted as a memory tape.	10

- 3.1 Schematic diagram of the classical two-state toy model of an information engine. The two states are labeled as $|0\rangle$ and $|1\rangle$. The agent (demon) makes continuous measurements (denoted by the magnifying glass in the figure) on the two-state system to learn whether the system is in the state $|0\rangle$ or the state $|1\rangle$. The ground state and excited state energies of the system are E_g and E_e with $E_e - E_g = \Delta > 0$. When the system absorbs heat $Q_{\text{in}} = \Delta$ from the heat reservoir (depicted by the sun in the schematic diagram) to go to the excited state, the agent instantly provides feedback (denoted by the trident) by switching the levels $|0\rangle(|1\rangle) \rightarrow |1\rangle(|0\rangle)$. In this process the agent takes the system from excited state energy E_e to the ground state energy E_g and extracts work $W_{\text{ext}} = \Delta$, which is stored in a work reservoir (depicted by the battery in the schematic diagram). After this, the demon repeats the process cyclically (see Fig. 3.2) 62
- 3.2 Stochastic model for the two state information engine. The graph \mathcal{G} and the corresponding joint states of the systems are shown here. Beside every node of \mathcal{G} the corresponding physical system is depicted in the boxes. The desired behavior (information engine mode) of the protocol corresponds to counter-clockwise cycle \mathcal{C} in the network \mathcal{G} shown above. The transitions $(0, -) \leftrightarrow (1, -)$ and $(0, +) \leftrightarrow (1, +)$ correspond to excitation and de-excitation of the system due to interactions with the thermal reservoir (depicted by the sun). The corresponding transition rates from Eqs. (3.4) and Eq. (3.3) are shown shown by the arrows between the physical pictures of the joint states. The transitions $(0, -) \leftrightarrow (0, +)$ and $(1, -) \leftrightarrow (1, +)$ correspond to feedback steps (denoted by the trident) and involves interaction with the work reservoir (battery). For the feedback-resolved model, the feedback Hamiltonian $H(D)$ from Eq. (3.8) is represented here by showing the control parameter (D) below the corresponding joint states. The grey colored states $(1, -)$ and $(0, +)$ show the situations when the control parameter $D(t)$ (which is a filtered form measurement signal $z(t)$) fails to capture the actual state of the system, whereas white colored states $(0, -)$ and $(1, +)$ are the situation when the actual state of the system is captured by the control parameter $D(t)$ 67
- 3.3 Steady state work extraction rate for the two state toy model in the fast feedback limit ($\epsilon \approx 0$). The vertical axis of the plots represent the ratio λ/γ . The horizontal axis of the plots represent $\beta\Delta$. The figure above shows values of $\langle \dot{W}_{\text{ext}}^{\text{ss}} \rangle / \Gamma\Delta$, (see Eq. (3.21)) i.e., steady state work extraction by the agent in the fast feedback limit, scaled by the factor $\Gamma\Delta$ 75
- 3.4 Operation mode phase diagram in fast feedback limit. The figure shows the sign of $\langle \dot{W}_{\text{ext}}^{\text{ss}} \rangle$ from Fig. 3.3. For the information engine region we have $\langle \dot{W}_{\text{ext}}^{\text{ss}} \rangle > 0$ and for the dissipator mode we have $\langle \dot{W}_{\text{ext}}^{\text{ss}} \rangle < 0$. The separation between these two operation modes are captured by the critical ratio r_{fast}^* (see Eq. (3.26)). 76

4.1	A schematic diagram for the double quantum dot Maxwell's demon (Annby-Aandersson model [4]). The two quantum dots are separated by a tunneling barrier. The agent (demon) is making measurement into the DQD system and providing feedback accordingly. The DQD is coupled to two electron reservoirs L and R with chemical potentials μ_L and μ_R respectively. The agent transports the electron from lower to higher chemical potential through measurement and feedback.	91
4.2	Schematics of the idealized classical protocol for the DQD Maxwell's demon (AA model) and the encoding of the protocol in feedback variables (D_1, D_2). The figure in the left shows the steps of the ideal feedback protocol of the AA model. The figure on the right shows the encoding of the protocol in the feedback variables (D_1, D_2). The red dots represent the eigenvalues of \hat{A}_1 and \hat{A}_2 as $(\xi^{(1)}, \xi^{(2)})$ corresponding to state of the DQD that feedback regions represent and the arrows show the desired direction of cycle of the control parameters.	93
4.3	Detector is lagging behind the quantum state. The figure above shows the evolution of the feedback variable and instantaneous expectation value of the observable \hat{A}_1 . The figure below plots the evolution of the feedback Hamiltonian. Parameters: $\beta = 1.0, \Gamma = 0.1, \mu_R = 1.5, \mu_L = -1.5, \epsilon_0 = 0.0, \epsilon_u = 5.0, \epsilon_l = -5.0, g = 25, \gamma_1 = 10.0, \lambda_1 = 1.0$ and simulation time step $\delta t = 10^{-4}$	103
4.4	Suppression of interdot tunneling due to quantum Zeno effect. Parameters: $\beta = 1.0, \Gamma = 0.1, \mu_R = 1.5, \mu_L = -1.5, \epsilon_0 = 0.0, \epsilon_u = 5.0, \epsilon_l = -5.0, g = 0.1, \gamma_1 = 10.0, \lambda_1 = 80.0$ and simulation time step $\delta t = 10^{-4}$	104
4.5	Suppression of the interdot tunneling due to random shuffling of the feedback Hamiltonian, Parameters: $\beta = 1.0, \Gamma = 0.1, \mu_R = 1.5, \mu_L = -1.5, \epsilon_0 = 0.0, \epsilon_u = 5.0, \epsilon_l = -5.0, g = 0.1, \gamma_1 = 10.0, \lambda_1 = 1.0$, and simulation time step $\delta t = 10^{-4}$	105
4.6	Evolution of population (above) and the coherence (below) during interdot electron transfer. This figure illustrates the quantum nature of the interdot transport of the electron. Parameters: $\beta = 1.0, \Gamma = 0.1, \mu_R = 1.5, \mu_L = -1.5, \epsilon_0 = 0.0, \epsilon_u = 5.0, \epsilon_l = -5.0, g = 0.1, \gamma_1 = 1.0, \lambda_1 = 0.6$ and simulation time step $\delta t = 10^{-4}$	107
4.7	Evolution of population (above) and the coherence (below) during interdot electron transfer. This figure illustrates the classical jump like behavior of the interdot transport of the electron. Parameters: $\beta = 1.0, \Gamma = 0.1, \mu_R = 1.5, \mu_L = -1.5, \epsilon_0 = 0.0, \epsilon_u = 5.0, \epsilon_l = -5.0, g = 0.1, \gamma_1 = 1.0, \lambda_1 = 6.0$ and simulation time step $\delta t = 10^{-4}$	108
5.1	Two paradigms of Maxwell's demon. The left figure depicts the AA model, a feedback-controlled model. On the right we show the corresponding memory-tape model or information ratchet. In both cases, heat from a thermal reservoir is converted to work, either through measurement and feedback, or through interaction with an information reservoir. We explore a strategy to convert a feedback-controlled model to a memory-tape model. The figure is taken from Ref. [2].	118

- 5.2 States of the double quantum dot system $x \equiv (\lambda, \sigma)$ and the protocol (\mathcal{C}_{AA}) for the AA model. Feedback steps (changes in λ , i.e, steps (b), (d) and (f)) are shown using double arrows, and electron jumps (changes in σ , i.e, steps (a), (c) and(e)) are shown using single arrow. The figure is taken from Ref. [2] 120
- 5.3 Reduced network $\mathcal{G}_r = (\mathbf{V}_x, \mathbf{E}_x)$. Energies of the states in \mathbf{V}_x are shown to the right of the network. Edges shown in red correspond to the feedback steps of the original AA model, and involve the flipping of the bit in the memory-tape model. The edges shown in blue correspond to the transitions where the electron hops into (out of) the DQD from (to) an electron reservoir and the dotted arrows show the corresponding energy exchange. The figure is taken from Ref. [2] 121
- 5.4 Full network $\mathcal{G}_f = (\mathbf{V}_y, \mathbf{E}_y)$ showing all 18 states of the combined DQD and bit. The full network \mathcal{G}_f is obtained from Fig. 5.3 by accounting for the bit-coupling in \mathcal{G}_r . The states in the full network are given by $\mathbf{V}_y = \mathbf{V}_x \times \mathbf{B}$ and the edges follow directly from the edges of the network \mathcal{G}_r , and the mapping of the edges is described in the Sec. 5.2.3.1. Equation (5.6) governs the dynamics of the variable $y \equiv (\lambda, \sigma, b)$ in this network. The figure is taken from Ref. [2] 127
- 5.5 Plots of $\Delta S/\beta$ and W when (a) δ is varied at fixed $\mu_R = 1.5$ and $\mu_L = 0$, and (b) $\beta\Delta\mu$ is varied by changing μ_R at fixed $\mu_L = 0$ and $\delta = 0.002$. In both cases we set $\beta = 1$, $r = e^{-1}$, $\epsilon_0 = 0$, and we take the limit $\tau \rightarrow \infty$. In both plots we see that $\Delta S \geq \beta W$ is satisfied. The regions corresponding to the information engine ($\Delta S > 0, W > 0$), Landauer eraser ($\Delta S < 0, W < 0$) and dud ($\Delta S > 0, W < 0$) are shaded green, red and white respectively. The figure is taken from Ref. [2] 139
- 5.6 Analytically obtained phase diagram when $\tau \rightarrow \infty$. In the green region the system operates as an information engine ($\Delta S > 0, W > 0$) and in the red region it acts as a Landauer eraser. The critical parameter values δ^* , δ' and $-\delta'$ are shown as function of $\beta\Delta\mu$ with $\Delta\mu = \mu_R - \mu_L$ with $\mu_L = 0$. We have taken $\epsilon_0 = 0$, $\beta = 1$ and $r = e^{-1}$ here. The figure is taken from Ref. [2] 142
- 5.7 Numerically obtained phase diagrams for different values of the interaction time, $\tau = 0.2, 2, 20$ and 200 . For finite τ , the final distribution of the memory-tape (δ') depends on the initial distribution (δ), but this dependence vanishes in the limit $\tau \rightarrow \infty$. With increasing τ , the phase diagram approaches the one shown in Fig. 5.6. We have fixed $r = e^{-1}$, $\beta = 1$, $\epsilon_0 = 0$. The figure is taken from Ref. [2] 144
- 5.8 Work and entropy production in (a) the Landauer eraser mode and (b) the information engine mode. Semi-analytical results and stochastic simulation results are compared. ΔS_n and W_n represent the change in single symbol entropy of the n th bit and average extracted work in the n th interval. For all the simulations, we have taken $\beta = 1$, $r = e^{-1}$ and $\epsilon_0 = 0$. Errors are calculated with the bootstrap method. The figure is taken from Ref. [2] 146
- 6.1 Evolution of the energy shell $\mathbf{S}_0 = \{\theta_0^{(j)} | j = 1, \dots, M\}$ to $\mathbf{S}_1 = \{\theta_1^{(j)} | j = 1, \dots, M\}$ for $A = 14$, $\tau = 1$ and adiabatic energy $E = 50$. We have taken $M = 1000$ here. The points in \mathbf{S}_0 are microcanonically distributed, i.e., uniformly spaced in the angle variables $\theta_0^{(j)}$ from 0 to 2π . The evolution under H_{FF} is done using a symplectic integrator of fourth-order with time step $\delta t = 10^{-6}$ 165

- 6.2 Angle variable map $\theta_f = \Theta_{T,[I_0]}^{FF}(\theta_i)$, corresponding to the energy shell evolution shown in Fig. 6.1. θ_i is the initial angle coordinate and θ_f is the final angle coordinate. The angle map $\Theta_{T,[I_0]}^{FF}$ has been constructed from the points $(\theta_0^{(j)}, \theta_1^{(j)})$ which are also plotted with the color representing the initial location $\theta_0^{(j)}$. The identity map $\theta_f = \theta_i$ is also shown using the dotted line. Since $\theta_f = \Theta_{T,[I_0]}^{FF}(\theta_i)$ does not intersect $\theta_f = \theta_i$, there is no fixed point under the evolution of the map $\Theta_{T,[I_0]}^{FF}(\theta_i)$ for the parameters $A = 14, E_0 = 50$ 167
- 6.3 Evolution of the energy shells. Parameters are same as Fig. 6.1 except with $A = 18$ 169
- 6.4 Angle variable map $\theta_f = \Theta_{T,[I_0]}^{FF}(\theta_i)$, corresponding to the energy shell evolution shown in Fig. 6.3. Here, $\theta_f = \Theta_{T,[I_0]}^{FF}(\theta_i)$ intersects $\theta_f = \theta_i$ at two points: (θ_a, θ_a) and (θ_r, θ_r) . Thus there are two fixed points under the evolution of the map $\Theta_{T,[I_0]}^{FF}(\theta_i)$ for the parameters $A = 18, E_0 = 50$. Here we have $|\partial\Theta_{T,[I_0]}^{FF}(\theta_a)| < 1$ and $|\partial\Theta_{T,[I_0]}^{FF}(\theta_r)| > 1$, hence θ_a (θ_r) is an attracting (repelling) or stable (unstable) fixed point of the map $\Theta_{T,[I_0]}^{FF}$ 170
- 6.5 The Fig. 6.5a shows the transition probability matrix \mathbf{T} and the Fig. 6.5b shows the evolution of probability distribution $\vec{P}_n = [P_j(nT)]_{j=0,\dots,K-1}^T$ under the transition probability matrix \mathbf{T} ; for parameters $A = 14, \tau = 1.0$ and energy shell $E = 50$. We have created $K = 100$ bins and the index $j = 0, \dots, K - 1$ is used for the label of the bins. The starting distribution for the evolution is taken as the uniform $P_j(0) = (1/K)$. The evolved distribution $\vec{P}_n = \mathbf{T}^n \vec{P}_0$ are plotted. The stationary distribution \vec{P}_s has been calculated by solving $\mathbf{T}\vec{P}_s = \vec{P}_s$ 173
- 6.6 The Fig. 6.6a shows the transition probability matrix \mathbf{T} and the Fig. 6.6b shows the evolution of probability distribution $\vec{P}_n = [P_j(nT)]_{j=0,\dots,K-1}^T$ under the transition probability matrix \mathbf{T} ; for parameters $A = 18, \tau = 1.0$ and energy shell $E = 50$. We have created $K = 100$ bins and the index $j = 0, \dots, K - 1$ is used for the label of the bins. The starting distribution for the evolution is taken as the uniform $P_j(0) = (1/K)$. The evolved distribution $\vec{P}_n = \mathbf{T}^n \vec{P}_0$ are plotted. The stationary distribution \vec{P}_s has been calculated by solving $\mathbf{T}\vec{P}_s = \vec{P}_s$. The stationary distribution $\vec{P}_s = [\delta_{jj^*}]_{j=0,\dots,K-1}^T$, where j^* is the index for the bin containing the attractive fixed point θ_a 174
- 6.7 Eigenvalues $\{s_i\}_{i=1,\dots,K}$ of \mathbf{T} is shown for the case with no fixed point $E_0 = 50, A = 14$. The Perron-Frobenius eigenvalue $s_{PF} = 1$ is highlighted with a red circle. Total $K = 100$ eigenvalues are plotted. The observed number of eigenvalues in the plot appear less than K due to degeneracy and near degeneracy of eigenvalues. Eigenvalues with $|s_i| \approx 1$ correspond to the metastable modes of the dynamics that take. 176
- 6.8 Eigenvalues $\{s_i\}_{i=1,\dots,K}$ of \mathbf{T} is shown for the case with fixed points $E_0 = 50, A = 18$. The Perron-Frobenius eigenvalue $s_{PF} = 1$ is highlighted with a red circle. Total $K = 100$ eigenvalues are plotted. The observed number of eigenvalues in the plot appear less than K due to degeneracy and near degeneracy of eigenvalues. Absence of eigenvalues with $|s_i| \approx 1$ implies that the dynamics relaxes to the stationary state quickly. Eigenvalues are real indicating absence of the cyclic modes in the dynamics. 177

List of Abbreviations

IBD	Information bearing degrees of freedom
NBD	Non-information bearing degrees of freedom
QD	Quantum dot
DQD	Double quantum dot
MTSP	Multiple-timescale perturbation
FCS	Full counting statistics
QFPME	Quantum Fokker-Planck master equation
OU	Ornstein–Uhlenbeck
MJ	Mandal-Jarzynski
AA	Annby-Andersson
FD	Fermi-Dirac
BE	Bose-Einstein
POVM	Positive operator valued measure
J	Jump
NJ	No-Jump
MCWF	Monte Carlo wave function
CW	Clockwise
CCW	Counter-clockwise
IPSL	Information processing second law
STA	Shortcuts to adiabaticity
FF	Fast-forward
LCD	Local counterdiabatic

Chapter 1: Introduction and background

1.1 Chapter overview

Sec. 1.2 presents a historical overview of Maxwell’s demon and the field of information thermodynamics. Sec. 1.3 presents the organization of the thesis, summary of theoretical tools and a thematic overview of the thesis. Sec. 1.4 summarizes the remaining chapters.

1.2 Historical overview of Maxwell’s demon

1.2.1 Maxwell’s thought experiment and Szilard’s engine

In a thought experiment described in 1867, Maxwell presented the idea that the second law of thermodynamics can be violated by manipulating a system at the microscopic level. This thought experiment involves a gas of molecules in a rigid, closed container with adiabatic walls. This gas starts in thermal equilibrium. There is a partition in the middle of the container, which splits the system into subsystems A and B as shown in Figure 1.1. The partition contains a trapdoor that allows only one molecule to pass from one side to another at a given time. Now we imagine that there exists a small intelligent being who is able to observe the motion of each molecule and provide feedback control on the trapdoor based on its observations. This intelligent being, or “demon”, observes the molecules that are going to hit the trapdoor in each of the

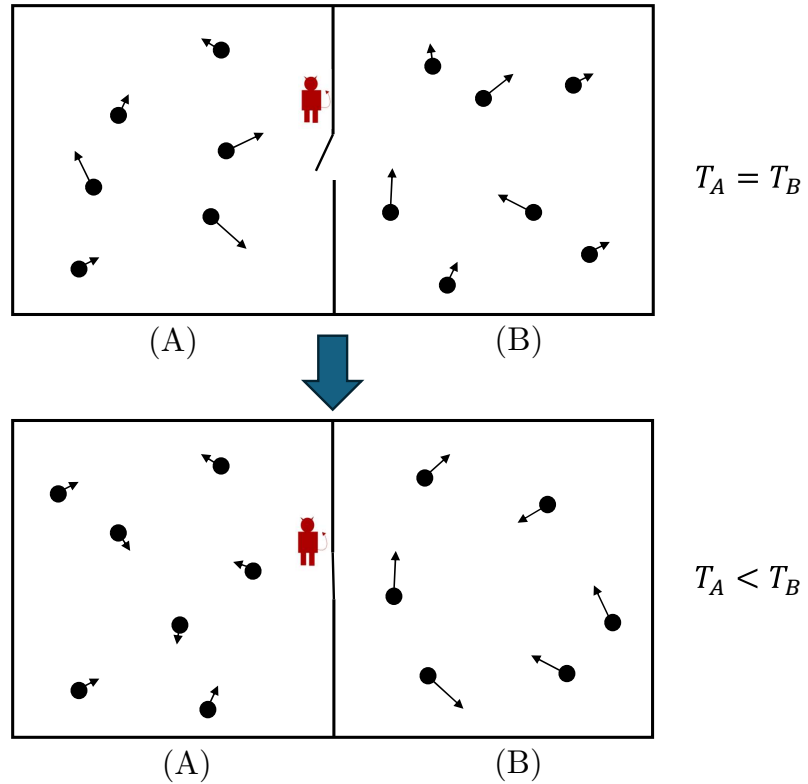


Figure 1.1: A schematic depiction of the original Maxwell's demon thought experiment. Initially both subsystems A and B are in thermal equilibrium. The demon creates a temperature difference between the subsystem by observing the system and providing feedback accordingly.

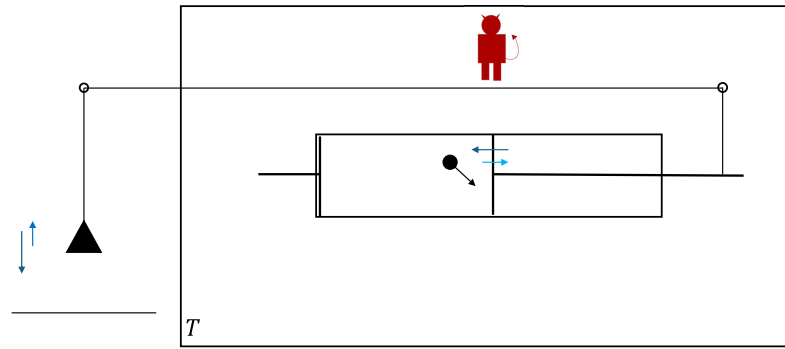
subsystems and controls the trapdoor based on the following rules:

- (i) if a molecule of subsystem A approaches the trapdoor then it will be allowed to pass to subsystem B only if its kinetic energy is higher than the average kinetic energy of the molecules of subsystem B at that instant of time.
- (ii) If a molecule of subsystem B approaches the trapdoor then it will be allowed to pass to subsystem A only if its kinetic is lower than the average kinetic of the molecules of the subsystem A at that instant of time.

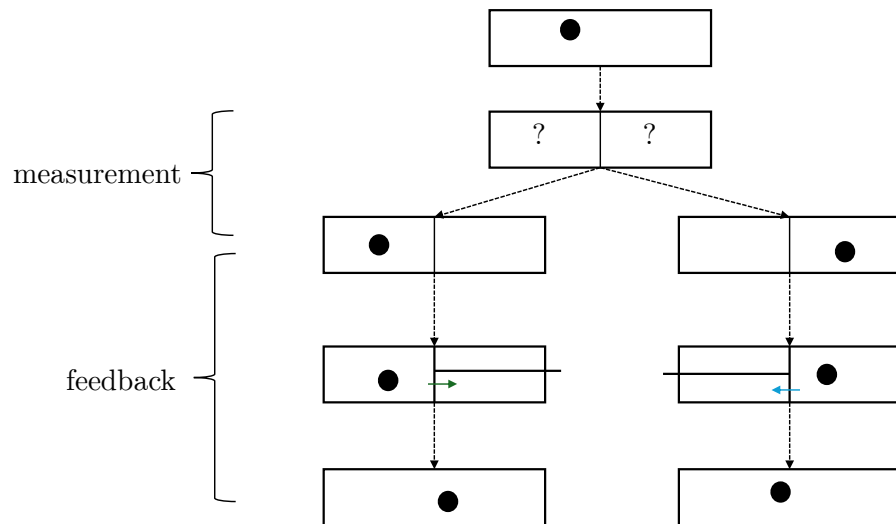
If the demon implements these rules, then with time the average kinetic energy of molecules in subsystem A decreases and the average kinetic energy of molecules in subsystem B increases.

Thus, even though we started in a situation where subsystems A and B had the same temperature, due to the microscopic manipulation of the system by the demon, subsystem A will have lower temperature than that of subsystem B after some time. In other words the demon has driven the system from a state with a uniform temperature to a state with a temperature difference without doing any work, which is a violation of the second law of thermodynamics.

A number of different versions of Maxwell’s demon have been introduced since Maxwell’s thought experiment [5]. Among these, an important model is the “Szilard engine” presented by Leo Szilard in 1929, which is relatively simple to analyse and highlights a deep connection between information processing and thermodynamics [6]. In this engine, the system is a single-molecule gas in a container with pistons on both ends (see Fig. 1.2). A thin partition can be inserted frictionlessly in the middle of the container. The process begins without the partition, and the container is placed in contact with a heat bath with temperature T . Then the partition is inserted into the container. Now a “demon” measures the location of the molecule with respect to the partition, i.e. whether it is to the left or to the right of the partition. The demon then slides the piston that is opposite the location of the particle to the partition and attaches a frictionless pulley system where a small mass is lifted when the piston moves towards its original location. For example, the mass is lifted when the piston moves towards the right if the molecule was located on the left side of the partition as can be seen in Fig. 1.2. The partition is removed to allow the single molecule gas to expand. Whenever the molecule hits the piston, it transfers some of its kinetic energy to the piston and this energy in turn gets converted to potential energy of the mass that is being lifted against gravity. Thus the system performs work by lifting the mass. The loss in the kinetic energy of the molecule is compensated as it absorbs heat from the bath throughout the process. If the lifting of the mass and the motion of the piston happens quasi-statically, then



(a) Schematic of Szilard's engine



(b) Protocol of Szilard's engine

Figure 1.2: The figure above shows a schematic depiction of the Szilard's engine and the figure below shows its operation protocol. Depending on the result of the measurement the demon provides two different feedback protocols to extract work out of the system.

the maximum amount of work is extracted from the system. When the piston hits the other side of the wall, the system gets restored to its initial state completing the cycle. In this cycle, if performed quasi-statically the heat from a single thermal reservoir is converted to work without any loss. Thus like Maxwell's original thought experiment, this model also exhibits a seemingly violation of the second law of thermodynamics.

In both Maxwell's and Szilard's thought experiments the information gathered by measurement is what allows the demon seemingly to violate the 2nd Law. In Szilard's engine, the link is particularly clear. By measuring whether the molecule is located to the left or the right of the partition, the demon gathers 1 bit of information (equivalent to answering a yes/no question). The demon uses this information to push the piston and attach the pulley accordingly in such a way that work is extracted work over the cycle. Thus heat is converted to work by acquiring 1 bit of information about the system per cycle, and the amount of heat that gets converted to work is

$$W_{\text{ext}} = k_B T \int_{V_i}^{V_f} \frac{dV}{V} = k_B T \ln 2 \quad (1.1)$$

where k_B is the Boltzmann's constant, T is the temperature of the heat bath, $V_i(V_f)$ is the initial(final) volume of the container with $V_f = 2V_i$. This calculation of the work is done using the ideal gas formula for the single molecule gas. See Ref. [7] for a discussion on Szilard engine with an ensemble picture. Experimental realizations of Szilard engines have also been performed using single electrons, confirming the extraction of $k_B T \ln 2$ of work for 1 bit of information [8].

1.2.2 Landauer's principle and Bennett's exorcism

In this section we discuss Landauer's principle, which connects information processing with thermodynamics. Landauer's principle can be summarised as follows: any *logically irreversible* step in a computational process must be associated with dissipation of heat [9][10][11]. The idea of logical irreversibility for an operation implies that it is impossible to reconstruct the logical state of the input from just the logical state of the output, thus the inverse of the operation does not exist. For example, consider a *bit erasure* operation that always converts the input bit to 0. The output bit 0 can be obtained from two inputs $\{0, 1\}$ and thus the inverse of this operation does not exist. This is an example of a many-to-one mapping. Information about the input is destroyed in these operations.

The memory device on which computation is performed is a physical object and on a classical level it is governed by Hamilton's equations of motion, under the assumption that the external environment and the memory device together form an isolated system. A many-to-one mapping for the logical state of the memory device is always associated with the contraction of phase space volume of the device. From Liouville's theorem, we know that phase space volume is conserved for the entire system under Hamiltonian dynamics. Thus, contraction in phase space in the memory device must be compensated by the increase of the phase space volume in the external environment. When an erasure operation takes place, both the phase space volume corresponding to 0 and 1 state is contracted to a single state (say 0) in the memory device which means the phase space volume in the memory device is contracted to the half of its original volume (Γ_0). For an isolated system the phase space volume is directly proportional to the available microstates of the system. Thus reduction of the phase space volume is associated with the reduction of the entropy

in the system. This phase space volume contraction in the system or the entropy reduction in the system is compensated in the external environment as dissipation of heat at least of the amount $k_B T \ln \frac{\Gamma_0}{\Gamma_0/2} = k_B T \ln 2$. Here we have assumed that the external environment is a heat bath at temperature T . The value $k_B T \ln 2$ is the minimum amount of heat that needs to be dissipated for the erasure of 1 bit of information. It has been argued that even though erasure is a logically irreversible operation, it can be done in thermodynamically reversible fashion with arbitrarily low dissipation for the execution of the protocol [12]. There have been a number of recent experimental studies on the verification of Landauer's principle, such as those of in Refs. [13, 14].

Charles Bennett used Landauer's principle to propose an explanation of Szilard engine [12]. The key idea is that the demon should be considered as a physical device and we need to take account of the demon's memory state, along with the states of the single molecule gas. Imagine the demon has a memory storage where it can store the information about the relative location of the gas molecule in the container with respect to the partition. The memory register of the demon can take up three distinct states. It has a state S which is the default state of the memory register and two other states L and R correspond to the relative location of the gas molecule (left and right) with respect to the partition. Now let us reinspect the Szilard's engine while accounting for the changes in the memory states of the demon. At the start of the cycle the demon is in state S , and the gas molecule can be on either the A or B side of the container with equal probability. Hence the initial statistical state of the composite system (gas molecule and demon's memory) can be described by saying that the system can be in the state AS or the state BS with equal probability. The protocol for the operation of Szilard engine and the change in the demon's memory is schematically depicted in the Fig. 1.3. Now the partition is inserted, and the demon measures about the location of the gas molecule. If the molecule is on the left side of

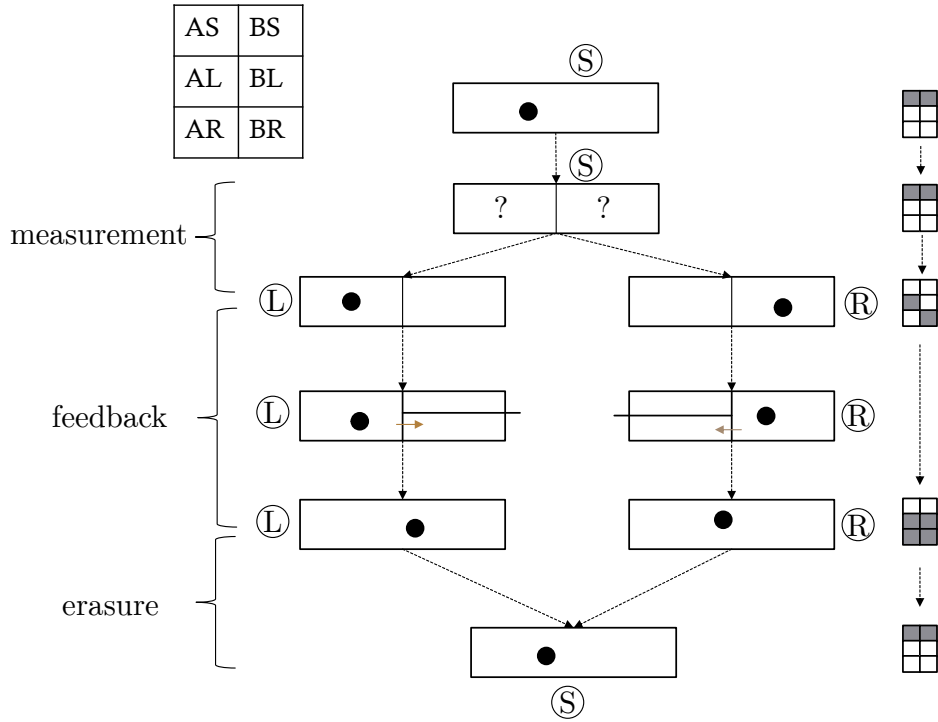


Figure 1.3: A schematic depiction of Bennett's analysis of the operation cycle of Szilard's engine with the memory register. Possible combined states of the engine and demon memory are shown in the table in the right upper corner. The first letter of the two letter description of the state denotes the state of the particle in gas container $\{A, B\}$ and the second letter shows the state of the demon memory $\{S, L, R\}$. The state of the register in each step is shown in a circle above the container pictures. The description of the statistical state of the overall system is depicted by shading state diagrams. Shaded boxes correspond to the possible state of the overall system. Note that another additional erasure step is required to take the full system to its initial condition.

the partition then the demon's register switches to state L and if the molecule is on the right side of the partition then the demon's register switches to state R , thus this act of observation leads to two mutually exclusive outcomes AL and BR . This switching of the memory state based on the state of the gas is an example of information copying (the memory state of the demon becomes correlated with the state of the system). It can be shown that copying operations can be done in a reversible manner with arbitrarily small energy cost [12]. Now depending on the outcome, the proper protocol is followed to insert and push the piston to extract work from the system (see Fig. 1.2). After the work extraction is done and the partition is reinserted again, the particle can be on either side of the partition and thus both A and B states equally likely. Clearly, after this step, both for the left-side protocol and right-side protocol the gas and is back to its initial state where A and B has equal probability. However, if we look into the composite system then we see the overall system has not returned to its initial statistical state. Now, for the case of left-side protocol the demon memory is in the state L and for the case of right side protocol the the demon memory is in the state R whereas in the initial state of the memory was state S . In this configuration the demon is retaining the memory of the result of the measurement operation, and to reset the memory to the original state state S this information needs to be erased, which is a logically irreversible operation. Thus, to restore the overall system to its initial state, the memory of the register is set to S both for the left side protocol and right side protocol and this erasure operation is associated with the dissipation of minimum $k_B T \ln 2$ amount of heat in the reservoir. Once we take account of this heat exchange associated with the erasure step, this heat exchange can compensate for the decrease in entropy associated with the conversion of heat to work. Thus overall the second law of thermodynamics is not violated when we consider the effect of the information processing inside the demon.

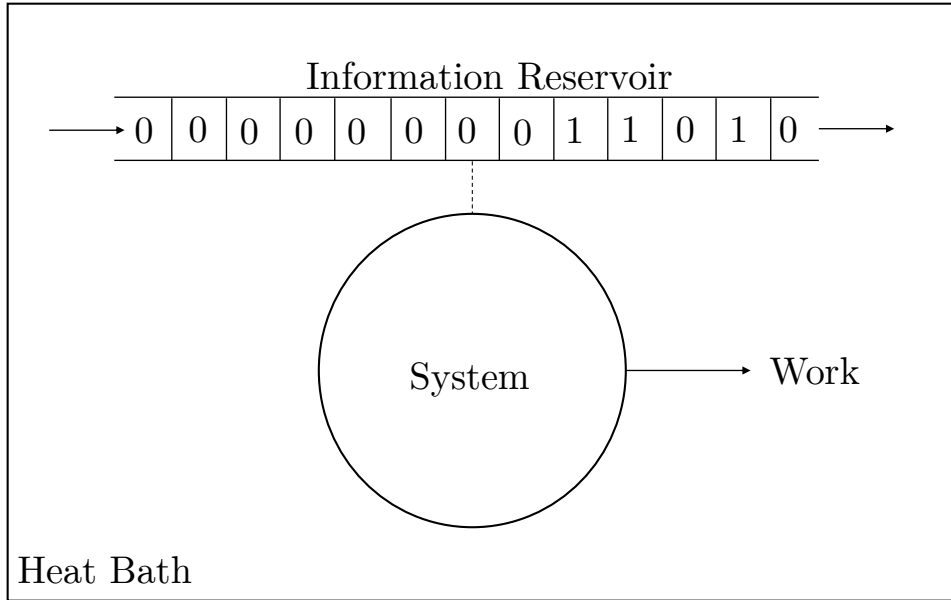


Figure 1.4: A schematic diagram of information engine that illustrates how empty information reservoir can act as a thermodynamic resource. Here the system extracts heat from a bath and directly converts it work, at the cost of randomizing the information reservoir which is depicted as a memory tape.

1.2.3 Information as a thermodynamic resource

This idea of taking the memory of the demon into consideration automatically leads to the idea of an information reservoir. Instead of doing the reset of the memory of the demon in the last step of the cycle we could have replaced the memory register of the demon with a new register which is initialized at S . This way the state of the composite system of demon and gas container is back to its initial state without dissipation of heat for the erasure process, but we end up with an additional memory register that contains information about the result of the observation step (the register is in the L or R state). Clearly, if we do this we are able to complete the cycle at the cost of randomizing the memory register from S to L or R , that is by writing information to the

register.

Now we consider a similar situation where we have a memory tape containing N bits (two state memory register) with every bit initialized at the blank state 0, then we will be able to run the cycle N times at the cost of randomizing the memory tape by writing down the data to it. Clearly like a heat or work reservoir (mass-pulley) this memory tape is also acting as a thermodynamic resource where randomizing the tape allows us to convert heat directly to work from a single thermal reservoir. Such memory tapes are examples of an *information reservoir* [15, 16]. The empty information reservoir is a thermodynamic resource, which can be used to rectify thermal fluctuations from a heat bath to work, at the cost of randomization of information reservoir. This randomization of the information reservoir corresponds to the recording of information about system (see Fig. 1.4 for a schematic diagram of an information engine).

1.2.4 A physical picture of information reservoirs

So far we have used this information reservoir in an abstract sense, but as pointed out in the discussion about Landauer’s principle the memory register (or the memory tape) is a physical memory storage device. In this section, we clarify the connection between logical state of the information reservoir and the microscopic state of the underlying physical device, using a classical Hamiltonian approach following Ref. [17]. We consider the case where the information reservoir consists of N bits and is connected to a thermal bath. We model the information reservoir as a many-particle classical system containing K particles. The exact description of the positions and momentum of all particles together represent classical microstate (ψ) of the information reservoir. This microstate ψ can be described as single point in the $6K$ dimensional phase space. We

assume that for the time scale under consideration, the ergodicity of the phase space of the reservoir is broken and it is split up into 2^N separate ergodic regions. Thermal transitions between these ergodic regions are almost negligible in the considered time scale due to large free-energy barriers. Each of these ergodic region corresponds to a *logical state* or *informational state* (σ) of the reservoir and can be described by a sequence of bits (e.g. 0110...00100) containing one of the possible 2^N combinations of N bits. We can construct a function $\hat{\sigma} : \{\psi\} \rightarrow \{\sigma\}$ that partitions the whole phase space into different regions corresponding to different logical states. The logical states of the information reservoir acts as the *information bearing degrees of freedom* (IBD) [18] which are relevant for the information processing. Under each logical state there are multiple microstates $\{\psi\}$ that corresponding to the *non-information bearing degrees of freedom* (NBD) which are not directly relevant for the information processing. The Hamiltonian for the isolated reservoir is $H_{\text{info}}(\psi)$. We assume that under constrained thermal equilibrium with the heat bath, the information reservoir exists in the logical state σ . We define the constrained equilibrium distribution of the microstates (ψ) under this logical state (σ) as

$$p^{\text{eq}}(\psi|\sigma) = \delta_{\sigma, \hat{\sigma}(\psi)} \frac{e^{-\beta H_{\text{info}}(\psi)}}{Z_\sigma} \quad (1.2)$$

where $\beta = \frac{1}{k_B T}$ and Z_σ is a normalization constant defined by $\int d\psi p^{\text{eq}}(\psi|\sigma) = 1$. The Shannon entropy \mathcal{S} corresponding to a phase space distribution $\phi(\psi)$ is defined as

$$\mathcal{S}[\phi] = - \int d\psi \phi(\psi) \ln \phi(\psi) \quad (1.3)$$

(Note that we have used natural logarithm in Eq. (1.3) for convenience instead of more common logarithm of base 2). Using these definitions, we write down the expression for the equilibrium entropy of the distribution of the microstates conditioned on the the logical state of the information reservoir as

$$\mathcal{S}_\sigma^{\text{eq}} = - \int d\psi p^{\text{eq}}(\psi|\sigma) \ln p^{\text{eq}}(\psi|\sigma). \quad (1.4)$$

Similarly we write down the average equilibrium energy as

$$\langle H_{\text{info}}(\psi) \rangle_\sigma^{\text{eq}} = \int d\psi p^{\text{eq}}(\psi|\sigma) H_{\text{info}}(\psi). \quad (1.5)$$

We assume that (i) the NBDs of the information reservoir reach their constrained thermal equilibrium $p^{\text{eq}}(\psi|\sigma)$ very rapidly compared to the time scales of our interest over which any change in σ takes place, and (ii) the average energy and entropy corresponding to all the possible logical states of the reservoir are equal when at thermal equilibrium, i.e., $\langle H_{\text{info}}(\psi) \rangle_\sigma^{\text{eq}} = \langle H_{\text{info}}(\psi) \rangle_{\sigma'}^{\text{eq}}$ and $\mathcal{S}_\sigma^{\text{eq}} = \mathcal{S}_{\sigma'}^{\text{eq}}$ for any σ and σ' . The assumption (i) implies that for all practical purposes the NBDs of the information reservoir always remain in thermal equilibrium when connected to an additional system of interest. If the additional system of interest takes the information reservoir from one logical state to the another, the equality of average energy criteria in assumption (ii) implies the change in logical state of the information reservoir does not have any energetic cost. The equality of the entropy of each logical state in the assumption (ii) leads to the conclusion that under any transformation of the IBDs the entropy change due to the NBDs can be neglected.

At any time t the full statistical description of microscopic state of the reservoir is given by $p_t(\psi)$ and it can be related to the conditional distribution of microstates under given logical states

as $p_t(\psi) = \sum_{\sigma} \bar{p}_t(\sigma) p_t(\psi|\sigma)$ where $\bar{p}_t(\sigma)$ is distribution of the logical states of the reservoir and $p_t(\psi|\sigma)$ is the conditional distribution of ψ given microstate t . Using this relation and assumptions (i) and (ii), it is possible to show that at any time t , the total entropy of the information reservoir $\mathcal{S}_{IR}(t) = -\int d\psi p_t(\psi) \ln p_t(\psi)$ can be split into two parts

$$\mathcal{S}_{IR}(t) = \mathcal{S}_{IBD}(t) + \sum_{\sigma} \bar{p}_t(\sigma) \mathcal{S}_{\sigma}^{\text{eq}}, \quad (1.6)$$

where $\mathcal{S}_{IBD}(t) = -\sum_{\sigma} \bar{p}_t(\sigma) \ln \bar{p}_t(\sigma)$ (see Ref. [17] for details). Here \mathcal{S}_{IBD} is the Shannon entropy associated with the logical states (σ). The other part of the contribution to the entropy comes from the conditional distribution of the microstates given the logical state of the reservoir. As we have assumed the conditional distribution of the microstates given the logical state thermalizes very rapidly and $\mathcal{S}_{\sigma}^{\text{eq}} = \mathcal{S}_{\sigma'}^{\text{eq}}$, we see that the change in the Shannon entropy of the information reservoir for a protocol comes almost exclusively from the information bearing degrees of freedom, and in this limit we have

$$\Delta \mathcal{S}_{IR} = \Delta \mathcal{S}_{IBD}. \quad (1.7)$$

Thus, the change in Shannon entropy of the distribution of logical states of the information reservoir is equal to the change in Shannon entropy of the memory storage device. This justifies the abstraction of a physical memory-storage device as a memory tape (information reservoir).

1.2.5 Autonomous and non-autonomous models of Maxwell's demons

In Maxwell's original thought experiment and the Szilard engine, an external agent (the demon) makes measurements on the system and provides feedback accordingly, to seemingly violate the second law of thermodynamics. In these models we exclude the details of physical nature of the agent from our consideration and only focus on the system that is being manipulated. These models of the Maxwell's demon fall into the paradigm of *non-autonomous* demons.

Alternatively, one can ask whether it is possible to replace the agent with a purely mechanical contraption or a physical gadget that is programmed to apply a control protocol to rectify thermal fluctuation to extractable work. We call this paradigm the *autonomous* demon [18]. Smoluchowski's trapdoor [19, 20, 21] and Feynman's ratchet-and-pawl [22, 23] are attempts to design such autonomous gadgets for the rectification of the thermal fluctuations to work. However, a close inspection on these models shows that they cannot cause a violation of the second law. For example, Feynman in his ratchet-and-pawl analysis showed that if both the thermal baths are set at the same temperature the ratchet-pawl contraption will also be affected by thermal fluctuations making it ineffective for rectification of heat to work [22]. Current consensus in the scientific community is that such mechanical feedback control system by itself cannot operate so as to convert heat directly to work without any dissipation. However, from Bennett's analysis, we can see that it may be possible to construct an autonomous systems that can convert heat to work without dissipation but only with the inclusion of an information reservoir in the model. Bennett argued that it is possible to convert heat from a single thermal reservoir directly to work using a mechanical device in a cyclic process, but the decrease in entropy due to this process must be compensated by randomizing the logical states of information reservoir which

initially existed in a low entropy state [12]. The construction of such a device is based on the idea of the physical nature of the information as suggested by Landauer [10]. Thus we can think of an autonomous version of Maxwell’s demon where a device and an information reservoir are in contact with a heat bath, and the device extracts heat from the heat bath and converts it directly to work in a cyclic process, while writing information about its physical states in the information reservoir. We will refer this class of autonomous Maxwell’s demons as *memory tape models* or *information ratchets* as they convert heat to work at the cost of writing information to a memory storage device. (see Fig. 1.4)

A stochastic model of such an autonomous Maxwell’s demon was proposed by Mandal and Jarzynski (MJ) [15]. The MJ model involves a system which has three states with equal energy, a pulley system with a mass, and a sliding memory tape containing N bits. The entire setup is immersed at a heat bath. The information reservoir, the pulley system and the system are coupled to each other in such a way that each bit of the memory tape interacts with the system for a fixed amount of time and then it is replaced with the next bit in the memory tape. It was shown that for proper sets of parameters this system can extract heat from the thermal reservoir to raise the mass against gravity in the pulley at the cost of writing information to the memory tape.

1.2.6 Information thermodynamics - a transdisciplinary field

Models similar to the MJ model have been developed for both classical and quantum systems [16, 24, 25, 26, 27, 28, 29, 30, 31, 32, 33, 34, 35, 36, 37, 38]. The computational and information-theoretic aspects of memory tape autonomous demons have also been explored in Refs. [39, 40, 41, 42, 43, 44, 45, 46, 47]. Over the last three decades, the field of stochastic

thermodynamics [48, 49] has emerged as a key area of research in the mesoscopic physics where fluctuations are prevalent. Investigations of models of Maxwell's demons have led to a better understanding of the connection between information theory and statistical physics and discovery of several fluctuation relations concerning feedback-controlled systems [49, 50, 51, 52, 53, 54, 55, 56, 57, 58]. These studies now have emerged as sub-field of information thermodynamics and also have lead to several experiments [5, 48, 59]. The design and implementation of these models of Maxwell's demons or information engines also require efficient engineering of mesoscopic systems which connects information thermodynamics to the fields of nanotechnology, chemistry, control systems and quantum technology. [60, 61, 62, 63, 64].

1.3 Organization and thematic overview of the thesis

1.3.1 From feedback-controlled systems to non-feedback systems

A key theme of this thesis is the investigation of the time evolution of the *statistical state* of a system when some form of control is applied to it. The chapters in the thesis are arranged such that we start our discussion with closed-loop or feedback-controlled systems and progress towards open-loop or non-feedback systems [62]. Chapters 2, 3 and 4 deal with closed-loop systems where we have an agent performing measurement-based feedback control on the system (non-autonomous demon) with the relevant theory presented in Chapter 2 and example toy models in Chapters 3 and 4 . In Chapter 5 we take the feedback-controlled model (non-autonomous demon) from Chapter 4 and convert it to a non-feedback model (autonomous demon) that can achieve the same behavior as the feedback-controlled model. Unlike previous chapters related to Maxwell's demons, in Chapter 6 we discuss an open-loop (non-feedback) control system that

is related to the field of shortcuts to adiabaticity [65]. In Chapter 7 we conclude the thesis by presenting future research directions.

1.3.2 Information as fuel in a double quantum dot

A large part of this thesis is related to the “Information as Fuel” (IaF) collaborative project where the goal is to implement an electronic model of Maxwell’s demon [4] in a double quantum dot (DQD) system [66]. Chapter 2 discusses the theory of continuous monitoring and feedback control that is required for investigation of the models of feedback-controlled Maxwell’s demons and also presents the multiple-timescale perturbation (MTSP) analysis for studying separation of timescales in such systems. Chapter 3 discusses a relatively simple toy model of feedback-control demon and shows how MTSP analysis can be used for analyzing such systems. Chapter 4 introduces a quantum version of the DQD Maxwell’s demon and presents trajectory simulations of the model. Chapter 5 is an independent spin-off from the original goal of the IaF project where I use the same DQD Maxwell’s demon [4] but investigate it in the context of information ratchets to study the connection between non-autonomous and autonomous paradigms of the Maxwell’s demon, and discuss the accounting of consumption of information resources required for such a model. Chapter 6 contains independent research work that is not related to the IaF collaboration but explores ideas related to non-feedback control of a driven system to achieve quasistatic behavior.

1.3.3 Modelling frameworks and theoretical tools

We explore various toy models throughout the thesis which are investigated using a variety theoretical tools and modelling frameworks. Here I give a brief summary of the modelling frameworks and theoretical tools used in each of the chapters. Chapter 2 presents the theory for non-autonomous feedback control [61, 62] primarily using a framework in which both the system of interest and the control parameter evolve under classical diffusive dynamics [48, 67]. Later in the same chapter, the cases of open quantum systems dynamics [63, 64] and discrete state stochastic dynamics [48] of the system are discussed. In Chapter 3, the dynamics of the toy model system are modelled with the framework of classical discrete-state stochastic processes and the control parameter dynamics are modelled with a classical diffusive process. This chapter focuses on the application of the master equation framework for such processes. Chapter 4 deals with a system that is modelled within the framework of open quantum systems and the control parameter is modelled with classical diffusive dynamics. Instead of using a master equation approach, this chapter explores a simulation-based approach [68] to investigate the properties of the system under consideration. In Chapter 5 the framework of classical discrete-state stochastic process is used to model the system and tools from network theory of master equations [69] and stochastic thermodynamics are used to analyze it. In Chapter 6 we investigate a toy model of classical periodically driven asymmetric double well system. The framework of this chapter is based on classical Hamiltonian mechanics [70, 71] of one degree of freedom system, and we additionally use tools from chaos theory, ergodic theory and dynamical systems theory [72, 73] to analyze this model.

1.4 Summary of chapters

The Chapters 2, 3 and 4 of this thesis correspond to works done in collaboration and the Chapters 5 and 6 correspond to works done independently by the author. Refs. [74, 75, 76] also deal with topics similar to the Chapters 2, 3 and 4 of this thesis.

Chapter 2: The key publication relevant to this chapter is Ref. [1]. The modelling framework for continuously monitored feedback controlled system is introduced in this chapter. This chapter contains a pedagogical review of the continuous measurement framework that is required to study non-autonomous models of Maxwell’s demon. Then, a master equation [1] formalism is discussed for studying continuously monitored feedback-controlled system. The master equation formalism is presented for feedback controlled classical diffusive systems extending of the original Quantum Fokker-Planck Master Equation (QFPME) [1] to classical diffusive systems. The multiple-timescale perturbation (MTSP) analysis for time scale separation is also presented for the classical diffusive feedback-controlled systems following the Fock-Liouville space based MTSP analysis of QFPME from Ref. [1]. Finally a comparison of the results for the classical diffusive system with the cases for quantum and discrete state stochastic systems is presented. Hence, this chapter presents a unified framework for modelling continuously monitored feedback-controlled classical, quantum and stochastic systems.

Chapter 3: The key publication relevant to this chapter is also Ref. [1]. In this chapter the formalism introduced in the previous chapter is used to study a toy model of information engine. This toy model was discussed as an example of the application of QFPME, and two different analysis methods were presented in Ref. [1]. In this chapter we discuss one of those methods, the MTSP based analysis, in detail.

Chapter 4: The key publication relevant to this chapter is Ref. [3]. This chapter discusses the quantum version of the classical nonautonomous model of DQD Maxwell’s demon [4] following Ref. [3]. In Ref. [3], the model was analyzed based on both the master equation and trajectory simulation methods of which we only discuss the trajectory simulation based approach in this chapter. The chapter presents the theoretical details of modelling of the quantum version of the demon and presents methods of implementation details of the simulations. Simulation results from Ref. [3] are presented in this chapter to discuss different qualitative behavior of the demon and the emergence of classical model from the quantum model.

Chapter 5: The key publication relevant to this chapter is Ref. [2]. In this chapter we discuss a simple strategy for constructing an information ratchet or memory-tape model of Maxwell’s demon from a feedback-controlled model. Here, we illustrate our approach by converting the feedback-controlled double quantum dot model [4] (the classical version of the model discussed in the previous chapter) to a memory-tape model. We use the underlying network structure of the original model to design a set of bit interaction rules for the information ratchet. The new model is solved analytically in the limit of long interaction times. For finite-time interactions, semi-analytical phase diagrams of operational modes are obtained. Stochastic simulations are presented to support the theoretical results. This chapter is directly adapted from Ref. [2].

Chapter 6: The results of this chapter are yet to be published. In this chapter the theory of flow-field based fast-forward shortcuts to adiabaticity [77] is extended to classical periodically driven (Floquet) Hamiltonian systems of one degree of freedom. Relevant background theory relating to the shortcuts to adiabaticity in classical system is presented at the beginning of the chapter. Then we discuss how the dynamical map for periodic evolution of the angle variable on the preserved energy shell can be constructed. We analyze a toy model of an asymmetric driven

double well and show a bifurcation phenomenon in the angle variable map. We also discuss the transfer operator theory to show how the probability distribution of the angle variable evolves in the periodic driving using the toy model under consideration.

Chapter 2: Unified perspective on non-autonomous feedback performed on continuously measured systems

This chapter is based primarily on work done in collaboration with Björn Annby-Andersson, Pharnam Bakhshinezhad, Guilherme De Sousa, Christopher Jarzynski, Peter Samuelsson, and Patrick P. Potts, which has been published in the article “Quantum Fokker-Planck Master Equation for Continuous Feedback Control” [1]. Guilherme De Sousa and I together worked on the Fock-Liouville space based multiple-timescale perturbation (MTSP) analysis of master equation to calculate the first-order corrections to the separation of time scales approximation in Ref. [1]. In this chapter we present the theory of continuous measurement and feedback formalism, the master equation and MTSP analysis from Ref. [1] in the framework of classical diffusive dynamics. Then we compare the classical diffusive case to the quantum and discrete stochastic counterparts.

2.1 Chapter overview

This chapter develops a theory that describes how the statistical state of a continuously monitored feedback-controlled system evolves in time. Sec. 2.2 of the chapter reviews classical measurement theory and the theory of continuous measurements following Refs. [61, 78]. In Sec. 2.3, the feedback-control master equation for classical diffusive and deterministic flow is

derived following the steps of the original derivation of the Quantum Fokker-Planck Master Equation (QFPME) [1, 74, 75]. Sec. 2.4 discusses multiple-timescale perturbation (MTSP) analysis of feedback-lag for the obtained master equation, in the context of the separation of timescales. Then the relation to linear response theory is explored. In Sec. 2.5, we compare the feedback-control master equation for the diffusive flow, and its perturbation limits, with their analogues for quantum and discrete-state stochastic systems.

In summary, this chapter presents a pedagogical discussion of continuous measurement and feedback-controlled dynamics, extending the results of Ref. [1] to classical continuous-degree-of-freedom systems, and a comparative analysis with the quantum and stochastic jump counterparts to illustrate the generality of the formalism across different types of systems. The results from this chapter will be used in Chapters 3 and 4 for analyzing model problems in the context of non-autonomous feedback control and Maxwell’s demons.

2.2 Review of classical continuous measurement formalism

The classical measurement process in the engineering and data assimilation literature is often described by the name *state based filtering* or *probabilistic state space models*, and in mathematics as *nonlinear stochastic filtering theory*. Here we present a simplified version of the key ideas of this theory following Refs. [61, 62, 79, 80], and by drawing classical analogues of quantum weak measurement theory discussed in Ref. [74, 75, 78].

2.2.1 Evolution without measurement

First we discuss a situation in which a system evolves without being measured by an external agent. With this discussion, we also introduce the distinction between a system's physical and statistical states.

We consider a classical one dimensional system whose *physical state* is described by a continuous variable X at time t . The dynamics of this state variable X can be a deterministic flow or a Markovian diffusive process, and can be described by an ordinary differential equation or a Langevin equation (stochastic differential equation), respectively. If we consider an ensemble of trajectories generated under these dynamics, then the probability density of the state variable at time t is given by $\rho(X, t)$, which is normalized as $\int dX \rho(X, t) = 1$. The master equation for the time evolution $\rho(X, t)$ is

$$\frac{\partial \rho(X, t)}{\partial t} = \hat{\mathcal{L}}_X \rho(X, t). \quad (2.1)$$

Here, $\hat{\mathcal{L}}_X$ is a linear operator that acts on the probability density $\rho(X, t)$. The subscript X in $\hat{\mathcal{L}}_X$ implies that the operator acts on functions of variable X . For example, if the dynamics of the physical state X are given by an Ornstein–Uhlenbeck process,

$$\dot{X} = -\alpha X + \xi, \quad \langle \xi(t) \rangle = 0, \quad \langle \xi(0)\xi(t) \rangle = 2\Delta\delta(t), \quad (2.2)$$

then the corresponding master equation for the evolution of $\rho(X, t)$ is

$$\frac{\partial \rho(X, t)}{\partial t} = \alpha \frac{\partial(X\rho(X, t))}{\partial X} + \Delta \frac{\partial^2(\rho(X, t))}{\partial X^2}. \quad (2.3)$$

In this case the operator $\hat{\mathcal{L}}_X$ is

$$\hat{\mathcal{L}}_X(*) = \alpha \frac{\partial(X*)}{\partial X} + \Delta \frac{\partial^2(*)}{\partial X^2}. \quad (2.4)$$

We also consider a time-dependent master equation where the linear operator $\hat{\mathcal{L}}_X(D(t))$ explicitly depends on a time-dependent parameter $D(t)$:

$$\frac{\partial \rho(X, t)}{\partial t} = \hat{\mathcal{L}}_X(D(t)) \rho(X, t). \quad (2.5)$$

First, we consider the case where $D(t)$ represents a predetermined control protocol. Later we will discuss how $D(t)$ can be related to measurement outcomes to create a measurement-based, feedback-controlled system.

To avoid the ambiguity with the *physical state* of the system X , we will use the term *statistical state* to refer to the probability distribution that captures our knowledge of the system. Suppose we start with a prior guess about the initial condition of the physical state X of our system. This guess or knowledge about the physical state is captured by the a distribution function $\rho_0(X)$, from which, we assume, the initial condition X has been sampled. This distribution function $\rho_0(X)$ is the initial statistical state of the system. Using $\rho_0(X)$ as the initial condition, one can obtain the distribution at time t as $\rho(X, t)$ by solving Eq. (2.5).

If exact knowledge about the initial system state, say $X = X_0$ at $t = 0$ is known, then the initial statistical state is given as $\rho_0(X) = \delta(X - X_0)$. Now the system evolves from $0 \leq t < \tau$. We assume that the evolution happens without any measurement on the system. However, it is possible to make a guess about the final state of the system at time $t = \tau$, since the statistical state

$\rho(X, t)$ has evolved deterministically under the master Eq. (2.5). The final distribution under this evolution is formally given as

$$\rho(X, \tau) = \mathcal{T}\{e^{\int_0^\tau dt \hat{\mathcal{L}}_X(D(t))} \delta(X - X_0)\} \quad (2.6)$$

where \mathcal{T} signifies time ordering in the integral. Similar arguments hold if there is uncertainty in the knowledge of initial state of the system. For any general initial statistical state $\rho_0(X)$, the final statistical state of the system is

$$\rho(X, \tau) = \mathcal{T}\{e^{\int_0^\tau dt \hat{\mathcal{L}}_X(D(t))} \rho_0(X)\}. \quad (2.7)$$

2.2.2 Evolution with a single purely Bayesian measurement

Now we introduce a single measurement to the setup discussed above. We imagine that an external agent makes an instantaneous measurement of an observable $O(X)$ of the system's state at time t' , where $0 < t' < \tau$. The initial statistical state of the system is $\rho_0(X)$ and let it evolve without measurement from $t = 0$ to $t = t'$. The statistical state of the system at $t = t'$ is

$$\rho(X, t') = \mathcal{T}\{e^{\int_0^{t'} dt \hat{\mathcal{L}}_X(D(t))} \rho(X, 0)\} \quad (2.8)$$

Suppose the agent obtains the measurement of $O(X)$ outcome $z_{t'}$ for the instantaneous measurement at time $t = t'$. We emphasize that the measurement process here has no *back-action*, i.e., the measurement process does not perturb the system state X . In this case the measurement is a *purely Bayesian* measurement [61], and the post-measurement statistical state of the system

at time t' is given by the conditional distribution $\rho(X, t'|z_t)$ if the agent keeps a record of the measurement outcome $z_{t'}$. The post-measurement statistical state $\rho(X, t'|z_t)$ is related to the pre-measurement statistical state $\rho(X, t')$ by Bayes' theorem:

$$\rho(X, t'|z_t) = \mathcal{M}_{z_{t'}} [\rho(X, t')] = \frac{\rho_{t'}(z_{t'}|X)\rho(X, t')}{\int dX \rho_{t'}(z_{t'}|X)\rho(X, t')} \quad (2.9)$$

Here $\rho_{t'}(z_{t'}|X)$ is the distribution function of the measurement outcome $z_{t'}$ given the system state is X at time t' . We refer to the distribution function $\rho_{t'}(z_{t'}|X)$ as the *measurement model*. The denominator in Eq. (2.9) is the probability distribution of obtaining the outcome $z_{t'}$ at $t = t'$, when all possible system configurations are considered. We write the denominator as the distribution function $\rho_{t'}(z_{t'})$, which can be understood as the expectation value of the measurement model $\rho_{t'}(z_{t'}|X)$ when the system state X is sampled from the distribution $\rho(X, t')$. Hence, we can write it as

$$\rho_{t'}(z_{t'}) = \int dX \rho_{t'}(z_{t'}|X)\rho(X, t') = \langle \rho_{t'}(z_{t'}|X) \rangle_{\rho(X, t')} \quad (2.10)$$

In Eq. (2.9), we have introduced the functional transformation $\mathcal{M}_{z_{t'}}$ to describe the measurement operation on the statistical state $\rho(X, t')$. Note that this transformation or Bayesian *measurement map* [79] given by $\mathcal{M}_{z_{t'}}$ is non-linear due to the normalization term $\rho_{t'}(z_{t'})$ in the denominator.

After the measurement, the statistical state of the system evolves again under the dynamics generated by $\hat{\mathcal{L}}_X(D(t))$ from time $t = t'$ to $t = \tau$. The final statistical state of the system is

$$\begin{aligned} \rho(X, \tau|z_{t'}) &= \mathcal{T}\{e^{\int_{t'}^{\tau} dt \hat{\mathcal{L}}_X(D(t))} \rho(X, t'|z_{t'})\} \\ &= \mathcal{T}\left\{e^{\int_{t'}^{\tau} dt \hat{\mathcal{L}}_X(D(t))} \mathcal{M}_{z_{t'}} \left[\mathcal{T}\{e^{\int_0^{t'} dt \hat{\mathcal{L}}_X(D(t))} \rho(X, 0)\} \right] \right\} \end{aligned} \quad (2.11)$$

The final statistical state $\rho(X, \tau | z_{t'})$ generally differs from the final state $\rho(X, \tau)$ in Eq. (2.7) when the system evolves without any measurement. The evolution of the statistical state without any measurement (Eq. (2.7)) is completely deterministic, but the measurement operation in Eq. (2.11) introduces stochasticity in the evolution of the statistical state through the measurement outcome $z_{t'}$. In this case, for every realization of the experiment the final statistical state $\rho(X, \tau | z_{t'})$ depends on the stochastic quantity $z_{t'}$.

2.2.3 Evolution with repeated frequent measurements

Now we consider similar dynamics governed by the master equation (2.5); but in contrast to the single measurement scenario we imagine a repeated measurement process. We discretize the time interval $t = 0$ to $t = \tau$ into N small time intervals of duration δt ; thus $N\delta t = \tau$. We assume the instantaneous measurement operations take place in a repetitive fashion after every δt interval starting from $t = 0$ to the final one at $t = (N - 1)\delta t$. We describe this series of measurements by the measurement outcomes $\{z_k\}_{k=0}^{N-1} = \{z_0, z_1, z_2, \dots, z_{N-1}\}$ and corresponding measurement maps $\{\mathcal{M}_{z_k}\}_{k=0}^{N-1}$, where z_k is the outcome of the measurement performed at $t_k = k\delta t$. We now introduce the notion of the measurement trajectory as the ordered sequence $\Gamma_k^{(z)} = (z_0, z_1, z_2, \dots, z_{k-1}, z_k)$ which denotes the outcomes obtained up to time $t = k\delta t$ in a particular realization of the experiment. Between measurements the dynamics are governed by the master equation (2.5). Due to the time-dependent nature of the operator $\hat{\mathcal{L}}_X(D(t))$, the evolution operators in different time intervals δt generally differ from each other. Therefore, we also discretize the control protocol $D(t)$ as the ordered sequence $\Gamma_k^{(D)} = (D_0, D_1, \dots, D_{k-1}, D_k)$. Using the sequence $\Gamma_k^{(D)}$ we can write the sequence of operators $\{\hat{\mathcal{L}}_X(D_k)\}_{k=0}^{N-1}$ to capture the

time-dependent nature of the dynamics of Eq. (2.5). Using these notations we describe the time evolution of the statistical state with repeated measurements as the ordered chain of operations:

$$\rho(X, \tau | \Gamma_{N-1}^{(z)}) = e^{\delta t \hat{\mathcal{L}}_X(D_{N-1})} \mathcal{M}_{z_{N-1}} \circ e^{\delta t \hat{\mathcal{L}}_X(D_{N-2})} \mathcal{M}_{z_{N-2}} \circ \dots \circ e^{\delta t \hat{\mathcal{L}}_X(D_1)} \mathcal{M}_{z_1} \circ e^{\delta t \hat{\mathcal{L}}_X(D_0)} \mathcal{M}_{z_0} [\rho_0(X)]. \quad (2.12)$$

We use the notation \circ to represent functional composition since the measurement maps are non-linear transformations, in contrast to exponentiated operators which are linear. The iterative state evolution in Eq. (2.12) is discussed below in detail.

In the evolution sequence given by Eq. (2.12), at any intermediate time $t = t_k$ with $k \geq 1$, we describe the (pre-measurement) statistical state of the system as

$$\rho(X, t_k | \Gamma_{k-1}^{(z)}) = e^{\delta t \hat{\mathcal{L}}_X(D_{k-1})} \mathcal{M}_{k_{N-1}} \circ \dots \circ e^{\delta t \hat{\mathcal{L}}_X(D_1)} \mathcal{M}_{z_1} \circ e^{\delta t \hat{\mathcal{L}}_X(D_0)} \mathcal{M}_{z_0} [\rho_0(X)] \quad (2.13)$$

The post measurement statistical state at $t = t_k$ is given as $\rho(X, t_k | z_k, \Gamma_{k-1}^{(z)}) \equiv \rho(X, t_k | \Gamma_k^{(z)})$ and it is obtained from the pre-measurement state $\rho(X, t_k | \Gamma_{k-1}^{(z)})$ by the Bayesian update map \mathcal{M}_{z_k} , following the definition from Eq. (2.9) as

$$\begin{aligned} \rho(X, t_k | \Gamma_k^{(z)}) &= \mathcal{M}_{z_k} \left[\rho(X, t_k | \Gamma_{k-1}^{(z)}) \right] \\ &= \left(\frac{\rho_{t_k}^{(m)}(z_k | X, \Gamma_{k-1}^{(z)})}{\rho_{t_k}^{(m)}(z_k | \Gamma_{k-1}^{(z)})} \right) \rho(X, t_k | \Gamma_{k-1}^{(z)}). \end{aligned} \quad (2.14)$$

Here, $\rho_{t_k}^{(m)}(z_k | X, \Gamma_{k-1}^{(z)})$ is the measurement model at time $t = t_k$ and the normalization factor is $\rho_{t_k}^{(m)}(z_k | \Gamma_{k-1}^{(z)}) = \int dX \rho_{t_k}^{(m)}(z_k | X, \Gamma_{k-1}^{(z)}) \rho(X, t_k | \Gamma_{k-1}^{(z)})$. The post-measurement state then evolves

under the master equation (2.5) from $t = t_k$ to $t = t_{k+1}$ to the state

$$\begin{aligned}\rho(X, t_{k+1} | \Gamma_k^{(z)}) &= e^{\delta t \hat{\mathcal{L}}_X(D_k)} \rho(X, t_k | \Gamma_k^{(z)}) \\ &= e^{\delta t \hat{\mathcal{L}}_X(D_k)} \mathcal{M}_{z_k} \left[\rho(X, t_k | \Gamma_{k-1}^{(z)}) \right].\end{aligned}\tag{2.15}$$

Eq. (2.15) is an iterative functional equation that takes the statistical state of the system $\rho(X, t_k | \Gamma_{k-1}^{(z)})$ to $\rho(X, t_{k+1} | \Gamma_k^{(z)})$ due to the instantaneous measurement at $t = t_k$ and then evolution for $t = t_k$ to $t = t_{k+1}$. With Eq. (2.15) the initial state $\rho_0(X)$ is evolved to the final state $\rho(X, \tau | \Gamma_{N-1}^{(z)})$ which is conditioned on the measurement record $\Gamma_{N-1}^{(z)}$.

This discretization scheme mentioned above leads to a trajectory of measurement outcomes $\Gamma_{N-1}^{(z)}$ for every realization. Following classical and quantum measurement theory Refs. [52, 55, 74, 78, 80, 81, 82], we introduce the notion of a path integral that corresponds to a sum over all possible measurement outcome trajectories as,

$$\int \mathcal{D}[\Gamma_{N-1}^{(z)}] := \int \int \cdots \int \int dz_{N-1} dz_{N-2} \dots dz_1 dz_0,\tag{2.16}$$

which will be useful later. Now we define the distribution function of the measurement trajectories,

$$P^{(m)}(\Gamma_{N-1}^{(z)}) = \left[\prod_{k=1}^{N-1} \rho_{t_k}^{(m)}(z_k | \Gamma_{k-1}^{(z)}) \right] \rho_{t_0}^{(m)}(z_0),\tag{2.17}$$

where, $\rho_{t_0}^{(m)}(z_0) = \int dX \rho_{t_0}^{(m)}(z_0 | X) \rho_0(X)$, and $\rho_{t_0}^{(m)}(z_0 | X)$ corresponds to the measurement model at $t = t_0$. The average over all possible measurement trajectories is then given as

$$\mathbf{E}[(*)] := \int \mathcal{D}[\Gamma_N^{(z)}] P^{(m)}(\Gamma_{N-1}^{(z)}) (*),\tag{2.18}$$

which we use later to derive the master equation.

2.2.4 Gaussian measurement model and continuous measurement equation

Next we specify our measurement model by choosing the form of the function $\rho_{t_k}^{(m)}(z_k|X, \Gamma_{k-1}^{(z)})$.

We consider that the agent is monitoring an observable $O(X)$ which is a function of the physical state X . We also assume that the observable does not change with time. Now we introduce a measurement rate or measurement strength λ that captures how close z_k was to the observable $O(X)$ at time $t = t_k$. A higher (lower) value of $\lambda\delta t$ implies more accurate (inaccurate) measurement. In the limit $\lambda \rightarrow \infty$ with a finite δt , we expect $z_k \rightarrow O(X)$. We further assume that the measurement model at time $t = t_k$ is independent of previous measurement outcomes: $\rho_{t_k}^{(m)}(z_k|X, \Gamma_{k-1}^{(z)}) = \rho_{t_k}^{(m)}(z_k|X)$. With these considerations, we choose a Gaussian measurement model [61, 80] in spirit of the Gaussian Kraus operators [78] for the quantum weak measurement model. For any $t = t_k$, this measurement model is

$$\rho_{t_k}^{(m)}(z_k|X) = \mathcal{N} e^{-2\lambda\delta t(z_k - O(X))^2} \quad (2.19)$$

where, $\mathcal{N} = \sqrt{2\lambda\delta t/\pi}$. This measurement model implies the signal generated from the measuring device follows a Gaussian distribution centered around $O(X)$ and has a spread that is controlled by $\lambda\delta t$. For a fixed value of λ , if we decrease the value of δt the spread of this distribution increases. From this we can write,

$$\begin{aligned} \rho_{t_k}^{(m)}(z_k|\Gamma_{k-1}^{(z)}) &= \int dX \rho_{t_k}^{(m)}(z_k|X) \rho(X, t_k|\Gamma_{k-1}^{(z)}) \\ &= \mathcal{N} \int dX e^{-2\lambda\delta t(z_k - O(X))^2} \rho(X, t_k|\Gamma_{k-1}^{(z)}) \end{aligned} \quad (2.20)$$

We perform a change in the measure of integration and write

$$\rho_{t_k}^{(m)}(z_k|\Gamma_{k-1}^{(z)}) = \mathcal{N} \int dO e^{-2\lambda\delta t(z_k-O)^2} \tilde{\rho}(O, t_k|\Gamma_{k-1}^{(z)}) \quad (2.21)$$

where the distribution $\tilde{\rho}(O, t_k|\Gamma_{k-1}^{(z)})$ and $\rho(X, t_k|\Gamma_{k-1}^{(z)})$ are related by

$$dO \tilde{\rho}(O, t_k|\Gamma_{k-1}^{(z)}) = \int dX \delta(O - O(X)) \rho(X, t_k|\Gamma_{k-1}^{(z)}) \quad (2.22)$$

The variable O should not be confused with the function $O(X)$. If δt is small enough, then the spread of the distribution $\mathcal{N}e^{-2\lambda\delta t(z_k-O)^2}$ is much wider than the spread of the distribution $\tilde{\rho}(O, t_k|\Gamma_{k-1}^{(z)})$ in the variable O . Thus, $\tilde{\rho}(O, t_k|\Gamma_{k-1}^{(z)})$ can be approximated as a delta function $\delta(O - \langle O \rangle_{k-1})$ located at the mean

$$\langle O \rangle_{k-1} = \int dO O \tilde{\rho}(O, t_k|\Gamma_{k-1}^{(z)}). \quad (2.23)$$

With this approximation, we rewrite Eq. (2.21) as

$$\rho_{t_k}^{(m)}(z_k|\Gamma_{k-1}^{(z)}) \approx \mathcal{N} \exp \left[-2\lambda\delta t(z_k - \langle O \rangle_{k-1})^2 \right]. \quad (2.24)$$

Then the Bayesian update rule from Eq. (2.14) can be rewritten as

$$\rho(X, t_k|\Gamma_k^{(z)}) = \exp \left[-2\lambda\delta t \left\{ (z_k - O(X))^2 - (z_k - \langle O \rangle_{k-1})^2 \right\} \right] \rho(X, t_k|\Gamma_{k-1}^{(z)}). \quad (2.25)$$

Since z_k is sampled from a Gaussian distribution $\rho_{t_k}^{(m)}(z_k|\Gamma_{k-1}^{(z)})$ in Eq. (2.24), it has the mean $\mathbf{E}[z_k] = \langle O \rangle_{k-1}$ and variance $Var[z_k] = 1/4\lambda\delta t$. We can make a transformation of variables and introduce a new Gaussian random variable ΔW_k :

$$\frac{\Delta W_k}{\sqrt{\delta t}} = 2\sqrt{\lambda\delta t}(z_k - \langle O \rangle_{k-1}). \quad (2.26)$$

Here ΔW_k is sampled from a Gaussian distribution with $\mathbf{E}[\Delta W_k] = 0$ and variance $\mathbf{E}[\Delta W_k^2] = \delta t$. Since δt is a small number we can approximate any realization of ΔW_k^2 by its mean as $\Delta W_k^2 \approx \mathbf{E}[\Delta W_k^2] = \delta t$ in the spirit of the Ito calculus [48, 78]. Using the expression of ΔW_k from Eq. (2.26) in the expression for $\rho(X, t_k|\Gamma_k^{(z)})$, and expanding the exponential terms, we get

$$\begin{aligned} \rho(X, t_k|\Gamma_k^{(z)}) &= (1 + 2\sqrt{\lambda}\Delta W_k(O(X) - \langle O \rangle_{k-1}) - 2\lambda\delta t(\langle O \rangle_{k-1} - O(X))^2)\rho(X, t_k|\Gamma_{k-1}^{(z)}) \\ &\quad + \frac{1}{2}4\lambda\Delta W_k^2(O(X) - \langle O \rangle_{k-1})^2\rho(X, t_k|\Gamma_{k-1}^{(z)}) + \mathcal{O}(\Delta W_k^3) \end{aligned} \quad (2.27)$$

Since $\Delta W_k^2 \approx \delta t$, the terms quadratic in ΔW_k become proportional to δt upon averaging. In the limit $\delta t \rightarrow 0$ we treat the measurement as a continuous signal $\Gamma_k^{(z)} \equiv z(t)$, and we replace $\langle O \rangle_{k-1} \rightarrow \langle O \rangle_t$ to denote its instantaneous value. Using Ito calculus, the limiting value of ΔW_k can be identified as the increment of Brownian motion or *Wiener increment* $dW(t)$ when $\delta t \rightarrow 0$. The Wiener increment dW has the following properties: $\mathbf{E}[dW(t)] = 0$ and $dW^2(t) = dt$ where dt is the infinitesimal differential version of δt and, $\mathbf{E}[A(t)dW(t)] = 0$ for any $A(t)$. Thus, taking the limit $\delta t \rightarrow 0$, we obtain the Ito stochastic differential equation (SDE)

$$d\rho(X, t|z(t)) = 2\sqrt{\lambda}dW(t)(O(X) - \langle O \rangle_t)\rho(X, t|z(t)). \quad (2.28)$$

This equation in classical stochastic filtering theory literature known as the *Kushner Equation* or *Kushner–Stratonovich Equation* [61, 62, 83] for continuous measurement.

When the measurement is followed by an evolution under the master equation, we use Eq. (2.27) in Eq. (2.15), and expand the exponential to obtain,

$$\begin{aligned}
& \rho(X, t_{k+1} | \Gamma_k^{(z)}) \\
&= e^{\delta t \hat{\mathcal{L}}_X(D_k)} \rho(X, t_k | \Gamma_k^{(z)}) \\
&= \left[1 + \delta t \hat{\mathcal{L}}_X(D_k) + \mathcal{O}(\delta t^2) \right] \left(1 + 2\sqrt{\lambda} \Delta W_k (O(X) - \langle O \rangle_{k-1}) - 2\lambda \delta t (\langle O \rangle_{k-1} - O(X))^2 \right) \rho(X, t_k | \Gamma_{k-1}^{(z)}) \\
&+ \frac{1}{2} 4\lambda \Delta W_k^2 \left[1 + \delta t \hat{\mathcal{L}}_X(D_k) + \mathcal{O}(\delta t^2) \right] (O(X) - \langle O \rangle_{k-1})^2 \rho(X, t_k | \Gamma_{k-1}^{(z)}) + \mathcal{O}(\Delta W_k^3).
\end{aligned} \tag{2.29}$$

In the limit $\delta t \rightarrow 0$ limit the equation above reduces to the following stochastic partial differential equation (SPDE):

$$d\rho(X, t | z(t)) = dt \hat{\mathcal{L}}_X(D(t)) \rho(X, t | z(t)) + 2\sqrt{\lambda} dW(O(X) - \langle O \rangle_t) \rho(X, t | z(t)) \tag{2.30}$$

which is a variation of the Kushner equation (2.28) with a deterministic part. This equation in context of quantum mechanics is known as the *Belavkin equation* [61, 78], and here we will refer to Eq. (2.30) as the *classical Belavkin equation* by analogy with the quantum case. Note that Eq. (2.30) is a nonlinear-SPDE for $\rho(X, t | z(t))$ as the average $\langle O \rangle_t$ depends on the statistical state $\rho(X, t | z(t))$ as $\langle O \rangle_t = \int dX O(X) \rho(X, t | z(t))$. However the non-linearity is attached to the stochastic part of Eq. (2.30).

We have derived Eq. (2.28) and Eq. (2.30) following analogies with quantum weak mea-

surement theory [74, 78]. For simplicity we have kept our discussion limited to the case where the physical state of the system X , the observable $O(X)$ and the control parameter $D(t)$ are all scalar quantities. The generalization of Eq. (2.28) and Eq. (2.30) to the multivariate case is possible [61, 62]. A special case of Eq. (2.30) is also of interest: when the operator $\mathcal{L}(D(t))$ corresponds to linear diffusion or Ornstein–Uhlenbeck (OU) process, we obtain the equation for the Kalman-Bucy filter [62].

2.3 Master equation for continuously monitored feedback-controlled diffusive flows

In this section, we derive a master equation for continuously monitored, feedback-controlled diffusive systems as an extension of the QFPME to classical diffusive and deterministic processes. The derivation shown here follows the same steps as the derivation of the QFPME for quantum systems given in Ref. [1, 74].

2.3.1 Filtering equation for the measurement signal

So far we have considered the case where the control protocol $D(t)$ (or equivalently $\Gamma_N^{(D)}$) was predetermined. To introduce the feedback control in our model we now make the value of the control parameter $D(t)$ at time $t = t'$ functionally dependent on the past measurement signal up to that time instant $z(t)$, $0 \leq t \leq t'$. In the discrete case we write it as $D_k \equiv D_k[\Gamma_k^{(z)}]$. This also implies that the trajectory of the control parameter $\Gamma_k^{(D)}$ is a function of the trajectory of measurement signal $\Gamma_k^{(z)}$, i.e. $\Gamma_k^{(D)} \equiv \Gamma_k^{(D)}[\Gamma_k^{(z)}]$. The choice of this functional relation between D_k and $\Gamma_k^{(z)}$ defines a filtering process that converts the measurement signal from the detector

to a feedback control protocol. For our model, we chose the filtering to be a low-pass filter (exponential smoothing) over the measurement trajectory:

$$D_k \equiv D_k[\Gamma_k^{(z)}] = \sum_{i=0}^k \gamma \delta t e^{-\gamma(k-i)\delta t} z_i \quad (2.31)$$

For the continuous case this relation is written as

$$D(t) = \int_{-\infty}^t ds \gamma e^{-\gamma(t-s)} z(s) \quad (2.32)$$

This signal filtering protocol mimics a detector with a finite bandwidth [1, 61, 74] where the control protocol is a smoothed version of the measurement signal. In Eqs. (2.31) and (2.32), we have introduced the signal filtering rate (or bandwidth) γ , which controls weighting coefficients for the averaging of the measurement signal. A large value of γ implies the filtering kernel dies out quickly and does not go back much in the past trajectory; and hence the control parameter D_k will be very close to the state of the current measurement signal output z_k . As a result the noise from the measurement signal will affect the feedback signal more and feedback will be noisy. In contrast, a small value of γ implies that the filtering kernel takes account of the long past of the measurement trajectory. In this case the control parameter D_k will move slowly compared to the measurement signal variable z_k and thus the feedback signal will be lagging behind the measurement signal but will be relatively smoother.

Notice that the current control parameter D_k can be calculated from the state of the control parameter at the previous time instant (D_{k-1}) and the current measurement outcome z_k . This can

be seen by rewriting the Eq. (2.31) as

$$\begin{aligned} D_k &= \gamma \delta t z_k + \sum_{i=0}^{k-1} \gamma \delta t e^{-\gamma(k-i)\delta t} z_i \\ &= \gamma \delta t z_k + e^{-\gamma \delta t} D_{k-1} \end{aligned} \quad (2.33)$$

Now by replacing z_k with ΔW_k from Eq. (2.26) and expanding $e^{-\gamma \delta t}$ in a Taylor series we get,

$$D_k - D_{k-1} = \gamma \delta t (\langle O \rangle_{k-1} - D_{k-1}) + \frac{\gamma}{2\sqrt{\lambda}} \Delta W_k + \mathcal{O}(\delta t^2). \quad (2.34)$$

Taking the limit $\delta t \rightarrow 0$, and treating $D(t)$ as a continuous signal, we obtain the stochastic differential equation (SDE)

$$dD(t) = \gamma (\langle O \rangle_t - D(t)) dt + \frac{\gamma}{2\sqrt{\lambda}} dW(t) \quad (2.35)$$

From Eq. (2.35) we see that the control parameter evolves under an Ornstein–Uhlenbeck process similar to an overdamped Brownian particle under a time-dependent quadratic potential centered at $\langle O \rangle_t$. [1]

2.3.2 Derivation of master equation

Using the path averaging introduced in Eq. (2.18), we define a joint distribution

$$\rho(X, \tilde{D}, t_k) = \mathbf{E} \left[\rho(X, t_k | \Gamma_{k-1}^{(z)}) \delta(D_k[\Gamma_k^{(z)}] - \tilde{D}) \right]. \quad (2.36)$$

This definition can be understood as an average of the function $\rho(X, t_k | \Gamma_{k-1}^{(z)})$ over the distribution of measurement trajectories up to time $t = t_k$, with a constraint that only the measurement trajectories that result in the feedback variable $D(t_k) = D_k$ at time $t = t_k$ contribute to the average. For the continuous case we denote this joint distribution as

$$\begin{aligned}\rho(X, \tilde{D}, t) &= \mathbf{E} \left[g(D[z(t)], X, \tilde{D}, t) \right] \\ &= \mathbf{E} \left[\rho(X, t | z(t)) \delta(D[z(t)] - \tilde{D}) \right]\end{aligned}\tag{2.37}$$

where we have defined $g(D[z(t)], X, \tilde{D}, t) = \rho(X, t | z(t)) \delta(D[z(t)] - \tilde{D})$. Notice that the dependence of $g(D[z(t)], X, \tilde{D}, t)$ on $z(t)$ is implicit and is encoded by the two functions $D(t)[z(t)]$ and $\rho(X, t | z(t))$. We already know the stochastic differential equations (SDE) for the evolution of these quantities from Eq. (2.30) and Eq. (2.35). From now on we will denote $g(D[z(t)]; X, \tilde{D}, t)$ as g ; $D(t)[z(t)]$ as D ; and $\rho(X, t | z(t))$ as ρ for conciseness.

We now follow the standard method of derivation of a Fokker-Planck equation from a SDE [61]. To obtain a stochastic differential equation for the evolution of $g = \rho \delta(D - \tilde{D})$, we first need to obtain the SDE for the evolution of $\delta(D - \tilde{D})$. Using *Ito's Lemma* on Eq. (2.35), we can write down a SDE of $\delta(D - \tilde{D})$ for a fixed \tilde{D} as

$$\begin{aligned}d\delta(D - \tilde{D})|_{\tilde{D}} &= dt \gamma (\langle O \rangle_t - D) \left[\frac{\partial \delta(D - \tilde{D})}{\partial D} \right]_{\tilde{D}} + dt \frac{1}{2} \left(\frac{\gamma}{2\sqrt{\lambda}} \right)^2 \left[\frac{\partial^2 \delta(D - \tilde{D})}{\partial D^2} \right]_{\tilde{D}} \\ &\quad + dW \left(\frac{\gamma}{2\sqrt{\lambda}} \right) \left[\frac{\partial \delta(D - \tilde{D})}{\partial D} \right]_{\tilde{D}}\end{aligned}\tag{2.38}$$

Now to obtain the SDE for g (for a fixed \tilde{D} , we omit the subscripts from now on) we have

$$dg = \delta(D - \tilde{D}) d\rho + \rho d\delta(D - \tilde{D}) + d\delta(D - \tilde{D}) d\rho\tag{2.39}$$

Using the expression for $d\delta(D - \tilde{D})$ from Eq. (2.38), the expression for $d\rho$ from Eq. (2.30), and $dW(t)^2 = dt$, we write,

$$dg = dt \left[\delta(D - \tilde{D}) \hat{\mathcal{L}}_X(D) \rho + \gamma (O(X) - D) \frac{\partial \delta(D - \tilde{D})}{\partial D} \rho + \frac{\gamma^2}{8\lambda} \frac{\partial^2 \delta(D - \tilde{D})}{\partial D^2} \rho \right] + dW(t) [\dots] \quad (2.40)$$

where we have collected the terms proportional to dt and $dW(t)$ separately. We have omitted the details of the terms proportional to $dW(t)$ for conciseness here since eventually they will vanish. We now use some properties of delta functions on the terms that are proportional to dt . For the first term, using $\delta(x - a)f(x) = \delta(x - a)f(a)$, we get

$$\begin{aligned} \delta(D - \tilde{D}) \hat{\mathcal{L}}_X(D) \rho &= \delta(D - \tilde{D}) \hat{\mathcal{L}}_X(\tilde{D}) \rho \\ &= \hat{\mathcal{L}}_X(\tilde{D}) \left[\delta(D - \tilde{D}) \rho \right] = \hat{\mathcal{L}}_X(\tilde{D}) g. \end{aligned} \quad (2.41)$$

For the second term we use $\delta(x - a)f(x) = \delta(x - a)f(a)$ and $\frac{\partial \delta(x-y)}{\partial x} = -\frac{\partial \delta(x-y)}{\partial y}$ to get the following simplification:

$$\begin{aligned} \gamma (O(X) - D) \frac{\partial \delta(D - \tilde{D})}{\partial D} \rho &= -\gamma (O(X) - D) \frac{\partial \delta(D - \tilde{D})}{\partial \tilde{D}} \rho \\ &= -\gamma \frac{\partial}{\partial \tilde{D}} \left[(O(X) - \tilde{D}) \delta(D - \tilde{D}) \rho \right] \\ &= -\gamma \frac{\partial}{\partial \tilde{D}} \left[(O(X) - \tilde{D}) g \right] \end{aligned} \quad (2.42)$$

For the third term, using $\frac{\partial^2 \delta(x-y)}{\partial x^2} = \frac{\partial^2 \delta(x-y)}{\partial y^2}$, we get

$$\frac{\gamma^2}{8\lambda} \frac{\partial^2 \delta(D - \tilde{D})}{\partial D^2} \rho = \frac{\gamma^2}{8\lambda} \frac{\partial^2 \delta(D - \tilde{D})}{\partial \tilde{D}^2} \rho = \frac{\gamma^2}{8\lambda} \frac{\partial^2 g}{\partial \tilde{D}^2} \quad (2.43)$$

Thus we can rewrite Eq. (2.40) as

$$dg = dt \left[\hat{\mathcal{L}}_X(\tilde{D})g - \gamma \frac{\partial}{\partial \tilde{D}} \left[(O(X) - \tilde{D}) g \right] + \frac{\gamma^2}{8\lambda} \frac{\partial^2 g}{\partial \tilde{D}^2} \right] + dW(t) [\dots] \quad (2.44)$$

Now we take average over all measurement trajectories (note that $\mathbf{E}[dW(\dots)] = 0$), and then

defining $\frac{\partial \rho}{\partial t} := \frac{d\mathbf{E}[g]}{dt}$, we get the final result:

$$\boxed{\frac{\partial \rho(X, \tilde{D}, t)}{\partial t} = \hat{\mathcal{L}}_X(\tilde{D})\rho(X, \tilde{D}, t) + \gamma \frac{\partial}{\partial \tilde{D}} \left[(\tilde{D} - O(X)) \rho(X, \tilde{D}, t) \right] + \frac{\gamma^2}{8\lambda} \frac{\partial^2 \rho(X, \tilde{D}, t)}{\partial \tilde{D}^2}} \quad (2.45)$$

For convenience we define the Ornstein-Uhlenbeck operator of \tilde{D} with $O(X)$ as a parameter as

$$\hat{\mathcal{F}}_{\tilde{D}}(X)(*) = \gamma \frac{\partial}{\partial \tilde{D}} \left[(\tilde{D} - O(X)) (*) \right] + \frac{\gamma^2}{8\lambda} \frac{\partial^2}{\partial \tilde{D}^2} (*) \quad (2.46)$$

With this we rewrite Eq. (2.45) as

$$\boxed{\frac{\partial \rho(X, \tilde{D}, t)}{\partial t} = \left[\hat{\mathcal{L}}_X(\tilde{D}) + \hat{\mathcal{F}}_{\tilde{D}}(X) \right] \rho(X, \tilde{D}, t)} \quad (2.47)$$

This equation can be interpreted as follows. $\rho(X, \tilde{D}, t)$ describes evolving statistical state of an ensemble of physical system state X and the control parameter \tilde{D} , which is being calculated by measuring the observable $O(X)$ and then filtering the measurement outcomes by Eq. (2.32).

The operator $\hat{\mathcal{L}}_X(\tilde{D})$ generates the dynamics of X , which depend on the control parameter \tilde{D} . The operator $\hat{\mathcal{F}}_{\tilde{D}}(X)$ generates the dynamics of the control parameter \tilde{D} , which depends on the evolution of the state variable X through the measurements of the observable $O(X)$. This equation (Eq. (2.47)) is Markovian and deterministic in comparison to the Classical Belavkin

equation (Eq. (2.30)), which is non-Markovian [since it has an explicit dependence on the past trajectory $z(t)$] and stochastic. Reducing a non-Markovian equation to a Markovian equation by adding filtering and averaging is an example of Markovian embedding of the dynamics.

2.3.3 Effective coupled Langevin equations for the system-detector dynamics

From Eq. (2.45) we can write down Langevin equations that would generate the given Fokker-Planck Eq. (2.45). Suppose X obeys a Langevin equation with a term $F(X, \tilde{D})$ and a noise term $\eta_X(t)$ where $\eta_X(t)$, is white noise with the properties, $\langle \eta(t) \rangle = 0$ and $\langle \eta_X(0)\eta_X(t) \rangle = 2\Delta\delta(t)$. The associated Fokker-Planck dynamics of X are given by $\hat{\mathcal{L}}_X(\tilde{D})$, with \tilde{D} as the control parameter. Then we consider a coupled Langevin dynamics of X and \tilde{D} :

$$\dot{X} = F(X, \tilde{D}) + \eta_X(t) \quad (2.48)$$

$$\dot{\tilde{D}} = \gamma(O(X) - \tilde{D}) + \eta_{\tilde{D}}(t) \quad (2.49)$$

where the noise $\eta_{\tilde{D}}(t)$ is white noise with the following properties

$$\langle \eta_{\tilde{D}}(t) \rangle = 0, \quad \langle \eta_{\tilde{D}}(0)\eta_{\tilde{D}}(t) \rangle = \frac{\gamma^2}{4\lambda}\delta(t) \quad (2.50)$$

These coupled Langevin equations will generate a dynamics that correspond to the joint system-controller master equation (2.45). These Langevin equations can be directly simulated to generate the statistical properties of the feedback-controlled system without explicitly simulating the underlying measurement and filtering processes.

2.4 Separation of timescales using multiple-timescale perturbation (MTSP) approach

2.4.1 General formal solution

In this section we present a multiple-timescale perturbation (MTSP) analysis [1, 72, 84, 85, 86] of the detector and system dynamics, when the detector dynamics are fast. We start with the feedback control master equation Eq. (2.45) and introduce two natural timescales - for the system dynamics, $(1/\Gamma_{(\mathcal{L}_X)})$, and for the control parameter dynamics, $(1/\gamma)$. Now introduce a scaled Ornstein–Uhlenbeck (OU) operator

$$\tilde{\mathcal{F}}_{\tilde{D}}(X) = \Gamma_{(\mathcal{L}_X)} \frac{\partial}{\partial \tilde{D}} \left(\tilde{D} - O(X) \right) + \frac{\gamma \Gamma_{(\mathcal{L}_X)}}{8\lambda} \frac{\partial^2}{\partial \tilde{D}^2} \quad (2.51)$$

We rewrite Eq. (2.45) as

$$\frac{\partial \rho(X, \tilde{D}, t)}{\partial t} = \left[\hat{\mathcal{L}}_X(\tilde{D}) + \frac{1}{\epsilon} \tilde{\mathcal{F}}_{\tilde{D}}(X) \right] \rho(X, \tilde{D}, t), \quad (2.52)$$

where ϵ is a slowness parameter defined as

$$\epsilon = \frac{\Gamma_{(\mathcal{L}_X)}}{\gamma}. \quad (2.53)$$

Next we introduce the two time scales τ_1 and τ_2 in the spirit of multiple-timescale perturbation (MTSP) analysis and rewrite Eq. (2.52) as

$$\left(\frac{\partial}{\partial \tau_1} + \frac{1}{\epsilon} \frac{\partial}{\partial \tau_2} \right) \tilde{\rho}(X, \tilde{D}, \tau_1, \tau_2) = \left[\hat{\mathcal{L}}_X(\tilde{D}) + \frac{1}{\epsilon} \tilde{\mathcal{F}}_{\tilde{D}}(X) \right] \tilde{\rho}(X, \tilde{D}, \tau_1, \tau_2) \quad (2.54)$$

where we have replaced $\rho(X, \tilde{D}, t)$ with its two-time analogue $\tilde{\rho}(X, \tilde{D}, \tau_1, \tau_2)$. If we replace $t = \tau_1 = \epsilon \tau_2$, in Eq. (2.54) we recover the original problem given in Eq. (2.52). Now we substitute the two-timed perturbation series:

$$\tilde{\rho}(X, \tilde{D}, \tau_1, \tau_2) = \sum_{k'=0}^{\infty} \epsilon^{k'} \tilde{\rho}_{k'}(X, \tilde{D}, \tau_1, \tau_2) \quad (2.55)$$

in Eq. (2.54), multiply both sides by ϵ and then collect terms in every power of ϵ to get a chain of perturbation equations. For ϵ^0 we get

$$\left(\frac{\partial}{\partial \tau_2} - \tilde{\mathcal{F}}_{\tilde{D}}(X) \right) \tilde{\rho}_0(X, \tilde{D}, \tau_1, \tau_2) = 0, \quad (2.56)$$

for which we have the following formal solution:

$$\tilde{\rho}_0(X, \tilde{D}, \tau_1, \tau_2) = e^{\tau_2 \tilde{\mathcal{F}}_{\tilde{D}}(X)} \tilde{\rho}_0(X, \tilde{D}, \tau_1, 0). \quad (2.57)$$

For any ϵ^k with $k \geq 1$ we have

$$\left(\frac{\partial}{\partial \tau_2} - \tilde{\mathcal{F}}_{\tilde{D}}(X) \right) \tilde{\rho}_k(X, \tilde{D}, \tau_1, \tau_2) = - \left(\frac{\partial}{\partial \tau_1} - \hat{\mathcal{L}}_X(\tilde{D}) \right) \tilde{\rho}_{k-1}(X, \tilde{D}, \tau_1, \tau_2), \quad (2.58)$$

for which the formal solution can be written as,

$$\begin{aligned}
\tilde{\rho}_k(X, \tilde{D}, \tau_1, \tau_2) &= e^{\tau_2 \tilde{\mathcal{F}}_{\tilde{D}}(X)} \tilde{\rho}_k(X, \tilde{D}, \tau_1, 0) - \int_0^{\tau_2} ds e^{(\tau_2-s)\tilde{\mathcal{F}}_{\tilde{D}}(X)} \left[\frac{\partial}{\partial \tau_1} - \hat{\mathcal{L}}_X(\tilde{D}) \right] \tilde{\rho}_{k-1}(X, \tilde{D}, \tau_1, s) \\
&= e^{\tau_2 \tilde{\mathcal{F}}_{\tilde{D}}(X)} \tilde{\rho}_k(X, \tilde{D}, \tau_1, 0) - \int_0^{\tau_2} dz e^{z\tilde{\mathcal{F}}_{\tilde{D}}(X)} \left[\frac{\partial}{\partial \tau_1} - \hat{\mathcal{L}}_X(\tilde{D}) \right] \tilde{\rho}_{k-1}(X, \tilde{D}, \tau_1, \tau_2 - z).
\end{aligned} \tag{2.59}$$

Setting $\tau_2 = (\tau_1/\epsilon)$ in Eqs. (2.57) and (2.59) gives us the regular perturbation solutions to the original problem Eq. (2.47). Replacing $\tau_2 = (\tau_1/\epsilon)$ in Eqs. (2.57) and (2.59) and taking the strong separation of the timescale limits $\epsilon \rightarrow 0$, $\tau_2 \rightarrow \infty$ with finite $\tau_1 = \epsilon\tau_2$, may lead to secular or divergent behavior. We seek to avoid this problem by the MTSP method.

Next we simplify our analysis by assuming that we are only interested in the dynamics happening at the slow timescales. To do this we use the spectral properties of the operator $\tilde{\mathcal{F}}_{\tilde{D}}(X)$. It can be shown that given a value of X , for the OU operator $\tilde{\mathcal{F}}_{\tilde{D}}(X)$, there is an unique normalized stationary distribution

$$\Pi(\tilde{D}|X) = \sqrt{\frac{4\lambda}{\gamma\pi}} \exp\left[-\frac{4\lambda}{\gamma}(\tilde{D} - O(X))^2\right]. \tag{2.60}$$

Thus, the null-space $\ker(\tilde{\mathcal{F}}_{\tilde{D}}(X))$ of the operator $\tilde{\mathcal{F}}_{\tilde{D}}(X)$ is spanned only by one function $\Pi(\tilde{D}|X)$. We define the null-space projection operator $\hat{\mathcal{P}}_{\tilde{\mathcal{F}}_{\tilde{D}}(X)}$ as

$$\hat{\mathcal{P}}_{\tilde{\mathcal{F}}_{\tilde{D}}(X)}(*) = \Pi(\tilde{D}|X) \int d\tilde{D} (*) \tag{2.61}$$

and the projection operator outside of the null-space is defined as

$$\hat{\mathcal{Q}}_{\tilde{\mathcal{F}}_{\tilde{D}}(X)} = \hat{\mathbf{1}} - \hat{\mathcal{P}}_{\tilde{\mathcal{F}}_{\tilde{D}}(X)}, \quad (2.62)$$

where $\hat{\mathbf{1}}$ is the identity operator. From the spectral properties of $\tilde{\mathcal{F}}_{\tilde{D}}(X)$, it can also be shown that any arbitrary starting distribution $P_0(X, \tilde{D})$ gets projected to $\ker(\tilde{\mathcal{F}}_{\tilde{D}}(X))$ in the long-time limit under the dynamics of $\tilde{\mathcal{F}}_{\tilde{D}}(X)$, i.e,

$$\lim_{s \rightarrow \infty} e^{s\tilde{\mathcal{F}}_{\tilde{D}}(X)} P_0(X, \tilde{D}) = \hat{\mathcal{P}}_{\tilde{\mathcal{F}}_{\tilde{D}}(X)} P_0(X, \tilde{D}) \quad (2.63)$$

Now, under a strong separation of timescales we have a finite $\epsilon \ll 1$, a finite τ_1 , and $\tau_2 = (\tau_1/\epsilon) \gg \tau_1$. Thus, τ_2 can be approximated as $\tau_2 \rightarrow \infty$ while keeping τ_1 finite and independent of τ_2 . Now we take the limit $\tau_2 \rightarrow \infty$ on the both sides of Eqs. (2.57) and (2.59) to get

$$\rho_0(X, \tilde{D}, \tau_1) = \Pi(\tilde{D}|X) f_0(X, \tau_1), \quad (2.64)$$

$$\begin{aligned} \rho_k(X, \tilde{D}, \tau_1) &= \Pi(\tilde{D}|X) f_k(X, \tau_1) - \lim_{\tau_2 \rightarrow \infty} \int_0^{\tau_2} dz e^{z\tilde{\mathcal{F}}_{\tilde{D}}(X)} \left[\frac{\partial}{\partial \tau_1} - \hat{\mathcal{L}}_X(\tilde{D}) \right] \tilde{\rho}_{k-1}(X, \tilde{D}, \tau_1, \tau_2 - z) \\ &\quad (2.65) \end{aligned}$$

where the functions $\rho_k(X, \tilde{D}, \tau_1)$ and $f_k(X, \tau_1)$ are defined for any $k \geq 0$ as

$$\rho_k(X, \tilde{D}, \tau_1) = \lim_{\tau_2 \rightarrow \infty} \tilde{\rho}_k(X, \tilde{D}, \tau_1, \tau_2), \quad (2.66)$$

$$\begin{aligned}
f_k(X, \tau_1) &= \frac{1}{\Pi(\tilde{D}|X)} \lim_{\tau_2 \rightarrow \infty} e^{\tau_2 \tilde{\mathcal{F}}_{\tilde{D}}(X)} \tilde{\rho}_k(X, \tilde{D}, \tau_1, 0) \\
&= \frac{1}{\Pi(\tilde{D}|X)} \hat{\mathcal{P}}_{\tilde{\mathcal{F}}_{\tilde{D}}} \tilde{\rho}_k(X, \tilde{D}, \tau_1, 0).
\end{aligned} \tag{2.67}$$

Notice that the limit in the second term on the r.h.s. of Eq. (2.65) diverges if the integral has any term linear in τ_2 . To avoid this divergent (secular) behavior, we impose the condition that the source term of Eq. (2.58) must be outside of the $\ker(\tilde{\mathcal{F}}_{\tilde{D}}(X))$. Hence impose the condition,

$$\hat{\mathcal{P}}_{\tilde{\mathcal{F}}_{\tilde{D}}(X)} \left[-\left(\frac{\partial}{\partial \tau_1} - \hat{\mathcal{L}}_X(\tilde{D}) \right) \tilde{\rho}_{k-1}(X, \tilde{D}, \tau_1, \tau_2) \right] = 0, \tag{2.68}$$

which implies

$$\int d\tilde{D} \left(\frac{\partial}{\partial \tau_1} - \hat{\mathcal{L}}_X(\tilde{D}) \right) \tilde{\rho}_{k-1}(X, \tilde{D}, \tau_1, \tau_2) = 0. \tag{2.69}$$

With the condition above the secular terms in Eq. (2.65), arising due to the null space component of the source term are avoided. Hence we can rewrite Eq. (2.65) using the condition Eq. (2.68) as

$$\rho_k(X, \tilde{D}, \tau_1) = \Pi(\tilde{D}|X) f_k(X, \tau_1) - \lim_{\tau_2 \rightarrow \infty} \int_0^{\tau_2} dz e^{z \tilde{\mathcal{F}}_{\tilde{D}}(X)} \hat{\mathcal{Q}}_{\tilde{\mathcal{F}}_{\tilde{D}}(X)} \left[\frac{\partial}{\partial \tau_1} - \hat{\mathcal{L}}_X(\tilde{D}) \right] \tilde{\rho}_{k-1}(X, \tilde{D}, \tau_1, z) \tag{2.70}$$

Since all the eigenvalues of the operator $\tilde{\mathcal{F}}_{\tilde{D}}$ outside the null-space are negative [67], we assume that any transient generated by the source term almost instantly decays and can be neglected.

With this assumption we rewrite the Eq. (2.70) as

$$\rho_k(X, \tilde{D}, \tau_1) = \Pi(\tilde{D}|X) f_k(X, \tau_1) + \tilde{\mathcal{F}}_{\tilde{D}}^+(X) \left[\frac{\partial}{\partial \tau_1} - \hat{\mathcal{L}}_X(\tilde{D}) \right] \rho_{k-1}(X, \tilde{D}, \tau_1) \tag{2.71}$$

where we have introduced the pseudo-inverse or Drazin inverse [63, 87] of the operator $\tilde{\mathcal{F}}_{\tilde{D}}(X)$

as

$$\tilde{\mathcal{F}}_{\tilde{D}}^+(X) = - \int_0^\infty dz e^{z\tilde{\mathcal{F}}_{\tilde{D}}(X)} \hat{\mathcal{Q}}_{\tilde{\mathcal{F}}_{\tilde{D}}(X)} \quad (2.72)$$

Notice that in this equation the first term on the r.h.s. of Eq. (2.71) is completely inside the $\ker(\tilde{\mathcal{F}}_{\tilde{D}}(X))$ and the second term of the r.h.s. of Eq. (2.71) is completely outside of $\ker(\tilde{\mathcal{F}}_{\tilde{D}}(X))$.

Thus, for any $k \geq 0$, we have,

$$f_k(X, \tau_1) = \int d\tilde{D} \rho_k(X, \tilde{D}, \tau_1) \quad (2.73)$$

If we write the slow-time scale solution under separation of time scale as

$$\rho(X, \tilde{D}, \tau_1) = \sum_{k=0}^{\infty} \epsilon^k \rho_k(X, \tilde{D}, \tau_1), \quad (2.74)$$

then the $f_k(X, t)$'s are null-space projection weights of the operator $\tilde{\mathcal{F}}_{\tilde{D}}(X)$ for the order of the perturbation expansion:

$$\begin{aligned} \hat{\mathcal{P}}_{\tilde{\mathcal{F}}_{\tilde{D}}(X)} \rho(X, \tilde{D}, \tau_1) &= \hat{\mathcal{P}}_{\tilde{\mathcal{F}}_{\tilde{D}}(X)} \sum_{k=0}^{\infty} \epsilon^k \rho_k(X, \tilde{D}, \tau_1) \\ &= \Pi(D|X) \sum_{k=0}^{\infty} \epsilon^k f_k(X, \tau_1) \end{aligned} \quad (2.75)$$

From this equation, we define the overall null-space projection factor of $\rho(X, \tilde{D}, \tau_1)$ as

$$f(X, \tau_1) = \sum_{k=0}^{\infty} \epsilon^k f_k(X, \tau_1) \quad (2.76)$$

Notice that $f(X, \tau_1)$ is the marginal distribution of the system variable X at the slow time-scale

τ_1 , under the separation of timescales limit:

$$f(X, \tau_1) = \int d\tilde{D} \rho(X, \tilde{D}, \tau_1) \quad (2.77)$$

To determine the complete expression of $\rho_k(X, \tilde{D}, t)$ at any order (k) with $k \geq 1$, we must solve for $f_k(X, \tau_1)$ and the complete expression of the perturbation correction in the previous order, $\rho_{k-1}(X, \tilde{D}, \tau_1)$. To determine $f_k(X, \tau_1)$, we use the expression for $\rho_k(X, \tilde{D}, t)$, (containing an unknown $f_k(X, \tau_1)$) in the secularity removal condition (Eq. (2.68)) in the next order ($k + 1$):

$$\hat{\mathcal{P}}_{\tilde{\mathcal{F}}_{\tilde{D}}(X)} \left[\frac{\partial}{\partial \tau_1} - \hat{\mathcal{L}}_X(\tilde{D}) \right] \rho_k(X, \tilde{D}, \tau_1) = 0. \quad (2.78)$$

Thus for any $\Pi(\tilde{D}|X)$ we have,

$$\int d\tilde{D} \left[\frac{\partial}{\partial \tau_1} - \hat{\mathcal{L}}_X(\tilde{D}) \right] \rho_k(X, \tilde{D}, \tau_1) = 0 \quad (2.79)$$

Now substituting the expression of $\rho_k(X, \tilde{D}, \tau_1)$ from Eq. (2.65), we get

$$\begin{aligned} & \int d\tilde{D} \left[\frac{\partial}{\partial \tau_1} - \hat{\mathcal{L}}_X(\tilde{D}) \right] \left(\Pi(\tilde{D}|X) f_k(X, \tau_1) \right) \\ & + \int d\tilde{D} \left[\frac{\partial}{\partial \tau_1} - \hat{\mathcal{L}}_X(\tilde{D}) \right] \left(\tilde{\mathcal{F}}_{\tilde{D}}^+(X) \left[\frac{\partial}{\partial \tau_1} - \hat{\mathcal{L}}_X(\tilde{D}) \right] \rho_{k-1}(X, \tilde{D}, \tau_1) \right) = 0 \end{aligned} \quad (2.80)$$

which can be written as

$$\begin{aligned} & \frac{\partial f_k(X, \tau_1)}{\partial \tau_1} - \left(\int d\tilde{D} \hat{\mathcal{L}}_X(\tilde{D}) \Pi(\tilde{D}|X) \right) f_k(X, \tau_1) \\ & - \int d\tilde{D} \hat{\mathcal{L}}_X(\tilde{D}) \left(\tilde{\mathcal{F}}_{\tilde{D}}^+(X) \left[\frac{\partial}{\partial \tau_1} - \hat{\mathcal{L}}_X(\tilde{D}) \right] \rho_{k-1}(X, \tilde{D}, \tau_1) \right) = 0 \end{aligned} \quad (2.81)$$

2.4.2 0th and 1st order terms

Next we show the explicit calculation for the 0th and 1st order terms in the perturbation expansion. Using Eq. (2.64) in Eq. (2.79) we get the equation for $f_0(X, \tau_1)$ as

$$\frac{\partial f_0(X, \tau_1)}{\partial \tau_1} = \hat{\mathcal{L}}_X^{(0)} f_0(X, \tau_1), \quad (2.82)$$

$$\hat{\mathcal{L}}_X^{(0)} = \int d\tilde{D} \hat{\mathcal{L}}_X(\tilde{D}) \Pi(\tilde{D}|X). \quad (2.83)$$

Eq. (2.82) can be solved for some given initial condition $f_0(X, 0)$ to obtain $f_0(X, \tau_1)$.

Now setting $k = 1$ in Eq. (2.81) and using the expression for $\rho_0(X, \tilde{D}, \tau_1)$, we obtain

$$\left[\frac{\partial f_1(X, \tau_1)}{\partial \tau_1} - \hat{\mathcal{L}}_X^{(0)} f_1(X, \tau_1) \right] - \int d\tilde{D} \hat{\mathcal{L}}_X(\tilde{D}) \left(\tilde{\mathcal{F}}_{\tilde{D}}^+(X) \left[\frac{\partial}{\partial \tau_1} - \hat{\mathcal{L}}_X(\tilde{D}) \right] \Pi(\tilde{D}|X) f_0(X, \tau_1) \right) = 0 \quad (2.84)$$

Since we have $\tilde{\mathcal{F}}_{\tilde{D}}^+(X) \Pi(\tilde{D}|X) = 0$, we get the equation for $f_1(X, \tau_1)$ as:

$$\frac{\partial f_1(X, \tau_1)}{\partial \tau_1} = \hat{\mathcal{L}}_X^{(0)} f_1(X, \tau_1) + \hat{\mathcal{L}}_X^{(1)} f_0(X, \tau_1) \quad (2.85)$$

where

$$\hat{\mathcal{L}}_X^{(1)} = - \int d\tilde{D} \hat{\mathcal{L}}_X(\tilde{D}) \tilde{\mathcal{F}}_{\tilde{D}}^+(X) \hat{\mathcal{L}}_X(\tilde{D}) \Pi(\tilde{D}|X), \quad (2.86)$$

and $\hat{\mathcal{L}}_X^{(0)}$ is given in Eq. (2.83). Given an initial condition $f_1(X, 0)$, and the solution $f_0(X, \tau_1)$ obtained from Eq. (2.82) with the initial condition $f_0(X, \tau_1)$, one can solve for $f_1(X, \tau_1)$ in

Eq. (2.84). Using $f_0(X, \tau_1)$ and $f_1(X, \tau_1)$ we write the expression of $\rho_1(X, \tilde{D}, \tau_1)$ as

$$\rho_1(X, \tilde{D}, \tau_1) = \Pi(\tilde{D}|X)f_1(X, \tau_1) - \tilde{\mathcal{F}}_{\tilde{D}}^+(X)\hat{\mathcal{L}}_X(\tilde{D})\Pi(D|\tilde{X})f_0(X, \tau_1). \quad (2.87)$$

Since we are neglecting the transient dynamics, we choose an initial condition of the joint dynamics to be completely inside the null-space of the operator $\tilde{\mathcal{F}}_D$, i.e. of the form:

$$\rho(X, \tilde{D}, 0) = f(X, 0)\Pi(\tilde{D}|X) \quad (2.88)$$

Now we have freedom of choice in how to distribute $f(X, 0)$ in different orders of perturbation.

It is often convenient to choose

$$f_0(X, 0) = f(X, 0), \quad (2.89)$$

$$f_k(X, 0) = 0, \quad k \geq 1, \quad (2.90)$$

such that the initial condition $f(X, 0)$ is completely captured in the 0th order term of the perturbation.

2.4.3 Effective master equation for system state under fast feedback

Switching back to the original variable $\tau_1 \rightarrow t$, truncating the perturbation series in Eq. (2.76) at order $k = 1$ and using Eqs. (2.82), (2.84) we obtain the evolution equation for $f^{[1]}(X, t) =$

$f_0(X, t) + \epsilon f_1(X, t)$, as

$$\begin{aligned}\frac{\partial f^{[1]}(X, t)}{\partial t} &= \hat{\mathcal{L}}_X^{(0)} f_0(X, t) + \epsilon \hat{\mathcal{L}}_X^{(0)} f_1(X, t) + \epsilon \hat{\mathcal{L}}_X^1 f_0(X, t) \\ &= \hat{\mathcal{L}}_X^{(0)} f^{[1]}(X, t) + \epsilon \hat{\mathcal{L}}_X^{(1)} f^{[1]}(X, t) - \epsilon^2 \hat{\mathcal{L}}_X^{(1)} f_1(X, t)\end{aligned}\tag{2.91}$$

Thus replacing $f^{[1]}(X, t)$ by $f(X, t)$ we obtain an equation that is correct up to the order $\mathcal{O}(\epsilon)$ as

$$\frac{\partial f(X, t)}{\partial t} = \left[\hat{\mathcal{L}}_X^{(0)} + \epsilon \hat{\mathcal{L}}_X^{(1)} \right] f(X, t) + \mathcal{O}(\epsilon^2)\tag{2.92}$$

This equation gives us the evolution of the marginal distribution of the system variable under separation of timescales and can be solved for $f(X, t)$ given an initial condition $f(X, 0)$. From the solution $f(X, t)$, one can also obtain the joint system detector distribution under the separation of timescales approximation:

$$\rho(X, \tilde{D}, t) = \left[1 - \epsilon \tilde{\mathcal{F}}_{\tilde{D}}^+ \hat{\mathcal{L}}_X(\tilde{D}) \right] \Pi(\tilde{D}|X) f(X, t) + \mathcal{O}(\epsilon^2).\tag{2.93}$$

Finally, we point out that Eq. (2.92) can alternatively be derived using Nakazima-Zwanzig projection operator methods [1, 74].

2.4.4 Connection to linear response theory

The separation of timescales calculations shown above can be interpreted in terms of linear response theory. At leading order, the control parameter is in the equilibrium distribution $\Pi(\tilde{D}|X)$ when the state of the system is X . The operator $\hat{\mathcal{L}}_X^{(0)}$ can be then understood as an averaged or *mean field* operator of the family of operators: $\{\hat{\mathcal{L}}_X(\tilde{D})\}$ where the parameter \tilde{D} has

been sampled from the distribution $\Pi(\tilde{D}|X)$. Thus we write,

$$\hat{\mathcal{L}}_X^{(0)} = \int d\tilde{D} \hat{\mathcal{L}}_X(\tilde{D}) \Pi(\tilde{D}|X) = \langle \hat{\mathcal{L}}_X(\tilde{D}) \rangle_{\Pi(\tilde{D}|X)} \quad (2.94)$$

where $\langle \dots \rangle_\phi$ signifies the ensemble average over a distribution ϕ .

At first order in ϵ , there is a small lag in the dynamics of the control parameter \tilde{D} . The effect of the lag is to drive the controller distribution away from its stationary state (leading order distribution). Hence we consider $\hat{\mathcal{L}}_X(\tilde{D})$ as an observable (or parameterized operator) of \tilde{D} , whose equilibrium average is given by $\hat{\mathcal{L}}_X^{(0)}$. At 0th order $\hat{\mathcal{L}}_X^{(0)}$ generates the dynamics of the $f(X, t)$. We see that $\hat{\mathcal{L}}_X^{(1)}$ captures the response away from this equilibrium average $\hat{\mathcal{L}}_X^{(0)}$ due to a small perturbation to the equilibrium distribution $\Pi(\tilde{D}|X)$. We note that $\hat{\mathcal{L}}_X^{(1)}$ can be expressed as,

$$\hat{\mathcal{L}}_X^{(1)} = \int d\tilde{D} \hat{\mathcal{L}}_X(\tilde{D}) \int_0^\infty dz e^{z\tilde{\mathcal{F}}_{\tilde{D}}(X)} (I - \mathcal{P}_{\tilde{\mathcal{F}}_{\tilde{D}}(X)}) \hat{\mathcal{L}}_X(\tilde{D}) \Pi(\tilde{D}|X) \quad (2.95)$$

which can be written as

$$\begin{aligned} \hat{\mathcal{L}}_X^{(1)} &= \int_0^\infty dz \int d\tilde{D} \hat{\mathcal{L}}_X(\tilde{D}) e^{z\tilde{\mathcal{F}}_{\tilde{D}}(X)} \hat{\mathcal{L}}_X(\tilde{D}) \Pi(\tilde{D}|X) \\ &\quad - \int_0^\infty dz \left(\int d\tilde{D} \hat{\mathcal{L}}_X(\tilde{D}) e^{z\tilde{\mathcal{F}}_{\tilde{D}}(X)} \Pi(\tilde{D}|X) \right) \left(\int dD' \hat{\mathcal{L}}_X(D') \Pi(D'|X) \right) \end{aligned} \quad (2.96)$$

This can be written as a linear response type relation

$$\hat{\mathcal{L}}_X^{(1)} = \int_0^\infty dz \hat{\mathcal{C}}_{\hat{\mathcal{L}}_X(\tilde{D})}^{\Pi(\tilde{D}|X)}(z) \quad (2.97)$$

where $\hat{\mathcal{C}}_{\hat{\mathcal{L}}_X(\tilde{D})}^{\Pi(\tilde{D}|X)}(z)$ is the auto-correlation operator of $\hat{\mathcal{L}}_X(\tilde{D})$ in the equilibrium distribution $\Pi(\tilde{D}|X)$

(by analogy with auto-correlation function), i.e.,

$$\hat{C}_{\hat{\mathcal{L}}_X(\tilde{D})}^{\Pi(\tilde{D}|X)}(z) = \langle \hat{\mathcal{L}}_X(\tilde{D}_z) \hat{\mathcal{L}}_X(\tilde{D}_0) \rangle_{\Pi(\tilde{D}|X)} - \langle \hat{\mathcal{L}}_X(\tilde{D}_z) \rangle_{\Pi(\tilde{D}|X)} \langle \hat{\mathcal{L}}_X(\tilde{D}_0) \rangle_{\Pi(\tilde{D}|X)} \quad (2.98)$$

Since the distribution $\Pi(\tilde{D}|X)$ is stationary, we use $\langle \hat{\mathcal{L}}_X(\tilde{D}_z) \rangle_{\Pi(\tilde{D}|X)} = \langle \hat{\mathcal{L}}_X(\tilde{D}_0) \rangle_{\Pi(\tilde{D}|X)} = \mathcal{L}_X^{(0)}$

to write

$$\hat{C}_{\hat{\mathcal{L}}_X(\tilde{D})}^{\Pi(\tilde{D}|X)}(z) = \langle \hat{\mathcal{L}}_X(\tilde{D}_z) \hat{\mathcal{L}}_X(\tilde{D}_0) \rangle_{\Pi(\tilde{D}|X)} - (\hat{\mathcal{L}}_X^{(0)})^2 \quad (2.99)$$

Similar to linear response theory, here we also see that in the presence of a small delay in feedback, the dynamics of the system is related to the auto-correlations of the operator $\mathcal{L}_X(\tilde{D})$ calculated with the stationary control parameter distribution $\Pi(\tilde{D}|X)$ at the fast feedback limit (i.e., when there is no delay).

2.5 Comparison with feedback-control equation for quantum and discrete stochastic systems

2.5.1 Comparison with quantum Fokker-Planck master equation (QFPME)

In this section we compare the discussion presented so far for the classical case with the original quantum Fokker-Planck master equation of continuous feedback control [1, 74]. For a single realization of the experiment, the statistical state of the quantum system at discretized time t_k is given by a conditional density matrix $\hat{\rho}_c^k(t_k)$, where the superscript k implies the density matrix is conditioned on the measurement record $\Gamma_{k-1}^{(z)}$ similar to Eq. (2.13) for the classical case.. In analogy with the Bayesian update rule shown in Eq. (2.14), the update equation for the

quantum state due to an instantaneous measurement operation at time t_k is given by,

$$\begin{aligned}\hat{\rho}_c^{k+1}(t_k) &= \mathcal{M}_{z_k} [\hat{\rho}_c^k(t_k)] \\ &= \frac{\hat{K}(z_k)\hat{\rho}_c^k(t_k)\hat{K}^\dagger(z_k)}{\text{Tr}\left\{\hat{K}(z_k)\hat{\rho}_c^{k-1}(t_k)\hat{K}^\dagger(z_k)\right\}}\end{aligned}\quad (2.100)$$

Here, \mathcal{M}_{z_k} denotes a measurement operation that leads to outcome z_k and $\hat{K}(z_k)$ are corresponding Kraus operators [78, 88]. In contrast to the classical case, which we considered to be back action free, we consider a general case here with the possibility of back action due to measurement. In the Gaussian weak measurement model [78], for a Hermitian operator $\hat{A} = \sum_a |a\rangle\xi_a\langle a|$ corresponding to the observable of interest, the measurement Kraus operator is given as

$$\hat{K}(z) = \left(\frac{2\lambda\delta t}{\pi}\right)^{\frac{1}{4}} e^{-\lambda\delta t(z-\hat{A})^2} \quad (2.101)$$

The probability density function of obtaining the outcome z_k , given previous measurement records $\Gamma_{k-1}^{(z)}$, is

$$\begin{aligned}\rho_{t_k}^{(m)}(z_k|\Gamma_{k-1}^{(z)}) &= \text{Tr}\left\{\hat{K}(z_k)\hat{\rho}_c^{k-1}\hat{K}^\dagger(z_k)\right\} \\ &= \left(\frac{2\lambda\delta t}{\pi}\right)^{\frac{1}{2}} \sum_a e^{-2\lambda\delta t(z_k-\xi_a)^2} \langle a|\hat{\rho}_c^{k-1}(t_k)|a\rangle\end{aligned}\quad (2.102)$$

This equation is the analogue of Eq. (2.21) that we have obtained for the classical case. Similar to the *Kushner Equation* (Eq. (2.30)) in the classical case, one can derive the *Belavkin equation* (see Refs. [1, 61, 74, 78] for the derivation) for the quantum case as

$$d\hat{\rho}_c(t) = dt\hat{\mathcal{L}}(D)\hat{\rho}_c(t) + \lambda dt\mathcal{D}[\hat{A}]\hat{\rho}_c(t) + dW(t)\sqrt{\lambda}\{\hat{A} - \langle\hat{A}\rangle_c, \hat{\rho}_c(t)\} \quad (2.103)$$

where $\{X, Y\} = XY + YX$ is the anti-commutator, $\langle \hat{A} \rangle_c = \text{Tr}\left\{\hat{A}\hat{\rho}_c\right\}$, $\hat{\mathcal{L}}(D)$ is the feedback-controlled Lindbladian, and $\mathcal{D}[\hat{A}]$ is a dissipator in the eigenbasis of the operator \hat{A} . We note that in Eq. (2.103), we have two terms that are proportional to dt . The first term on the r.h.s. of the equation generates the Markovian dynamics of the system due to the Lindbladian $\hat{\mathcal{L}}(D)$, the second term $\lambda dt \mathcal{D}[\hat{A}]\hat{\rho}_c$ generates decoherence in the basis of the observable \hat{A} . Thus the second term creates a *back-action* due to measurement in the quantum state $\hat{\rho}_c$. Note that for the classical case with *purely Bayesian* measurements [61], the back-action term is absent in the Eq. (2.30). Now using the filtering Eq. (2.32) in the Belavkin equation (Eq. (2.103)), and following the same steps discussed for the classical case, one can obtain the Quantum Fokker Planck Master Equation [1]:

$$\frac{\partial \hat{\rho}_t(\tilde{D})}{\partial t} = \hat{\mathcal{L}}(D)\hat{\rho}_t(\tilde{D}) + \lambda \mathcal{D}[\hat{A}]\hat{\rho}_t(\tilde{D}) + \hat{\mathcal{F}}\hat{\rho}_t(\tilde{D}), \quad (2.104)$$

where $\hat{\mathcal{F}}$ is a superoperator form of the OU operator:

$$\hat{\mathcal{F}}\hat{\rho}(\tilde{D}) = -\frac{\gamma}{2} \frac{\partial}{\partial \tilde{D}} \{\hat{A} - \tilde{D}, \hat{\rho}(\tilde{D})\} + \frac{\gamma^2}{8\lambda} \frac{\partial^2}{\partial \tilde{D}^2} \hat{\rho}(\tilde{D}) \quad (2.105)$$

and the object $\hat{\rho}(\tilde{D})$ is the joint state of the system and the control parameter. From $\hat{\rho}(\tilde{D})$ we obtain the state of the quantum system by marginalizing over the control parameter \tilde{D} ,

$$\hat{\rho}_t = \int d\tilde{D} \hat{\rho}_t(\tilde{D}), \quad (2.106)$$

and the distribution of the control parameter \tilde{D} at any time instant t , can be obtained as

$$p_t(\tilde{D}) = \text{Tr}\left\{\hat{\rho}(\tilde{D})\right\} \quad (2.107)$$

Similar to the classical case, we can also perform a multiple-timescale analysis for the quantum problem. This analysis can be performed directly with density matrices and superoperators (see [74]) or alternatively, we cast the master equation into the Fock-Liouville space where superoperators become matrices and perform the analysis in that space (see [1]). Similar to the Eq. (2.92), it is possible to obtain a Markovian master equation for the quantum state in the limit of separation of time-scales of the system dynamics and the controller dynamics. If the fastest time-scale of the system and the measurement back action is given by $(1/\Gamma)$, then we define $\epsilon = (\Gamma/\gamma)$ and get the Markovian master equation,

$$\hat{\rho}_t = (\hat{\mathcal{L}}^{(0)} + \epsilon \hat{\mathcal{L}}^{(1)}) \hat{\rho}_t \quad (2.108)$$

where the superoperator $\hat{\mathcal{L}}^{(0)}$ is defined as

$$\hat{\mathcal{L}}^{(0)} \hat{\rho}_t = \int d\tilde{D} \hat{\mathcal{L}}(\tilde{D}) \sum_{aa'} |a\rangle \Pi(\tilde{D}|a, a') \langle a| \hat{\rho}_t |a'\rangle \langle a'| \quad (2.109)$$

with $\Pi(\tilde{D}|a, a')$ is defined similar to Eq. (2.60) as

$$\Pi(\tilde{D}|a, a') = \sqrt{\frac{4\lambda}{\pi\gamma}} \exp \left[-\frac{4\lambda}{\gamma} \left(\tilde{D} - \frac{\xi_a + \xi_{a'}}{2} \right)^2 \right]. \quad (2.110)$$

The superoperator $\hat{\mathcal{L}}^{(1)}$ is defined as

$$\hat{\mathcal{L}}^{(1)} \hat{\rho}_t = - \int d\tilde{D} \mathcal{L}(\tilde{D}) \hat{\mathcal{F}}^+ \mathcal{L}(\tilde{D}) \sum_{aa'} |a\rangle \Pi(\tilde{D}|a, a') \langle a| \hat{\rho}_t |a'\rangle \langle a'| \quad (2.111)$$

where the superoperator $\hat{\tilde{\mathcal{F}}} = \frac{\Gamma}{\gamma} \hat{\mathcal{F}}$ and

$$\hat{\tilde{\mathcal{F}}}^+ = - \int_0^\infty dz e^{z\hat{\tilde{\mathcal{F}}}} \hat{Q}_{\hat{\tilde{\mathcal{F}}}} \quad (2.112)$$

2.5.2 Comparison with feedback-control master equation for classical discrete-state stochastic dynamics

One can obtain the feedback control equation for a classical discrete state process as a special case of the Quantum Fokker Planck Master Equation (Eq. (2.104)) when the dynamics of the populations are uncoupled from the dynamics of the coherence (see the supplemental of Ref. [1]). Alternatively, one can consider a classical, discrete-state, continuous-time Markov jump process under feedback control and follow the steps used for the continuous case to derive a similar master equation for the feedback control. In this case the statistical state of the system state and the controller state is described by a probability distribution column vector $\vec{P}(\tilde{D}, t) = [P_i(\tilde{D}, t)]_{i=1,\dots,N}^T$ where the probability distribution of the system state is obtained by marginalization

$$\vec{P}(t) = \int d\tilde{D} \vec{P}(\tilde{D}, t) \quad (2.113)$$

and the distribution of the controller state \tilde{D} is given by

$$p(\tilde{D}) = \sum_{i=1}^N P_i(\tilde{D}, t) \quad (2.114)$$

We consider a measurement of an observable O that gives the value $O(i) = \xi_i$ when the system is in the state i . If the system dynamics are governed by the rate matrix $R(\tilde{D})$, then the master

equation reads

$$\frac{\partial}{\partial t} \vec{P}(\tilde{D}, t) = R(\tilde{D}) \vec{P}(\tilde{D}, t) + \hat{\mathcal{F}} \vec{P}(\tilde{D}, t) \quad (2.115)$$

where $\hat{\mathcal{F}}$ is a diagonal matrix of OU operators:

$$\hat{\mathcal{F}}_{ij} = \delta_{ij} \left[\gamma \frac{\partial}{\partial \tilde{D}} \left(\tilde{D} - \xi_i \right) + \frac{\gamma^2}{8\lambda} \frac{\partial^2}{\partial \tilde{D}^2} \right] \quad (2.116)$$

Now if the dynamics generated by $R(\tilde{D})$ are of the order $(1/\Gamma)$, then the Markovian master equation for $\vec{P}(t)$ up to the first order of $\epsilon = \frac{\Gamma}{\gamma}$ can be written as

$$\frac{\partial}{\partial t} \vec{P}(t) = (R_0 + \epsilon R_1) \vec{P}(t) \quad (2.117)$$

where

$$R_0 = \int d\tilde{D} R(\tilde{D}) \Pi(\tilde{D}) \quad (2.118)$$

and $\Pi(\tilde{D})$ is a diagonal matrix with elements defined as

$$\Pi_{ij}(\tilde{D}) = \delta_{ij} \sqrt{\frac{4\lambda}{\pi\gamma}} \exp \left[-\frac{4\lambda}{\gamma} \left(\tilde{D} - \xi_i \right)^2 \right]. \quad (2.119)$$

The matrix R_1 is defined as

$$R_1 = - \int d\tilde{D} R(\tilde{D}) \hat{\mathcal{F}}^+ \hat{\mathcal{F}} R(\tilde{D}) \Pi(\tilde{D}) \quad (2.120)$$

Here the elements of the matrix $\hat{\mathcal{F}}^+$ are defined as

$$\hat{\mathcal{F}}_{ij}^+ = -\delta_{ij} \int_0^\infty dz e^{z\hat{\mathcal{F}}_{ij}} \hat{Q}_{\hat{\mathcal{F}}_{ij}} \quad (2.121)$$

where $\hat{\mathcal{F}} = \frac{\Gamma}{\gamma} \hat{\mathcal{F}}$.

Chapter 3: A classical two-state toy model of feedback-controlled information engine

This chapter is based on work done in collaboration with Björn Annby-Andersson, Pharnam Bakhshinezhad, Guilherme De Sousa, Christopher Jarzynski, Peter Samuelsson, and Patrick P. Potts, which has been published as “Quantum Fokker-Planck Master Equation for Continuous Feedback Control” in Ref. [1]. Guilherme De Sousa and I worked together on the multiple-timescale perturbation (MTSP) based analysis of the *classical toy model* of Ref. [1]. In this chapter we analyze this model using classical stochastic modelling and MTSP methods and show the results. This model can also be analyzed using full-counting statistics (FCS) methods as shown in Ref. [1, 74]. At the end of this chapter, in Appendix 3.5, we relate the constants arising in our MTSP calculation with those arising in the FCS method to show the equivalence of the results.

3.1 Chapter overview

In this chapter, we discuss a simple toy model of a classical information engine, which can be considered as a non-autonomous Maxwell’s demon and we use the methodologies developed in the last chapter to analyze the model when measurement error and feedback-delay are present. A key purpose of this chapter is to illustrate an application of the feedback-control

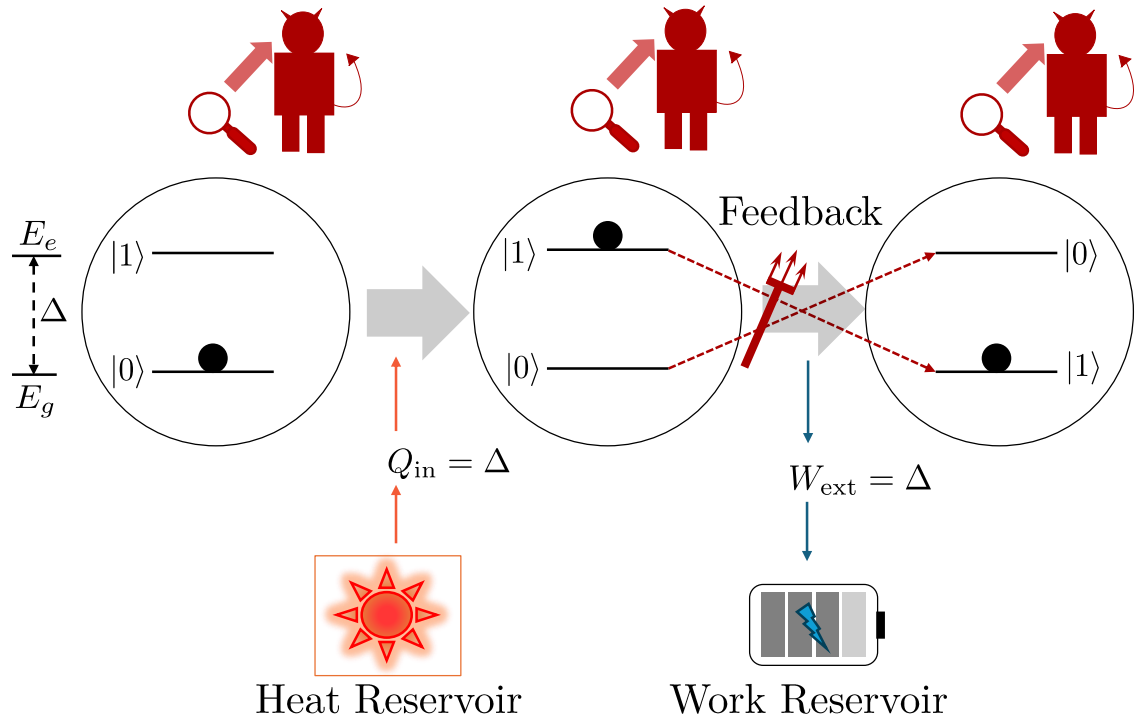


Figure 3.1: Schematic diagram of the classical two-state toy model of an information engine. The two states are labeled as $|0\rangle$ and $|1\rangle$. The agent (demon) makes continuous measurements (denoted by the magnifying glass in the figure) on the two-state system to learn whether the system is in the state $|0\rangle$ or the state $|1\rangle$. The ground state and excited state energies of the system are E_g and E_e with $E_e - E_g = \Delta > 0$. When the system absorbs heat $Q_{\text{in}} = \Delta$ from the heat reservoir (depicted by the sun in the schematic diagram) to go to the excited state, the agent instantly provides feedback (denoted by the trident) by switching the levels $|0\rangle$ ($|1\rangle$) \rightarrow $|1\rangle$ ($|0\rangle$). In this process the agent takes the system from excited state energy E_e to the ground state energy E_g and extracts work $W_{\text{ext}} = \Delta$, which is stored in a work reservoir (depicted by the battery in the schematic diagram). After this, the demon repeats the process cyclically (see Fig. 3.2)

master equation and perturbation results developed in the previous chapter.

Sec. 3.2 of this chapter discusses physical setup and modelling of the system. Then the ideal protocol for the operation of the demon is explained. Next, we consider a feedback-resolved model for the imperfect protocol in which measurement error and feedback-delay are present. This imperfect demon is modeled using the framework presented in Chapter 2 for the classical discrete-state stochastic system with continuous measurement and feedback.

In section 3.3, we analyze of the feedback-resolved model. We use the feedback control master equation for a continuously monitored classical discrete state stochastic system (see 2.5.2) and corresponding multiple time scale perturbation results to solve for the steady state probability distributions of the feedback-resolved model. Then we coarse-grain the feedback-resolved model to calculate the average steady state work extraction rate in the presence of measurement error and feedback lag. We see that the system can act either as an information engine or as a dissipator when measurement errors are present. Then we analyze two limiting scenarios of the model corresponding to the cases of fast feedback with inaccurate measurement, and lagging feedback with accurate measurement.

3.2 Physical setup and stochastic modelling

We consider a two-state system that is weakly coupled to a thermal bath at temperature T (or at inverse temperature $\beta = 1/k_B T$, with k_B as Boltzmann's constant). The system can exchange heat from the thermal bath to go from the ground state to the excited state or vice-versa. This system is continuously being monitored by an external agent (or demon). First we consider an idealized feedback protocol, where the measurement process is accurate and there is

no delay in the response to the measurement. In this protocol, the agent instantaneously changes the energy level configuration of the two-state system, whenever the system absorbs heat from the bath (see Fig. 3.1). When changing the energy level configuration, the agent takes the system from the excited state to ground state and extracts work in the process. This protocol is repeated in a cyclic fashion. Thus, in this cyclic protocol, the agent rectifies thermal fluctuations from the heat bath and directly converts them to work using continuous measurement and feedback. Hence, this protocol can be considered as a toy system of an information engine. Since we have an explicit consideration of an external agent doing the measurement and feedback, this setup represents a non-autonomous Maxwell’s demon. Such two-state information engines are ubiquitous in the stochastic and information-thermodynamics literature and similar toy models can also be found in Refs. [27, 89, 90].

3.2.1 Stochastic modelling

To create a stochastic model of the protocol, we assign labels $|0\rangle$ and $|1\rangle$ to the system’s states (in the spirit of a quantum two-level model) and denote their energies by E_0 and E_1 respectively. We also define the ground state and excited state energy of the system as E_g and E_e with $E_e - E_g = \Delta > 0$. The two possible energy level configurations (energy landscapes) of the system are denoted as the ‘(−)’ configuration: $(E_0 = E_g, E_1 = E_e)$ and the ‘(+)’ configuration: $(E_1 = E_g, E_0 = E_e)$ and we suggestively write them as the Hamiltonians \hat{H}_- and \hat{H}_+ (see Fig. 3.2):

$$\hat{H}_- = E_g|0\rangle\langle 0| + E_e|1\rangle\langle 1|, \quad (3.1)$$

$$\hat{H}_+ = E_e|0\rangle\langle 0| + E_g|1\rangle\langle 1|. \quad (3.2)$$

The demon makes measurements on the state of the system and then provides feedback by changing the energy landscape of the system. Hence both the state of the system and the energy level configurations, are dynamical quantities. The complete description of the system is provided by specifying the *joint state* of the system –the system state ($|0\rangle$ or $|1\rangle$) and energy level configuration (\hat{H}_- or \hat{H}_+) together. Thus, there are four possible joint states of the system: $(0, -)$, $(0, +)$, $(1, -)$ and $(1, +)$. Here the first entry of the tuple refers to the system state and the second entry to the energy level configuration. For example, $(0, -)$ implies the system is in state $|0\rangle$ and the energy level configuration is given by the Hamiltonian \hat{H}_- . The energies corresponding to these joint states are $E_{(0,-)} = E_g$, $E_{(0,+)} = E_e$, $E_{(1,-)} = E_e$, and $E_{(1,+)} = E_g$.

We assume the system is weakly coupled to a thermal bath of inverse temperature β . For thermodynamic consistency, the transitions between the states $|0\rangle \leftrightarrow |1\rangle$ at any of the energy level configurations (\hat{H}_- or \hat{H}_+) must follow *local detailed balance*. We denote the transition rate for $|0\rangle \rightarrow |1\rangle$ ($|1\rangle \rightarrow |0\rangle$) under the energy level configuration \hat{H}_- as $R_{10}^{(-)}(R_{01}^{(-)})$ and similarly for the energy level configuration \hat{H}_+ as $R_{10}^{(+)}(R_{01}^{(+)})$ (see Fig. 3.2). Then the local detailed balance relations are

$$\frac{R_{10}^{(-)}}{R_{01}^{(-)}} = e^{-\beta(E_{(1,-)} - E_{(0,-)})} = e^{-\beta(E_e - E_g)} = e^{-\beta\Delta}, \quad (3.3)$$

$$\frac{R_{10}^{(+)}}{R_{01}^{(+)}} = e^{-\beta(E_{(1,+)} - E_{(0,+)})} = e^{-\beta(E_g - E_e)} = e^{+\beta\Delta}, \quad (3.4)$$

Eqs. (3.3) and (3.4) only define the ratios of the transition rates but do not completely specify them. We model the thermal bath as a weakly coupled *bosonic bath* with which the two-state system exchanges the quantum of energy Δ . The coupling constant of the system with the bath is given as Γ , which defines the natural timescale $(1/\Gamma)$ of the dynamics due to bath coupling. We

denote the average number of bosons of energy Δ at inverse temperature β as

$$n_B = \frac{1}{e^{\beta\Delta} - 1} \quad (3.5)$$

which is the Bose-Einstein distribution function. Now we fix the transition rates as

$$R_{01}^{(-)} = \Gamma(n_B + 1), \quad R_{10}^{(-)} = \Gamma n_B; \quad (3.6)$$

$$R_{01}^{(+)} = \Gamma n_B, \quad R_{10}^{(+)} = \Gamma(n_B + 1). \quad (3.7)$$

These rates satisfy the detailed balance relations presented in Eqs. (3.3), (3.4).

3.2.2 Idealized feedback protocol

In the ideal protocol the agent (demon) continuously monitors state of the system by making measurements in the basis of $\{|0\rangle, |1\rangle\}$ with the observable $\hat{\sigma}_z = (-1)|0\rangle\langle 0| + (+1)|1\rangle\langle 1|$, which implies that an error-free measurement will give the outcome $\xi_0 = -1$ for the state $|0\rangle$, and $\xi_1 = +1$ for the state $|1\rangle$. Based on the measurement outcome, the agent provides feedback by changing the energy level configuration of the two-state system. The protocol starts with the system in state $|0\rangle$ and the energy level configuration in \hat{H}_- . Thus, the joint state of the system is $(0, -)$ (see Fig. 3.2) and the corresponding energy is $E_{(0,-)} = E_g$. Now due to interaction with the weakly coupled thermal bath, the system absorbs heat $Q_{\text{in}}^{(1)} = \Delta$, and goes from $|0\rangle$ to $|1\rangle$ with the energy level configuration still at \hat{H}_- . After this transition, the system state is $|1\rangle$, and the energy configuration is \hat{H}_- , i.e., the joint state is $(1, -)$ and the corresponding energy is $E_{(1,-)} = E_e$. As soon as there is an excitation of the system (i.e., the measurement outcome of

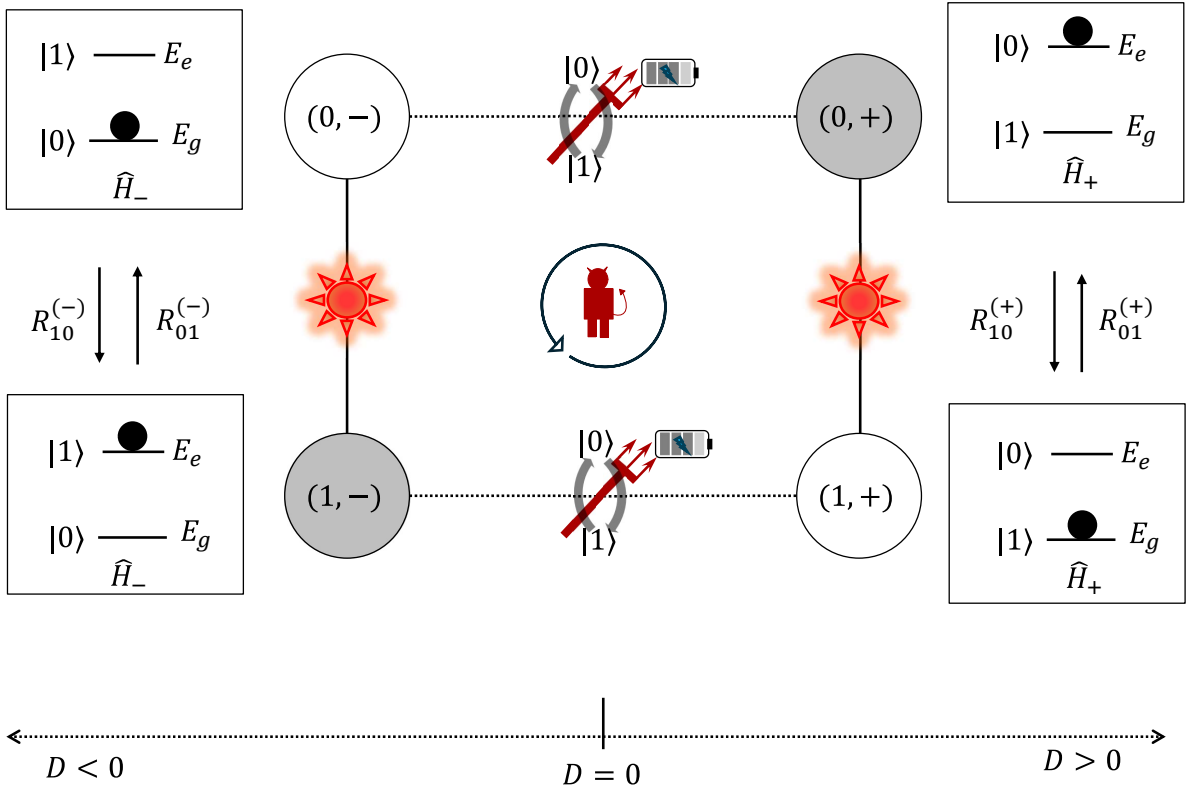


Figure 3.2: Stochastic model for the two state information engine. The graph \mathcal{G} and the corresponding joint states of the systems are shown here. Beside every every node of \mathcal{G} the corresponding physical system is depicted in the boxes. The desired behavior (information engine mode) of the protocol corresponds to counter-clockwise cycle \mathcal{C} in the network \mathcal{G} shown above. The transitions $(0, -) \leftrightarrow (1, -)$ and $(0, +) \leftrightarrow (1, +)$ correspond to excitation and de-excitation of the system due to interactions with the thermal reservoir (depicted by the sun). The corresponding transition rates from Eqs. (3.4) and Eq. (3.3) are shown shown by the arrows between the physical pictures of the joint states. The transitions $(0, -) \leftrightarrow (0, +)$ and $(1, -) \leftrightarrow (1, +)$ correspond to feedback steps (denoted by the trident) and involves interaction with the work reservoir (battery). For the feedback-resolved model, the feedback Hamiltonian $H(D)$ from Eq. (3.8) is represented here by showing the control parameter (D) below the corresponding joint states. The grey colored states $(1, -)$ and $(0, +)$ show the situations when the control parameter $D(t)$ (which is a filtered form measurement signal $z(t)$) fails to capture the actual state of the system, whereas white colored states $(0, -)$ and $(1, +)$ are the situation when the actual state of the system is captured by the control parameter $D(t)$.

$\hat{\sigma}_z$ changes from -1 to $+1$), the agent provides instantaneous feedback to switch the energy level configuration from \hat{H}_- to \hat{H}_+ . By doing this the demon extracts work $W_{\text{ext}}^{(1)} = \Delta$, as the system at the state $|1\rangle$ is taken from E_e to E_g . After the feedback step by the demon, the joint state is given as $(1, +)$ with energy $E_{(1,+)} = E_g$. Now a similar sequence is repeated, with the setup going from $(1, +)$ to $(0, +)$ by absorbing heat $Q_{\text{in}}^{(2)} = \Delta$, and thus we have $E_{(0,+)} = E_e$. Then the demon applies instantaneous feedback by switching the levels, and taking the joint state of the system from $(0, +)$ to $(0, -)$ while extracting work $W_{\text{ext}}^{(2)} = \Delta$. After this sequence of steps the system and the energy level configuration both are restored to their initial states: $(0, -)$. We represent this as the cyclic protocol $\mathcal{C} : (0, -) \rightarrow (1, -) \Rightarrow (1, +) \rightarrow (0, +) \Rightarrow (0, -)$; where ' \rightarrow ' signifies a thermal excitation step and ' \Rightarrow ' signifies an instantaneous feedback. The cycle \mathcal{C} corresponds to traversing the network shown in Fig. 3.2 in the counter-clockwise (CCW) direction. In one cycle of \mathcal{C} , in total $Q_{\text{in}}^{\text{cycle}} = Q_{\text{in}}^{(1)} + Q_{\text{in}}^{(2)} = 2\Delta$ heat has been extracted from the heat reservoir and completely converted to work $W_{\text{ext}}^{\text{cycle}} = W_{\text{ext}}^{(1)} + W_{\text{ext}}^{(2)} = 2\Delta$. In the ideal feedback limit the system spends almost no time at states $(1, -)$ and $(0, +)$. Hence, these two states act as transients (shown as grey circles in Fig. 3.2) for the transitions between two stable states $(0, -)$ and $(1, +)$ (shown as white circles in Fig. 3.2).

3.2.3 Imperfect feedback protocol: the feedback-resolved model

Now we consider the situation where the agent makes measurement errors due to an imperfect measurement device and also there is a finite bandwidth of detection, implying that the feedback response lags behind the actual state of the system. In this situation, the directed nature of the cycle \mathcal{C} is lost because of the possibility of thermal de-excitation and incorrect feedback

due to finite bandwidth and measurement errors. The system can now spend finite time in the states $(1, -)$ and $(0, +)$ and also can return the states $(0, -)$ and $(1, +)$ against the direction of the desired protocol in \mathcal{C} . Hence, the system executes stochastic dynamics on the corresponding graph with bi-directional edges $\mathcal{G} : (0, -) \leftrightarrow (1, -) \leftrightarrow (1, +) \leftrightarrow (0, +) \leftrightarrow (0, -)$ as shown in the Fig. 3.2.

To model such system, we introduce a ‘*feedback-resolved*’ model where the change in the energy level configuration takes place through a continuous control parameter $D \in \mathbb{R}$. We consider that the energy level configuration of the system is described by the *threshold* feedback [1] Hamiltonian $\hat{H}(D)$:

$$\hat{H}(D) = (1 - \theta(D))\hat{H}_- + \theta(D)\hat{H}_+ \quad (3.8)$$

where D is the control parameter and $\theta(D)$ is the Heaviside step function. At any time t , the value of the control parameter $D(t)$ is calculated as the low-pass filtered (with a smoothing rate or bandwidth γ) version of the continuous measurement signal $z(t)$ (see Eq. (2.32) and other details in Sec: 2.3.1)

$$D(t) = \int_{-\infty}^t ds \gamma e^{-\gamma(t-s)} z(s). \quad (3.9)$$

Thus, $1/\gamma$ is the natural time-scale for the evolution of the control parameter. To obtain the measurement signal $z(t)$, the agent measures the observable $\hat{\sigma}_z$. We assume that the measurement signal $z(t)$ is generated through an imperfect continuous measurement device that follows the Gaussian measurement model (see Sec: 2.2.4):

$$\rho(z| |i\rangle) = \sqrt{\frac{2\lambda\delta t}{\pi}} e^{-2\lambda\delta t(z-\xi_i)^2}, \quad i \in \{0, 1\}, \quad (3.10)$$

where λ is the measurement strength.

Since the feedback Hamiltonian $\hat{H}(D)$ depends on the control parameter D , the transition rates between $|0\rangle$ and $|1\rangle$ are also dependent on D . Similar to Eq. (3.8), we define a threshold feedback rate matrix $R(D)$ using Eq. (3.6) and Eq. (3.7) as

$$R(D) = (1 - \theta(D))R^{(-)} + \theta(D)R^{(+)}, \quad (3.11)$$

$$R^{(-)} = \Gamma \begin{pmatrix} -n_B & (n_B + 1) \\ n_B & -(n_B + 1) \end{pmatrix}, \quad R^{(+)} = \Gamma \begin{pmatrix} -(n_B + 1) & n_B \\ (n_B + 1) & -n_B \end{pmatrix} \quad (3.12)$$

to describe the control parameter dependent transition rates between $|0\rangle \leftrightarrow |1\rangle$. At any time t , the probability of the system being in state $|0\rangle$ ($|1\rangle$) and the control parameter at the value D is given by the joint distribution function $P_{0(1)}(D, t)$. Following the discussion in Sec. 2.5.2 of Chapter 2, we describe the master equation for the joint statistical state of the system and control parameter $\vec{P}(D, t) = [P_0(D, t), P_1(D, t)]^T$ for the feedback-resolved model as

$$\frac{\partial}{\partial t} \vec{P}(D, t) = R(D) \vec{P}(D, t) + \hat{\mathcal{F}} \vec{P}(D, t) \quad (3.13)$$

where $\hat{\mathcal{F}}$ is a diagonal matrix of OU operators:

$$\hat{\mathcal{F}}_{ij} = \delta_{ij} \left[\gamma \frac{\partial}{\partial D} (D - \xi_i) + \frac{\gamma^2}{8\lambda} \frac{\partial^2}{\partial D^2} \right] \quad (3.14)$$

Now from this feedback-resolved model, we can obtain a coarse-grained description of the model by integrating the control parameter D in appropriate domains to obtain the probability vectors

of system state corresponding to \hat{H}_- and (\hat{H}_+) energy level configurations:

$$\begin{pmatrix} P_{(0,-)} \\ P_{(1,-)} \end{pmatrix} = \int dD(1 - \theta(D))\vec{P}(D, t); \quad \begin{pmatrix} P_{(0,+)} \\ P_{(1,+)} \end{pmatrix} = \int dD\theta(D)\vec{P}(D, t); \quad (3.15)$$

3.3 Analytical treatment of the model

In this section, we present an analytical treatment of the model in the multiple time scale approach with the smallness parameter $\epsilon = (\Gamma/\gamma)$ using the results from the Chapter 2. We discuss the analytical expression of the steady state work extraction rate both in strong separation of timescales (0th order approximation) limit when $\epsilon \rightarrow 0$, and then also discuss the corrections to in the first order. From the 0th order expression of power we discuss the criteria for information engine operation mode vs. the dissipator operation mode. Then we discuss the power production in another limiting case when the feedback delay is captured up to the 1st order in ϵ but the measurement strength (accuracy) is infinite.

3.3.1 Steady state power calculation

We calculate the average steady state work extraction rate or *power* as $\langle \dot{W}_{\text{ext}}^{ss} \rangle = (2\Delta)J^{ss}$, where J^{ss} is the stationary current in the graph \mathcal{G} along the direction of the desired protocol \mathcal{C} , i.e. in the CCW direction. Since there is only one cycle in the graph \mathcal{G} , the current across all the edges of \mathcal{G} are same (J^{ss}) due to conservation of probability. Thus, we can calculate the stationary current (or power) from any edge. We choose to calculate the current from $(1, +)$ to

$(0, +)$ across the edge $(1, +) \leftrightarrow (0, +)$. Hence we have,

$$\begin{aligned}\langle \dot{W}_{\text{ext}}^{ss} \rangle &= 2\Delta J^{ss} \\ &= 2\Delta J_{(0,+)} \leftarrow (1,+) \\ &= 2\Delta \left[R_{01}^{(+)} P_{(1,+)}^{ss} - R_{10}^{(+)} P_{(0,+)}^{ss} \right]\end{aligned}\tag{3.16}$$

Next, we discuss how to obtain expressions for $P_{(1,+)}^{ss}$ and $P_{(0,+)}^{ss}$, that are required for the power calculation by Eq. (3.16). Using the MTSP method (see Appendix. 3.4) we obtain the steady state solution to Eq. (3.13) as,

$$\vec{P}^{ss}(D) = \frac{1}{2} \begin{pmatrix} \Pi_{00}(D) \\ \Pi_{11}(D) \end{pmatrix} + \epsilon \begin{pmatrix} \hat{\mathcal{F}}_{00}^+ h(D) \\ -\hat{\mathcal{F}}_{11}^+ h(D) \end{pmatrix} + \mathcal{O}(\epsilon^2)\tag{3.17}$$

where $\Pi_{00(11)}(D)$ is a Gaussian distribution located at $-1(+1)$ with variance $\gamma/8\lambda$:

$$\Pi_{ii}(D) = \sqrt{\frac{4\lambda}{\gamma\pi}} \exp \left[-\frac{4\lambda}{\gamma}(D - \xi_i)^2 \right]\tag{3.18}$$

The function $h(D)$ is given as

$$h(D) = \frac{1}{2} [R_{10}(D)\Pi_{00}(D) - R_{01}(D)\Pi_{11}(D)].\tag{3.19}$$

The operators $\hat{\mathcal{F}}_{ii}^+$ are the Drazin inverse [63, 87] of the scaled OU operator $\hat{\mathcal{F}}_{ii} = (\Gamma/\gamma)\hat{\mathcal{F}}_{ii}$, and is defined in Eq. (2.121) in Chapter. 2 (also discussed in the Appendix. 3.5.2). The expressions for $\hat{\mathcal{F}}_{00}^+ h(D)$ and $\hat{\mathcal{F}}_{11}^+ h(D)$ can be calculated using the eigenfunctions of $\hat{\mathcal{F}}_{ii}$ which are presented in the Appendix. 3.5.1.

From Eq.(3.17) and Eq. 3.18, we see that, even in the fast feedback $\epsilon \rightarrow 0$ limit, the distributions $P_{0(1)}^{ss}(D) = \frac{1}{2}\Pi_{00(11)}(D)$ will have some spread in the control parameter space D due to error in the measurement process (i.e., due to finite value of λ/γ). Hence there is a finite probability of the wrong feedback being applied, characterized by the *error probability* η , given in Eq. (3.28) of Appendix 3.4, which represents the stationary state probability of finding the control parameter D in the wrong feedback regime for a given system state ($|0\rangle$ or $|1\rangle$).

Using Eq. (3.15) and (3.16), Eq. (3.17) we can obtain the expression of $\dot{W}_{\text{ext}}^{ss}$, which we write as a power series in ϵ :

$$\langle \dot{W}_{\text{ext}}^{ss} \rangle = \langle \dot{W}_{\text{ext}}^{ss,[0]} \rangle + \epsilon \langle \dot{W}_{\text{ext}}^{ss,[1]} \rangle + \mathcal{O}(\epsilon^2), \quad (3.20)$$

where, the 0th-order expression of the power is given as $\langle \dot{W}_{\text{ext}}^{ss,[0]} \rangle$

$$\langle \dot{W}_{\text{ext}}^{ss,[0]} \rangle = \Delta\Gamma [n_B(1 - \eta) - (n_B + 1)\eta], \quad (3.21)$$

Notice that even the 0th-order expression of power contains the error probability η . For the accurate measurement limit ($\eta \rightarrow 0$) we get the maximum value of $\dot{W}_{\text{ext}}^{ss,[0]}$ as $\Delta\Gamma n_B$. Eq. 3.21 implies any nonzero error probability η reduces the power from it due to feedback mistakes. For a fixed Δ and Γ the maximum power production is controlled by the average number of bosons (n_B) of energy Δ in the bath which decreases with decreasing temperature (increasing β). Thus we see $(\dot{W}_{\text{ext}}^{ss,[0]})/\Gamma\Delta$ decreases with $\beta\Delta$ as seen in Fig. 3.3.

From Eq. (3.20) we see that the first-order correction to the steady state work extraction

rate is $\epsilon \langle \dot{W}_{\text{ext}}^{ss,[1]} \rangle$, where

$$\begin{aligned} \langle \dot{W}_{\text{ext}}^{ss,[1]} \rangle &= -2\Delta \left[n_B \int_{-\infty}^{\infty} dD \theta(D) \hat{\mathcal{F}}_{11}^+ h(D) + (n_B + 1) \int_{-\infty}^{\infty} dD \theta(D) \hat{\mathcal{F}}_{00}^+ h(D) \right] \\ &= -\Delta \Gamma [(2n_B + 1)(m + z + kn_B)], \end{aligned} \quad (3.22)$$

and m , z and k are dimensionless parameters with defined by Eqs.(3.32), (3.33), (3.34) and the expressions given in Eqs. (3.58), (3.66), (3.74). See Appendix. 3.5 for details of the calculation of these constants. Thus using Eqs. (3.20), (3.21), (3.22), we write the power, including the first-order correction due to finite bandwidth effect (feedback delay effect), as

$$\langle \dot{W}_{\text{ext}}^{ss} \rangle = \Delta \Gamma [n_B(1 - \eta) - (n_B + 1)\eta] - \gamma^{-1} \Delta \Gamma^2 [(2n_B + 1)(m + z + kn_B)] \quad (3.23)$$

3.3.2 Thermodynamic operation modes: dissipator vs. information engine

Since the system under consideration interacts with a single heat bath, the first law of thermodynamics at steady state is given as

$$\langle \dot{Q}_{\text{in}}^{ss} \rangle = \langle \dot{W}_{\text{ext}}^{ss} \rangle \quad (3.24)$$

where $\langle \dot{Q}_{\text{in}}^{ss} \rangle$ is the average heat intake rate from the thermal reservoir at steady state, and $\langle \dot{W}_{\text{ext}}^{ss} \rangle$ is the average work extraction rate at steady state. Now if $\langle \dot{W}_{\text{ext}}^{ss} \rangle > 0$, the agent is directly converting heat from the thermal reservoir to work by measurement and feedback, thus it is acting as a *Maxwell's demon* or *information engine*. Whereas if $\langle \dot{W}_{\text{ext}}^{ss} \rangle < 0$, the performs work on the system, which is converted to heat and is dissipated to the reservoir. Thus in this case

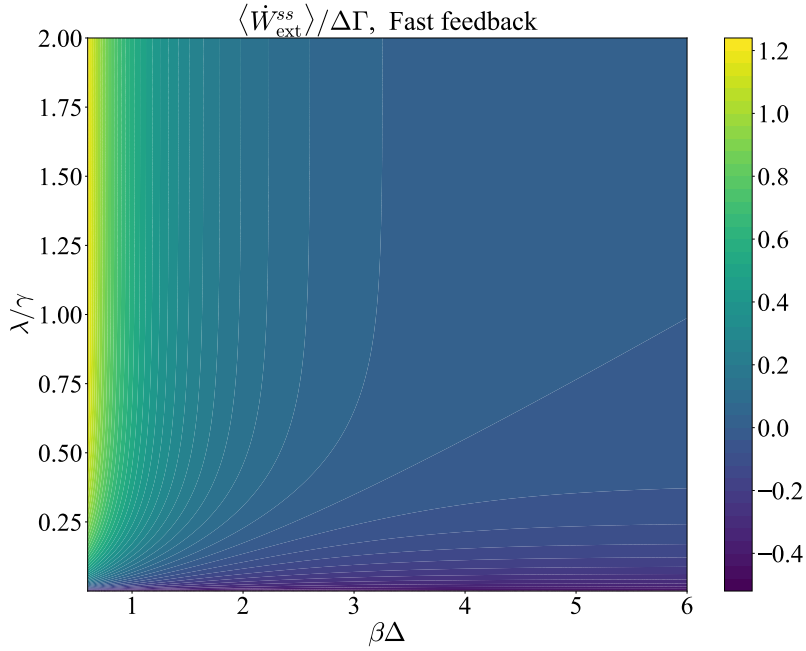


Figure 3.3: Steady state work extraction rate for the two state toy model in the fast feedback limit ($\epsilon \approx 0$). The vertical axis of the plots represent the ratio λ/γ . The horizontal axis of the plots represent $\beta\Delta$. The figure above shows values of $\langle \dot{W}_{\text{ext}}^{\text{ss}} \rangle / \Gamma\Delta$, (see Eq. (3.21)) i.e., steady state work extraction by the agent in the fast feedback limit, scaled by the factor $\Gamma\Delta$.

the overall setup is acting as a *dissipator* where the work, a useful thermodynamic resource, is getting converted to thermal fluctuations, i.e. it is being wasted. The dissipator behavior of the system arises due to the imperfect nature of measurement-feedback by the demon.

3.3.3 Criteria for information engine mode in fast feedback limit ($\epsilon \approx 0$)

In the fast feedback limit ($\gamma \gg \Gamma$ or $\epsilon \ll 1$), we approximate $\epsilon \approx 0$ in the expression for $\langle \dot{W}_{\text{ext}}^{\text{ss}} \rangle$ in Eq.(3.20), we can write the criterion for the information engine operational mode of the model $\langle \dot{W}_{\text{ext}}^{\text{ss}} \rangle \approx \langle \dot{W}_{\text{ext}}^{\text{ss},[0]} \rangle > 0$ as :

$$\eta < \eta^* = \frac{n_B}{2n_B + 1} = \frac{e^{-\beta\Delta}}{e^{-\beta\Delta} + 1} \quad (3.25)$$

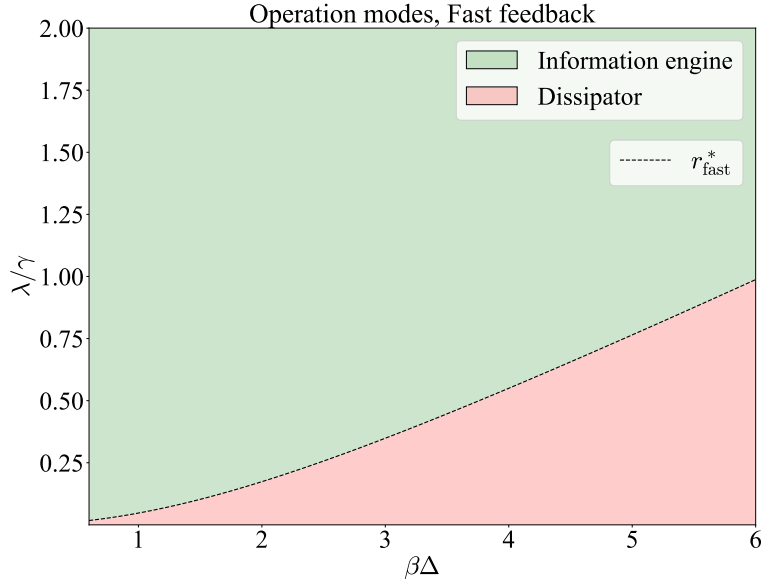


Figure 3.4: Operation mode phase diagram in fast feedback limit. The figure shows the sign of $\langle \dot{W}_{\text{ext}}^{ss} \rangle$ from Fig. 3.3. For the information engine region we have $\langle \dot{W}_{\text{ext}}^{ss} \rangle > 0$ and for the dissipator mode we have $\langle \dot{W}_{\text{ext}}^{ss} \rangle < 0$. The separation between these two operation modes are captured by the critical ratio r_{fast}^* (see Eq. (3.26)).

where η^* the critical error probability of feedback (in the fast-feedback limit) that leads to a change in the operational mode from information engine to dissipator once crossed. Note that η is a monotonically decreasing function of the ratio of measurement strength and feedback bandwidth (λ/γ) (see Eq. (3.29)). Thus the criteria for the information engine operation mode (for $\epsilon \approx 0$ limit) in Eq (3.25) can also be expressed as

$$\frac{\lambda}{\gamma} > r_{\text{fast}}^* = \frac{1}{4} [\text{erfc}^{-1}(2\eta^*)]^2 = \frac{1}{4} \left[\text{erfc}^{-1} \left(\frac{2e^{-\beta\Delta}}{e^{-\beta\Delta} + 1} \right) \right]^2 \quad (3.26)$$

where r_{fast}^* depends on the inverse temperature of the bath β and the energy gap of the two state model Δ and erfc^{-1} stands for the inverse of the co-error function [91]. Hence for $(\lambda/\gamma) > r_{\text{fast}}^*$ we get the information engine operation mode and, for $(\lambda/\gamma) < r_{\text{fast}}^*$ we get dissipator

operation mode. The variation of r_{fast}^* with $\beta\Delta$ is shown in the Fig. 3.4, where r_{fast}^* creates a boundary between the information engine and dissipator regime which can be understood as follows. For a fixed Δ with increasing β (decreasing temperature) $\dot{W}_{\text{ext}}^{ss,[0]}$ decreases (due to decreasing n_B). Hence feedback errors become more costly with increasing β , and more accuracy (stronger measurements) are required to compensate for the decrease in power production to achieve the information engine regime. This leads to the increasing nature of r_{fast}^* with $\beta\Delta$ in the Fig. 3.4.

3.3.4 Steady state power in strong measurement ($\lambda \gg \gamma$) but lagging controller ($\epsilon \neq 0$)

When $\lambda \gg \gamma$, limit the error probability becomes extremely small ($\eta \approx 0$) since the distribution $\Pi_{00(11)}(D)$ is sharply peaked at its mean $-1(+1)$, as reflected in Eq. (3.29). In this limit, we have $\theta(D)\Pi_{00}(D) \approx 0$ and $\phi(D)\Pi_{11}(D) \approx 0$, which imply $m \approx 0$ and $z \approx 0$ from Eq. (3.32) and Eq. (3.33). It can also be shown that in this limit $k \approx \ln 2$ (see Appendix. 3.5.4). Thus in this limit the average work extraction is

$$\langle \dot{W}_{\text{ext}}^{ss} \rangle = \Gamma n_B \Delta [1 - \epsilon(2n_B + 1) \ln 2] \quad (3.27)$$

Thus the lag of the control parameter with respect to system dynamics causes a decrease in the steady-state average work extraction.

3.4 Appendix: MTSP solution for steady states

Here we discuss the steady state solution to Eq. (3.13) in the separation of time scales limit following the results shown in Sec. 2.5.2 of Chapter 2. For convenience we define $\phi(D) = 1 - \theta(D)$, and using the expression of Π_{ij} from Eq. (3.18) define the *error probability* η as

$$\begin{aligned}\eta &= \int_{-\infty}^{\infty} dD \theta(D) \Pi_{00}(D) \\ &= \int_{-\infty}^{\infty} dD \phi(D) \Pi_{11}(D)\end{aligned}\tag{3.28}$$

which can be written as

$$\eta = \frac{1}{2} \left[1 - \operatorname{erf} \left(\sqrt{\frac{4\lambda}{\gamma}} \right) \right]\tag{3.29}$$

Now we solve for the 0th order effective rate matrix R_0 from Eq. (2.118) as

$$R_0 = \int dDR(D) \Pi(D) = \Gamma(n_B + \eta) \begin{pmatrix} -1 & 1 \\ 1 & -1 \end{pmatrix},\tag{3.30}$$

and for the 1st order effective rate matrix R_1 , using Eq. (2.120) we get,

$$R_1 = - \int dDR(D) \hat{\tilde{\mathcal{F}}}^+ R(D) \Pi(D) = \Gamma(m - z - kn_B) \begin{pmatrix} -1 & 1 \\ 1 & -1 \end{pmatrix},\tag{3.31}$$

where, m , z and k are dimensionless parameters that are determined by the ratio λ/γ and formally can be written as

$$m = \Gamma \int_{-\infty}^{\infty} dD \theta(D) \hat{\mathcal{F}}_{00}^+ \theta(D) \Pi_{00}(D) = \Gamma \int_{-\infty}^{\infty} dD \phi(D) \hat{\mathcal{F}}_{11}^+ \phi(D) \Pi_{11}(D) \quad (3.32)$$

$$z = \Gamma \int_{-\infty}^{\infty} dD \theta(D) \hat{\mathcal{F}}_{11}^+ \theta(D) \Pi_{00}(D) = \Gamma \int_{-\infty}^{\infty} dD \phi(D) \hat{\mathcal{F}}_{00}^+ \phi(D) \Pi_{11}(D) \quad (3.33)$$

$$k = \Gamma \int_{-\infty}^{\infty} dD \theta(D) \hat{\mathcal{F}}_{11}^+ \Pi_{00}(D) = \Gamma \int_{-\infty}^{\infty} dD \phi(D) \hat{\mathcal{F}}_{00}^+ \Pi_{11}(D) \quad (3.34)$$

Now we define marginal distribution of the states of the two-state system when the control parameter D is integrated out as $\vec{P}(t) = [P_0(t), P_1(t)]^T$, and assume that it can be expressed as a series $\sum_{k=0}^{\infty} \epsilon^k \vec{P}^{(k)}(t)$. Then the equations for the $\vec{P}^{(0)}(t)$ and $\vec{P}^{(1)}(t)$ are given as

$$\frac{d\vec{P}^{(0)}(t)}{dt} = R_0 \vec{P}^{(0)}(t) \quad (3.35)$$

$$\frac{d\vec{P}^{(1)}(t)}{dt} = R_0 \vec{P}^{(1)}(t) + \epsilon R_1 \vec{P}^{(0)}(t) \quad (3.36)$$

Solving these for the steady-state solution with the normalization conditions $P_0^{(0)}(t) + P_1^{(0)}(t) = 1$ and $P_0^{(1)}(t) + P_1^{(1)}(t) = 0$, we get

$$\vec{P}^{ss,(0)} = \begin{pmatrix} 1/2 \\ 1/2 \end{pmatrix}; \quad \vec{P}^{ss,(1)} = \begin{pmatrix} 0 \\ 0 \end{pmatrix}. \quad (3.37)$$

Thus we have $\vec{P}^{ss} = [1/2, 1/2]^T + \mathcal{O}(\epsilon^2)$, which implies the distribution of $|0\rangle$ and $|1\rangle$ remains the same in the steady state, which is expected from the symmetry of the problem. Using the

expression of \vec{P}^{ss} , we write the steady state joint system-controller distribution as,

$$\vec{P}^{ss}(D) = \Pi(D)\vec{P}^{ss} - \epsilon\hat{\tilde{\mathcal{F}}}^+R(D)\Pi(D)\vec{P}^{ss} + \mathcal{O}(\epsilon^2) \quad (3.38)$$

where $\Pi(D) = \text{diag}([\Pi_{00}(D), \Pi_{11}(D)])$ and $\hat{\tilde{\mathcal{F}}}^+ = \text{diag}\left(\left[\hat{\tilde{\mathcal{F}}}_{00}^+(D), \hat{\tilde{\mathcal{F}}}_{11}^+(D)\right]\right)$. The equation above can also be written in the form presented in Eq. (3.17).

3.5 Appendix: Evaluation of the dimensionless parameters (m, z, k) arising in first order perturbation scheme

3.5.1 Eigenspectrum of Fokker-Planck operator for Ornstein–Uhlenbeck (OU) process

We denote the n th eigenvalue of the OU operator $\hat{\tilde{\mathcal{F}}}_{ii}$ as $\lambda_n^{(i)}$ and the corresponding right eigenvector as $|\lambda_n^{(i)}\rangle \equiv \phi_n^{(i)}(D)$ and the left eigenvector as $\langle \lambda_n^{(i)}| \equiv \tilde{\phi}_n^{(i)}(D)$. Where we have

$$\hat{\tilde{\mathcal{F}}}_{ii}|\lambda_n^{(i)}\rangle \equiv \left[\Gamma\partial_D(D - \xi_i) + \frac{\gamma\Gamma}{8\lambda}\partial_D^2\right]\phi_n^{(i)}(D) = \lambda_n^{(i)}\phi_n^{(i)}(D) \equiv \lambda_n^{(i)}|\lambda_n^{(i)}\rangle, \quad (3.39)$$

$$\langle \lambda_n^{(i)}|\hat{\tilde{\mathcal{F}}}_{ii} \equiv \left[-\Gamma(D - \xi_i)\partial_D + \frac{\gamma\Gamma}{8\lambda}\partial_D^2\right]\tilde{\phi}_n^{(i)}(D) = \lambda_n^{(i)}\tilde{\phi}_n^{(i)}(D) \equiv \langle \lambda_n^{(i)}|\lambda_n^{(i)}. \quad (3.40)$$

The eigenvalue and eigenfunctions[67] are given as

$$\lambda_n^{(i)} = -n\Gamma, \quad n = 0, 1, 2, 3, \dots \quad (3.41)$$

$$\begin{aligned}
|\lambda_n^{(i)}\rangle \equiv \phi_n^{(i)}(D) &= \frac{1}{2^n n!} H_n \left[\sqrt{\frac{4\lambda}{\gamma}} (D - \xi_i) \right] \Pi_{ii}(D) \\
&= \frac{1}{2^n n!} \sqrt{\frac{4\lambda}{\gamma\pi}} H_n \left[\sqrt{\frac{4\lambda}{\gamma}} (D - \xi_i) \right] e^{-\frac{4\lambda}{\gamma}(D - \xi_i)^2},
\end{aligned} \tag{3.42}$$

$$\langle \lambda_n^{(i)} | \equiv \tilde{\phi}_n^{(i)}(D) = H_n \left[\sqrt{\frac{4\lambda}{\gamma}} (D - \xi_i) \right] \tag{3.43}$$

. where, H_n is the Hermite polynomial [92] of order n . If we define the inner-product between two functions as $\langle f | g \rangle = \int dD f(D) g(D)$, then we have a bi-orthogonality relation among the eigenfunctions of the OU operator $\hat{\mathcal{F}}_{ii}$:

$$\langle \lambda_m^{(i)} | \lambda_n^{(i)} \rangle = \delta_{mn}. \tag{3.44}$$

We now define the null space projector of the operator $\hat{\mathcal{F}}_{ii}$ as

$$\hat{\mathcal{P}}_{\hat{\mathcal{F}}_{ii}} = |\lambda_0^{(i)}\rangle \langle \lambda_0^{(i)}| \equiv \Pi_{ii}(D) \int dD(*) \tag{3.45}$$

and, for convenience, we define a dimensionless quantity

$$\alpha = \frac{4\lambda}{\gamma}. \tag{3.46}$$

The projector outside the null-space can be written as

$$\hat{\mathcal{Q}}_{\hat{\mathcal{F}}_{ii}} = \sum_{n=1}^{\infty} |\lambda_n^{(i)}\rangle \langle \lambda_n^{(i)}| \equiv \Pi_{ii}(D) \sum_{n=1}^{\infty} \frac{1}{2^n n!} H_n [\sqrt{\alpha}(D - \xi_i)] \int dD' H_n [\sqrt{\alpha}(D' - \xi_i)] (*) \tag{3.47}$$

and $\hat{\mathcal{P}}_{\hat{\mathcal{F}}_{ii}}$ and $\hat{\mathcal{Q}}_{\hat{\mathcal{F}}_{ii}}$ sum to identity operator

$$\hat{\mathcal{P}}_{\hat{\mathcal{F}}_{ii}} + \hat{\mathcal{Q}}_{\hat{\mathcal{F}}_{ii}} = \hat{\mathbf{1}} \quad (3.48)$$

3.5.2 Evaluating integrals containing Drazin inverses

To evaluate the constants m, z and k , we will evaluate integrals of the form

$$\int_{-\infty}^{\infty} dDf(D) \hat{\mathcal{F}}_{ii}^+ g(D) \equiv \langle f | \hat{\mathcal{F}}_{ii}^+ | g \rangle \quad (3.49)$$

where the pseudo-inverse operator is

$$\hat{\mathcal{F}}_{ii}^+ = - \int_0^{\infty} dz e^{z \hat{\mathcal{F}}_{ii}} \hat{\mathcal{Q}}_{\hat{\mathcal{F}}_{ii}} \quad (3.50)$$

Now using the eigenfunction expansion of the operator $\hat{\mathcal{F}}_{ii}^+$ we write

$$\begin{aligned} \langle f | \hat{\mathcal{F}}_{ii}^+ | g \rangle &= - \sum_{n=1}^{\infty} \int_0^{\infty} dz \langle f | e^{z \hat{\mathcal{F}}_{ii}} | \lambda_n^{(i)} \rangle \langle \lambda_n^{(i)} | g \rangle \\ &= - \sum_{n=1}^{\infty} \int_0^{\infty} dz e^{-n\Gamma z} \langle f | \lambda_n^{(i)} \rangle \langle \lambda_n^{(i)} | g \rangle \\ &= - \left(\frac{1}{\Gamma} \right) \sum_{n=1}^{\infty} \left(\frac{1}{n} \right) \langle f | \lambda_n^{(i)} \rangle \langle \lambda_n^{(i)} | g \rangle \end{aligned} \quad (3.51)$$

Expressing the inner-products as integrals we get,

$$\int_{-\infty}^{\infty} dD f(D) \hat{\tilde{\mathcal{F}}}_{ii}^+ g(D) = - \left(\frac{1}{\Gamma} \right) \sum_{n=1}^{\infty} \left(\frac{1}{n} \right) \left[\int_{-\infty}^{\infty} dD f(D) \phi_n^{(i)}(D) \right] \left[\int_{-\infty}^{\infty} dD' \tilde{\phi}_n^{(i)}(D') g(D') \right] \quad (3.52)$$

3.5.3 Series expansion expressions for m, z and k

We now obtain series sum expressions for the dimensionless constants m, z and k . These series sum expressions can be used to evaluate the constants m, z and k to desired accuracy. We also relate these constants to three other constants, C_0, C_1 and C_2 , that arises in the Full Counting Statistics (FCS) based analysis of this model as given in Ref. [1, 74].

3.5.3.1 Expression for m

Using Eq. (3.32), we write

$$m = \Gamma \int_{-\infty}^{\infty} dD \theta(D) \hat{\tilde{\mathcal{F}}}_{00}^+ \theta(D) \Pi_{00}(D) \quad (3.53)$$

then using Eq. (3.52) we get

$$\begin{aligned} m &= - \sum_{n=1}^{\infty} \left(\frac{1}{n} \right) \left[\int_{-\infty}^{\infty} dD \theta(D) \phi_n^{(0)}(D) \right] \left[\int_{-\infty}^{\infty} dD' \tilde{\phi}_n^{(0)}(D') \theta(D') \Pi_{00}(D') \right] \\ &= - \sum_{n=1}^{\infty} \left(\frac{1}{n} \right) \frac{1}{2^n n!} \left[\int_0^{\infty} dD H_n [\sqrt{\alpha}(D+1)] \Pi_{00}(D) \right] \left[\int_0^{\infty} dD' H_n [\sqrt{\alpha}(D'+1)] \Pi_{00}(D') \right] \\ &= - \sum_{n=1}^{\infty} \left(\frac{1}{n} \right) \frac{1}{2^n n!} \left(\frac{\alpha}{\pi} \right) \left[\int_0^{\infty} dD H_n [\sqrt{\alpha}(D+1)] e^{-\alpha(D+1)^2} \right]^2 \end{aligned} \quad (3.54)$$

Now substituting $y = \sqrt{\alpha}(D + 1)$ we get,

$$m = - \sum_{n=1}^{\infty} \left(\frac{1}{n} \right) \frac{1}{2^n n!} \left(\frac{1}{\pi} \right) \left[\int_0^{\infty} dy H_n[y] e^{-y^2} - \int_0^{\sqrt{\alpha}} dy H_n[y] e^{-y^2} \right]^2 \quad (3.55)$$

Finally, using the Hermite indefinite integration formula (see Ref. [91])

$$\int_0^x dy H_n[y] e^{-y^2} = H_{n-1}(0) - e^{-x^2} H_{n-1}[x] \quad (3.56)$$

we obtain the expression of m as

$$m = - \sum_{n=1}^{\infty} \left(\frac{1}{n} \right) \frac{1}{2^n n!} \left(\frac{1}{\pi} \right) e^{-2\alpha} H_{n-1}^2[\sqrt{\alpha}] \quad (3.57)$$

changing the sum index $k = n - 1$, and replacing $\alpha = (4\lambda/\gamma)$ we write

$$m = - \frac{e^{-\frac{8\lambda}{\gamma}}}{\pi} \sum_{k=0}^{\infty} \left(\frac{1}{k+1} \right) \frac{\left(H_{k+1} \left[\sqrt{\frac{4\lambda}{\gamma}} \right] \right)^2}{2^{(k+1)}(k+1)!} = -C_1 \quad (3.58)$$

where the constant C_1 is defined in Refs. [1, 74].

3.5.3.2 Expression for z

Before evaluating the constant z , we present two integrals involving Hermite polynomials that will be useful. The first integral $I_1^{(n)}(\alpha)$ is

$$I_1^{(n)}(\alpha) = \int_0^{\infty} dD H_n[\sqrt{\alpha}(D - 1)] e^{-\alpha(D-1)^2} = \frac{e^{-\alpha}}{\sqrt{\alpha}} (-1)^{n-1} H_{n-1}[\sqrt{\alpha}], \quad (3.59)$$

which has been calculated in similarly as m using the formula in Eq. (3.56) and the Hermite symmetry relation $H_n[-y] = (-1)^n H_n[y]$. The next integral $I_2^{(n)}(\alpha)$ is given as

$$I_2^{(n)}(\alpha) = \int_0^\infty dD H_n[\sqrt{\alpha}(D-1)] e^{-\alpha(D+1)^2} \quad (3.60)$$

Now using the Hermite expansion formula [93]

$$H_n[x+y] = \sum_{k=0}^n \binom{n}{k} H_k[x] (2y)^{n-k}; \quad \binom{n}{k} = \frac{n!}{k!(n-k)!}, \quad (3.61)$$

we can show:

$$I_2^{(n)}(\alpha) = (-4\sqrt{\alpha})^n \int_0^\infty dD e^{-\alpha(D+1)^2} + \sum_{k=1}^n \binom{n}{k} (-4\sqrt{\alpha})^{n-k} \int_0^\infty dD H_k[\sqrt{\alpha}(D-1)] e^{-\alpha(D+1)^2}. \quad (3.62)$$

Now using the definition of η from Eq. (3.28), we get

$$I_2^{(n)}(\alpha) = (-4\sqrt{\alpha})^n \sqrt{\frac{\pi}{\alpha}} \eta + \sum_{k=1}^n \binom{n}{k} (-4\sqrt{\alpha})^{n-k} \int_0^\infty dD H_k[\sqrt{\alpha}(D+1)] e^{-\alpha(D+1)^2} \quad (3.63)$$

Using Eq. (3.56), and the Hermite symmetry relation $H_n[-y] = (-1)^n H_n[y]$ leads to

$$\begin{aligned} I_2^{(n)}(\alpha) &= \int_0^\infty dD H_n[\sqrt{\alpha}(D-1)] e^{-\alpha(D+1)^2} \\ &= (-4\sqrt{\alpha})^n \sqrt{\frac{\pi}{\alpha}} \eta + \frac{e^{-\alpha}}{\sqrt{\alpha}} \sum_{k=1}^n \binom{n}{k} (-4\sqrt{\alpha})^{n-k} H_{k-1}[\sqrt{\alpha}] \end{aligned} \quad (3.64)$$

Now we evaluate z using the integral formula with Drazin inverse presented in Eq. (3.52) as

$$z = - \sum_{n=1}^{\infty} \left(\frac{1}{n} \right) \frac{1}{2^n n!} \left(\frac{\alpha}{\pi} \right) I_1^{(n)}(\alpha) I_2^{(n)}(\alpha) \quad (3.65)$$

Substituting the integrals $I_1^{(n)}(\alpha)$ and $I_2^{(n)}(\alpha)$ from Eq. (3.59) and Eq. (3.64) and simplifying we get

$$z = \eta C_0 - C_2, \quad (3.66)$$

where

$$C_0 = 2e^{-\frac{4\lambda}{\gamma}} \sqrt{\frac{4\lambda}{\gamma\pi}} \sum_{n=0}^{\infty} \frac{\left(2\sqrt{\frac{4\lambda}{\gamma}}\right)^n}{(n+1)!(n+1)} H_n \left[\sqrt{\frac{4\lambda}{\gamma}} \right], \quad (3.67)$$

$$C_2 = e^{-2\alpha} \sum_{n=0}^{\infty} \sum_{k=0}^n \frac{(-1)^k \left(2\sqrt{\frac{4\lambda}{\gamma}}\right)^{n-k}}{2^{k+1}(n+1)!(k+1)\pi} \binom{n}{k} H_n \left[\sqrt{\frac{4\lambda}{\gamma}} \right] H_k \left[\sqrt{\frac{4\lambda}{\gamma}} \right] \quad (3.68)$$

This expression for C_0 and C_2 match with the ones obtained using the full counting statistics (FCS) based calculation presented in [1, 74].

3.5.3.3 Expression for k

Using Eq. (3.34) we write,

$$k = \Gamma \int_{-\infty}^{\infty} dD \theta(D) \hat{\mathcal{F}}_{11}^+ \Pi_{00}(D) \quad (3.69)$$

using Eq. (3.52) we get

$$k = - \sum_{n=1}^{\infty} \frac{1}{n} \left[\int_{-\infty}^{\infty} dD \theta(D) \phi_n^{(1)}(D) \right] \left[\int_{-\infty}^{\infty} dD' \tilde{\phi}_n^{(1)}(D') \Pi_{00}(D') \right] \quad (3.70)$$

which using Eq. (3.59), can be written as

$$k = - \sum_{n=1}^{\infty} \frac{1}{n} \left[\sqrt{\frac{\alpha}{\pi}} \frac{1}{2^n n!} I_1^{(n)}(\alpha) \right] \left[\int_{-\infty}^{\infty} dD' H_n [\sqrt{\alpha}(D' - 1)] \Pi_{00}(D') \right] \quad (3.71)$$

using the expansion formula in Eq. (3.61), we can write

$$k = - \sum_{n=1}^{\infty} \frac{1}{n} \left[\sqrt{\frac{\alpha}{\pi}} \frac{1}{2^n n!} I_1^{(n)}(\alpha) \right] \left[\sum_{k=0}^n \binom{n}{k} (-4\alpha)^{n-k} \int_{-\infty}^{\infty} dD' \tilde{\phi}_k^{(0)}(D') \Pi_{00}(D') \right] \quad (3.72)$$

From the bi-orthonormality property of the eigenfunctions of $\hat{\mathcal{F}}_{00}$, we have $\langle \lambda_k^{(0)} | \lambda_0^{(0)} \rangle = \delta_{k0}$.

This gives us

$$\begin{aligned} k &= - \sum_{n=1}^{\infty} \frac{1}{n} \left[\sqrt{\frac{\alpha}{\pi}} \frac{1}{2^n n!} I_1^{(n)}(\alpha) \right] \left[\sum_{k=0}^n \binom{n}{k} (-4\sqrt{\alpha})^{n-k} \delta_{k0} \right] \\ &= - \sum_{n=1}^{\infty} \frac{1}{n} \left[\sqrt{\frac{\alpha}{\pi}} \frac{1}{2^n n!} I_1^{(n)}(\alpha) \right] (-4\sqrt{\alpha})^n \end{aligned} \quad (3.73)$$

Finallyy, substituting the expression of $I_1^{(n)}(\alpha)$ from Eq. (3.59) we get

$$k = 2e^{-\alpha} \sqrt{\frac{\alpha}{\pi}} \sum_{n=1}^{\infty} \frac{(2\sqrt{\alpha})^{n-1}}{n! n} H_{n-1} [\sqrt{\alpha}] \equiv C_0 \quad (3.74)$$

where $\alpha = (4\lambda/\gamma)$ and this matches with the expression of C_0 in Eq. (3.67).

3.5.4 Limiting value of k for accurate measurements

We introduce a Gaussian distribution function of D centered at y as

$$\Pi(D; y) = \sqrt{\frac{4\lambda}{\gamma\pi}} e^{-[-\frac{4\lambda}{\gamma}(D-y)^2]}. \quad (3.75)$$

If the propagator $e^{s\hat{\mathcal{F}}_{11}}$ is applied to a Gaussian initial state, the evolved state also remains a Gaussian with the mean and standard deviation decaying towards their equilibrium values. Thus we can write

$$e^{s\hat{\mathcal{F}}_{11}}\Pi_{00}(D) = \Pi(D; 1 - 2e^{-s}), \quad (3.76)$$

$$e^{s\hat{\mathcal{F}}_{00}}\Pi_{11}(D) = \Pi(D; 2e^{-s} - 1) \quad (3.77)$$

Now we evaluate the integral k from Eq. (3.34):

$$\begin{aligned} k &= \int_{-\infty}^{\infty} dD \theta(D) \hat{\mathcal{F}}_{11}^+ \Pi_{00}(D) \\ &= - \int_0^{\infty} dD \int_0^{\infty} ds e^{s\hat{\mathcal{F}}_{11}} (\hat{\mathbf{1}} - \hat{\mathcal{P}}_{\hat{\mathcal{F}}_{11}}) \Pi_{00}(D) \\ &= - \int_0^{\infty} ds \int_0^{\infty} dD [\Pi(D; 1 - 2e^{-s}) - \Pi_{11}(D)] \\ &\approx - \int_0^{\ln 2} ds (-1) = \ln 2, \end{aligned} \quad (3.78)$$

where in the last line we have made the approximation that the integrand is non-zero only when the center of the Gaussian $\Pi(D; 1 - 2e^{-s})$ is in the left of $D = 0$, i.e. from $s = 0$ to $s = \ln 2$.

Chapter 4: Feedback controlled Maxwell’s demon in a double quantum dot (DQD) - quantum trajectory analysis

This chapter is based on the work done in collaboration with Björn Annby-Andersson, Pharnam Bakhshinezhad, Daniel Holst, Guilherme De Sousa, Christopher Jarzynski, Peter Samuelsson and Patrick P. Potts. A preprint related to this work has been posted as “Maxwell’s demon across the quantum-to-classical transition” [3]. I worked on the implementation and execution of the quantum jump trajectory simulations of the DQD Maxwell’s demon of Ref. [3] with help from Björn Annby-Andersson. In this chapter we present the quantum trajectory simulation based analysis of the DQD Maxwell’s demon model following Ref. [3] using the same datasets. Parameters for different characteristic behavior of the simulation were calculated theoretically and provided to me by Björn Annby-Andersson. For master equation based approach to the model and further details on energetics, see Ref. [75, 76].

4.1 Chapter overview

In this chapter we investigate the qualitative behavior of a double quantum dot (DQD) Maxwell’s demon, by simulating quantum trajectories. This model of Maxwell’s demon is based on a protocol originally introduced by Averin et. al. [94] and later used for DQD system [66, 95, 96] by Annby-Andersson et. al. [4]. The classical version of this Annby-Andersson model

(AA model) has been analyzed in the Ref. [4] which considers both the ideal and non-ideal feedback control. In this chapter we focus on the case of this model when quantum effects are present and the measurement-feedback is imperfect. The model is investigated using the continuous weak measurement and feedback formalism for non-autonomous (quantum) systems discussed in Chapter 2. However, instead of using the master equation approach of Chapter 3, we use an alternate simulation-based approach to investigate the model. This chapter serves as an investigation of the non-autonomous Maxwell's demon starting from the microscopic quantum description. We will revisit this model in Chapter 5 to discuss the connection between non-autonomous and autonomous Maxwell's demon.

Sec. 4.2 of this chapter discusses the physical setup of the model and presents the details of modelling. Sec. 4.2.1 discusses a brief overview of AA model [4], which is relevant for both this and the next chapter in this thesis. The description of the AA model [4] in Sec. 4.2.1 has been adapted from Ref. [2]. In Sec. 4.2.2 we present the open quantum systems approach based modelling of the DQD Maxwell's demon following Ref. [3]. Sec. 4.3 discusses the equations of motion of the joint dynamics of the the DQD and the control parameter. Sec. 4.4 discusses results from the trajectory simulations to show some of the key features of the model that arise due to the interplay of coherence generation, weak measurements and feedback delay. In this section we also present a qualitative discussion on how the classical jump picture emerges from the quantum coherent transport in this model.

Lastly, we point out that in this chapter we only investigate the trajectory simulations of the model and its qualitative features. The analytical approach to this model has not been presented in this thesis. For the master equation based analysis of the microscopic quantum model and discussion on the emergence of the classical description (AA model, [4]) from the quantum model,

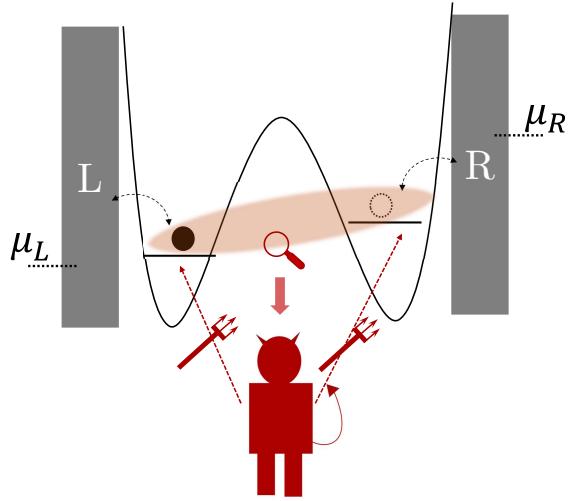


Figure 4.1: A schematic diagram for the double quantum dot Maxwell’s demon (Annby-A Andersson model [4]). The two quantum dots are separated by a tunneling barrier. The agent (demon) is making measurement into the DQD system and providing feedback accordingly. The DQD is coupled to two electron reservoirs L and R with chemical potentials μ_L and μ_R respectively. The agent transports the electron from lower to higher chemical potential through measurement and feedback.

we refer the reader to Refs. [3, 75].

4.2 Physical Setup and modelling

4.2.1 Idealized classical protocol

Here we consider a model of Maxwell’s demon (information engine) in a system of two quantum dots coupled in a series (see Fig. 4.1). A quantum dot (QD) is an artificial nano-scale structure that can confine an electron and act as ‘artificial atom’ with tunable energy levels [95, 96, 97]. The charge state of a quantum dot can be labeled as either empty or occupied based on the absence or presence of an confined electron. The physical system in this model consists of two coupled QDs in series with a tunneling barrier, and each of the QD is connected

to an electron reservoir maintained at a fixed chemical potential ($\mu_{L/R}$) and temperature T ; see Refs. [4, 94]. We consider a situation where an external agent (demon) controls the energy levels of each dot, and switches the energy level configuration of the double quantum dot (DQD) among three possible configurations: ϵ_l , ϵ_0 , and ϵ_u with, $\epsilon_l < \epsilon_0 < \epsilon_u$. Due to Coulomb blockade only a single electron can reside in the DQD system. Hence the possible *occupation states* of the DQD are: (i) $|L\rangle$: the left dot contains the excess electron, (ii) $|R\rangle$: the right dot contains the excess electron, (iii) $|0\rangle$: both dots are unoccupied. The agent is continuously monitors the DQD system and applies the feedback protocol accordingly. The electron reservoirs coupled to the left and right dots are maintained at chemical potentials μ_L and μ_R . If $\mu_R > \mu_L$, transferring an electron from the left to the right reservoir requires electrical work of $(\mu_R - \mu_L)$ to be performed against a voltage bias. Thus, if by the feedback protocol, the agent transfers one electron from the left to the right reservoir, it is equivalent to charging up an battery with the energy of $(\mu_R - \mu_L)$.

In the ideal (classical) mode of operation the DQD starts in the empty state, with the energy level of the left dot at ϵ_0 and that of the right dot at ϵ_u , where $(\epsilon_u - \mu_{L/R}) \gg k_B T$ and k_B is Boltzmann's constant. The steps of the protocol are shown in the Fig. 4.2. When (a) an electron enters the left dot from the left reservoir, (b) the agent instantaneously applies feedback to change the energy levels of both the left and right dots to ϵ_l , where $(\mu_{L/R} - \epsilon_l) \gg k_B T$. During this first feedback step, the external agent extracts $(\epsilon_0 - \epsilon_l)$ work. Next, the system is monitored until (c) the electron tunnels from the left to the right dot, at which point (d) feedback is applied to change the energy level of the left dot to ϵ_u and the right dot to ϵ_0 . The external agent performs $(\epsilon_0 - \epsilon_l)$ work during this second feedback step, cancelling the work extraction of the previous step. Finally, (e) when the electron jumps from the right dot to the right reservoir, (f) feedback is applied again to switch the energy levels of the DQD back to their initial values. No work is

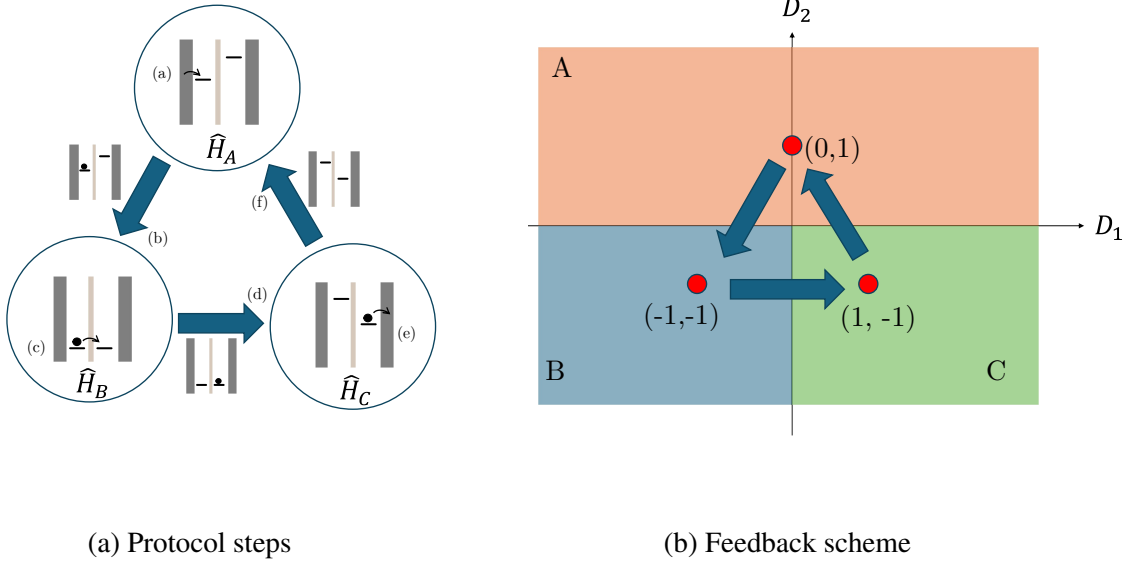


Figure 4.2: Schematics of the idealized classical protocol for the DQD Maxwell's demon (AA model) and the encoding of the protocol in feedback variables (D_1, D_2). The figure in the left shows the steps of the ideal feedback protocol of the AA model. The figure on the right shows the encoding of the protocol in the feedback variables (D_1, D_2). The red dots represent the eigenvalues of \hat{A}_1 and \hat{A}_2 as $(\xi^{(1)}, \xi^{(2)})$ corresponding to state of the DQD that feedback regions represent and the arrows show the desired direction of cycle of the control parameters.

performed during this step, as the DQD is empty. This cyclic protocol transfers an electron from the left to the right reservoir. Since no net work is performed by the external agent, the energy for this transfer must come from the thermal reservoirs. Thus the feedback-driven cycle ultimately converts heat into chemical work, of the amount $W_{\text{ext}} = (\mu_R - \mu_L)$; see Ref. [4] for more details.

4.2.2 The feedback-resolved model: quantum model with weak measurement and finite-bandwidth feedback

Now we present a quantum description of the DQD system and also consider a situation where the feedback by the agent (demon) can be imperfect, where the measurement by the agent affects the quantum state of the system (back action). We consider the situation when the demon

is monitoring the system in a way that can be modelled by weak continuous quantum measurements [63, 78] and the feedback of the demon is also not instantaneous and can have response delay due to the finite bandwidth detector [61]. We model this system under the formalism discussed in Chapter 2 following Ref. [1].

The Hamiltonian for the DQD system is,

$$\hat{H}(\epsilon_L, \epsilon_R) = \epsilon_L |L\rangle\langle L| + \epsilon_R |R\rangle\langle R| + g(|L\rangle\langle R| + |R\rangle\langle L|), \quad (4.1)$$

where $\epsilon_L (\epsilon_R)$ stands for energy of the left (right) quantum dot and g is the inter-dot coupling. The quantum dot is also weakly coupled with two electron reservoirs with the coupling constant Γ , with the left (right) dot being coupled to the left (right) electron reservoir. Note that this Hamiltonian generates coherence between $|L\rangle$ and $|R\rangle$ but does not generate any coherence between $|0\rangle$ and $|L\rangle(|R\rangle)$. We label the electron reservoirs by $\alpha \in L, R$ for left (L) and right (R) reservoirs. The transition rate for an electron from (to) the reservoir α to (from) the quantum dot α at energy level ϵ is given as $\gamma_\alpha(\epsilon)(\kappa_\alpha(\epsilon))$ and these transition rates can be expressed as

$$\gamma_\alpha(\epsilon) = \Gamma f_\alpha^{\text{FD}}(\epsilon) \quad (4.2)$$

$$\kappa_\alpha(\epsilon) = \Gamma(1 - f_\alpha^{\text{FD}}(\epsilon)), \quad (4.3)$$

where $f_\alpha^{\text{FD}}(\epsilon)$ is the Fermi-Dirac distribution:

$$f_\alpha^{\text{FD}}(\epsilon) = \frac{1}{e^{\beta(\epsilon - \mu_\alpha)} + 1}. \quad (4.4)$$

Here $\beta = 1/k_B T$ is the inverse temperature and μ_α is the chemical potential of the electron reservoir. Note that the ratio of the transition rates satisfy the generalized local detailed balance relation:

$$\frac{\gamma_\alpha(\epsilon)}{\kappa_\alpha(\epsilon)} = e^{-\beta(\epsilon - \mu_\alpha)}. \quad (4.5)$$

We model the dynamics of the state of the DQD system, $\hat{\rho}_t$, by the Lindblad master equation [64] $\partial_t \hat{\rho}_t = \mathcal{L}(\epsilon_L, \epsilon_R) \hat{\rho}_t$, where the Lindbladian superoperator $\mathcal{L}(\epsilon_L, \epsilon_R)$ is defined as

$$\mathcal{L}(\epsilon_L, \epsilon_R) \hat{\rho} = -i \left[\hat{H}(\epsilon_L, \epsilon_R), \rho \right] + \sum_{\alpha=L,R} (\gamma_\alpha(\epsilon_\alpha) \mathcal{D} [|\alpha\rangle\langle 0|] + \kappa_\alpha(\epsilon_\alpha) \mathcal{D} [|0\rangle\langle \alpha|]), \quad (4.6)$$

where $\mathcal{D}[\hat{\sigma}] \hat{\rho} = \hat{\sigma} \hat{\rho} \hat{\sigma}^\dagger - (1/2)(\hat{\sigma}^\dagger \hat{\sigma} \hat{\rho} + \hat{\rho} \hat{\sigma}^\dagger \hat{\sigma})$. The first term on the r.h.s. of Eq. (4.6) is the von-Neumann term (with $\hbar = 1$) that generates unitary evolution and the terms under the summation are dissipators corresponding to coupling with the electron reservoir that generates transitions of electron between the reservoir and quantum dots.

Here we consider a situation where the agent is making measurement of two observable: $\hat{A}_1 = -|L\rangle\langle L| + |R\rangle\langle R|$ and $\hat{A}_2 = |0\rangle\langle 0| - (|L\rangle\langle L| + |R\rangle\langle R|)$. The use of two observables is required to avoid incorrect interpretation of the state of the system [3, 4, 76]. Here, \hat{A}_1 measures which of the QD the electron is located it; and the corresponding outcomes $\xi_L^{(1)} = -1$ ($\xi_R^{(1)} = +1$) corresponds to the electron being in the left (right) dot. The observable \hat{A}_2 measures the overall charge state of the DQD, and the corresponding outcome $\xi_0^{(2)} = +1$ implies the DQD is empty, and the outcome $\xi_{L,R}^{(2)} = -1$ implies the DQD is occupied. Note that the measurement of \hat{A}_2 does not give any information about which of the dot in DQD the electron is in. The measurement of \hat{A}_1 causes decoherence in the $|L\rangle, |R\rangle$ basis but the measurement of \hat{A}_2 does not. The

Hamiltonian in Eq. (4.1) does not create any coherence between $|0\rangle$ and $|L\rangle$ ($|R\rangle$) and we have $[\hat{H}(\mathbf{D}), \hat{A}_2] = 0$. Thus, the measurement of \hat{A}_2 act as a completely classical measurement. Note that since the observable \hat{A}_1 and \hat{A}_2 commute with each-other, $[\hat{A}_1, \hat{A}_2] = 0$, we can simultaneously measure both the observable and also reduce their uncertainties independently. The observables \hat{A}_1 and \hat{A}_2 are continuously monitored by the agent, and we model these measurements using the Gaussian POVM for weak measurements, (discussed previously in Chapter 2, see also Eq. (4.10) in Sec. 4.3.1 of this chapter for additional details) with measurement strength λ_1 and λ_2 respectively. The measurement signals from these observable are then filtered with exponential smoothing with bandwidth γ_1 and γ_2 respectively to obtained filtered measurement signals $D_1(t)$ and $D_2(t)$. These filtered signals $\mathbf{D}(t) = (D_1(t), D_2(t))$ are used by the agent to estimate the state of the system and to provide feedback accordingly (discussed previously in Chapter 2, see also Eq. (4.11) in Sec. 4.3.1 of this chapter for additional details).

The agent provides feedback by changing the energy levels of the DQD. We describe the feedback protocol by making the energy levels (ϵ_α) dependent on the filtered measurement outcome (\mathbf{D}) which now acts as the control parameter, i.e., $\epsilon_\alpha \rightarrow \epsilon_\alpha(\mathbf{D})$. Thus, we replace the Hamiltonian in Eq.(4.1) and the Lindbladian in Eq. (4.6) with their feedback-controlled analogues: $\hat{H}(\epsilon_L, \epsilon_R) \rightarrow \hat{H}(\mathbf{D}) \equiv \hat{H}(\epsilon_L(\mathbf{D}), \epsilon_R(\mathbf{D}))$ and $\mathcal{L}(\epsilon_L, \epsilon_R) \rightarrow \mathcal{L}(\mathbf{D}) \equiv \mathcal{L}(\epsilon_L(\mathbf{D}), \epsilon_R(\mathbf{D}))$. Now in the feedback protocol discussed Sec. 4.2, the energy level configuration $(\epsilon_L(\mathbf{D}), \epsilon_R(\mathbf{D}))$ of the DQD cycles through three energy landscapes $A : (\epsilon_0, \epsilon_u)$, $B : (\epsilon_l, \epsilon_l)$ and $C : (\epsilon_u, \epsilon_0)$ and we label the corresponding Hamiltonian and Lindbladians as \hat{H}_j and \mathcal{L}_j respectively, where $j \in A, B, C$. We now encode the feedback protocol in the feedback Hamiltonian as:

$$\hat{H}(\mathbf{D}) = \theta(D_2)\hat{H}_A + [1 - \theta(D_1)][1 - \theta(D_2)]\hat{H}_B + \theta(D_1)[1 - \theta(D_2)]\hat{H}_C \quad (4.7)$$

and correspondingly for the feedback Lindbladian as:

$$\mathcal{L}(\mathbf{D}) = \theta(D_2)\mathcal{L}_A + [1 - \theta(D_1)][1 - \theta(D)_2]\mathcal{L}_B + \theta(D_1)[1 - \theta(D_2)]\mathcal{L}_C, \quad (4.8)$$

where $\theta(D)$ is Heaviside step function. The encoding of the feedback protocol can be understood as follows (see Fig. 4.2). The control parameter \mathbf{D} is the filtered version of the measurement outcomes. For $D_2 > 0$ we interpret that the measurement of the observable \hat{A}_2 as 1, which implies that the DQD is unoccupied, for this situation we set the energy level configuration of the DQD to A . For $D_2 < 0$, we interpret that the DQD is occupied by the electron and based on the measurement of the observable \hat{A}_1 we try to determine whether the electron is in the left or right dot and apply the feedback protocol accordingly. Given $D_2 < 0$, for $D_1 < 0$ we interpret the outcome of the observable \hat{A}_1 is $\xi_L^{(1)} = -1$ and the electron is in the left dot and set the energy level configuration of the DQD to B . Similarly, for $D_2 < 0$ and $D_1 > 0$ we interpret the location of the electron to be in the right dot and set the energy level configuration of the DQD to C .

4.3 Theory and methods

4.3.1 Evolution map of the quantum state

Here we discuss the evolution of the quantum state of the DQD for a single run of the experiment. We model the stochastic evolution of the quantum state of the DQD by the conditional density matrix $\hat{\rho}_c(t)$, which describe the state of the DQD system at anytime, conditioned on the entire past measurement record of the observable \hat{A}_1 and \hat{A}_2 and the entire record of exchange of the electron between DQD and the electron reservoirs. Under the measurement and feedback

scheme discussed previously in Sec. 4.2, the time evolution of $\hat{\rho}_c$ from any time t to $t + dt$ is described by the evolution map

$$\hat{\rho}_c(t + dt) = \left(\sum_{j=1}^4 dN_j(t) \mathcal{E}_J^{(j)}(\mathbf{D}) + dN_0(t) \mathcal{E}_{NJ}(\mathbf{D}) \right) \mathcal{M}_2(z_2) \mathcal{M}_1(z_1) \hat{\rho}_c(t). \quad (4.9)$$

The Eq. (4.9) represents a stochastic quantum map, and details of the each of the operations in this map are described below. Here, $\mathcal{M}_1(z_1)$ and $\mathcal{M}_2(z_2)$ represent measurement operations corresponding to detector 1 and detector 2, respectively:

$$\mathcal{M}_l(z)\hat{\rho} = \frac{\hat{K}_l(z)\hat{\rho}\hat{K}_l^\dagger(z)}{\text{tr}\{\hat{K}_l^\dagger(z)\hat{K}_l(z)\hat{\rho}\}}, \quad \hat{K}_l(z) = \left(\frac{2\lambda_l dt}{\pi} \right)^{1/4} e^{-\lambda_l dt(z - \hat{A}_l)^2}, \quad l = 1, 2. \quad (4.10)$$

The distribution of the measurement outcomes $z_l(t)$ is given by $P_l^{(t)}(z) = \text{tr}\{\hat{K}_l^\dagger(z)\hat{K}_l(z)\hat{\rho}_c(t)\}$. $\mathcal{E}_J^{(j)}(\mathbf{D})$ and $\mathcal{E}_{NJ}(\mathbf{D})$ correspond to ‘Jump’ and ‘No Jump’ evolution of the quantum-jump unravelling of the Lindbladian given in Eq. (4.6). In the evolution map given in Eq. (4.9), the random variables $\{z_l\}$ capture the stochasticity due to the measurement process and the random variables $\{dN_j\}$ capture the stochasticity due to the interaction with the electron reservoirs. At any instant, the value of the control parameter $\mathbf{D}(t) = (D_1(t), D_2(t))$ is calculated from the past measurement outcomes $(z_1(t), z_2(t))$ through the filtering relation [1, 61]

$$D_j(t) = \int_{-\infty}^t ds \gamma_j e^{-\gamma_j(t-s)} z_j(s), \quad j = 1, 2. \quad (4.11)$$

The unravelling of the Lindbladian term in Eq. (4.6) leads to four possible quantum jumps which we describe by the jump operators: $\hat{c}_1(\mathbf{D}) = \sqrt{\gamma_L(\epsilon_L(\mathbf{D}))}|L\rangle\langle 0|$, $\hat{c}_2(\mathbf{D}) = \sqrt{\kappa_L(\epsilon_L(\mathbf{D}))}|0\rangle\langle L|$, $\hat{c}_3(\mathbf{D}) = \sqrt{\gamma_R(\epsilon_R(\mathbf{D}))}|R\rangle\langle 0|$ and $\hat{c}_4(\mathbf{D}) = \sqrt{\kappa_R(\epsilon_R(\mathbf{D}))}|0\rangle\langle R|$. The corresponding evolution

of the quantum state is given by

$$\mathcal{E}_j^{(j)}(\mathbf{D})\hat{\rho}_c = \frac{\hat{c}_j(\mathbf{D})\hat{\rho}_c\hat{c}_j^\dagger(\mathbf{D})}{\text{tr}\{\hat{c}_j^\dagger(\mathbf{D})\hat{c}_j(\mathbf{D})\hat{\rho}_c\}}, \quad j = 1, \dots, 4, \quad (4.12)$$

where the state of the DQD is $\hat{\rho}_c(t)$ at time instant t . Here we use $\hat{\rho}_c(t)$ instead of $\hat{\rho}_c$ to imply that the evolution operation are being applied on the conditional density matrix $\hat{\rho}_c(t)$ which is obtained from $\hat{\rho}_c$ by applying the measurement operation. The probability of a particular jump j happening during the time interval t to $t + dt$ is given by $p_j(t) = dt \text{tr}\{\hat{c}_j^\dagger(\mathbf{D})\hat{c}_j(\mathbf{D})\hat{\rho}_c\}$, and the stochastic jump random variables $\{dN_j(t), j = 1, \dots, 4\}$ are distributed as

$$dN_j(t) = \begin{cases} 1, & \text{Pr}[1] = p_j(t), \\ 0, & \text{Pr}[0] = 1 - p_j(t), \end{cases} \quad (4.13)$$

where $\text{Pr}[0(1)]$ denotes the probability of observing $dN_j(t) = 0(1)$. The stochastic jump variables satisfy $E[dN_j(t)] = p_j(t)$, and $dN_i(t)dN_j(t) = \delta_{ij}dN_j(t)$, with $E[\cdot]$ being the ensemble average over all possible trajectories of jumps. We also define a similar stochastic variable

$$dN_0(t) = 1 - \sum_{j=1}^4 dN_j(t) \quad (4.14)$$

for the ‘No Jump’ evolution during the interval $[t, t + dt]$. For $dN_0(t)$, we have the expectation value $E[dN_0(t)] = p_0(t) = 1 - \sum_j p_j(t)$. For the ‘No Jump’ case, the quantum state evolves

under the effective non-unitary Hamiltonian,

$$\hat{H}_{\text{eff}}(\mathbf{D}) = \hat{H}(\epsilon_L(\mathbf{D}), \epsilon_R(\mathbf{D})) - \frac{i}{2} \sum_{j=1}^4 \hat{c}_j^\dagger(\mathbf{D}) \hat{c}_j(\mathbf{D}), \quad (4.15)$$

where, $\hat{H}(\epsilon_L(\mathbf{D}), \epsilon_R(\mathbf{D}))$ is the feedback Hamiltonian as defined in the Eq. (4.1). The No-Jump (NJ) evolution is given by,

$$\mathcal{E}_{\text{NJ}}(\mathbf{D}) \hat{\rho}_c = \frac{e^{-i\hat{H}_{\text{eff}}(\mathbf{D})dt} \hat{\rho}_c e^{i\hat{H}_{\text{eff}}^\dagger(\mathbf{D})dt}}{\text{tr}\{e^{-i\hat{H}_{\text{eff}}(\mathbf{D})dt} \hat{\rho}_c e^{i\hat{H}_{\text{eff}}^\dagger(\mathbf{D})dt}\}}. \quad (4.16)$$

4.3.2 Trajectory and ensemble level equations of motion

It can be shown (see Appendix 4.5) that under the continuous weak measurement framework joint dynamics of the quantum state $\hat{\rho}_c$ from the map Eq. (4.9) can be written as

$$\begin{aligned} d\hat{\rho}_c &= -idt[\hat{H}(\mathbf{D}), \hat{\rho}_c] \\ &+ \sum_{j=1}^4 \left(-\frac{dt}{2} \{ \hat{c}_j^\dagger(\mathbf{D}) \hat{c}_j(\mathbf{D}), \hat{\rho}_c \} + dt \text{tr}\{ \hat{c}_j^\dagger(\mathbf{D}) \hat{c}_j(\mathbf{D}) \hat{\rho}_c \} \hat{\rho}_c + dN_j(t) \frac{\hat{c}_j(\mathbf{D}) \hat{\rho}_c \hat{c}_j^\dagger(\mathbf{D})}{\text{tr}\{ \hat{c}_j^\dagger(\mathbf{D}) \hat{c}_j(\mathbf{D}) \hat{\rho}_c \}} - dN_j(t) \hat{\rho}_c \right) \\ &+ dt \lambda_1 \mathcal{D}[\hat{A}_1] \hat{\rho}_c + dW_1 \sqrt{\lambda_1} \{ \hat{A}_1 - \langle \hat{A}_1 \rangle_c, \hat{\rho}_c \} + dW_2 \sqrt{\lambda_2} \{ \hat{A}_2 - \langle \hat{A}_2 \rangle_c, \hat{\rho}_c \}, \end{aligned} \quad (4.17)$$

where $\{dN_j\}$ are Poisson jump variables for quantum jumps. For detector variable $\mathbf{D} = (D_1, D_2)$ the dynamics be written as

$$dD_j = dt \gamma_j (\langle \hat{A}_j \rangle_c - D_j) + dW_j \frac{\gamma_j}{2\sqrt{\lambda_j}}, \quad j = 1, 2 \quad (4.18)$$

where, dW_1 and dW_2 are Wiener increments that captures the effect of the measurement of the observables \hat{A}_1 and \hat{A}_2 respectively (see Chapter 2). Eq. (4.17) and Eq. (4.18) together form a set of coupled stochastic differential equations that describe the joint dynamics of the quantum state of the DQD and the feedback control parameter. Here the first term in Eq. (4.17) represents unitary evolution due to the feedback Hamiltonian. The term under the summation arises from the quantum jump unravelling [63, 78] of the Lindbladian Eq. (4.6), and represents the effect of coupling with the electron reservoirs. The first terms in the third line captures the backaction due to the measurement of the observable \hat{A}_1 . The last two terms of the equations, containing Wiener increments, capture the effect of the stochastic kicks in the quantum state due to the measurement processes.

Equations (4.17) and (4.18) together describe the equations of motion for the model. We generate the trajectories of the state of our model by using a modification of the Monte Carlo wave function (MCWF) algorithm [68, 98] to incorporate the feedback. For our simulations we directly use the evolution map in the Eq. (4.9) with an assumption that the charge detection by the detector-2 is accurate. See Appendix. 4.6 for the details of ideal-charge detection approximation and Appendix. 4.7 for the details of simulation scheme. In the next section we present the results of the simulation studies.

Alternatively, one can investigate the model in an equivalent ensemble picture using the QFPME [1] with the feedback Lindbladian $\mathcal{L}(\mathbf{D})$ from Eq. (4.6):

$$\partial_t \hat{\rho}_t(\mathbf{D}) = \mathcal{L}(\mathbf{D})\hat{\rho}_t + \sum_{j=1,2} \left[\gamma_j \partial_{D_j} \mathcal{A}_j(D_j) \hat{\rho}_t(\mathbf{D}) + \frac{\gamma_j^2}{8\lambda_j} \partial_{D_j}^2 \hat{\rho}_t(\mathbf{D}) \right], \quad (4.19)$$

where $\mathcal{A}_j(D_j)\hat{\rho} = (1/2)\{\hat{A}_j - D_j, \hat{\rho}\}$. In this chapter we are keeping our discussion limited

to the study of the qualitative behavior of the model using the trajectory approach only, for the discussion on the master equation approach and further discussion on the quantitative energetics of the demon, see Refs. [3, 75].

4.4 Qualitative features from trajectory simulations

By simulating the quantum trajectories of the DQD system we see different interesting behaviors emerge for different parameter regimes. We set the model in the ideal charge detector regime thus the detector-2 is accurate, fast and does not cause any decoherence as discussed in the Appendix 4.6. For our simulations we have taken the parameters: the inverse temperature $\beta = 1.0$, the coupling constant with the electron reservoirs $\Gamma = 0.1$, the chemical potential for the electron reservoirs as $\mu_R = 1.5, \mu_L = -1.5$, and the energy level configurations of the dots $\epsilon_0 = 0.0, \epsilon_u = 5.0, \epsilon_l = -5.0$. We illustrate the interplay between the interdot-coupling constant g , measurement strength λ_1 of the detector-1 and the bandwidth γ_1 of detector-1 by showing three different configurations of these parameters showing three different qualitative features in the model. Figures 4.3, 4.4 and 4.5 shows the evolution of $D_1, \langle \hat{A}_1 \rangle_c = \text{Tr} \left\{ \hat{\rho}_c \hat{A}_1 \right\}$ and $\hat{H}(\mathbf{D})$ obtained from trajectory simulations.

4.4.1 Delayed feedback effect

For Fig. 4.3 we have $g = 25, \gamma_1 = 10, \lambda_1 = 1$, and in this setup we see that the measurement strength is very weak ($\lambda_1/g = 0.04, \lambda_1/\gamma_1 = 0.1$). Thus the evolution of instantaneous expectation value of the detector 1 observable $\langle \hat{A}_1 \rangle_c$ preserves the quantum Rabi oscillation like behavior with some stochasticity from weak measurements. We also see that the detector vari-

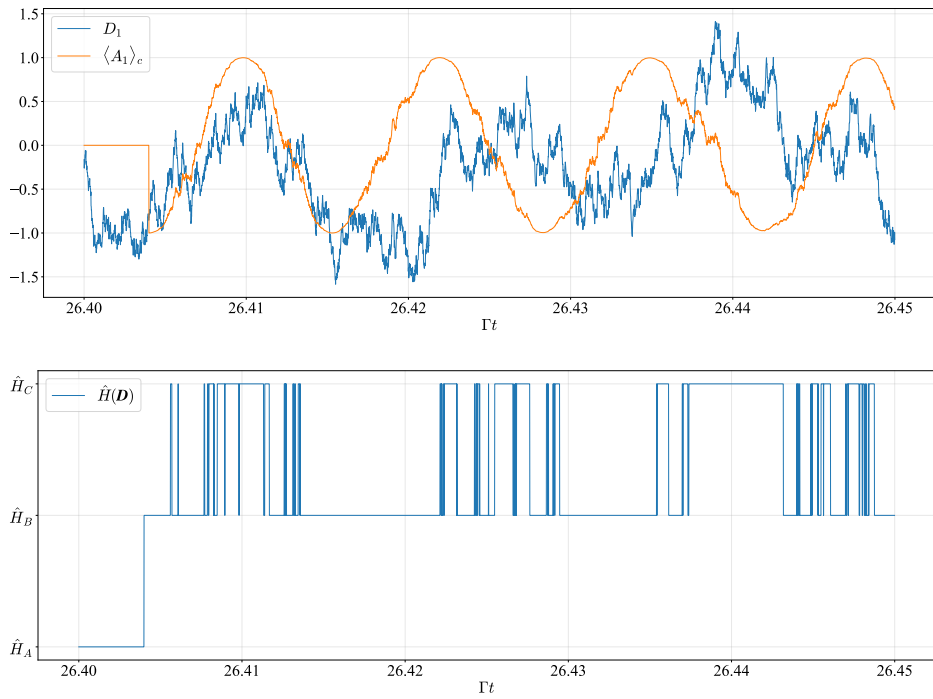


Figure 4.3: Detector is lagging behind the quantum state. The figure above shows the evolution of the feedback variable and instantaneous expectation value of the observable \hat{A}_1 . The figure below plots the evolution of the feedback Hamiltonian. Parameters: $\beta = 1.0, \Gamma = 0.1, \mu_R = 1.5, \mu_L = -1.5, \epsilon_0 = 0.0, \epsilon_u = 5.0, \epsilon_l = -5.0, g = 25, \gamma_1 = 10.0, \lambda_1 = 1.0$ and simulation time step $\delta t = 10^{-4}$

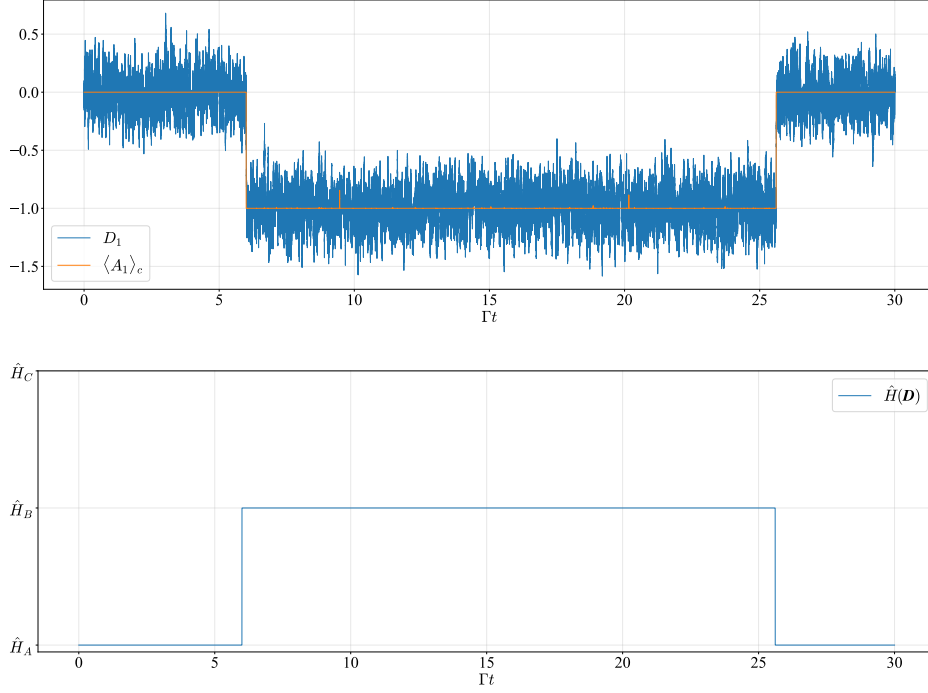


Figure 4.4: Suppression of interdot tunneling due to quantum Zeno effect. Parameters: $\beta = 1.0$, $\Gamma = 0.1$, $\mu_R = 1.5$, $\mu_L = -1.5$, $\epsilon_0 = 0.0$, $\epsilon_u = 5.0$, $\epsilon_l = -5.0$, $g = 0.1$, $\gamma_1 = 10.0$, $\lambda_1 = 80.0$ and simulation time step $\delta t = 10^{-4}$

able D_1 and correspondingly the feedback Hamiltonian $\hat{H}(\mathbf{D})$ are lag behind the evolution of the quantum state ($g/\gamma_1 = 2.5$). This can be particularly seen around $\Gamma t \approx 26.42$ in Fig. 4.3, where we see that $\langle \hat{A}_1 \rangle_c$ has switched to positive value but the feedback variable D_1 is still fluctuating around -1 and the the feedback Hamiltonian is set to \hat{H}_B instead of the ideal feedback configuration \hat{H}_C .

4.4.2 Quantum Zeno effect

For Fig. 4.4 we have $g = 0.1$, $\gamma_1 = 10.0$, $\lambda_1 = 80.0$, and we observe the quantum Zeno effect [99] on the trajectory level. For this setup we see that the measurement is strong ($\lambda_1/\gamma_1 = 8$, $\lambda_1/g = 800$). The feedback is fast compared to the coherence generation ($\gamma_1/g = 100$). Whenever coherence between the the state $|L\rangle$ and $|R\rangle$ is generated, it is destroyed quickly by

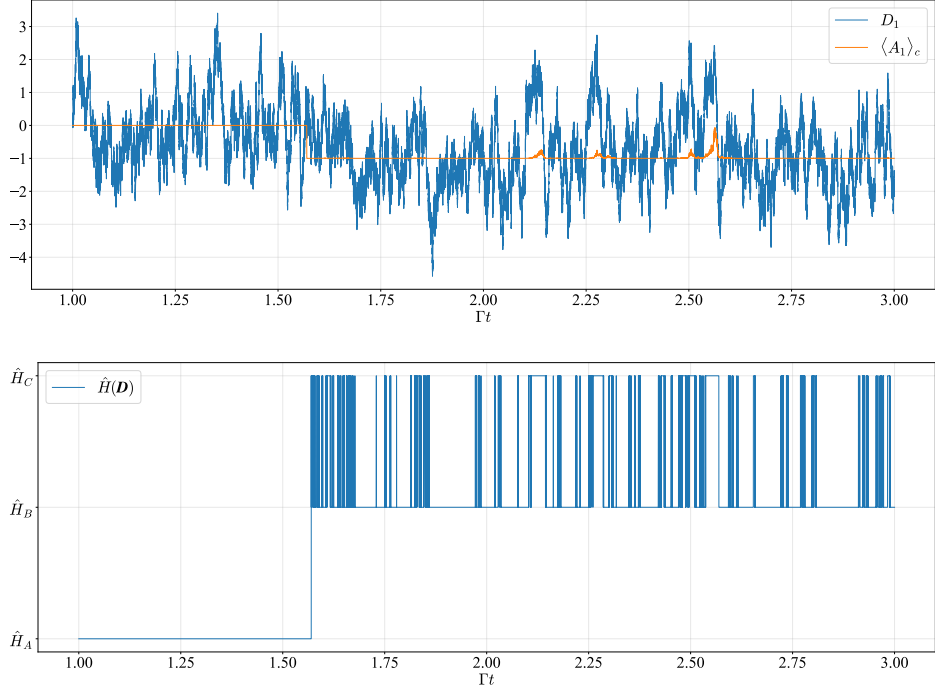


Figure 4.5: Suppression of the interdot tunneling due to random shuffling of the feedback Hamiltonian, Parameters: $\beta = 1.0, \Gamma = 0.1, \mu_R = 1.5, \mu_L = -1.5, \epsilon_0 = 0.0, \epsilon_u = 5.0, \epsilon_l = -5.0, g = 0.1, \gamma_1 = 10.0, \lambda_1 = 1.0$, and simulation time step $\delta t = 10^{-4}$

the continuous measurement, and thus the coherent transport of the electron between left and right quantum dot is suppressed. This can be seen in the Fig. 4.4 by observing that $\langle \hat{A} \rangle_c \approx -1$ as long as the electron is inside the DQD, thus the electron fails to tunnel to the right dot from the left dot in \hat{H}_B configuration due to strong continuous measurement and eventually jumps back to the left electron reservoir directly from the energy level ϵ_l and the feedback then instantly switches $\hat{H}_B \rightarrow \hat{H}_A$ due to fast feedback.

4.4.3 Phase damping effect due to random feedback

For Fig. 4.5, we have $g = 0.1, \gamma_1 = 10.0, \lambda_1 = 1.0$ we see a *Zeno-like phase damping* effect due to random shuffling the feedback Hamiltonian $\hat{H}(\mathbf{D})$ due to a noisy feedback ($\lambda_1/\gamma_1 = 0.1, g/\gamma_1 = 0.01$). The ratio of measurement strength and interdot coupling is $\lambda_1/g = 10$, which

is higher than the very weak measurement scenario of Fig. 4.3 but lower than the case of the strong-measurement Zeno-effect scenario of Fig. 4.4. The ratio of the measurement strength and feedback bandwidth ($\lambda_1/\gamma_1 = 0.1$) here is kept the same as in the case of Fig. 4.3. However, in this situation (Fig. 4.5) we also get a Zeno-like suppression of quantum tunneling between the dots due to fast switching of the feedback Hamiltonian compared to generation of the coherence (Note, that for Fig. 4.3 we had $g/\gamma_1 = 2.5$, whereas here in Fig. 4.5 we have $g/\gamma_1 = 0.01$). Due to this fast nature of feedback we get a random change in the detuning ($|\epsilon_L - \epsilon_R|$) of the Hamiltonian $\hat{H}(\mathbf{D}) = \hat{H}_B \leftrightarrow \hat{H}_C$, which leads to a decay in the coherence of the the quantum state ρ_c without affecting the population, eventually leading to a *phase-damping* effect [88]. Due to this phase-damping, the electron the coherent transport of the electron is suppressed similar to the case of the quantum Zeno effect. Note that here (Fig. 4.5) this suppression of coherent quantum transport happens due to quick random shuffling of the feedback Hamiltonian in contrast to the suppression of quantum transport in Fig. 4.4, which was primarily due to strong measurement.

4.4.4 Quantum to classical transition

Figures 4.6 and 4.7 show the evolution of the quantum state $\hat{\rho}_c$ by plotting the population and coherence parts of the density matrices during and interdot tunneling. For both figures we have $g = 0.1, \gamma_1 = 1.0$ but for the quantum case (Fig. 4.6) we have taken $\lambda_1 = 0.6$ and for the classical case (Fig. 4.7) we have, $\lambda_1 = 6.0$. For both plots we see that the population is transferred from the state $|L\rangle$ to $|R\rangle$. However, for the quantum case this interdot transition is relatively slow and associated with an oscillation in the coherence (Fig. 4.6). Whereas for the classical case, we see the change in population is relatively sharp and the interdot transition

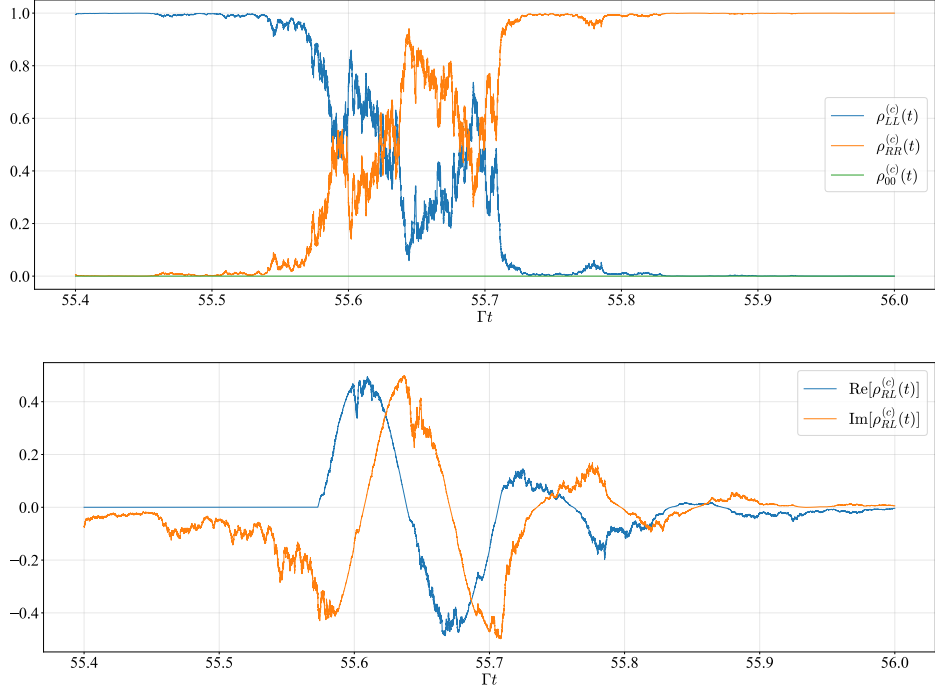


Figure 4.6: Evolution of population (above) and the coherence (below) during interdot electron transfer. This figure illustrates the quantum nature of the interdot transport of the electron. Parameters: $\beta = 1.0$, $\Gamma = 0.1$, $\mu_R = 1.5$, $\mu_L = -1.5$, $\epsilon_0 = 0.0$, $\epsilon_u = 5.0$, $\epsilon_l = -5.0$, $g = 0.1$, $\gamma_1 = 1.0\lambda_1 = 0.6$ and simulation time step $\delta t = 10^{-4}$

happens with a short spike in the coherence (Fig. 4.7). Thus we see that for stronger measurement ($\lambda_1/\gamma_1 = 6$, $\lambda_1/g = 60$) here, the transport of electron from left to the right dot behaves like a discrete stochastic jump event even though the microscopically the transport is coherent in nature. It is possible to assign an effective classical jump rate to this transition using the master equation approach [3, 75] and obtain a classical discrete state model for the DQD demon described in [4] from this underlying microscopic picture.

4.5 Appendix: Quantum evolution map to the stochastic master equation

Under the weak measurement scheme [78], we model the measurement process by generating a Gaussian white noise around the instantaneous conditional expectation value ($\langle A_j \rangle_c =$

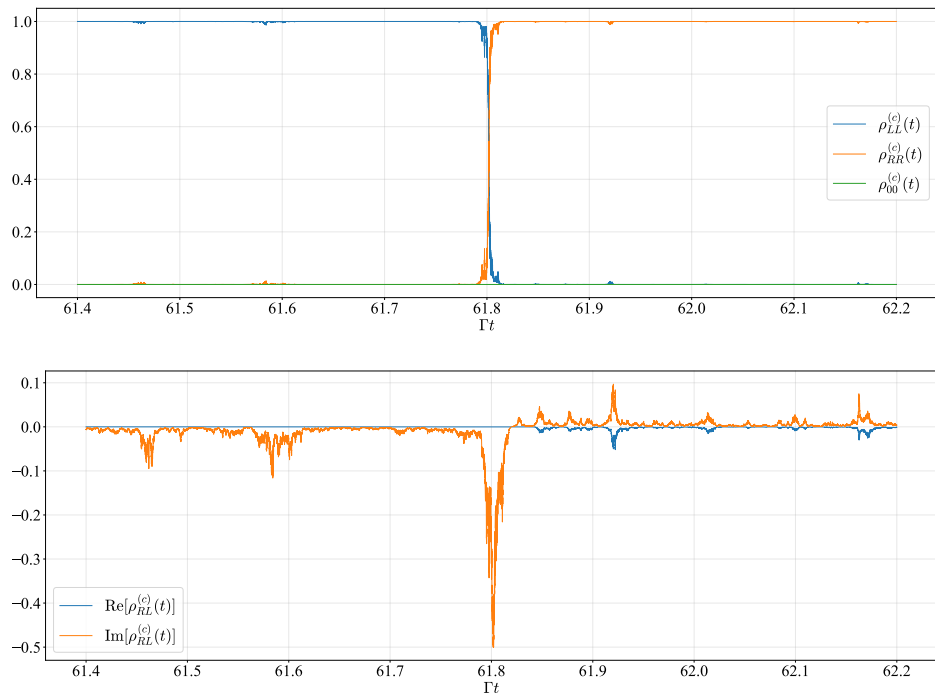


Figure 4.7: Evolution of population (above) and the coherence (below) during interdot electron transfer. This figure illustrates the classical jump like behavior of the interdot transport of the electron. Parameters: $\beta = 1.0, \Gamma = 0.1, \mu_R = 1.5, \mu_L = -1.5, \epsilon_0 = 0.0, \epsilon_u = 5.0, \epsilon_l = -5.0, g = 0.1, \gamma_1 = 1.0\lambda_1 = 6.0$ and simulation time step $\delta t = 10^{-4}$

$\text{tr}\{\hat{A}_j\hat{\rho}_c(t)\})$ of the observable as,

$$z_j(t) = \langle \hat{A}_j \rangle_c + \frac{1}{2\sqrt{\lambda_j}dt} dW_j, \quad j = 1, 2 \quad (4.20)$$

where dW_1 and dW_2 are Wiener increments with the properties: $\mathbf{E}[dW_{1,2}] = 0$ and in $dW_i dW_j = \delta_{ij} dt$, under Ito calculus. After the measurement operations the quantum state $\hat{\rho}_c(t)$ evolves to

$$\begin{aligned} \hat{\rho}_c^*(t) &= \hat{\rho}_c(t) + dt\lambda_1\mathcal{D}[\hat{A}_1]\hat{\rho}_c(t) + dt\lambda_2\mathcal{D}[\hat{A}_2]\hat{\rho}_c(t) \\ &\quad + \sqrt{\lambda_1}dW_1\{\hat{A}_1 - \langle \hat{A}_1 \rangle_c, \hat{\rho}_c\} + \sqrt{\lambda_2}dW_2\{\hat{A}_2 - \langle \hat{A}_2 \rangle_c, \hat{\rho}_c\} \end{aligned} \quad (4.21)$$

where, $\hat{\rho}_c^*(t) = \mathcal{M}_1(z_1(t))\mathcal{M}_2(z_2(t))\hat{\rho}_c(t)$. The measurement operator $\hat{A}_2 = |0\rangle\langle 0| - (|L\rangle\langle L| + |R\rangle\langle R|)$ does not cause any decoherence in the $|L\rangle\langle L| \oplus |R\rangle\langle R|$ subspace. Thus we can drop the back-action term containing $\mathcal{D}[\hat{A}_2]$ from our consideration; and thus we get,

$$\hat{\rho}_c^*(t) = \hat{\rho}_c(t) + dt\lambda_1\mathcal{D}[\hat{A}_1]\hat{\rho}_c(t) + \sqrt{\lambda_1}dW_1\{\hat{A}_1 - \langle \hat{A}_1 \rangle_c, \hat{\rho}_c\} + \sqrt{\lambda_2}dW_2\{\hat{A}_2 - \langle \hat{A}_2 \rangle_c, \hat{\rho}_c\} \quad (4.22)$$

After the measurement, we apply the evolution of the DQD under the effect of the electron to obtain the final time evolved state $\hat{\rho}_c(t + dt)$ as

$$\hat{\rho}_c(t + dt) = \sum_{j=1}^4 dN_j(t)\mathcal{E}_{\text{J}}^{(j)}(\mathbf{D}(t))\hat{\rho}_c^*(t) + \left(1 - \sum_{j=1}^4 dN_j(t)\right)\mathcal{E}_{\text{NJ}}(\mathbf{D}(t))\hat{\rho}_c^*(t) \quad (4.23)$$

We expand the exponential in the no-jump evolution up to $\mathcal{O}(dt)$ and get the following expression,

$$\mathcal{E}_{\text{NJ}}(\mathbf{D})\hat{\rho}_c^*(t) = \frac{\hat{\rho}_c^*(t) + dt(-i\hat{H}_{\text{eff}}(\mathbf{D})\hat{\rho}_c^*(t) + i\hat{\rho}_c^*(t)\hat{H}_{\text{eff}}^\dagger(\mathbf{D}))}{1 + dt \text{tr}\{-i\hat{H}_{\text{eff}}(\mathbf{D})\hat{\rho}_c^*(t) + i\hat{\rho}_c^*(t)\hat{H}_{\text{eff}}^\dagger(\mathbf{D})\}} \quad (4.24)$$

Now using the definition of $H_{\text{eff}}(\mathbf{D})$ from Eq. (4.15) in the expression above we get,

$$\mathcal{E}_{\text{NJ}}(\mathbf{D})\hat{\rho}_c^*(t) = \frac{\left[\hat{\rho}_c^*(t) - idt[\hat{H}(\mathbf{D}), \hat{\rho}_c^*(t)] - \frac{dt}{2} \sum_{j=1}^4 \{\hat{c}_j^\dagger(\mathbf{D})\hat{c}_j(\mathbf{D}), \hat{\rho}_c^*(t)\}\right]}{\left[1 - dt \sum_{j=1}^4 \text{tr}\{\hat{c}_j^\dagger(\mathbf{D})\hat{c}_j(\mathbf{D})\hat{\rho}_c^*(t)\}\right]} \quad (4.25)$$

Expanding the denominator and keeping terms upto $\mathcal{O}(dt)$ we get,

$$\mathcal{E}_{\text{NJ}}(\mathbf{D})\hat{\rho}_c^*(t) = \hat{\rho}_c^*(t) - idt[\hat{H}(\mathbf{D}), \hat{\rho}_c^*(t)] - \frac{dt}{2} \sum_{j=1}^4 \{\hat{c}_j^\dagger(\mathbf{D})\hat{c}_j(\mathbf{D}), \hat{\rho}_c^*(t)\} + dt \sum_{j=1}^4 \text{tr}\{\hat{c}_j^\dagger(\mathbf{D})\hat{c}_j(\mathbf{D})\hat{\rho}_c^*(t)\}\hat{\rho}_c^*(t) \quad (4.26)$$

Note that $dN_k dW_j$, and $dN_k dt$ contribute to evolution terms that are of order $(dt)^{\frac{3}{2}}$ and $(dt)^2$. Since we are interested in the evolution equation up to $\mathcal{O}(dt)$, we use Eqs.(4.22) and (4.26) in Eq. (4.23), and by dropping the terms with $dN_k dW_j$, $dW_j dt$ and $dN_k dt$, we get

$$\begin{aligned} \hat{\rho}_c(t+dt) - \hat{\rho}_c(t) &= -idt[\hat{H}(\mathbf{D}), \hat{\rho}(t)] + dt\lambda_1\mathcal{D}[\hat{A}_1]\hat{\rho}_c(t) \\ &\quad - \frac{dt}{2} \sum_{j=1}^4 \{\hat{c}_j^\dagger(\mathbf{D})\hat{c}_j(\mathbf{D}), \hat{\rho}(t)\} + dt \sum_{j=1}^4 \text{tr}\{\hat{c}_j^\dagger(\mathbf{D})\hat{c}_j(\mathbf{D})\hat{\rho}(t)\}\hat{\rho}(t) \\ &\quad + \sum_{j=1}^4 dN_j(t)(\mathcal{E}_j^{(j)}(\mathbf{D}(t) - 1)\hat{\rho}_c(t) \\ &\quad + \sqrt{\lambda_1}dW_1\{\hat{A}_1 - \langle \hat{A}_1 \rangle_c, \hat{\rho}_c(t)\} + \sqrt{\lambda_2}dW_2\{\hat{A}_2 - \langle \hat{A}_2 \rangle_c, \hat{\rho}_c(t)\} \end{aligned} \quad (4.27)$$

Finally by replacing $d\hat{\rho}_c = \hat{\rho}_c(t+dt) - \hat{\rho}_c(t)$ in the equation above we get the stochastic master equation shown in Eq. (4.17).

4.6 Appendix: Ideal charge detection assumption

Since the detector 2 performs classical back action-free measurement on the system, we can consider the limit of accurate detector by taking $\lambda_2/\gamma_2 \rightarrow \infty$ without affecting the sys-

tem. We assume here that the feedback due to the detector 2 is fast (responsive) enough in comparison to the other timescales of the system and the bandwidth of the detector 2 satisfies $\gamma_2 \gg \max\{\Gamma, g, |\epsilon_{u/l} - \epsilon_0|, \gamma_1\}$. For the fast and accurate measurement of the detector-2 we get an ideal-charge detection of the DQD. Thus, under these assumptions, whenever an electron enters or leaves the DQD, the corresponding changes of the feedback Hamiltonian $\hat{H}_A \leftrightarrow \hat{H}_B$ or $\hat{H}_A \leftrightarrow \hat{H}_C$ are instantaneous.

To implement this approximation, discretize the Eq. (4.11) in time as a deference equation:

$$D_j(k\delta t) = \delta t \gamma_j z_j(k\delta t) + (1 - \delta t \gamma_j) D_j((k-1)\delta t), \quad (4.28)$$

where δt is the time-step and $t = k\delta t$. Here $(\gamma_j \delta t)$ is the smoothing factor of the filter and for simulating quantum trajectories δt needs to be chosen such that we have $0 \leq (\gamma_j \delta t) \leq 1$. To achieve the fast limit of the detector we take the maximum possible value of γ_2 in the simulation by setting $\gamma_2 \delta t = 1$. Thus, for the fast detector 2 we have,

$$D_2(k\delta t) = z_2(k\delta t). \quad (4.29)$$

This implies that the measurement signal $z_2(t)$ from the detector 2 is directly converted to feed-back variable $D_2(t)$ without any filtering.

For detector 2, (observable: $\hat{A}_2 = +|0\rangle\langle 0| - (\hat{\mathbf{1}} - |0\rangle\langle 0|)$) we have the POVM $\hat{K}_2(z)$ in the measurement basis as

$$\hat{K}_2(z_2) = \left(\frac{2\lambda_2 \delta t}{\pi}\right)^{1/4} \left[e^{-\lambda_2 \delta t (z_2 - (+1))^2} |0\rangle\langle 0| + e^{-\lambda_2 \delta t (z_2 - (-1))^2} (\hat{\mathbf{1}} - |0\rangle\langle 0|) \right]. \quad (4.30)$$

Next we want to increase the measurement strength of the detector 2 to the infinite limit ($\lambda_2 \rightarrow \infty$) while keeping δt fixed to achieve the strong measurement limit in the POVM $\hat{K}_2(z_2)$, which we can approximate as projective measurement POVM:

$$\hat{K}_2(z_2) = \begin{cases} |0\rangle\langle 0|, z_2 = +1, \\ (\hat{\mathbf{1}} - |0\rangle\langle 0|), z_2 = -1 \\ 0, \text{ otherwise} \end{cases} \quad (4.31)$$

and for a quantum state $\hat{\rho}_c(t)$, the corresponding distribution of z_2 is given as $P_2^{(t)}(z_2 = +1) = \text{tr}\{|0\rangle\langle 0|\hat{\rho}_c(t)\}$ and $P_2^{(t)}(z_2 = -1) = 1 - \text{tr}\{|0\rangle\langle 0|\hat{\rho}_c(t)\}$. For the implementation of the effect of detector-2 measurements in the simulations, we use this ideal-charge detection approximation (See Appendix. 4.7).

4.7 Appendix: Monte Carlo wave function simulation scheme with feedback control

Here we implement the quantum jump trajectory [100, 101] simulation under feedback control by modifying the standard Monte Carlo wave function (MCWF) [68, 98] algorithm to incorporate measurement and feedback. To study the model under consideration, we implement a simulation scheme that captures the dynamics of the detector and the quantum state together. At any time instant t , we describe the quantum state of the DQD system by the wave function:

$$|\psi(t)\rangle = c_0(t)|0\rangle + c_L(t)|L\rangle + c_R(t)|R\rangle \quad (4.32)$$

Here the coefficients $\{c_j(t)\}_{j=L,R,E}$ depend on the complete history of the measurement outcomes. The conditional density matrix corresponding to this quantum state is by $\hat{\rho}_c(t) = |\psi(t)\rangle \langle \psi(t)|$. We have either $c_0(t) = 1, c_L(t) = c_R(t) = 0$ or, $c_0(t) = 0, |c_L(t)|^2 + |c_R(t)|^2 = 1$. The quantum state vector $|\psi(t)\rangle$ is represented as a 3×1 normalized column vector. The control parameter starts with unupdated state at $\mathbf{D}(t - \delta t) = (D_1(t - \delta t), D_2(t - \delta t))$.

Detector 1 measurement: To simulate the effect of the measurement, first a random variable $\xi \in \{-1, 0, +1\}$ is sampled based on the distribution

$$\Pr(\xi) = \begin{cases} |c_L(t)|^2, \xi = -1 \\ |c_0(t)|^2, \xi = 0 \\ |c_R(t)|^2, \xi = +1. \end{cases} \quad (4.33)$$

Then the measurement outcome is sampled from the normal distribution with ξ mean (μ) and $1/(2\sqrt{\lambda_1 \delta t})$ standard deviation (σ):

$$z_1(t) \sim \mathcal{N}\left(\mu = \xi, \sigma^2 = \frac{1}{4\lambda_1 \delta t}\right). \quad (4.34)$$

Then using the sampled value of $z_1(t)$, the matrix representation of $\hat{K}_1(z_1(t))$ is calculated. We then modify the quantum state $|\psi(t)\rangle$ to a intermediate new state as

$$|\tilde{\psi}(t)\rangle = \frac{\hat{K}_1(z_1(t)) |\psi(t)\rangle}{|\hat{K}_1(z_1(t)) |\psi(t)\rangle|.} \quad (4.35)$$

Next the updated control parameter $D_1(t)$ is calculated using the measurement outcome $z_1(t)$ as:

$$D_1(t) = \delta t \gamma_1 z_1(t) + (1 - \delta t \gamma_1) D_1(t - \delta t). \quad (4.36)$$

Detector 2 measurement: The second detector performs projective measurements in the system.

Thus, we have $z_2(t) \in \{-1, 1\}$ and the distribution of $z_2(t)$ is given as

$$\Pr(z_2(t)) = \begin{cases} |\langle 0 | \tilde{\psi}(t) \rangle|^2, & z_2(t) = 1, \\ 1 - |\langle 0 | \tilde{\psi}(t) \rangle|^2, & z_2(t) = -1. \end{cases} \quad (4.37)$$

Now the updated control parameter is given as

$$D_2(t) = z_2(t), \quad (4.38)$$

since we are working at the ideal detector limit where $\gamma_2 \rightarrow \infty$. The post measurement state after detector 2 measurement $|\psi'(t)\rangle$ is given as

$$|\psi'(t)\rangle = \begin{cases} |0\rangle, & z_2(t) = 1, \\ (\hat{\mathbf{1}} - |0\rangle\langle 0|)|\tilde{\psi}(t)\rangle, & z_2(t) = -1. \end{cases} \quad (4.39)$$

Since we are working in the ideal charge detection approximation, the quantum state $|\tilde{\psi}(t)\rangle$ is either $|0\rangle$ or of the form $c_L(t)|L\rangle + c_R(t)|R\rangle$, and thus the post-measurement state $|\psi'(t)\rangle$ remains unchanged from the state $|\tilde{\psi}(t)\rangle$ under the measurement by detector 2.

State Update:

The final time-evolved state $|\psi(t + dt)\rangle$ can be obtained by the stochastic evolution equation

$$|\psi(t + \delta t)\rangle = \sum_{k=0}^4 dN_k(t) \frac{\hat{c}_k(D_1(t), D_2(t)) |\psi'(t)\rangle}{|\hat{c}_k(D_1(t), D_2(t)) |\psi'(t)\rangle|}, \quad (4.40)$$

where $\hat{c}_1 = \sqrt{\gamma_L(\epsilon_L)} |L\rangle\langle 0|$, $\hat{c}_2 = \sqrt{\kappa_L(\epsilon_L)} |0\rangle\langle L|$, $\hat{c}_3 = \sqrt{\gamma_R(\epsilon_R)} |R\rangle\langle 0|$, $\hat{c}_4 = \sqrt{\kappa_R(\epsilon_R)} |0\rangle\langle R|$ and $\hat{c}_0 = e^{-i\delta t \hat{H}_{\text{eff}}}$, where, $\epsilon_{L/R} \equiv \epsilon_{L/R}(D_1(t), D_2(t))$ and the effective non-unitary Hamiltonian $H_{\text{eff}}(D_1(t), D_2(t))$ is given by Eq. (4.15). The matrix representation of the operator \hat{c}_0 is calculated numerically by direct exponentiation of the matrix $-i\delta t H_{\text{eff}}(D_1(t), D_2(t))$. Each of the stochastic variables are defined by the Eqs. (4.13) and (4.14). To simulate this step, first the stochastic variable corresponding to No-Jump evolution $dN_0(t)$, is sampled as

$$\Pr(dN_0(t)) = \begin{cases} \delta t \sum_{k=1}^4 \langle \psi'(t) | \hat{c}_k^\dagger \hat{c}_k | \psi'(t) \rangle, & dN_0 = 0 \\ 1 - \delta t \sum_{k=1}^4 \langle \psi'(t) | \hat{c}_k^\dagger \hat{c}_k | \psi'(t) \rangle, & dN_0 = 1. \end{cases} \quad (4.41)$$

If the sampling results in $dN_0(t) = 1$, then the updated state is calculated directly as

$$|\psi(t + \delta t)\rangle = \frac{\hat{c}_0 |\psi'(t)\rangle}{|\hat{c}_0 |\psi'(t)\rangle|}. \quad (4.42)$$

If the sampling results in $dN_0(t) = 0$ then another Monte Carlo step is made to determine which jump is happening by sampling the variable k^* where $k^* \in \{1, 2, 3, 4\}$. The distribution of k^* is given as,

$$\Pr(k^*) = \frac{\langle \psi'(t) | \hat{c}_{k^*}^\dagger \hat{c}_{k^*} | \psi'(t) \rangle}{\sum_{k'=1}^4 \langle \psi'(t) | \hat{c}_{k'}^\dagger \hat{c}_{k'} | \psi'(t) \rangle}, \quad k^* \in \{1, 2, 3, 4\}. \quad (4.43)$$

Then the quantum state is updated by applying the corresponding jump operator to k^* as,

$$\psi(t + \delta t) = \frac{\hat{c}_{k^*} |\psi'(t)\rangle}{|\hat{c}_{k^*} |\psi'(t)\rangle|}. \quad (4.44)$$

Chapter 5: From the feedback-controlled DQD demon to autonomous information ratchet

This chapter is adapted from an independent research project that has been published as the paper “From a feedback-controlled demon to an information ratchet in a double quantum dot” [2]. This project started as a spin-off of the IaF project related to the DQD Maxwell’s demon. Here we convert the classical version of the model discussed in Chapter 4 to an autonomous Maxwell’s demon and identify and analyze its modes of operation..

5.1 Chapter overview

In this chapter we use the double quantum dot (DQD) electronic Maxwell’s demon model from Ref. [4], which we refer to in this chapter as the Annby-Andersson (AA) model, to develop and illustrate a general strategy for converting a non-autonomous, feedback-controlled model of Maxwell’s demon into an autonomous, memory-tape model, or information ratchet, as illustrated schematically in Fig. 5.1. A number of authors have previously explored the connections between feedback-controlled and memory-tape models [27, 33, 89, 102, 103]. Horowitz *et al* [89] designed a feedback-controlled information motor based on the system-bit interactions of Ref. [15]. Barato and Seifert [27, 28] discussed a stochastic-thermodynamics [49] framework that encompasses both feedback-controlled and memory-tape models. Shiraishi *et al* [103] showed

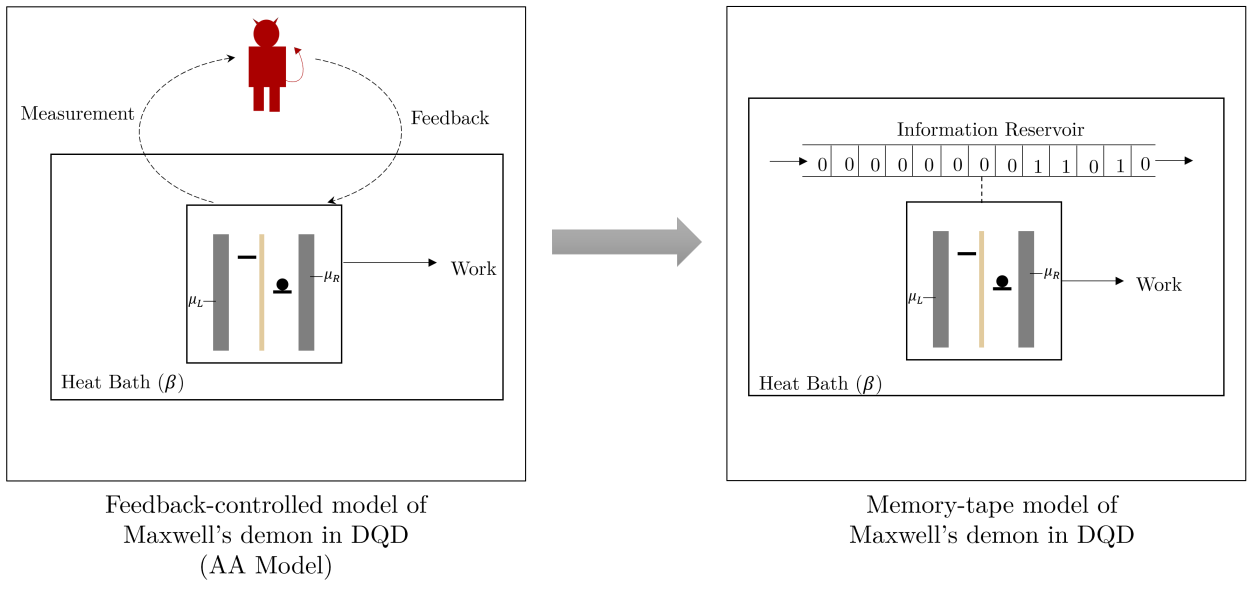


Figure 5.1: Two paradigms of Maxwell's demon. The left figure depicts the AA model, a feedback-controlled model. On the right we show the corresponding memory-tape model or information ratchet. In both cases, heat from a thermal reservoir is converted to work, either through measurement and feedback, or through interaction with an information reservoir. We explore a strategy to convert a feedback-controlled model to a memory-tape model. The figure is taken from Ref. [2].

that the measurement-feedback model introduced in Ref. [89] can be reduced to the simplified MJ model of Ref. [26, 27, 28]. Strasberg *et al* [33] described a system with a spin-valve and a quantum dot that can mimic the thermodynamic behaviour of the MJ model and can be mapped to a Brownian ratchet. They also presented a feedback-controlled model that captures the effective dynamics of the corresponding memory-tape model, and they compared how the second law of thermodynamics applies to these two paradigms.

Our approach uses network-based modelling [49, 104] of a system of master equations, originally introduced by Schnakenberg[69], to show how a non-autonomous demon with a seemingly complicated feedback protocol can systematically be modified to construct a memory-tape model that mimics its behavior. We then present a theoretical analysis of the resulting memory-tape model. Our model has distinct regions in parameter space where it operates either as an *information engine* or as a *Landauer eraser*. We solve the model exactly in the limit when each bit interacts with the DQD for an infinite amount of time, obtaining analytic expressions for thermodynamic quantities and critical parameter values. We also semi-analytically explore the finite time bit-interaction situation and construct the corresponding phase diagrams. Lastly, we discuss a scheme for the stochastic simulation of memory-tape models and use it to simulate our model and to verify our semi-analytical results. We limit our discussion to a completely classical stochastic model and leave quantum models as a future avenue for research.

This chapter is organized as follows. Details of network-based stochastic modelling [49, 69, 104] are presented in Sec. 5.2. In Sec 5.2.1 we map the AA model to a nine-state network by converting its control parameter to a stochastic variable. In Sec. 5.2.2 and Sec. 5.2.3, we discuss how to couple the DQD with incoming bits to mimic the behavior of the feedback-controlled demon. A summary of the general modelling scheme is presented in Sec. 5.2.4. The analysis of

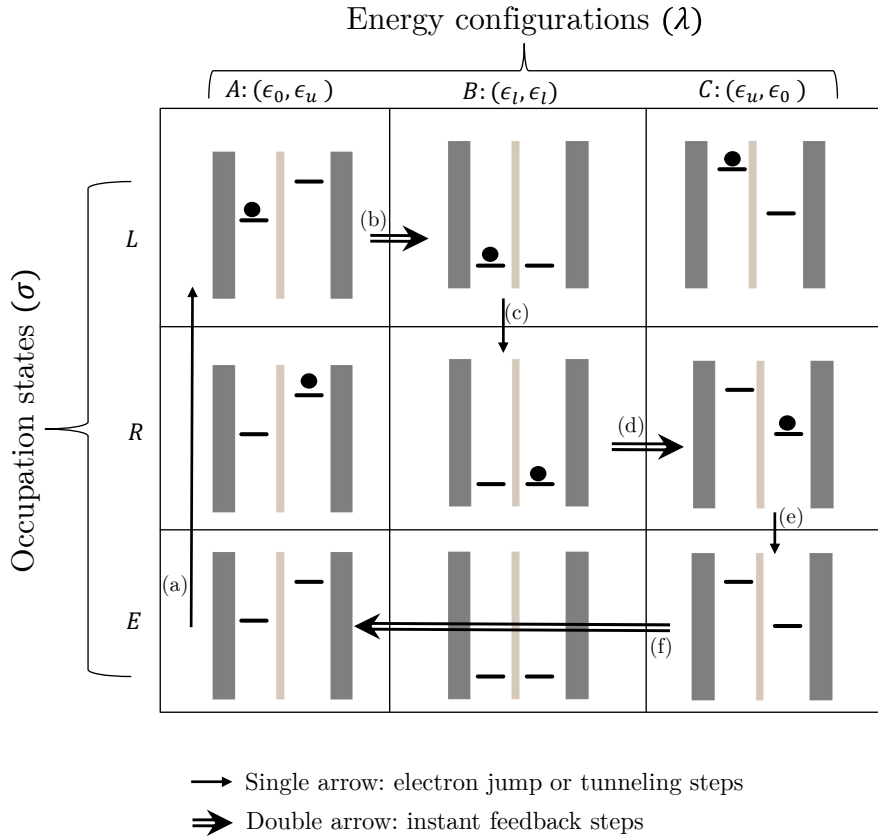


Figure 5.2: States of the double quantum dot system $x \equiv (\lambda, \sigma)$ and the protocol (\mathcal{C}_{AA}) for the AA model. Feedback steps (changes in λ , i.e., steps (b), (d) and (f)) are shown using double arrows, and electron jumps (changes in σ , i.e., steps (a), (c) and (e)) are shown using single arrow. The figure is taken from Ref. [2]

memory-tape models is discussed in Sec. 5.3.1. In Sec. 5.3.2 we discuss the thermodynamics of our model and solve for analytical expressions of thermodynamic quantities in Sec. 5.3.3. Phase diagrams of operational modes are discussed in Sec. 5.3.4 and the stochastic simulation scheme for the model is presented in Sec. 5.3.5. Finally a discussion of the content of this chapter and some related future research directions are discussed in Sec. 5.4

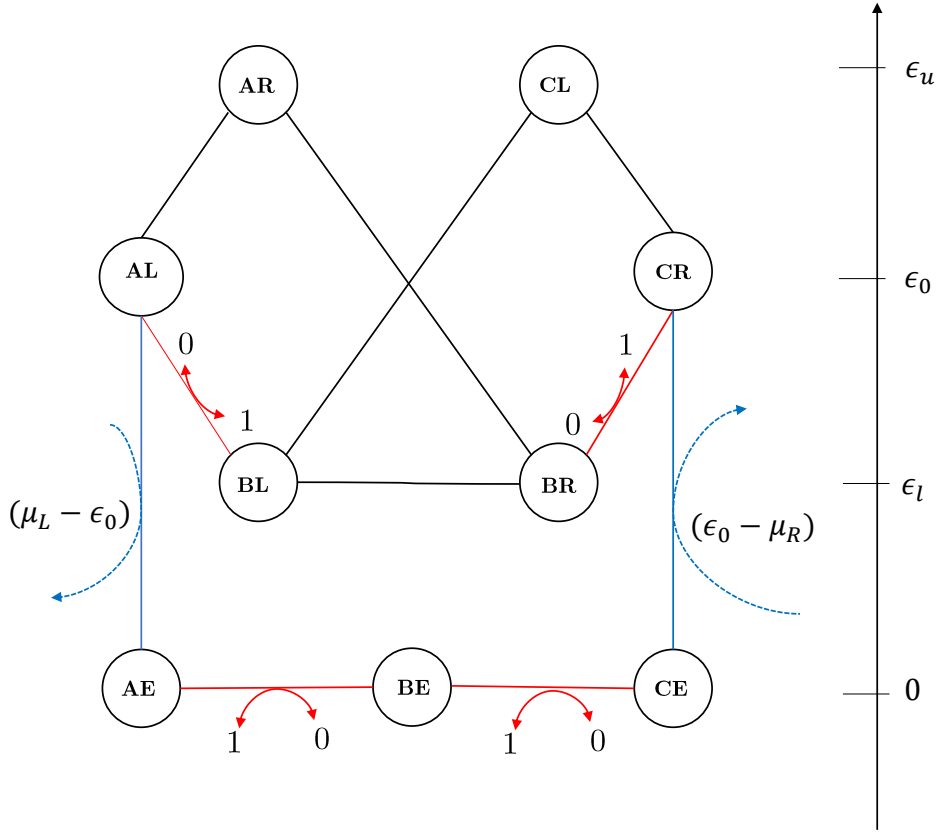


Figure 5.3: Reduced network $\mathcal{G}_r = (V_x, E_x)$. Energies of the states in V_x are shown to the right of the network. Edges shown in red correspond to the feedback steps of the original AA model, and involve the flipping of the bit in the memory-tape model. The edges shown in blue correspond to the transitions where the electron hops into (out of) the DQD from (to) an electron reservoir and the dotted arrows show the corresponding energy exchange. The figure is taken from Ref. [2]

5.2 Memory-tape model of Maxwell's demon in DQD system

The (ideal classical) protocol of the AA model has been reviewed previously in Sec. 4.2.1 and here we show it again in Fig. 5.2, where electron transition events are indicated by single arrows, and feedback steps by double arrows. The labels of the arrows in Fig. 5.2 refer to the steps of the protocol discussed in Sec. 4.2.1. The states in Fig. 5.2 that are not included in the ideal protocol for the AA model are relevant for the memory tape model, as discussed later in this chapter.

5.2.1 DQD demon with thermal feedback control

5.2.1.1 DQD+controller joint state space: the reduced network

We now construct a network representation of the states of the AA model, as a first step toward designing a corresponding memory-tape model. In the AA model, the DQD occupation state σ is a dynamic variable with three possible states, $\sigma \in \Sigma = \{L, E, R\}$, as described in Sec. 4.2.1. (Here the state E correspond to *ket0* of Chapter. 4). The DQD *energy configuration* λ acts as a control parameter, also with three possible states: $\lambda \in \Lambda = \{A, B, C\}$ where $A \equiv (\epsilon_0, \epsilon_u)$, $B \equiv (\epsilon_l, \epsilon_l)$ and $C \equiv (\epsilon_u, \epsilon_0)$. Combining the energy configurations and the occupation states leads to nine possible states for the *DQD state variable*: $x \in \mathbf{V}_x = \Lambda \times \Sigma = \{AL, AE, \dots, CR\}$. The ideal cyclic protocol \mathcal{C}_{AA} , described above, follows the path $AE \rightarrow AL \Rightarrow BL \rightarrow BR \Rightarrow CR \rightarrow CE \Rightarrow AE$, where double arrows signify feedback steps; see Fig. 5.2.

We now consider a situation in which the energy configuration λ is no longer a control

parameter, but instead is a dynamical variable on the same footing as the occupation state σ . In our model, the entire system is maintained at a temperature T using a thermal bath, and λ is now a stochastic variable that evolves under the effect of the thermal noise from the bath. The system-variable $x \equiv (\lambda, \sigma)$ evolves among the nine states in \mathbf{V}_x as a continuous time Markov jump process. We justify the Markov assumption by assuming that the system-bath coupling is weak and the correlations between the system and the bath decay on a timescale faster than that of the jumps. We make the following assumptions about our model: (i) The elementary transitions in our process involve a change in either λ , or σ , but not both simultaneously, i.e., the system is *bipartite* [104]. (ii) If $\lambda = B$, then the excess electron cannot hop into or out of the electron reservoirs; thus, the transitions $BE \leftrightarrow BL$ and $BE \leftrightarrow BR$ are not allowed. (iii) Direct transitions between A and C states are forbidden. These assumptions are modelling choices, but all of the forbidden transitions can be justified physically by assuming sufficiently high energy barriers between corresponding states.

Under these assumptions, we obtain a network $\mathcal{G}_r = (\mathbf{V}_x, \mathbf{E}_x)$ where $\mathbf{V}_x \equiv V(\mathcal{G}_r)$ is the set of 9 vertices and $\mathbf{E}_x \equiv E(\mathcal{G}_r)$ is the set of 11 bidirectional edges (see Fig. 5.3), describing the stochastic dynamics [49, 69, 104] of the variable $x \equiv (\lambda, \sigma)$. The subscript r in \mathcal{G}_r indicates a *reduced* 9-state network, in contrast with a *full* 18-state network \mathcal{G}_f to be defined later. As the control parameter λ is now converted to a stochastic variable which evolves under the thermal noise, the state $x \equiv (\lambda, \sigma)$ will not in general follow the protocol \mathcal{C}_{AA} and is free to explore all the states in the network \mathcal{G}_r .

5.2.1.2 Dynamics in the reduced network

We set the energies of the empty states AE, BE, CE to zero and assign energies to all other states based on the energy level of the dot that contains the electron: states BL and BR have energy ϵ_l ; states AL and CR have energy ϵ_0 ; and states AR and CL have energy ϵ_u , with $\epsilon_l < \epsilon_0 < \epsilon_u$ as in Sec. 4.2.1. We impose the condition of local detailed balance on the transition rates for the thermal transitions $x_i \leftrightarrow x_j$ with $x_i, x_j \in V(\mathcal{G}_r)$, when there is no exchange of electron with the left or the right reservoir:

$$\frac{R_{x_i x_j}^r}{R_{x_j x_i}^r} = e^{-\beta(E_i^r - E_j^r)} \quad , \quad (5.1)$$

where $\beta = (k_B T)^{-1}$ is the inverse temperature, and the superscript r again refers to the reduced network. E_i^r (E_j^r) is the energy of the state x_i (x_j) and $R_{x_i x_j}^r$ is the transition rate for the jump $x_j \rightarrow x_i$. The right-hand side of Eq. (5.1) is the ratio of probabilities of the system being in state x_i and x_j , in the canonical ensemble. Strictly speaking, the DQD system is quantal in nature and the tunneling events of the excess electron between two dots (i.e., $\sigma = L \leftrightarrow \sigma = R$) are coherent transfers, a purely quantal phenomenon (see Chapter 4 for discussion on the quantum model). However, in our model we treat these events as classical thermal jumps in the spirit of Ref. [4]. Thus, we assume the local detailed balance relation Eq. (5.1) for the edges: $AL \leftrightarrow AR$, $BL \leftrightarrow BR$ and $CL \leftrightarrow CR$.

When an electron jumps from the right reservoir, maintained at the chemical potential μ_R to the energy level ϵ_0 of the right dot, there is an energy cost of $(\epsilon_0 - \mu_R)$ and similarly if an electron jumps from the level ϵ_0 of the left dot to the left electron reservoir set at the chemical potential

μ_L the energy exchange is $(\mu_L - \epsilon_0)$. Thus for the transitions $AL \leftrightarrow AE$ and $CR \leftrightarrow CE$ (shown in blue in Fig. 5.3), we can write the local detailed balance relations as,

$$\begin{aligned} \frac{R_{AE AL}^r}{R_{AL AE}^r} &= e^{-\beta(\mu_L - \epsilon_0)}, \\ \frac{R_{CR CE}^r}{R_{CE CR}^r} &= e^{-\beta(\epsilon_0 - \mu_R)}. \end{aligned} \quad (5.2)$$

The coupling with the electron reservoir creates *thermodynamic forces* [49, 69, 105, 106] in \mathcal{G}_r and leads to violation of global detailed balance when $\mu_L \neq \mu_R$. When Eqs. (5.1) and (5.2) are satisfied and $\mu_L \neq \mu_R$, the dynamics of x in \mathcal{G}_r reach a non-equilibrium steady state (NESS) [49]. In this state, electrons flow in the thermodynamically preferred direction, i.e., from the right (left) reservoir to the left (right) reservoir when $\mu_R > \mu_L$ ($\mu_L > \mu_R$), resulting in an overall counterclockwise (clockwise) flow (which we will abbreviate as CCW (CW) flow throughout the article) of probability current in \mathcal{G}_r . This flow is in contrast with the feedback-controlled model, which transfers electrons against the thermodynamically preferred direction. Therefore we next consider how to couple the DQD to an information reservoir, in the form of a stream of bits, so as to make the evolution of the DQD mimic that of the AA model.

5.2.2 Conversion to autonomous demon: bit-coupling strategy

Our information reservoir is a memory tape containing n classical bits. Each bit (b) can be in one of the two states in $\mathbf{B} = \{0, 1\}$. The energies of the two bit states are degenerate, and we set them to zero. As in Ref. [15] the DQD interacts with a bit for an interval of duration τ , after which the next bit arrives. We can visualize this process by imagining that the bits are placed, equally spaced, on a tape that moves frictionlessly past the DQD, which interacts with the bit that

is nearest to it at any given time.

In our model the coupling between the DQD and the bit occurs along the four edges of \mathcal{G}_r that correspond to instant feedback steps in the AA model. These edges are shown in red in Fig. 5.3. (Note that we have split the $CE \implies AE$ feedback step of the original AA model into two steps: $CE \leftrightarrow BE$ and $BE \leftrightarrow AE$ in our model.) Specifically, the DQD transitions corresponding to these four edges can occur only when the state of the interacting bit b also flips. We set up the coupling rules so that CW flow of probability current along \mathcal{C}_{AA} is favoured when b flips from 0 to 1, and CCW flow is favored when b flips from 1 to 0. For example, the transition $AL \rightarrow BL$ must be accompanied by a bit flip $0 \rightarrow 1$, and the reverse transition $BL \rightarrow AL$ occurs only if the interacting bit flips from 1 to 0. Similar comments apply to the edges $BR \leftrightarrow CR$, $CE \leftrightarrow BE$ and $BE \leftrightarrow AE$. These DQD-bit coupling rules are indicated by curved red arrows in Fig. 5.3. With this coupling scheme, an excess of 0's in the incoming bit stream biases the flow of probability in the CW direction. This bias opposes the thermodynamic direction of the probability current when $\mu_R > \mu_L$. Similarly, if $\mu_L > \mu_R$ then an excess of 1's opposes the thermodynamic direction of the probability current.

5.2.3 Details of the memory-tape model

5.2.3.1 DQD+controller+bit joint state space: full network

The joint evolution of the DQD state (x) and the nearest bit (b) occurs in the *bit-coupled network* $\mathcal{G}_f = (\mathbf{V}_y, \mathbf{E}_y)$, which call as the *full network*; see Fig. 5.4. Here $\mathbf{V}_y \equiv V(\mathcal{G}_f) = \mathbf{V}_x \times \mathbf{B}$ is the set of vertices representing the 18 possible states of the variable $y = (x, b) \equiv (\lambda, \sigma, b)$, and $\mathbf{E}_y \equiv E(\mathcal{G}_f)$ is the set of 18 bidirectional edges that reflect on the bit-coupling rules described

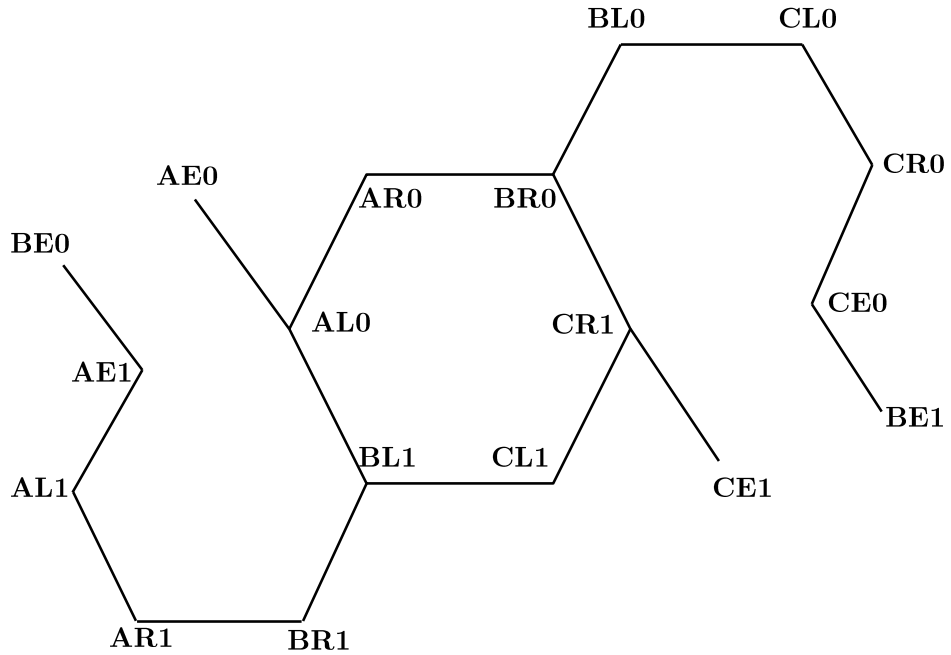


Figure 5.4: Full network $\mathcal{G}_f = (\mathbf{V}_y, \mathbf{E}_y)$ showing all 18 states of the combined DQD and bit. The full network \mathcal{G}_f is obtained from Fig. 5.3 by accounting for the bit-coupling in \mathcal{G}_r . The states in the full network are given by $\mathbf{V}_y = \mathbf{V}_x \times \mathbf{B}$ and the edges follow directly from the edges of the network \mathcal{G}_r , and the mapping of the edges is described in the Sec. 5.2.3.1. Equation (5.6) governs the dynamics of the variable $y \equiv (\lambda, \sigma, b)$ in this network. The figure is taken from Ref. [2]

in Sec. 5.2.2. Each edge of \mathcal{G}_r that does not involve bit coupling is represented by two different edges of \mathcal{G}_f , corresponding to the two possible bit states. That is, an edge $x_i \leftrightarrow x_j \in E(\mathcal{G}_r)$ corresponds to the edges $(x_i, 0) \leftrightarrow (x_j, 0)$ and $(x_i, 1) \leftrightarrow (x_j, 1)$ in $E(\mathcal{G}_f)$, when $x_i \leftrightarrow x_j$ does not involve bit coupling. An edge $x'_i \leftrightarrow x'_j \in E(\mathcal{G}_r)$ that is coupled to the bit transition $0 \leftrightarrow 1$ is mapped to only one edge, $(x'_i, 0) \leftrightarrow (x'_j, 1) \in E(\mathcal{G}_f)$. There are four such edges in \mathcal{G}_f : $BE0 \leftrightarrow AE1$, $AL0 \leftrightarrow BL1$, $BR0 \leftrightarrow CR1$, and $CE0 \leftrightarrow BE1$; see Figs. 5.3 and 5.4.

5.2.3.2 Dynamics in the full network and repeated bit interaction

As the $b = 0$ and 1 bit states are energetically degenerate, the transition rates for the edges in $E(\mathcal{G}_f)$ obey the same detailed balance conditions as the corresponding edges in $E(\mathcal{G}_r)$. Edges $y_i \leftrightarrow y_j$ in $E(\mathcal{G}_f)$ with no electron reservoir coupling satisfy

$$\frac{R_{y_i y_j}}{R_{y_j y_i}} = e^{-\beta(E_i - E_j)}, \quad (5.3)$$

where E_i and E_j are the energies of the states y_i and y_j respectively (compare Eq. (5.3) with Eq. (5.1)). When there is coupling with the electron reservoirs, the local detailed balance relations are given as,

$$\begin{aligned} \frac{R_{AE0 AL0}}{R_{AL0 AE0}} &= \frac{R_{AE1 AL1}}{R_{AL1 AE1}} = e^{-\beta(\mu_L - \epsilon_0)}, \\ \frac{R_{CR0 CE0}}{R_{CE0 CR0}} &= \frac{R_{CR1 CE1}}{R_{CE1 CR1}} = e^{-\beta(\epsilon_0 - \mu_R)}. \end{aligned} \quad (5.4)$$

(compare Eq. (5.4) with Eq. (5.2)). Equations (5.3) and (5.4) ensure the thermodynamic consistency of the model, but do not yet completely specify the dynamics of y . We assume that the

timescale of the stochastic dynamics of y due to thermal jumps is on the order of unity, and our choice of the transition rates consistent with Eqs. (5.3) and (5.4) are shown in Table 5.1. Appendix 5.5 presents a detailed discussion of the choice of the transition rates and corresponding timescales.

During every interaction interval of duration τ , the joint dynamics of the DQD and bit are described by a Markov jump process for the state variable $y = (x, b)$ in \mathcal{G}_f , with transition rates shown in Table 5.1. In a continuous time Markov jump process, the jump times follow a Poisson distribution as discussed in detail in Appendix 5.7. At the end of each interaction interval, when a new bit b_{in} arrives, the state of the DQD x remains unchanged, and the state of the interacting bit b takes on the value of the incoming bit b_{in} . Thus when the outgoing and incoming bit states differ, there is an effective *virtual jump*, due to the fact that the “old” interacting bit is replaced by the next bit in the memory tape.

5.2.4 Summary of the modelling strategy

Here we summarize our approach for creating an autonomous, memory-tape model of Maxwell’s demon from the non-autonomous, feedback-controlled AA model. We first create a network representation of the states of the feedback-controlled model by identifying the dynamical states of the system ($\sigma \in \Sigma$) and the states of the control parameter ($\lambda \in \Lambda$). We then convert the control parameter λ to a stochastic dynamic variable that jumps among the states of Λ . The joint state of the system and parameter is given by $x \equiv (\lambda, \sigma) \in \mathbf{V}_x$. The next step is to identify a network $\mathcal{G}_r = (\mathbf{V}_x, \mathbf{E}_x)$ whose edges correspond to possible transitions. For thermodynamic consistency, the transition rates must satisfy Eqs. (5.1) and (5.2). There is no unique

way to construct the network \mathcal{G}_r and different choices of the allowed transitions lead to different memory-tape models. For our DQD system, we focused on designing a model that mimics the feedback-controlled model's behavior, and is simple enough for analytical and semi-analytical treatment.

Next, the DQD is connected to a sliding memory-tape (information reservoir). By interacting with only the nearest bit on the tape, the DQD interacts with each bit for a fixed time τ . During that time, the coupling between the DQD and the interacting bit b occurs along those edges in the network \mathcal{G}_r that correspond to the instantaneous feedback steps of the AA model. The bit coupling rules are chosen so that incoming bits in the 0 state bias the resulting current in one direction (CW in our model) and incoming bits in the 1 state bias it in the other direction. In this way a memory tape with a surplus of 0's or 1's generates an effective force, which can be harnessed to oppose the thermodynamic forces arising from reservoirs at different chemical potentials.

The joint state of the DQD and interacting bit is described by a variable $y \equiv (x, b)$ that evolves by a Markov jump process in the network $\mathcal{G}_f = (\mathbf{V}_y, \mathbf{E}_y)$. As we assume the bit states 0 and 1 to be energetically degenerate, the transition rates in the \mathcal{G}_f follow from those in \mathcal{G}_r ; see Eqs. (5.3) and (5.4).

While we illustrate our strategy with the AA model and a specific network structure of its dynamics, this approach can be implemented with other feedback controlled models where an underlying network structure can be identified and then modified in a similar fashion as our approach, to obtain a memory-tape model.

Table 5.1: Transition rates for jumps of the variable y in \mathcal{G}_f . $R_{y_j y_i}$ denotes the transition rate from y_j to y_i . Here we have taken $r = e^{-\beta\epsilon}$ with $\epsilon = (\epsilon_u - \epsilon_0) = (\epsilon_0 - \epsilon_l)$. These rates are used construct the matrix \mathbf{R} which is shown in Eq. (5.34) in Appendix 5.6

$$\begin{aligned}
R_{CL0 \ CR0} &= r \\
R_{CR0 \ CL0} &= 1 \\
R_{CL1 \ CR1} &= r \\
R_{CR1 \ CL1} &= 1 \\
R_{BL0 \ CL0} &= 1 \\
R_{CL0 \ BL0} &= r^2 \\
R_{BL1 \ CL1} &= 1 \\
R_{CL1 \ BL1} &= r^2 \\
R_{BL0 \ BR0} &= 1 \\
R_{BR0 \ BL0} &= 1 \\
R_{BL1 \ BR1} &= 1 \\
R_{BR1 \ BL1} &= 1 \\
R_{AR0 \ BR0} &= r^2 \\
R_{BR0 \ AR0} &= 1 \\
R_{AR1 \ BR1} &= r^2 \\
R_{BR1 \ AR1} &= 1 \\
R_{AL0 \ AR0} &= 1 \\
R_{AR0 \ AL0} &= r \\
R_{AL1 \ AR1} &= 1 \\
R_{AR1 \ AL1} &= r \\
R_{AE0 \ AL0} &= e^{-\beta(\mu_L - \epsilon_0)} \\
R_{AL0 \ AE0} &= 1 \\
R_{AE1 \ AL1} &= e^{-\beta(\mu_L - \epsilon_0)} \\
R_{AL1 \ AE1} &= 1 \\
R_{CR0 \ CE0} &= 1 \\
R_{CE0 \ CR0} &= e^{-\beta(\mu_R - \epsilon_0)} \\
R_{CR1 \ CE1} &= 1 \\
R_{CE1 \ CR1} &= e^{-\beta(\mu_R - \epsilon_0)} \\
R_{BE0 \ AE1} &= 1 \\
R_{AE1 \ BE0} &= 1 \\
R_{CE0 \ BE1} &= 1 \\
R_{BE1 \ CE0} &= 1 \\
R_{AL0 \ BL1} &= r \\
R_{BL1 \ AL0} &= 1 \\
R_{BR0 \ CR1} &= 1 \\
R_{CR1 \ BR0} &= r
\end{aligned}$$

5.3 Analysis and results

5.3.1 Methods

Following Ref. [15], let $\mathbf{p}(t_n)$ be a column vector with nine entries that describes the probability distribution of the states of the DQD state variable x in \mathcal{G}_r (in the order $AE, BE, CE, BL, BR, AL, CR, AR, CL$) at time $t_n \equiv n\tau$ that marks the start of an interaction interval. Each incoming bit is independently sampled from the same probability distribution, with p_0 (or p_1) denoting the probability of the bit to arrive in state 0 (or 1). It is convenient to specify this distribution by the single parameter $\delta = p_0 - p_1$, which measures the excess of 0's among the incoming bits. The statistical state of the variable $y \equiv (x, b)$ in \mathcal{G}_f at time t_n (just after the arrival of the n 'th bit) is given by the 18-dimensional vector

$$\mathbf{p}_f(t_n) = \mathbf{M}\mathbf{p}(t_n), \quad \mathbf{M} = \begin{pmatrix} p_0\mathbf{I} \\ p_1\mathbf{I} \end{pmatrix}, \quad (5.5)$$

with \mathbf{I} being a 9×9 identity matrix. The first nine elements of $\mathbf{p}_f(t)$ correspond to the bit state $b = 0$ and the last nine elements to the the state $b = 1$. From $t = t_n$ to t_{n+1} the probability distribution in \mathcal{G}_f evolves under the master equation

$$\frac{d}{dt}\mathbf{p}_f(t) = \mathbf{R}\mathbf{p}_f(t), \quad (5.6)$$

where \mathbf{R} is the 18×18 rate matrix whose off-diagonal elements are the transition rates listed in Table 5.1, and whose diagonal elements are $R_{y_i y_i} = -\sum_{y_j \neq y_i} R_{y_j y_i}$; see Eq. (5.34) for an explicit expression for \mathbf{R} . At the end of the interaction interval, just before the next bit arrives, the joint

probability distribution is obtained from the solution of Eq. (5.6), namely

$$\mathbf{p}_f(t_n + \tau) = e^{\mathbf{R}\tau} \mathbf{M} \mathbf{p}(t_n). \quad (5.7)$$

To obtain the probability distribution of x in \mathcal{G}_r at the end of the interaction interval, we project from the 18-state network \mathcal{G}_f to the 9-state network \mathcal{G}_r ,

$$\mathbf{p}(t_n + \tau) = \mathbf{P}_D e^{\mathbf{R}\tau} \mathbf{M} \mathbf{p}(t_n), \quad \mathbf{P}_D = \begin{pmatrix} \mathbf{I} & \mathbf{I} \end{pmatrix}. \quad (5.8)$$

Equivalently,

$$\mathbf{p}((n+1)\tau) = \mathbf{T} \mathbf{p}(n\tau), \quad \mathbf{T} = \mathbf{P}_D e^{\mathbf{R}\tau} \mathbf{M}. \quad (5.9)$$

This transition matrix \mathbf{T} (which depends on the parameter τ) evolves the probability distribution of x in \mathcal{G}_r over a single interaction interval. The evolution over n successive intervals is described by the transition matrix \mathbf{T}^n . From the Perron-Frobenius theorem [107] it follows that any distribution \mathbf{p} in \mathcal{G}_r evolves asymptotically to a unique periodic steady state

$$\mathbf{q}_{\text{pss}} = \lim_{n \rightarrow \infty} \mathbf{T}^n \mathbf{p} . \quad (5.10)$$

The periodic steady state \mathbf{q}_{pss} is a function of the interaction interval τ , and can be calculated by solving for the invariant vector of the matrix \mathbf{T} ,

$$\mathbf{T} \mathbf{q}_{\text{pss}} = \mathbf{q}_{\text{pss}}. \quad (5.11)$$

Once the periodic steady state for the DQD has been reached, the joint state of the DQD and bit at the start of every interaction interval is given by $\mathbf{M}\mathbf{q}_{\text{pss}}$, and the joint state at a time $t_n + \Delta t$, with $0 \leq \Delta t < \tau$, is

$$\mathbf{p}_f(t_n + \Delta t) = e^{\mathbf{R}\Delta t} \mathbf{M}\mathbf{q}_{\text{pss}} \quad . \quad (5.12)$$

For the remainder of this chapter, when analyzing the behavior of our model, we will assume that the periodic steady state has been reached.

5.3.2 Thermodynamics of the memory-tape model

5.3.2.1 Calculation of work

Let the *circulation* $\Phi(\tau)$ denote the average number of electrons transferred from the left to the right reservoir during each interaction interval. The average chemical work performed by the DQD system per time interval τ is then

$$W(\tau) = (\mu_R - \mu_L)\Phi(\tau). \quad (5.13)$$

If the sign of $\mu_R - \mu_L$ is the same as that of $\Phi(\tau)$, then electrons flow from the lower to higher chemical potential, that is against the thermodynamic force. From Fig. 5.3 we see that

$$\begin{aligned} \Phi(\tau) &= \int_0^\tau dt J_{CR \rightarrow CE}^r = \int_0^\tau dt J_{CE \rightarrow BE}^r \\ &= \int_0^\tau dt J_{BE \rightarrow AE}^r = \int_0^\tau dt J_{AE \rightarrow AL}^r, \end{aligned} \quad (5.14)$$

where $J_{x_j \rightarrow x_i}^r \equiv J_{x_i x_j}^r$ is the probability current along $x_j \rightarrow x_i$ in \mathcal{G}_r , projected from the corresponding currents in \mathcal{G}_f . We can determine $\Phi(\tau)$ by calculating any one of these integrals.

The probability current along $y_j \rightarrow y_i$ of \mathcal{G}_f is

$$J_{y_i y_j} = R_{y_i y_j} p_{y_j}(t) - R_{y_j y_i} p_{y_i}(t). \quad (5.15)$$

When two edges $x_j 0 \leftrightarrow x_i 0$ and $x_j 1 \leftrightarrow x_i 1$ in \mathcal{G}_f correspond to the edge $x_j \leftrightarrow x_i$ in \mathcal{G}_r , we have

$$J_{x_i x_j}^r(t) = J_{x_i 0 \ x_j 0}(t) + J_{x_i 1 \ x_j 1}(t), \quad (5.16)$$

but when the transition $x_j \rightarrow x_i$ is coupled with a bit flip $b' \rightarrow b''$, we have

$$J_{x_i x_j}^r(t) = J_{x_i b'' \ x_j b'}(t). \quad (5.17)$$

Since the $CE \leftrightarrow BE$ transition is coupled to the bit flit $0 \leftrightarrow 1$, the edge $CE \leftrightarrow BE$ in \mathcal{G}_r corresponds to a single edge, $CE0 \leftrightarrow BE1$ in \mathcal{G}_f , hence

$$\Phi(\tau) = \int_0^\tau dt \ J_{BE \ CE}^r = \int_0^\tau dt \ J_{BE1 \ CE0}. \quad (5.18)$$

Moreover, since $BE1$ is connected to only one edge, $CE0 \leftrightarrow BE1$, we have $\dot{p}_{BE1} = J_{BE1 \ CE0}$; see Fig. 5.4. Therefore,

$$\begin{aligned} \Phi(\tau) &= \int_0^\tau dt \ \dot{p}_{BE1} = [p_{BE1}(\tau) - p_{BE1}(0)] \\ &= [(e^{\mathbf{R}\tau} - \mathbf{I}) \mathbf{Mq}_{\text{pss}}]_{y=BE1}, \end{aligned} \quad (5.19)$$

where we have used Eq. (5.12) to get to the second line. We will use this result in Sec. 5.3.3.1.

5.3.2.2 Calculation of entropy change of the bit

Let p'_0 and p'_1 denote the probabilities of the outgoing bit to be in the states 0 and 1. These values are determined by summing over the appropriate states $y = (x, b)$ in \mathcal{G}_f at the end of an interaction interval:

$$\begin{aligned} p'_0 &= \sum_{x \in V(\mathcal{G}_r)} (e^{\mathbf{R}\tau} \mathbf{M} \mathbf{q}_{\text{pss}})_{y=(x,0)} \\ p'_1 &= \sum_{x \in V(\mathcal{G}_r)} (e^{\mathbf{R}\tau} \mathbf{M} \mathbf{q}_{\text{pss}})_{y=(x,1)} . \end{aligned} \quad (5.20)$$

The parameter

$$\delta' = p'_0 - p'_1, \quad (5.21)$$

specifies the distribution of the outgoing bit. The entropy corresponding to this distribution is $S' = -\sum_{i=0,1} p'_i \ln p'_i$, while that of the incoming bit is $S = -\sum_{i=0,1} p_i \ln p_i$. Thus in the periodic steady state, the change in *single-symbol entropy* [39] of the interacting bit is $\Delta S = S' - S$. Because ΔS does not account for correlations that develop between successive outgoing bits, it provides only an upper bound on the net entropy change (per bit) of the information reservoir. We discuss this point in detail in the next section (5.3.2.3), in the context of the second law of thermodynamics.

5.3.2.3 The first and the second laws of thermodynamics

In the periodic steady-state, the change in the internal energy of the DQD over one interaction interval is zero, on average. If chemical work is performed by the flow of electrons from low to high chemical potential, then the energy required for this process must be extracted as heat from the thermal reservoir that maintains the entire system at a fixed temperature T . We write the first law of thermodynamics at the periodic steady state for this model as

$$Q(\tau) = W(\tau) = (\mu_R - \mu_L)\Phi(\tau), \quad (5.22)$$

where $Q(\tau)$ is the average heat extracted from the thermal reservoir, per interaction interval.

In Refs. [39, 40], a general form of the second law for information ratchets, called the *Information Processing Second Law* (IPSL), was derived. In the periodic steady state the IPSL is written as

$$(\ln 2)\Delta h_\mu \geq \beta W, \quad (5.23)$$

where Δh_μ is the change in the *Shannon entropy rate* (see Refs. [39, 40]) and W is the average work extracted during one interaction interval. The entropy rate Δh_μ includes the effect of correlations among the bits in the incoming and outgoing bit-streams. In our model we have assumed that incoming bits are uncorrelated with each other and have been generated through a *memoryless* [40] process. For finite τ , the outgoing bits become correlated with each other, and thus the output is *memoryful* [40]. However, in the limit $\tau \rightarrow \infty$ these correlations become lost, and the Shannon entropy rate Δh_μ reduces to the change in single-symbol entropy $\Delta S/(\ln 2)$, hence for

our model Eq. (5.23) becomes (in that limit)

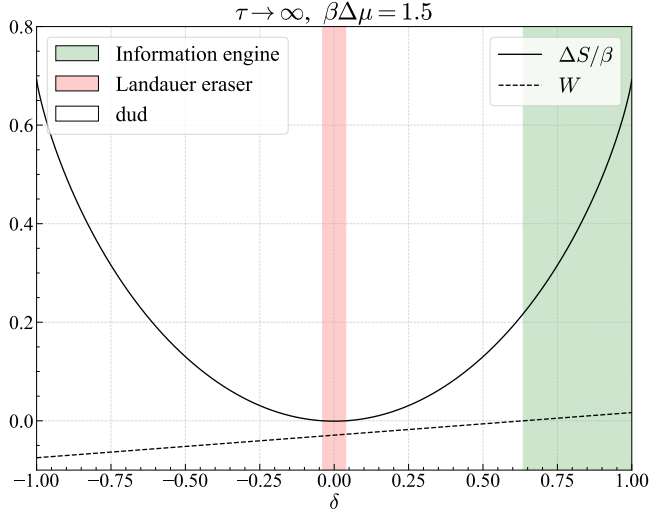
$$\Delta S \geq \beta W \quad . \quad (5.24)$$

Equation (5.23) is a general result for any memory-tape Maxwell demon and Eq. (5.24) is a limiting case of the IPSL when correlations are neglected. When correlations are non-negligible, Eq. (5.23) can identify functional modes of operation that are not indicated by Eq. (5.24); see Refs. [39, 42, 44]. However, it is common to use the single symbol entropy for the analysis of memory-tape models [15, 16, 26, 27, 33] and Eq. (5.24) has been derived previously in the context of Hamiltonian dynamics [17] and stochastic dynamics [28]. In our model, we ignore the effect of the correlations among the bits for simplicity and assume the validity of Eq. (5.24) as an approximation to Eq. (5.23) even for finite τ . The analysis of the effect of correlations among the bits and calculation of Δh_μ is outside the scope of this chapter; see Ref. [44] for the Δh_μ calculation in context of the MJ model. Henceforth, by ‘‘entropy’’ we always refer to single-symbol entropy unless otherwise specified.

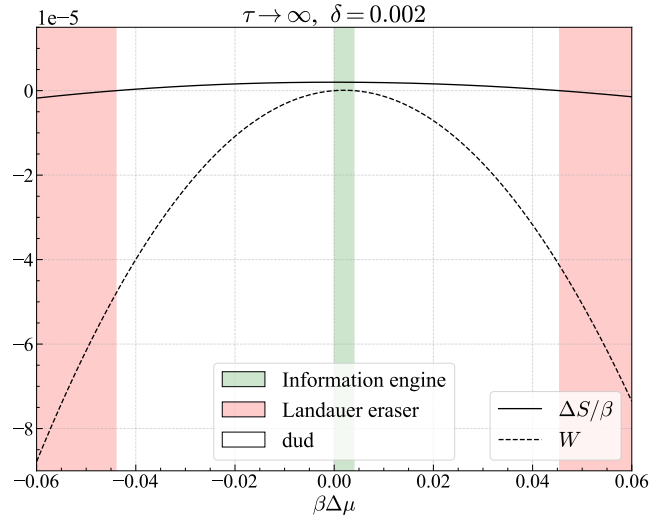
5.3.3 Analytical results for $\tau \rightarrow \infty$

5.3.3.1 Thermodynamic quantities

There are two relevant time scales in our model. We have taken the time scale associated with the thermal jumps in \mathcal{G}_f , which are governed by Eq. (5.6), to be of order unity. The other time scale is the parameter τ that defines how long the DQD interacts with each bit. From the



(a) δ variation



(b) $\Delta\mu$ variation

Figure 5.5: Plots of $\Delta S/\beta$ and W when (a) δ is varied at fixed $\mu_R = 1.5$ and $\mu_L = 0$, and (b) $\beta\Delta\mu$ is varied by changing μ_R at fixed $\mu_L = 0$ and $\delta = 0.002$. In both cases we set $\beta = 1$, $r = e^{-1}$, $\epsilon_0 = 0$, and we take the limit $\tau \rightarrow \infty$. In both plots we see that $\Delta S \geq \beta W$ is satisfied. The regions corresponding to the information engine ($\Delta S > 0, W > 0$), Landauer eraser ($\Delta S < 0, W < 0$) and dud ($\Delta S > 0, W < 0$) are shaded green, red and white respectively. The figure is taken from Ref. [2]

Perron-Frobenius theorem [107], we have

$$\lim_{\tau \rightarrow \infty} e^{\mathbf{R}\tau} \mathbf{p}_f = \boldsymbol{\Pi}, \quad \forall \mathbf{p}_f, \quad (5.25)$$

where $\mathbf{R}\boldsymbol{\Pi} = \mathbf{0}$. The expression for $\boldsymbol{\Pi}$ is given by Eq. (5.35) in Appendix 5.6. If τ is sufficiently large then Eq. (5.11) becomes

$$\mathbf{q}_{\text{pss}}^\infty = \lim_{\tau \rightarrow \infty} \mathbf{P}_D e^{\mathbf{R}\tau} \mathbf{M} \mathbf{q}_{\text{pss}} = \mathbf{P}_D \boldsymbol{\Pi}. \quad (5.26)$$

Using Eqs. (5.35) and (5.26), we get

$$\begin{aligned} \mathbf{q}_{\text{pss}}^\infty &= \mathcal{N} \left[\frac{2\kappa_L}{r} \frac{(\kappa_L + \kappa_R)}{r} \frac{2\kappa_R}{r} \frac{2}{r^2} \frac{2}{r^2} \frac{2}{r} \frac{2}{r} 2 2 \right]^T, \\ \mathcal{N} &= \frac{r^2}{4(1+r+r^2) + 3r(\kappa_L + \kappa_R)}, \end{aligned} \quad (5.27)$$

where $\kappa_L = e^{-\beta(\mu_L - \epsilon_0)}$, $\kappa_R = e^{-\beta(\mu_R - \epsilon_0)}$, and $r = e^{-\beta\epsilon}$ with $\epsilon = (\epsilon_u - \epsilon_0) = (\epsilon_0 - \epsilon_l)$. Here we have taken symmetric energy gaps in the dots for simplicity of calculation and conciseness of results. The method of analysis would be the same if ϵ_u and ϵ_l were taken as free parameters.

In the $\tau \rightarrow \infty$ limit, the circulation (Φ_∞) can be calculated using Eq. (5.19). The probabilities $p_{BE1}(0)$ and $p_{BE1}(\infty)$ are given by the *BE1* elements of $\mathbf{M} \mathbf{q}_{\text{pss}}^\infty$ and $\boldsymbol{\Pi}$, respectively. Using Eqs. (5.13), (5.19), (5.25) and (5.27) we get

$$W_\infty = \frac{\mathcal{N}(\mu_R - \mu_L)}{r} \left[\left(\frac{1+\delta}{2} \right) \kappa_R - \left(\frac{1-\delta}{2} \right) \kappa_L \right]. \quad (5.28)$$

Using Eqs. (5.25), (5.20) and (5.21), we can describe the distribution of the outgoing bits as

$p'_{0,1} = (1 \pm \delta')/2$, where

$$\delta' = \frac{r(\kappa_L - \kappa_R)}{4(1 + r + r^2) + 3r(\kappa_L + \kappa_R)}, \quad (5.29)$$

which can be used to calculate the entropy of the outgoing bits as $S' = -\sum_{i=0,1} p'_i \ln p'_i \in [0, \ln 2]$.

5.3.3.2 Operational mode phase diagram

In the limit $\tau \rightarrow \infty$, bits in the outgoing bit-stream are uncorrelated and thus Eqs. (5.23) and (5.24) are equivalent, and both the final distribution δ' and the entropy of the outgoing bit become independent of δ ; see Eq. (5.29). The entropy change $\Delta S_\infty \equiv \lim_{\tau \rightarrow \infty} (S' - S)$ is a symmetric concave upwards function of δ with a negative value at its minimum ($\min_\delta \{\Delta S_\infty\} < 0$) at $\delta = 0$ when $\mu_L \neq \mu_R$. Thus, in the region with $|\delta| < |\delta'|$ (shaded red in Fig. 5.5a), we have $\Delta S_\infty < 0$ and $W_\infty < 0$ (using Eq. (5.24)). By Eq. (5.29), we see that when

$$|\delta| < |\delta'| = \left| \frac{r(\kappa_L - \kappa_R)}{4(1 + r + r^2) + 3r(\kappa_L + \kappa_R)} \right|, \quad (5.30)$$

information is erased from the incoming memory-tape, and the system consumes work, i.e., it acts as a Landauer eraser. Therefore, for a given value of $\Delta\mu = \mu_R - \mu_L$, the Landauer eraser region in the operational mode phase diagram is bounded by $\pm\delta'$, as indicated by the red regions in Fig. 5.6

By Eq. (5.24), $W_\infty > 0$ implies $\Delta S_\infty > 0$. Let δ^* denote the value of δ at which $\Phi_\infty =$

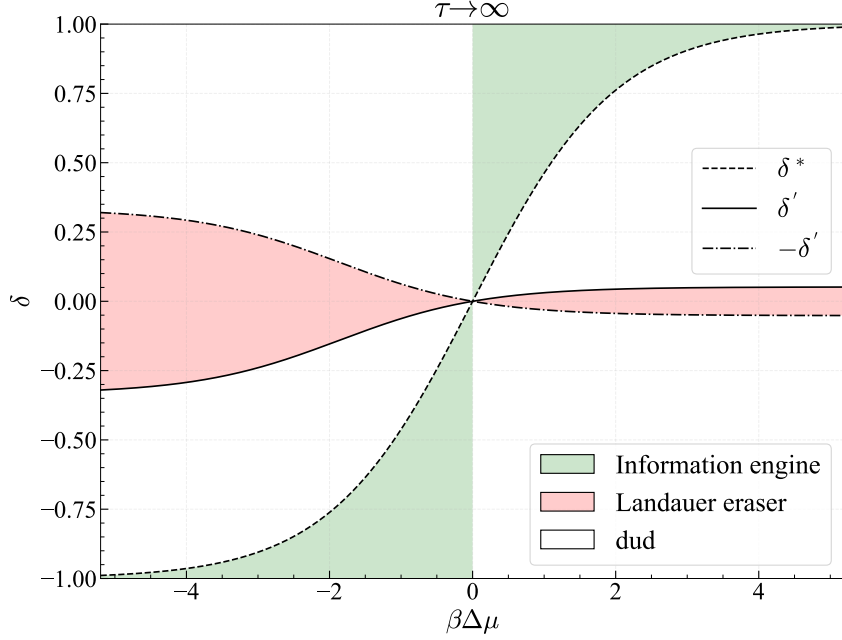


Figure 5.6: Analytically obtained phase diagram when $\tau \rightarrow \infty$. In the green region the system operates as an information engine ($\Delta S > 0, W > 0$) and in the red region it acts as a Landauer eraser. The critical parameter values δ^* , δ' and $-\delta'$ are shown as function of $\beta\Delta\mu$ with $\Delta\mu = \mu_R - \mu_L$ with $\mu_L = 0$. We have taken $\epsilon_0 = 0$, $\beta = 1$ and $r = e^{-1}$ here. The figure is taken from Ref. [2]

$W_\infty/\Delta\mu$ changes its sign, for fixed μ_R and μ_L . Using Eq. (5.28) we obtain

$$\delta^* = \frac{\kappa_L - \kappa_R}{\kappa_L + \kappa_R}. \quad (5.31)$$

Thus, $W_\infty > 0$ when $\delta > \delta^*$ and $\mu_R > \mu_L$, or when $\delta < \delta^*$ and $\mu_R < \mu_L$. In these regions of parameter space, shown in green in Fig. 5.6, the system produces work at the cost of writing information to the memory-tape and the DQD acts as an information engine.

In the regions of parameter space where $\Delta S_\infty > 0 > W_\infty$, information is written to the memory-tape and the system consumes work, hence the model is a *dud* [15].

5.3.4 Semi-analytical results for finite τ

For finite interaction time τ , we can numerically diagonalize the transition rate matrix as

$\mathbf{R} = \mathbf{U}\mathbf{D}_{\mathbf{R}}\mathbf{V}$, where $\mathbf{D}_{\mathbf{R}}$ is diagonal and $\mathbf{U}\mathbf{V} = \mathbf{V}\mathbf{U} = I$. We then have

$$\mathbf{T} = \mathbf{P}_{\mathbf{D}}\mathbf{U}e^{\mathbf{D}_{\mathbf{R}}\tau}\mathbf{V}\mathbf{M}, \quad (5.32)$$

and the evaluation of $e^{\mathbf{D}_{\mathbf{R}}\tau}$ is straightforward. Once \mathbf{T} is obtained in this manner, the periodic steady state \mathbf{q}_{pss} is calculated using Eq. (5.11), and thermodynamic quantities are determined as described in Sec. 5.3.2.

Following this semi-analytical approach, we have obtained phase diagrams for different values of τ , using the second law inequality Eq. (5.24), which is now the single symbol approximation to the IPSL in Eq. (5.23). Fig. 5.7 shows these phase diagrams. The competition between the effects of bit-coupling (δ) and the thermodynamic bias ($\Delta\mu$) determines the direction of probability current, i.e, the sign of Φ , in the network. With increasing values of τ , the system has more time to relax to the equilibrium state Π before a new bit arrives, and the phase diagram approaches the one shown in Fig. 5.6.

In our model, the information engine region ($W > 0$) appears only in the first and third quadrants of the phase diagrams. In these regions an increase in $|\Delta\mu|$ increases the effective thermodynamic forces and suppresses the information engine region for a fixed value of δ , as seen in Figs. 5.6 and 5.7.

For small values of τ , the frequency of the virtual jumps in \mathcal{G}_f (see Sec. 5.2.3.2) increases, as bits get replaced more frequently. These virtual jumps drive the probability current against the

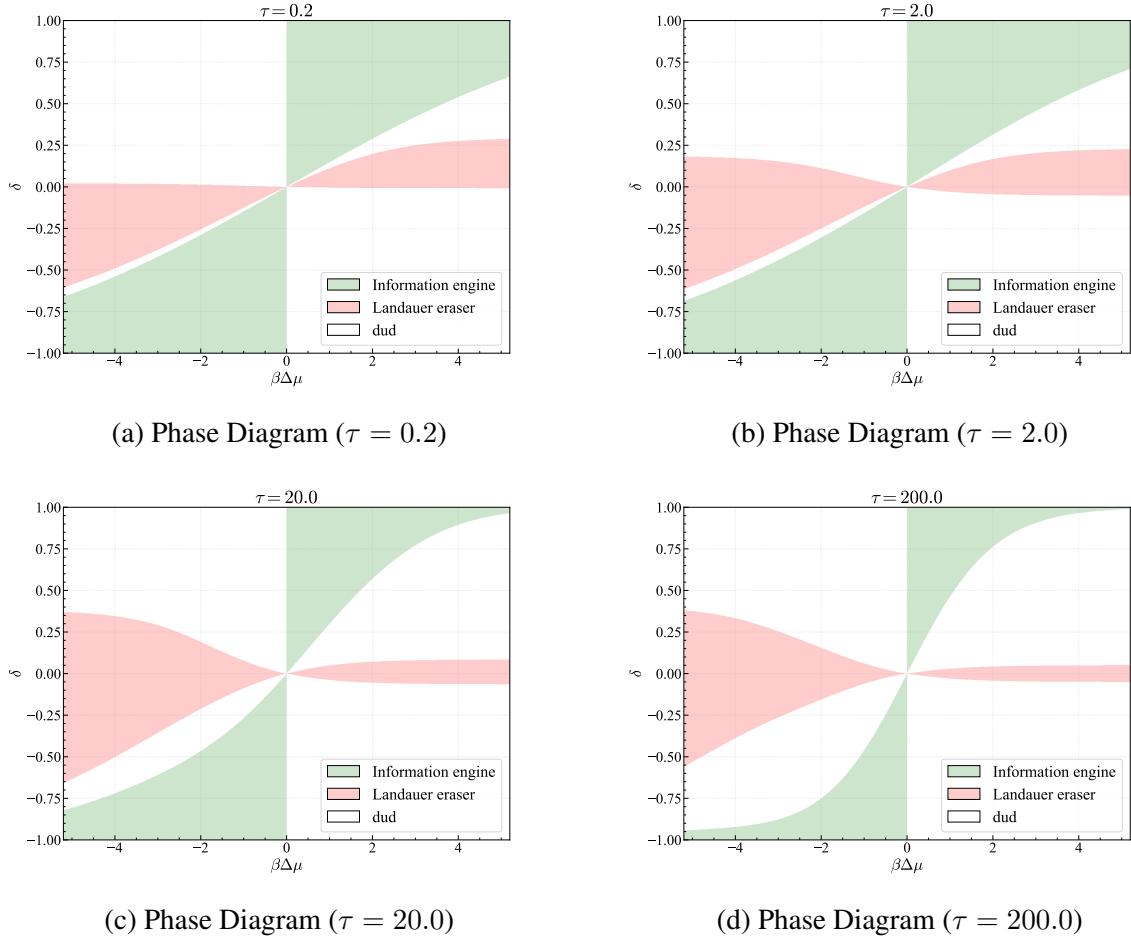


Figure 5.7: Numerically obtained phase diagrams for different values of the interaction time, $\tau = 0.2, 2, 20$ and 200 . For finite τ , the final distribution of the memory-tape (δ') depends on the initial distribution (δ), but this dependence vanishes in the limit $\tau \rightarrow \infty$. With increasing τ , the phase diagram approaches the one shown in Fig. 5.6. We have fixed $r = e^{-1}$, $\beta = 1$, $\epsilon_0 = 0$. The figure is taken from Ref. [2]

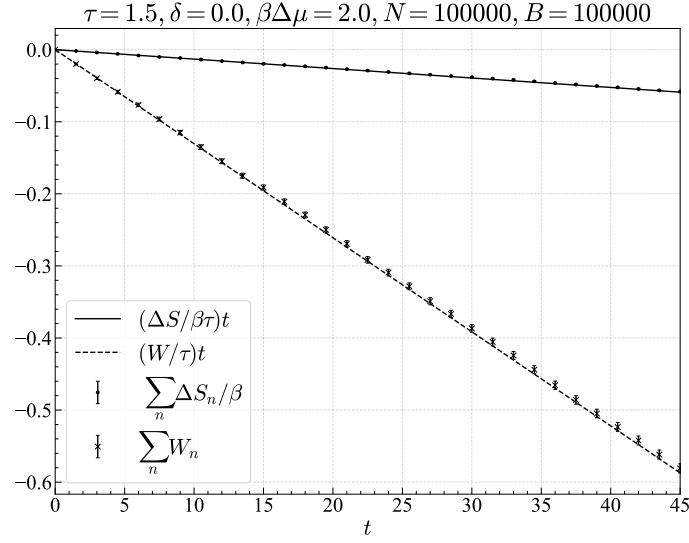
thermodynamic force in \mathcal{G}_r . Hence when τ is increased the information engine region decreases; see Fig. 5.7.

The entropy $S(\delta) = -\sum_i p_i \ln p_i$, with $p_{0,1}(\delta) = (1 \pm \delta)/2$, is a concave downward function with a maximum at $\delta = 0$. As a result, when $\delta = 0$ and $\delta' \neq 0$ we have $\Delta S = S(\delta') - S(\delta) < 0$. This explains why the Landauer eraser region ($\Delta S < 0$) contains the entire $\delta = 0$ axis in the phase diagram (except for the origin $\delta = \beta\Delta\mu = 0$, where $\Delta S = 0$).

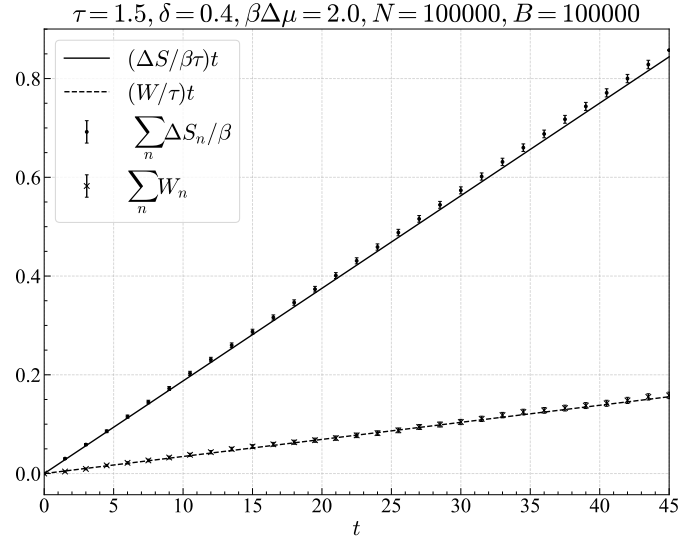
5.3.5 Stochastic simulation

We have also performed stochastic simulations of the system. The variable $y = (\lambda, \sigma, b)$ was initialized by sampling $x = (\lambda, \sigma)$ from the distribution \mathbf{q}_{pss} , and b from the distribution δ . During each bit interaction interval, y evolves under a Markov jump process, with the rates listed in Table 5.1. At the end of each interval, the value of b is replaced by the (randomly sampled) state of the incoming bit. See Appendix 5.7 for further simulation details.

Figs. 5.8a and 5.8b show work and entropy production when the system acts as a Landauer eraser and as an information engine, respectively. The total change in entropy ($\sum_n \Delta S_n$) of the memory-tape was calculated by summing the change in single symbol entropy over each bit (ΔS_n) in the memory-tape. Similarly, total work ($\sum_n W_n$) was obtained by summing over the work done over each interval (W_n). In these figures, the semi-analytical results obtained by the approach described in Sec. 5.3.4 are represented by straight lines with slopes $\Delta S/\tau$ and W/τ . $N = 10^5$ trajectories were generated, and statistical errors in ΔS_n and W_n were calculated using the bootstrap method, by resampling $B = 10^5$ times with replacements [108]. The increasing errors in $\sum_n \Delta S_n$ and $\sum_n W_n$ reflect the accumulation of statistical errors with each additional



(a) Landauer Eraser



(b) Information Engine

Figure 5.8: Work and entropy production in (a) the Landauer eraser mode and (b) the information engine mode. Semi-analytical results and stochastic simulation results are compared. ΔS_n and W_n represent the change in single symbol entropy of the n th bit and average extracted work in the n th interval. For all the simulations, we have taken $\beta = 1$, $r = e^{-1}$ and $\epsilon_0 = 0$. Errors are calculated with the bootstrap method. The figure is taken from Ref. [2]

interaction interval.

5.4 Discussion

We have presented a strategy for constructing a memory-tape model of Maxwell’s demon, from a feedback-controlled model. We have illustrated this strategy using the Annby-Andersson model [4], a feedback-controlled Maxwell’s demon in a double quantum dot (DQD). In our approach, we replace the feedback controller with a stochastic variable evolving under the same thermal environment as the DQD. We then couple our system to an information reservoir and design suitable bit interaction rules to mimic the effects of the feedback controller. In analyzing our model, we obtained an exact solution in the limit of infinitely long interaction time τ , and used a semi-analytical approach involving numerical matrix diagonalization for finite τ . As illustrated by these results as well as stochastic simulations, our model can act both as an information engine and as a Landauer eraser, for suitable parameter values.

Our research strengthens the connection between two paradigms of information thermodynamics: Maxwell’s original, non-autonomous paradigm of a “nimble-fingered” demon performing feedback control at the level of thermal fluctuations; and the autonomous paradigm, due to Bennett [12], in which the demon is replaced by a physical gadget, thermodynamically driven by the continual randomization of a stream of bits (the memory-tape). In effect, given a demon, we show how to design a gadget that mimics it.

Our approach makes use of the underlying network structure of a feedback-controlled system, and it relates to recent stochastic thermodynamic studies of bipartite systems [104, 109, 110]. Specifically, the dynamics of $y = (\lambda, \sigma, b)$ in \mathcal{G}_f can be described as bipartite system dynamics

by splitting y in two random variables: σ and $\bar{x} \equiv (\lambda, b)$ that do not change simultaneously. This is in contrast with the original MJ model [15] which lacks the bipartite structure; see [104].

Double quantum dot systems are promising candidates for the experimental implementation of information engines [66]. While there have been a number of realizations of feedback-controlled demons [5, 59], experimental realizations of memory-tape models are yet to be explored. By showing how to design a memory-tape model that mimics a feedback controlled system, our approach may be useful in the design of physical implementations of autonomous information engines.

Although our analysis has been entirely at the level of classical stochastic dynamics, it would be worth studying analogous quantum models (see e.g. [35]). A future research direction might explore design principles for quantum analogs of the memory-tape model. Lastly, we limited our discussion of the information-theoretic aspects of this model to the single symbol entropy. The study of the effects of correlations among the bits offers another avenue for future research.

5.5 Appendix: Transition rates and the detailed balance relations

Equations (5.3) and (5.4) together give ratios of the transition rates which guarantee the thermodynamic consistency of the model but do not completely define the transition rates for the dynamics of y in the network \mathcal{G}_f . Thus, there is freedom in the choice of transition rates along the edges of \mathcal{G}_f as long as the ratios in Eqs. (5.3) and (5.4) are maintained. When there is no

coupling with an electron reservoir, we have taken

$$R_{y_i y_j} = \Gamma e^{-\beta(E_i - E_j)}, \quad (5.33)$$

$$R_{y_j y_i} = \Gamma$$

for $E_i > E_j$, which satisfies Eq. (5.3). The pre-factor Γ is the inverse-timescale of the thermal jumps of the system and we have taken $\Gamma = 1$. For example the transition rates along the $CL0 - CR0$ edge are given as $R_{CL0 \rightarrow CR0} = e^{-\beta(\epsilon_u - \epsilon_0)} = e^{-\beta\epsilon} = r$ and $R_{CR0 \rightarrow CL0} = 1$, where we have taken $(\epsilon_u - \epsilon_0) = (\epsilon_0 - \epsilon_l) = \epsilon$ and $r = e^{-\beta\epsilon}$. We have assigned the rest of the rates in the Table 5.1 in a similar fashion when there is no coupling with an electron reservoir.

When there is an exchange of electron with the dot and the electron reservoir ($\sigma = L/R \leftrightarrow \sigma = E$), Eq. 5.4 ensures the thermodynamic consistency of the transition rates. Here we use the convention that when the electron enters the dot from the electron reservoir ($\sigma = E \rightarrow \sigma = L/R$) the transition rate is Γ_{res} , and when the electron leaves the dot to the electron reservoir ($\sigma = L/R \rightarrow \sigma = E$) the transition rates are given as $\Gamma_{\text{res}} e^{-\beta(\mu_{L/R} - \epsilon_0)}$ which is consistent with Eq. (5.4). For simplicity we have also taken $\Gamma_{\text{res}} = 1$. Thus for example, $R_{AE0 \rightarrow AL0} = e^{-\beta(\mu_L - \epsilon_0)}$ and $R_{AL0 \rightarrow AE0} = 1$. The other transitions involving the electron reservoirs are similarly set, as seen in Table 5.1.

Note that the shortest timescale of the dynamics of the thermal jumps is given as $1 / \max\{\Gamma, \Gamma_{\text{res}}\}$ which we have taken as 1 in our model. It should be noted that the time scale of the thermal jump is in general different from the duration of the bit interaction interval τ , which is another temporal parameter of our model.

5.6 Appendix: Rate matrix and unique stationary state for \mathcal{G}_f

The rate matrix \mathbf{R} and stationary distribution $\boldsymbol{\Pi}$ are (see next page)

$$\mathbf{R} =$$

$$\left(\begin{array}{cccccccccccccccccc} -1 & 0 & 0 & 0 & 0 & \kappa_L & 0 & 0 & 0 & 0 & 0 & 0 & 0 & 0 & 0 & 0 & 0 & 0 & 0 & 0 \\ 0 & -1 & 0 & 0 & 0 & 0 & 0 & 0 & 0 & 1 & 0 & 0 & 0 & 0 & 0 & 0 & 0 & 0 & 0 & 0 \\ 0 & 0 & -2 & 0 & 0 & 0 & \kappa_R & 0 & 0 & 0 & 1 & 0 & 0 & 0 & 0 & 0 & 0 & 0 & 0 & 0 \\ 0 & 0 & 0 & K_1 & 1 & 0 & 0 & 0 & 1 & 0 & 0 & 0 & 0 & 0 & 0 & 0 & 0 & 0 & 0 & 0 \\ 0 & 0 & 0 & 1 & K_2 & 0 & 0 & 1 & 0 & 0 & 0 & 0 & 0 & 0 & 0 & 0 & 0 & 1 & 0 & 0 \\ 1 & 0 & 0 & 0 & 0 & K_3 & 0 & 1 & 0 & 0 & 0 & 0 & 0 & r & 0 & 0 & 0 & 0 & 0 & 0 \\ 0 & 0 & 1 & 0 & 0 & 0 & K_4 & 0 & 1 & 0 & 0 & 0 & 0 & 0 & 0 & 0 & 0 & 0 & 0 & 0 \\ 0 & 0 & 0 & 0 & r^2 & r & 0 & -2 & 0 & 0 & 0 & 0 & 0 & 0 & 0 & 0 & 0 & 0 & 0 & 0 \\ 0 & 0 & 0 & r^2 & 0 & 0 & r & 0 & -2 & 0 & 0 & 0 & 0 & 0 & 0 & 0 & 0 & 0 & 0 & 0 \\ 0 & 1 & 0 & 0 & 0 & 0 & 0 & 0 & 0 & -2 & 0 & 0 & 0 & 0 & 0 & \kappa_L & 0 & 0 & 0 & 0 \\ 0 & 0 & 1 & 0 & 0 & 0 & 0 & 0 & 0 & 0 & -1 & 0 & 0 & 0 & 0 & 0 & 0 & 0 & 0 & 0 \\ 0 & 0 & 0 & 0 & 0 & 0 & 0 & 0 & 0 & 0 & 0 & -1 & 0 & 0 & 0 & 0 & \kappa_R & 0 & 0 & 0 \\ 0 & 0 & 0 & 0 & 0 & 1 & 0 & 0 & 0 & 0 & 0 & 0 & K_2 & 1 & 0 & 0 & 0 & 0 & 0 & 1 \\ 0 & 0 & 0 & 0 & 0 & 0 & 0 & 0 & 0 & 0 & 0 & 0 & 1 & K_1 & 0 & 0 & 0 & 1 & 0 & 0 \\ 0 & 0 & 0 & 0 & 0 & 0 & 0 & 0 & 0 & 1 & 0 & 0 & 0 & 0 & K_5 & 0 & 1 & 0 & 0 \\ 0 & 0 & 0 & 0 & 0 & r & 0 & 0 & 0 & 0 & 0 & 1 & 0 & 0 & 0 & K_6 & 0 & 0 & 1 \\ 0 & 0 & 0 & 0 & 0 & 0 & 0 & 0 & 0 & 0 & 0 & 0 & 0 & r^2 & r & 0 & -2 & 0 \\ 0 & 0 & 0 & 0 & 0 & 0 & 0 & 0 & 0 & 0 & 0 & 0 & r^2 & 0 & 0 & r & 0 & -2 \end{array} \right),$$

(5.34)

$$\begin{aligned}
\Pi = \frac{r^2}{4(1+r+r^2) + 3r(\kappa_L + \kappa_R)} & \left[\begin{array}{c} \kappa_L r^{-1} \\ \kappa_L r^{-1} \\ \kappa_R r^{-1} \\ r^{-2} \\ r^{-2} \\ r^{-1} \\ r^{-1} \\ 1 \\ 1 \\ \kappa_L r^{-1} \\ \kappa_R r^{-1} \\ \kappa_R r^{-1} \\ r^{-2} \\ r^{-2} \\ r^{-1} \\ r^{-1} \\ 1 \\ 1 \end{array} \right] & (5.35)
\end{aligned}$$

where $\kappa_L = e^{-\beta(\mu_L - \epsilon_0)}$, $\kappa_R = e^{-\beta(\mu_R - \epsilon_0)}$, $K_1 = -r^2 - 1$, $K_2 = -r^2 - r - 1$, $K_3 = -\kappa_L - r - 1$, $K_4 = -\kappa_R - r$, $K_5 = -\kappa_L - r$ and $K_6 = -\kappa_R - r - 1$. Here the states in $V(\mathcal{G}_f)$ are ordered as follows: ($AE0, BE0, CE0, BL0, BR0, AL0, CR0, AR0, CL0, AE1, BE1, CE1, BL1, BR1, AL1, CR1, AR1, CL1$).

5.7 Appendix: Details of stochastic simulation scheme

5.7.1 Poisson jumps

We implement the Gillespie Algorithm [111, 112, 113] to simulate the continuous time Markov jump process for y in \mathcal{G}_f , when the DQD system is interacting with a bit. If a system is in state y_j at time t , then the time interval for the next jump event is generated from the Poisson distribution as follows:

$$\Delta t = \frac{1}{\sum_{y \neq y_j} R_{yy_j}} \ln \frac{1}{\xi_1} \quad (5.36)$$

where ξ_1 is sampled uniformly in the interval $(0, 1]$. After remaining in the state y_j over the time interval $[t, t + \Delta t)$, the system jumps to a new state (say $y_{j'}$). To find $y_{j'}$, all states in $V(\mathcal{G}_f)$ are arranged in order (say, $(0, 1, 2, \dots, 16, 17)$), then j' is chosen as the smallest integer label of the ordered states that satisfies:

$$\frac{\sum_{i=0, y_i \neq y_j}^{j'} R_{y_i y_j}}{\sum_{y \neq y_j} R_{yy_j}} > \xi_2 \quad (5.37)$$

where ξ_2 is sampled uniformly in the interval $(0, 1]$.

5.7.2 Virtual jumps

Virtual jumps occur when a new bit arrives. Specifically, if $y = (x_j, b_n)$ at time $t \in (n\tau, (n+1)\tau)$, and if $t + \Delta t > (n+1)\tau$, then instead of generating a jump using Eq. (5.37), a new bit state is generated at time $(n+1)\tau$.

The new incoming bit is sampled with probability p_0 (p_1) to be in state $b_{n+1} = 0$ ($b_{n+1} = 1$), the state y is updated to $y_{j'} \equiv (x_j, b_{n+1})$, and the time is set to $t = (n+1)\tau$. We express this

update rule as

$$b_{n+1} = \begin{cases} 0, & \text{with probability } p_0 \\ 1, & \text{with probability } p_1 \end{cases} \quad (5.38)$$

$$y((n+1)\tau) = (x_j, b_{n+1}) \quad (5.39)$$

when $t + \Delta t > (n+1)\tau$. If $b_{n+1} \neq b_n$ then this update constitutes a virtual jump, otherwise the state of y is unchanged.

Chapter 6: Fast-forward shortcuts to adiabaticity in classical Floquet-Hamiltonian systems - angle variable dynamics

The content of this chapter is based on independent research work and is yet to be published.

6.1 Chapter overview

In contrast to the previous chapters, here we do not consider any model of Maxwell's demon. Instead, we consider a situation where the behavior of a time-dependent system with a predefined protocol is modified to achieve a desired behavior without the intervention of an external agent. In the spirit of the discussion on autonomous demons presented in Chapters 1 and 5, we consider the shortcuts-to-adiabaticity (STA) problem [65] discussed here as a form of non-feedback or open-loop control. We investigate STA in classical Floquet (periodic) Hamiltonian systems where the system's dynamics are accelerated while preserving features of the quasistatic dynamics by adding an additional potential to the original Hamiltonian of the system. Among different forms of STA for classical Hamiltonian systems we will focus the discussion of this chapter on flow-field based methods [77, 114]. In this chapter we will extend the fast-forward method of STA to periodically driven Hamiltonian systems in contrast to the protocol presented in the Ref. [77], where a time-dependence of the Hamiltonian is turned on for a finite interval of

time. Additionally it was pointed out in Ref. [77] that the microcanonical measure on the adiabatic energy shell is not preserved under the evolution generated by the fast-forward Hamiltonian unless the system is driven under a scale-invariant protocol. Here we investigate the dynamics of a periodically driven system with a non-scale-invariant protocol and study the angle variable dynamics using tools from chaotic dynamics and ergodic theory [73].

This chapter is organized as follows: in Sec. 6.2 we review shortcuts to adiabaticity for classical Hamiltonian systems, following Refs. [65, 77]. In Sec. 6.3 we set up the theoretical formalism for studying angle variable dynamics under a fast-forward Hamiltonian. In Sec. 6.4 we present numerical studies for the angle variable dynamics for a periodically driven asymmetric double well system, for two sets of parameters illustrating the behavior of the angle variable dynamics with and without fixed points.

6.2 Background: classical flow-field based methods for shortcuts to adiabaticity (STA)

Here we present a brief pedagogical review of flow-field-based methods for classical shortcuts to adiabaticity and also introduce notation and ideas that will be used throughout the chapter. We consider a time-dependent Hamiltonian $H(q, p, t)$ for a one-degree-of-freedom system, of the form

$$H(q, p, t) = \frac{p^2}{2} + U(q, t), \quad (6.1)$$

where time t varies in the window $0 \leq t \leq t_f$ and we have taken mass $m = 1$. We assume that at every time t , there exists a region \mathbb{S}_t in the (q, p) phase space, where the system executes *libration* [70] (periodic motion where the sign of \dot{q} changes), when the dynamics are generated by

the Hamiltonian $H(q, p, t)$ frozen at time t . Additionally, we assume the energy level surfaces of the frozen Hamiltonian $H(q, p, t)$ have the same topology in \mathbb{S}_t , and restrict our choice of initial conditions (which will be discussed later) to this region only.

The *action* [70, 71, 115, 116] $I(q, p, t)$ at any phase space point $(q, p) \in \mathbb{S}_t$ at time t is given by

$$I(q, p, t) = \frac{1}{2\pi} \Omega(H(q, p, t), t), \quad (6.2)$$

where the $\Omega(E, t)$ gives the phase space area enclosed by an energy level surface of energy E corresponding to the Hamiltonian $H(q, p, t)$ frozen at time t , i.e.,

$$\Omega(E, t) = \int_{-\infty}^{\infty} \int_{-\infty}^{\infty} dq' dp' \theta [E - H(q', p', t)], \quad (6.3)$$

with $\theta(x)$ being the Heaviside step function. A trajectory $(q(t), p(t))$ evolving under the Hamilton's equations of motion generated by the time-dependent Hamiltonian $H(q, p, t)$, does not preserve the action, i.e. $I(q(t), p(t), t)$ is not a *constant of motion*. However, for slowly driven systems, the action $I(q(t), p(t), t)$ becomes an *adiabatic invariant* [70, 71, 115] as we explain briefly below.

We define the initial energy shell \mathcal{E}_0 corresponding to energy E_0 , and action I_0 as

$$\mathcal{E}(0) = \{(q, p) \in \mathbb{S}_0 \mid H(q, p, 0) = E_0\}. \quad (6.4)$$

Since the action variable is not a constant of motion, all of the initial conditions in $\mathcal{E}(0)$ will not be mapped to a single level surface of the Hamiltonian $H(q, p, t_f)$, when evolved under the time-dependent Hamiltonian $H(q, p, t)$ for an arbitrary time interval $t = 0$ to $t = t_f$. However,

under an infinitely slow (quasistatic) evolution under the same protocol, i.e., evolution under the slow Hamiltonian $H(q, p, \epsilon t)$ from $t = 0$ to $t = (t_f/\epsilon)$ with $\epsilon \rightarrow 0^+$, the initial energy shell $\mathcal{E}(0)$ gets mapped to the *adiabatic energy shell* $\mathcal{E}(t_f)$:

$$\mathcal{E}(t_f) = \{(q, p) \in \mathbb{S}_{t_f} \mid H(q, p, t_f) = E^{\text{ad}}(t_f)\}, \quad (6.5)$$

Here the adiabatic energy $E^{\text{ad}}(t_f)$ corresponds to the level surface of $H(q, p, t_f)$, that contains the area $2\pi I_0$:

$$\Omega(E^{\text{ad}}(t_f), t_f) = 2\pi I_0. \quad (6.6)$$

We see that the action $I(q(t), p(t), t)$ for any point in $\mathcal{E}(t_f)$ is same the (I_0) as that of any point on initial energy shell $\mathcal{E}(0)$. If the evolution is slow but not infinitely slow, then the action is only approximately preserved, $|I(q(t_f/\epsilon), p(t_f/\epsilon), t_f/\epsilon) - I_0| = \mathcal{O}(\epsilon^2)$. Here action is an adaibatic (quasistatic) invariant.

In Ref. [77], it was shown that, given the Hamiltonian $H(q, p, t)$ and the initial action I_0 (or equivalently initial energy E_0), it is possible to construct *flow-fields* $v(q, t; I_0)$ and $a(q, t; I_0)$, and correspondingly two new STA Hamiltonians: (i) the *local counterdiabatic Hamiltonian* $H_{\text{LCD}}(q, p, t; I_0)$, and (ii) the *fast-forward Hamiltonian* $H_{\text{FF}}(q, p, t; I_0)$, which evolve $\mathcal{E}(0) \rightarrow \mathcal{E}(t_f)$ in any arbitrary time interval $t = 0$ to $t = t_f$, where $\mathcal{E}(t_f)$ is the adiabatic energy shell of $H(q, p, t_f)$. From now onward, throughout this chapter we will drop the parametric dependence on I_0 for the flow-fields and STA Hamiltonian for conciseness, but it is to be understood that flow-fields and the STA Hamiltonians are always defined for a fixed I_0 . The local counterdiabatic

Hamiltonian is defined as

$$H_{\text{LCD}}(q, p, t) = H(q, p, t) + K(q, p, t) \quad (6.7)$$

where $K(q, p, t)$ is defined by the flow field as

$$K(q, p, t) = pv(q, t) \quad (6.8)$$

The fast-forward Hamiltonian is given as

$$H_{\text{FF}}(q, p, t) = H(q, p, t) + U_{\text{FF}}(q, t) \quad (6.9)$$

where $U_{\text{FF}}(q, t)$ is a potential that is defined by the flow field as

$$-\frac{\partial U_{\text{FF}}(q, t)}{\partial q} = a(q, t) \quad (6.10)$$

While both H_{LCD} and H_{FF} evolve the initial energy shell $\mathcal{E}(0)$ to the target energy shell $\mathcal{E}(t_f)$, there is a major difference between the dynamics generated by H_{LCD} and H_{FF} – while evolving under H_{LCD} , the initial conditions that started on $\mathcal{E}(0)$ remain on the instantaneous adiabatic energy shell $\mathcal{E}(t)$ throughout the evolution from $t = 0$ to $t = t_f$; here, the instantaneous energy shell is defined by the condition:

$$\mathcal{E}(t) = \{(q, p) \in \mathbb{S}_t \mid H(q, p, t) = E^{\text{ad}}(t)\} \quad (6.11)$$

with $E^{\text{ad}}(t)$ satisfying

$$\Omega(E^{\text{ad}}(t), t) = 2\pi I_0. \quad (6.12)$$

In contrast, when evolving under H_{FF} , initial conditions taken from $\mathcal{E}(0)$ in general do not remain on the instantaneous adiabatic energy shell $\mathcal{E}(t)$ at intermediate times $t \in (0, t_f)$, but they return to the final target adiabatic energy shell $\mathcal{E}(t_f)$ at $t = t_f$.

In the next section we will investigate shortcuts to adiabaticity in Floquet-Hamiltonian systems using the fast-forward approach. However, the discussion can alternatively be explored through the local counterdiabatic approach. Here we briefly discuss how fast-forward and local counterdiabatic Hamiltonians are related to each other. For any time t , if $(q(t), p(t))$ are evolving under the Hamiltonian $H_{LCD}(q, p, t)$, then we can construct a time dependent canonical transformation of variables from $(q(t), p(t))$ to $(\tilde{q}(t), \tilde{p}(t))$, given by the type-3 generating function [70, 71]:

$$F_3(\tilde{q}, p, t) = -\tilde{q}p - \int_{\tilde{q}_0}^{\tilde{q}} d\tilde{q}' v(\tilde{q}', t) \quad (6.13)$$

and the relations $q = -\frac{\partial F_3}{\partial p}$ and $\tilde{p} = -\frac{\partial F_3}{\partial \tilde{q}}$ with \tilde{q}_0 as an arbitrary constant. With this transformation, it can be shown that the transformed variables $(\tilde{q}(t), \tilde{p}(t))$ evolve under the Hamiltonian $H_{FF}(\tilde{q}, \tilde{p}, t)$. Also, the Hamiltonians $H_{LCD}(q, p, t)$ and $H_{FF}(\tilde{q}, \tilde{p}, t)$ are related to each other by the generating function $F_3(\tilde{q}, p, t)$, as follows [70, 71]:

$$H_{FF}(\tilde{q}, \tilde{p}, t) = H_{LCD}(q, p, t) + \frac{\partial F_3(\tilde{q}, p, t)}{\partial t}. \quad (6.14)$$

In the most general case, \tilde{q}_0 can be chosen as an arbitrary function of time $\tilde{q}_0(t)$, which will give rise to a fast-forward Hamiltonian that differs from H_{FF} by a pure function of time but generates

the same equations of motion. At any time t , there will be a set of points $\mathcal{E}^{\text{FF}}(t)$ in the (\tilde{q}, \tilde{p}) phase space, which is an image of the adiabatic energy shell $\mathcal{E}(t)$ in the (q, p) phase space. Due to the properties of the canonical transformation, $\mathcal{E}^{\text{FF}}(t)$ will also have the same enclosed area as the corresponding adiabatic energy shell $\mathcal{E}(t)$ [70]. Thus for the evolution under $H_{\text{FF}}(\tilde{q}, \tilde{p}, t)$, we have a *local dynamic invariant* $J(\tilde{q}, \tilde{p}, t)$ as,

$$J(\tilde{q}, \tilde{p}, t) = \frac{1}{2\pi} \oint_{\mathcal{E}^{\text{FF}}(t)} \tilde{p} \, d\tilde{q} = I_0 \quad (6.15)$$

for a fixed I_0 at any time $t \in [0, t_f]$. Note that $\mathcal{E}^{\text{FF}}(t)$ is not necessarily located on any energy level surface of the Hamiltonian $H(q, p, t)$, in contrast to $\mathcal{E}(t)$ which always remains on the instantaneous adiabatic energy level surface of $H(q, p, t)$. In the next section we discuss how the fast-forward protocol can be applied to periodically driven systems.

6.3 Theory and methods: dynamical maps and transfer operator

6.3.1 Hamiltonian maps for fast-forward shortcuts to adiabaticity in Floquet systems

In Ref. [77], the fast-forward protocol was developed for a time-dependent Hamiltonian, where the time dependence is turned on for a finite interval of time and then turned off. Here we set up the formalism for investigating the application of the fast-forward protocol to a periodically driven, one-degree-of-freedom, classical Hamiltonian system. We define our system of interest by the Hamiltonian

$$H(q, p, \lambda(t)) = \frac{p^2}{2} + U(q, \lambda(t)) \quad (6.16)$$

In contrast to the discussion in the previous section, in Eq. (6.16) we have introduced the time-dependence in the Hamiltonian implicitly through a parameter $\lambda(t)$, which is a periodic function of time t with the period T :

$$\lambda(t) = \lambda(t + T). \quad (6.17)$$

We assume that the Hamiltonian $H(q, p, \lambda(t))$ and the periodic driving $\lambda(t)$ are continuous and smooth functions of time t , such that all time derivatives of $\lambda(t)$ and $H(q, p, \lambda(t))$ are well defined. This assumption also implies

$$\frac{\partial^n H}{\partial t^n} (q, p, \lambda(t)) = \frac{\partial^n H}{\partial t^n} (q, p, \lambda(t + T)). \quad (6.18)$$

Under Hamiltonian dynamics, the state of a system $z(t) = (q(t), p(t))$ at anytime t is a function of the initial conditions. Hamiltonian dynamics can also be described by Hamiltonian maps (see Refs. [73, 115, 116] for general discussion on Hamiltonian maps). The state of the system (a phase space point)

$$z(t) = (q(t), p(t))$$

is evolved for the time interval t to $t + T$ under the Hamiltonian $H(z, \lambda(t))$, then the evolved state $z(t + T)$ is related to the state $z(t)$ by the Hamiltonian map \mathcal{M}_T as:

$$z(t + T) = \mathcal{M}_T(z(t); t) \quad (6.19)$$

Since we are interested in time-periodic dynamics from $t = nT$ to $t = (n + 1)T$, we can express

the dynamics through a discrete map

$$z_{n+1} = \mathcal{M}_T(z_n), \quad (6.20)$$

where $z_n = z(nT)$, and \mathcal{M}_T stands for the Hamiltonian map generated by $H(z, \lambda(t))$ over the evolution of one period. We have dropped explicit time-dependence in the map \mathcal{M}_T as we are always considering periodic dynamics from the beginning of a time period $t = nT$ to the end of the period $t = (n + 1)T$. Here, \mathcal{M}_T is a two-dimensional invertible nonlinear map, parameterized by the period T . Note that the action is not a conserved quantity under \mathcal{M}_T , i.e., $I(z_n, t = nT) \neq I(z_{n+1}, t = (n + 1)T)$.

We aim to apply a fast-forward potential $U_{FF}(q, \lambda(t))$ to the periodically driven system $H(z, \lambda(t))$ such that a chosen energy shell $\mathcal{E}(t = nT) \equiv \mathcal{E}_n$ with action I_0 and energy E_0 , gets mapped to itself $\mathcal{E}_n \rightarrow \mathcal{E}_{n+1} = \mathcal{E}_n$ under the evolution generated by the fast-forward Hamiltonian

$$H_{FF}(q, p, \lambda(t)) = H(q, p, \lambda(t)) + U_{FF}(q, p, \lambda(t)) \quad (6.21)$$

for any periodic interval $t = nT$ to $t = (n + 1)T$. Similarly to the time-dependent flow-fields discussed in the previous section (and also in Ref.[77]), we introduce two λ -parameterized flow fields $\tilde{v}(q, \lambda)$ and $\tilde{a}(q, \lambda)$. For any given I_0 , the fast-forward potential is related to the flow-fields by

$$\tilde{a}(q, \lambda) = -\frac{\partial U_{FF}(q, \lambda)}{\partial \lambda}. \quad (6.22)$$

We denote the periodic Hamiltonian map for the evolution generated by the fast-forward Hamiltonian $H_{FF}(q, p, \lambda(t))$ from time $t = nT$ to $t = (n + 1)T$ as $\mathcal{M}_T^{FF}[I_0]$. Here, the I_0 in the square

bracket signifies that the $U_{FF}(q, p, \lambda(t))$ has been constructed for the the energy shell corresponding to the action I_0 (and adiabatic energy E_0). Evolution of the phase space point z_n under this Hamiltonian map is given as

$$z_{n+1} = \mathcal{M}_T^{FF}[I_0](z_n). \quad (6.23)$$

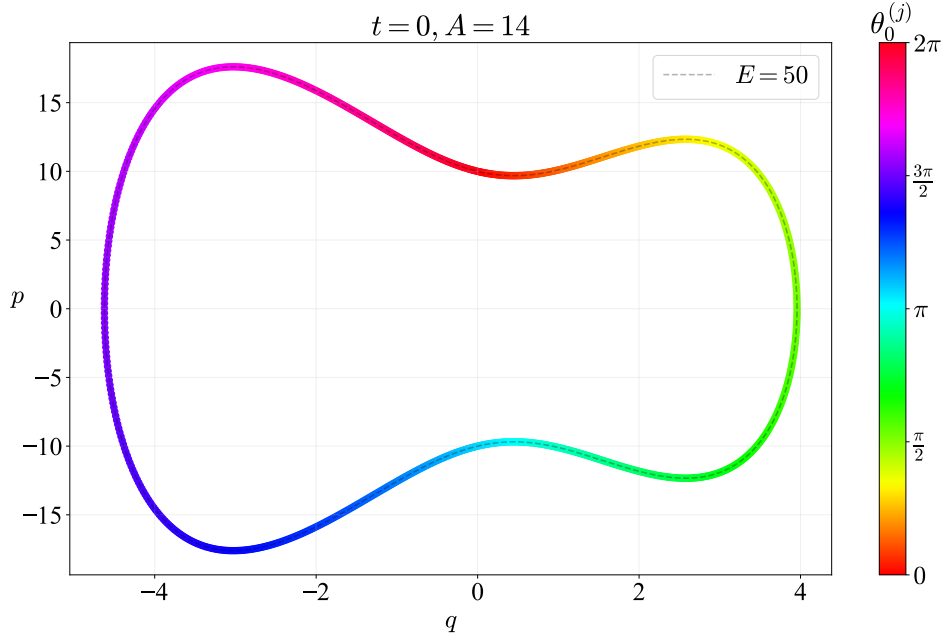
The evolved point z_{n+1} lands on the adiabatic energy \mathcal{E}_{n+1} if the initial condition $z_n \in \mathcal{E}_n$. Here, $\mathcal{M}_T^{FF}[I_0]$ is an invertible two-dimensional nonlinear stroboscopic map that evolves every point in the full (q, p) phase space for one time period T , and also has a special property that the adiabatic energy shell \mathcal{E}_n gets mapped to itself: $\mathcal{E}_{n+1} = \mathcal{E}_n$.

6.3.2 One-dimensional angle map ($\Theta_{T,[I_0]}^{FF}$) for dynamics on preserved energy shell

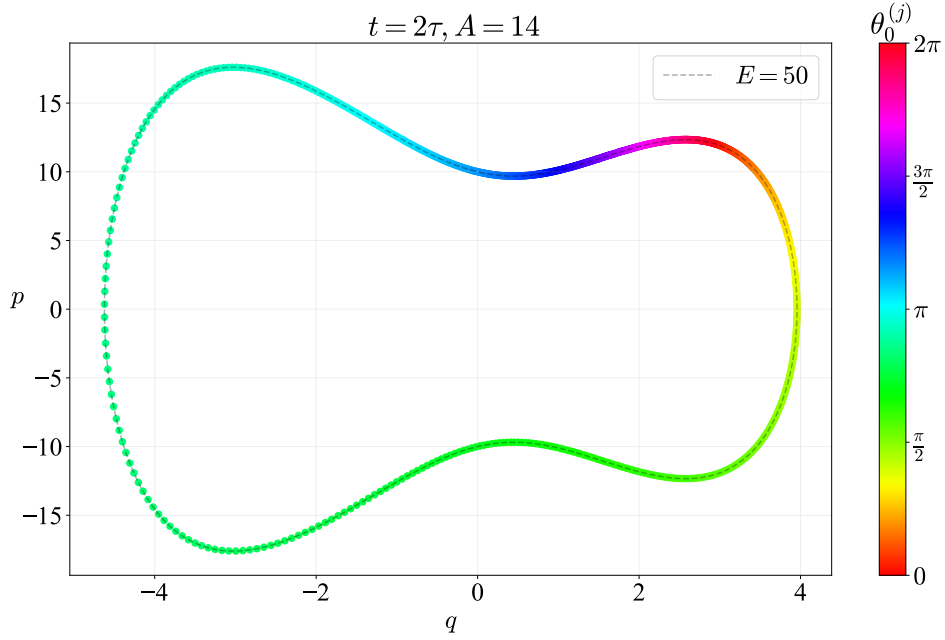
Next, we will introduce a one-dimensional map [72, 73, 115] for studying the dynamics of the angle variable on the energy shell \mathcal{E}_n under the evolution by $\mathcal{M}_T^{FF}[I_0]$. We consider the canonical transformation of $z_n \equiv (q_n, p_n)$ to the action-angle variables $y_n \equiv (\theta_n, I_n)$, which is given by the type-2 generating function [70, 71]

$$F_2(I_n, q_n) = \int_{q_n^{(\min)}}^{q_n} dq \bar{p}(q, I_n) \quad (6.24)$$

and the relations $p_n = \frac{\partial F_2}{\partial q}$, $\theta_n = \frac{\partial F_2}{\partial I}$ where $\theta_n \in [0, 2\pi)$. Here the function $\bar{p}(q, I)$ is implicitly defined by $H(q, \bar{p}, \lambda(nT)) = E^{\text{ad}}(nT)$ and $\Omega(E^{\text{ad}}(nT), nT) = 2\pi I$; and $q_n^{(\min)}$ is the left turning point of the adiabatic energy shell \mathcal{E}_n , i.e., $q_n^{(\min)} = \min_{q'} \{q' \mid \bar{p}(q', I_n) = 0\}$. Under this canonical coordinate transformation ($y_n = g(z_n)$), the two-dimensional periodic evolution map



(a) Initial energy shell



(b) Final energy shell

Figure 6.1: Evolution of the energy shell $\mathbf{S}_0 = \{\theta_0^{(j)} | j = 1, \dots, M\}$ to $\mathbf{S}_1 = \{\theta_1^{(j)} | j = 1, \dots, M\}$ for $A = 14$, $\tau = 1$ and adiabatic energy $E = 50$. We have taken $M = 1000$ here. The points in \mathbf{S}_0 are microcanonically distributed, i.e., uniformly spaced in the angle variables $\theta_0^{(j)}$ from 0 to 2π . The evolution under H_{FF} is done using a symplectic integrator of fourth-order with time step $\delta t = 10^{-6}$.

$\mathcal{M}_T^{FF}[I_0]$ transforms to the conjugate map $\tilde{\mathcal{M}}_T^{FF}[I_0] = g \circ \mathcal{M}_T^{FF}[I_0] \circ g^{-1}$ in the new action-angle coordinates [73], and we have:

$$\begin{aligned} y_{n+1} &= \tilde{\mathcal{M}}_T^{FF}[I_0](y_n) \\ &= \tilde{\mathcal{M}}_T^{FF}[I_0](\theta_n, I_n) \end{aligned} \tag{6.25}$$

Now we fix $I_n = I_0$ in the Eq. (6.25) to obtain the one-dimensional angle map on the adiabatic energy shell as $\Theta_{T,[I_0]}^{FF}(\theta) \equiv \tilde{\mathcal{M}}_T^{FF}[I_0](\theta, I = I_0)$. This angle map gives periodic evolution of the angle variable θ_n for the fixed action $I_n = I_0$, i.e.,

$$\theta_{n+1} = \Theta_{T,[I_0]}^{FF}(\theta_n) \tag{6.26}$$

6.3.3 Transfer operators for the evolution of the angle variable distribution

We can study the angle variable dynamics on the preserved energy shell by the transfer operator method [117]. Suppose we randomly sample a set of M angle variables $\mathbf{S}_n = \{\theta^{(i)}\}_{i=1,\dots,M}$ at $t = nT$, from the energy shell \mathcal{E}_n according to the probability density function $\eta_n(\theta)$ where $\theta \in [0, 2\pi)$; and evolve these points with the map $\Theta_{T,[I_0]}^{FF}$ to obtain the new set $\mathbf{S}_{n+1} = \Theta_{T,[I_0]}^{FF}(\mathbf{S}_n)$. If the points in the set \mathbf{S}_{n+1} are now distributed according to the probability density function $\eta_{n+1}(\theta)$, then $\eta_{n+1}(\theta)$ is obtained from $\eta_n(\theta)$ by the *transfer operator* or the *Ruelle-Perron-Frobenius* operator for the fast-forward dynamics $\hat{\mathcal{P}}_{T,[I_0]}^{FF}$:

$$\eta_{n+1}(\theta) = \hat{\mathcal{P}}_{T,[I_0]}^{FF} \eta_n(\theta) \tag{6.27}$$

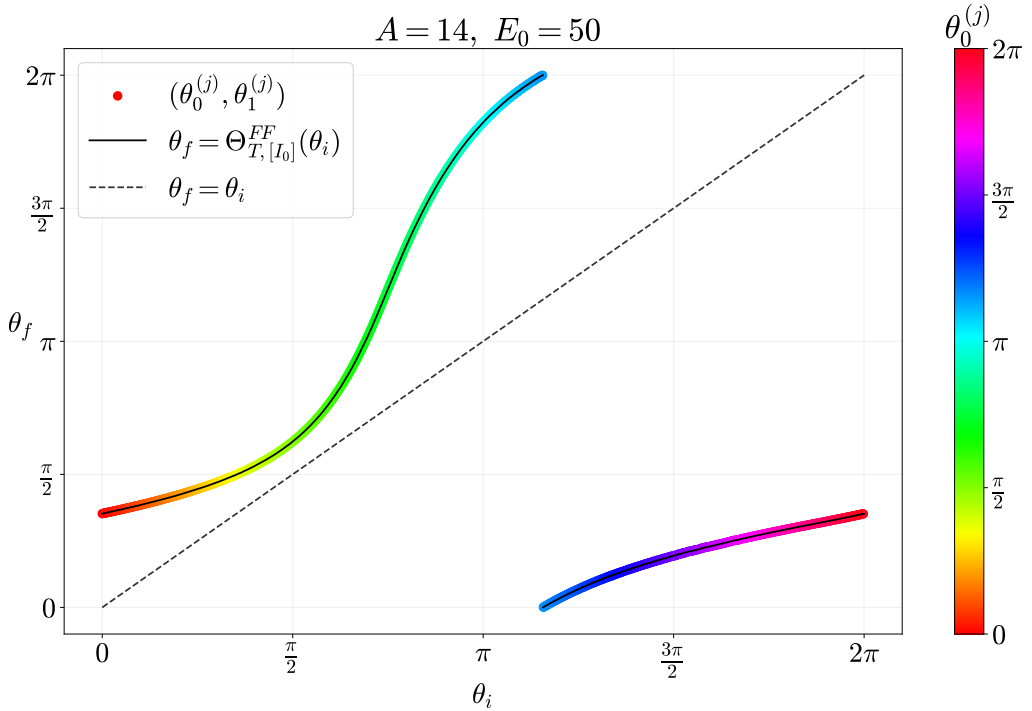


Figure 6.2: Angle variable map $\theta_f = \Theta_{T,[I_0]}^{FF}(\theta_i)$, corresponding to the energy shell evolution shown in Fig. 6.1. θ_i is the initial angle coordinate and θ_f is the final angle coordinate. The angle map $\Theta_{T,[I_0]}^{FF}$ has been constructed from the points $(\theta_0^{(j)}, \theta_1^{(j)})$ which are also plotted with the color representing the initial location $\theta_0^{(j)}$. The identity map $\theta_f = \theta_i$ is also shown using the dotted line. Since $\theta_f = \Theta_{T,[I_0]}^{FF}(\theta_i)$ does not intersect $\theta_f = \theta_i$, there is no fixed point under the evolution of the map $\Theta_{T,[I_0]}^{FF}(\theta_i)$ for the parameters $A = 14, E_0 = 50$.

The action of the operator $\hat{\mathcal{P}}_{T,[I_0]}^{FF}$ in Eq. (6.27) can be expressed as the integral equation

$$\eta_{n+1}(\theta) = \int_0^{2\pi} d\theta' \delta(\theta - \Theta_{T,[I_0]}^{FF}(\theta')) \eta_n(\theta') \quad (6.28)$$

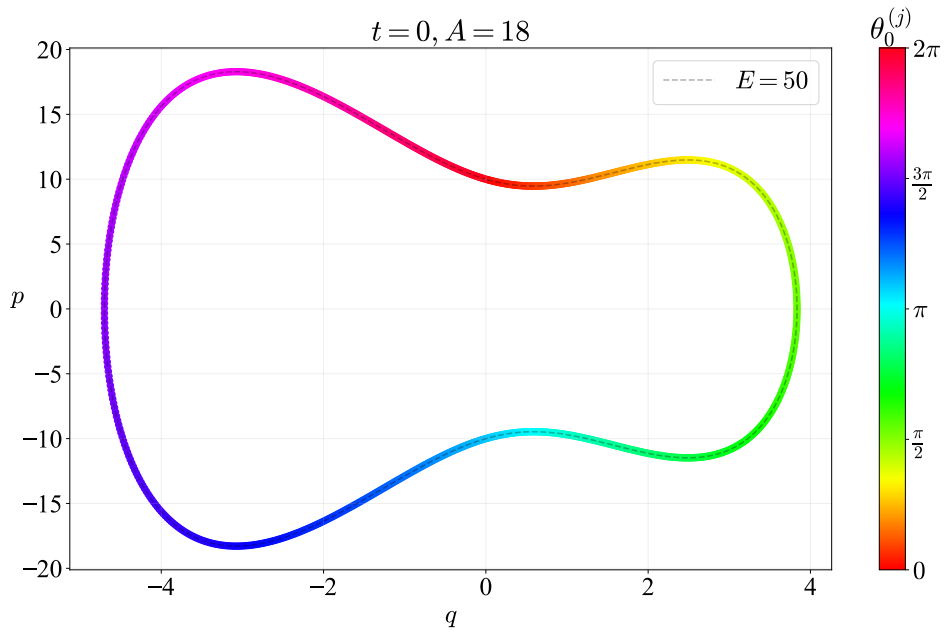
Eq. (6.28) is known as the *Frobenius-Perron equation* [73]. Since $\Theta_{T,[I_0]}^{FF}$ is a bijective mapping, we can write Eq.. (6.27) or Eq. (6.28) with the inverse function of $\Theta_{T,[I_0]}^{FF}$ as

$$\eta_{n+1}(\theta) = \frac{\eta_n(\theta_f^{-1}(\theta))}{\left| \partial \Theta_{T,[I_0]}^{FF}(\theta_f^{-1}(\theta)) \right|} \quad (6.29)$$

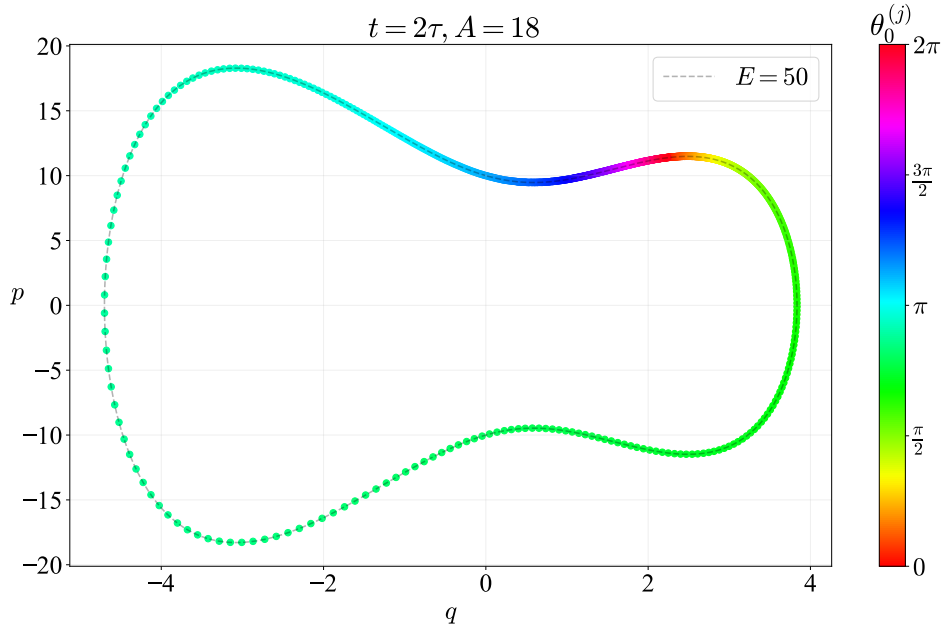
where $(\Theta_{T,[I_0]}^{FF})^{-1} \equiv \theta_f^{-1}$ is the inverse function of $\Theta_{T,[I_0]}^{FF}$, and $\partial \Theta_{T,[I_0]}^{FF}$ stands for the derivative function of $\Theta_{T,[I_0]}^{FF}$. Eq. (6.29) allows us to evolve the density $\eta_n(\theta')$ to $\eta_{n+1}(\theta)$ when the functions $\partial \Theta_{T,[I_0]}^{FF}$ and θ_f^{-1} are known, and thus provides a method of iteratively evolving an angle variable density with the Perron-Frobenius operator $\hat{\mathcal{P}}_{T,[I_0]}^{FF}$. The *invariant density* [73, 117] of the map $\Theta_{T,[I_0]}^{FF}$ is given as $\eta_s(\theta)$ which is an eigenfunction of the Perron-Frobenius operator with eigenvalue 1 :

$$\hat{\mathcal{P}}_{T,[I_0]}^{FF} \eta_s(\theta) = \eta_s(\theta) \quad (6.30)$$

We also point out that the adjoint (dual) to the Perron-Frobenius operator $\hat{\mathcal{P}}_{T,[I_0]}^{FF}$ is known as the *Koopman operator* [117, 118], which gives the composition of a function with the map $\Theta_{T,[I_0]}^{FF}$ and is often used in the control theory and engineering literature.



(a) Initial energy shell



(b) Final energy shell

Figure 6.3: Evolution of the energy shells. Parameters are same as Fig. 6.1 except with $A = 18$.

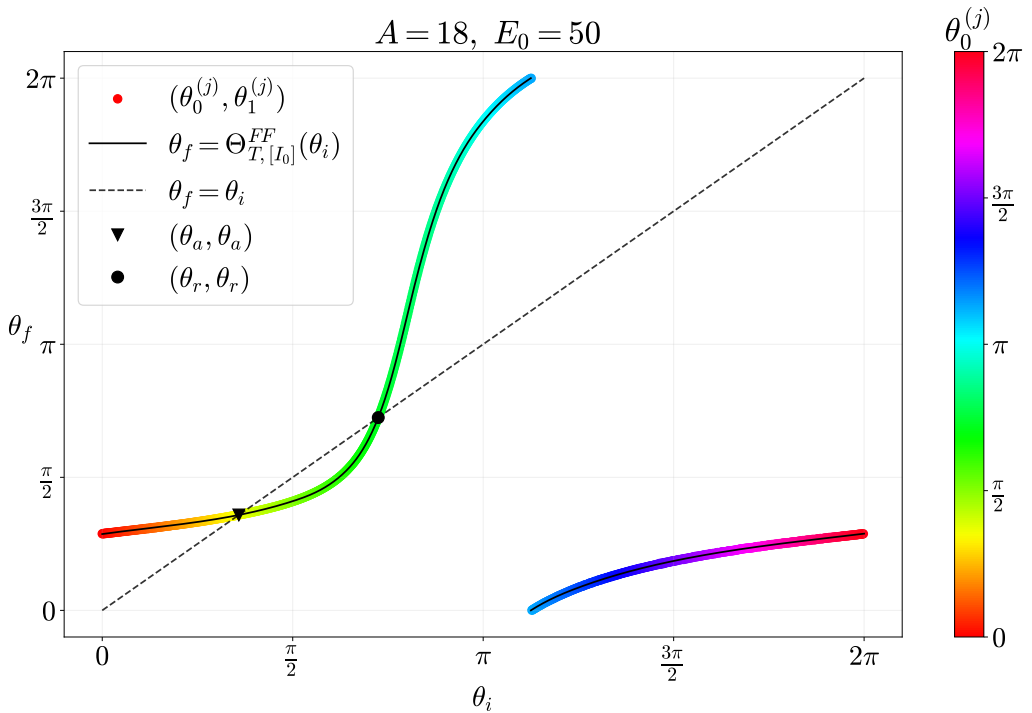


Figure 6.4: Angle variable map $\theta_f = \Theta_{T,[I_0]}^{FF}(\theta_i)$, corresponding to the energy shell evolution shown in Fig. 6.3. Here, $\theta_f = \Theta_{T,[I_0]}^{FF}(\theta_i)$ intersects $\theta_f = \theta_i$ at two points: (θ_a, θ_a) and (θ_r, θ_r) . Thus there are two fixed points under the evolution of the map $\Theta_{T,[I_0]}^{FF}(\theta_i)$ for the parameters $A = 18, E_0 = 50$. Here we have $|\partial\Theta_{T,[I_0]}^{FF}(\theta_a)| < 1$ and $|\partial\Theta_{T,[I_0]}^{FF}(\theta_r)| > 1$, hence θ_a (θ_r) is an attracting (repelling) or stable (unstable) fixed point of the map $\Theta_{T,[I_0]}^{FF}$.

6.3.4 Transition probability matrix and evolution of probability distributions on the energy shell

Instead of dealing with probability densities and Eq. (6.27), we discretize the angle variable space and investigate the evolution of a probability measure in this discretized space following *Ulam's method* [117]. We discretize the angle variable space $[0, 2\pi)$ into $K \gg 1$ bins of uniform size $(2\pi/K)$ and label them $j = 0, \dots, K - 1$, and construct a histogram, represented by a probability vector $\vec{P}_n = [P_0(nT), P_1(nT), \dots, P_{K-1}(nT)]^T$. Here, $P_j(nT)$ represents the probability that a point is in the j th bin, when it has been sampled from the distribution $\eta_n(\theta)$:

$$P_j(nT) = \int_{2\pi j/K}^{2\pi(j+1)/K} d\theta \eta_n(\theta). \quad (6.31)$$

Now we define the transition probability T_{ij} from the j th bin to the i th bin, as the probability of a randomly sampled point from a uniform distribution ($u_j(\theta)$) over the j th bin:

$$u_j(\theta) = \begin{cases} \frac{K}{2\pi}, & \frac{2\pi j}{K} \leq \theta < \frac{2\pi(j+1)}{K} \\ 0, & \text{otherwise} \end{cases} \quad (6.32)$$

to land in the i th bin, when evolved under the map $\Theta_{T,[I_0]}^{FF}$. Hence, we have

$$\begin{aligned} T_{ij} &= \int_{2\pi i/K}^{2\pi(i+1)/K} d\theta \hat{\mathcal{P}}_{T,[I_0]}^{FF} u_j(\theta) \\ &= \int_{2\pi i/K}^{2\pi(i+1)/K} \frac{d\theta u_j(\theta_f^{-1}(\theta))}{\left| \partial \Theta_{T,[I_0]}^{FF}(\theta_f^{-1}(\theta)) \right|}. \end{aligned} \quad (6.33)$$

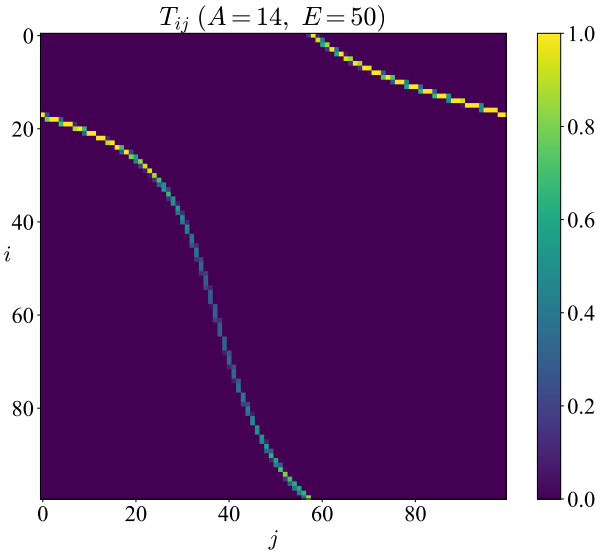
Collecting transition probabilities T_{ij} in a matrix form we construct the *transition probability matrix* \mathbf{T} . For large enough K , the distribution $u_j(\theta)$ approaches a delta function distribution, and in that case the matrix \mathbf{T} can be used to visualize the Kernel of the operator $\hat{\mathcal{P}}_{T,[I_0]}^{FF}$. From the Perron-Frobenius theorem we know that there is an invariant probability vector \vec{P}_s which corresponds to the Perron-Frobenius eigenvalue $s^{PF} = 1$ for the matrix \mathbf{T} , and any starting distribution \vec{q} converges to it under the dynamics generated by \mathbf{T} .

$$\lim_{n \rightarrow \infty} \mathbf{T}^n \vec{q} = \vec{P}_s, \quad \mathbf{T} \vec{P}_s = \vec{P}_s, \quad \forall \vec{q} \quad (6.34)$$

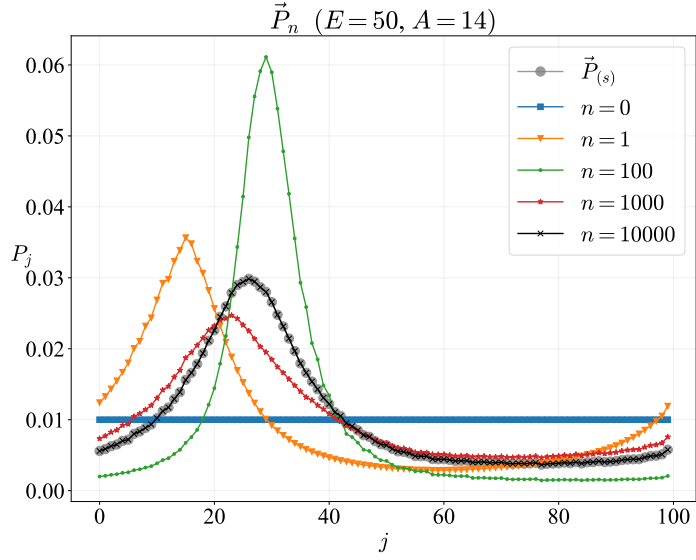
The eigenspectrum $\{s_i\}_{i=1,\dots,K}$ of the matrix \mathbf{T} gives us information about the relaxation rate to the invariant distribution for different eigenvectors of \mathbf{T} . A zero eigenvalue implies instantaneous decay of an eigenmode. For non-zero eigenvalues, smaller values of $|s_i|$ imply faster convergence towards \vec{P}_s , and $|s_i| \approx 1$ implies metastable eigenmodes, which take a long time to decay, and non-zero $\text{Im}\{s_i\}$ implies the cyclic nature of the eigenmode [119].

6.4 Toy model system

In this section we discuss the angle-variable dynamics and its statistical properties by numerically investigating a toy model. Our toy model uses the same asymmetric double well potential as Ref. [77] with a driving that is now periodic in time.

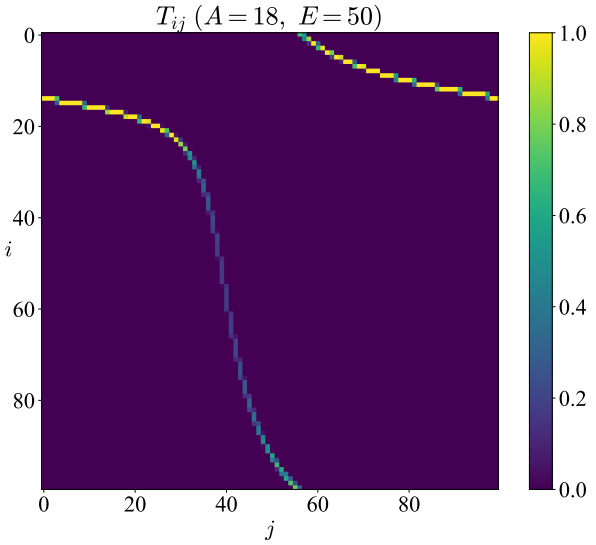


(a) Transition Matrix

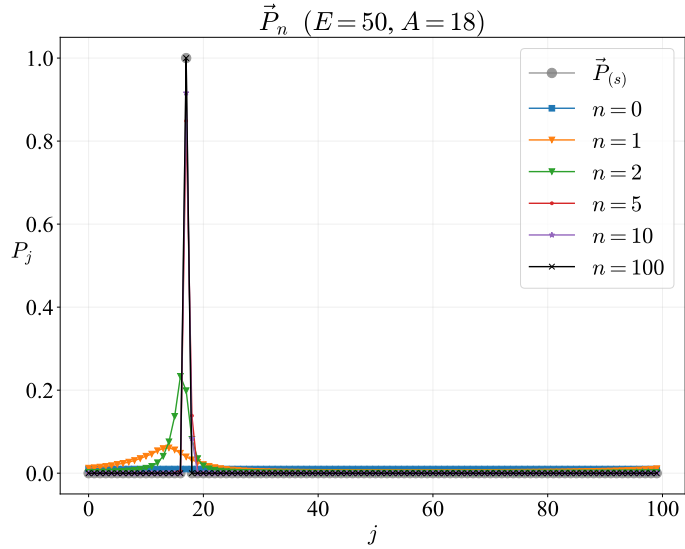


(b) Probability distribution on preserved energy shell

Figure 6.5: The Fig. 6.5a shows the transition probability matrix \mathbf{T} and the Fig. 6.5b shows the evolution of probability distribution $\vec{P}_n = [P_j(nT)]_{j=0,\dots,K-1}^T$ under the transition probability matrix \mathbf{T} ; for parameters $A = 14$, $\tau = 1.0$ and energy shell $E = 50$. We have created $K = 100$ bins and the index $j = 0, \dots, K - 1$ is used for the label of the bins. The starting distribution for the evolution is taken as the uniform $P_j(0) = (1/K)$. The evolved distribution $\vec{P}_n = \mathbf{T}^n \vec{P}_0$ are plotted. The stationary distribution \vec{P}_s has been calculated by solving $\mathbf{T}\vec{P}_s = \vec{P}_s$.



(a) Transition Matrix



(b) Probability distribution on preserved energy shell

Figure 6.6: The Fig. 6.6a shows the transition probability matrix \mathbf{T} and the Fig. 6.6b shows the evolution of probability distribution $\vec{P}_n = [P_j(nT)]_{j=0,\dots,K-1}^T$ under the transition probability matrix \mathbf{T} ; for parameters $A = 18$, $\tau = 1.0$ and energy shell $E = 50$. We have created $K = 100$ bins and the index $j = 0, \dots, K - 1$ is used for the label of the bins. The starting distribution for the evolution is taken as the uniform $P_j(0) = (1/K)$. The evolved distribution $\vec{P}_n = \mathbf{T}^n \vec{P}_0$ are plotted. The stationary distribution \vec{P}_s has been calculated by solving $\mathbf{T}\vec{P}_s = \vec{P}_s$. The stationary distribution $\vec{P}_s = [\delta_{jj^*}]_{j=0,\dots,K-1}^T$, where j^* is the index for the bin containing the attractive fixed point θ_a .

6.4.1 Setup: periodically driven asymmetric double well

We consider a one-dimensional (1D) periodically driven double well system given by the Hamiltonian $H(q, p, \lambda(t))$, which corresponds to evolution under the potential

$$U(q, \lambda(t)) = q^4 - 16q^2 + \lambda(t)q, \quad (6.35)$$

with the driving protocol:

$$\lambda(t; A, \tau) = A \cos\left(\frac{t\pi}{\tau}\right). \quad (6.36)$$

The parameter A controls the strength of the driving and τ controls the speed of the driving. To ensure the existence of the double well landscape of the potential at all time, we impose a restriction: $A \in \left(-\frac{128}{3}\sqrt{\frac{2}{3}}, \frac{128}{3}\sqrt{\frac{2}{3}}\right)$, which approximately corresponds to $-34.8372 < A < 34.8372$. This constraint also bounds the value of $\lambda(t)$ for any time t , since $|\lambda(t)| \leq |A|$ for the choice of our protocol. For any $\lambda \in [-A, A]$, there are three stationary points in the double well: two minima corresponding to the left and right wells, $q_{\min}^L(\lambda)$ and $q_{\min}^R(\lambda)$, and a central maximum $q_{\max}^C(\lambda)$. The period of the driving is $T = 2\tau$ and thus smaller (larger) τ corresponds to faster (slower) external driving. The dynamics under our choice of $H(z, \lambda(t))$ can be understood as a particle executing motion under a driven double well potential where the depths of the wells of the oscillator are periodically shifting due to an oscillatory slope in the linear term. At any time t , the phase portrait corresponding to the frozen Hamiltonian $H(z, \lambda(t))$ has three different regions separated by two *homoclinic orbits*, which meet at the fixed point $z = (q_{\max}^C(\lambda), 0)$. The separatrix energy is given as $E^{\text{sep}}(\lambda) = H(q_{\max}^C(\lambda), 0, \lambda)$. The energy level surface $\mathcal{E}_{\text{sep}}(\lambda) = \{z | H(z, \lambda) = E^{\text{sep}}(\lambda)\}$ acts as the *separatrix* creating a division between the topologically different regions of

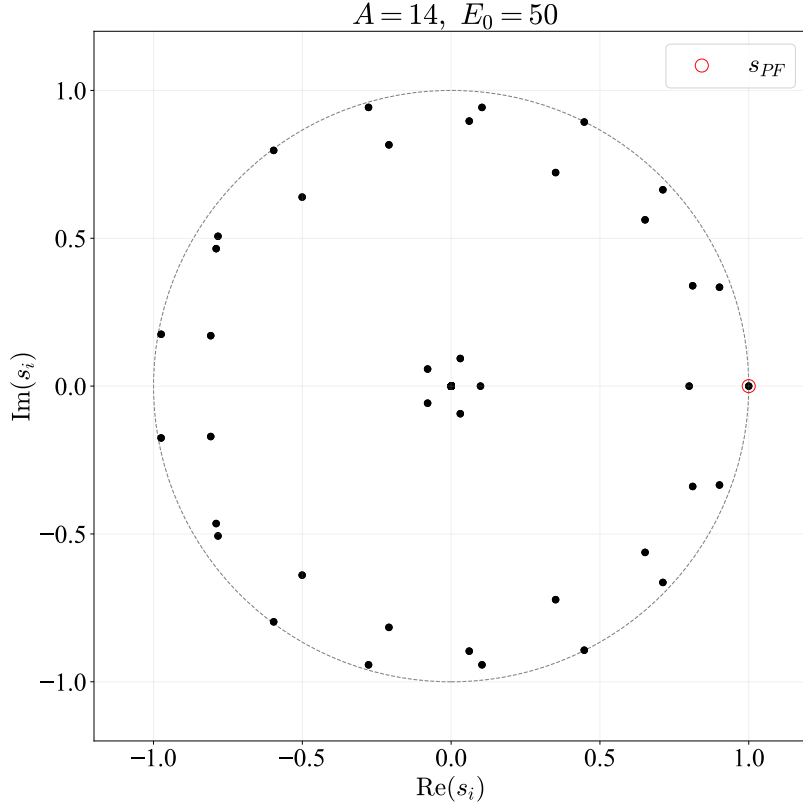


Figure 6.7: Eigenvalues $\{s_i\}_{i=1,\dots,K}$ of \mathbf{T} is shown for the case with no fixed point $E_0 = 50$, $A = 14$. The Perron-Frobenius eigenvalue $s_{PF} = 1$ is highlighted with a red circle. Total $K = 100$ eigenvalues are plotted. The observed number of eigenvalues in the plot appear less than K due to degeneracy and near degeneracy of eigenvalues. Eigenvalues with $|s_i| \approx 1$ correspond to the metastable modes of the dynamics that take.

the phase space [70].

Now, we choose the energy E_0 and corresponding action I_0 , such that $E^{\text{ad}}(\lambda(t)) > E^{\text{sep}}(\lambda(t))$ at any time t (See Appendix. 6.5 for the details of calculation of $E^{\text{ad}}(\lambda(t))$). This condition ensures that we are always in the libration region of phase space and throughout the variation of the control parameter $\lambda(t)$, no change in phase space topology takes place for the dynamics under consideration. The fast-forward potential is calculated using standard methods [77] for the Hamiltonian given in Eq. (6.16) (see Appendix. 6.6).

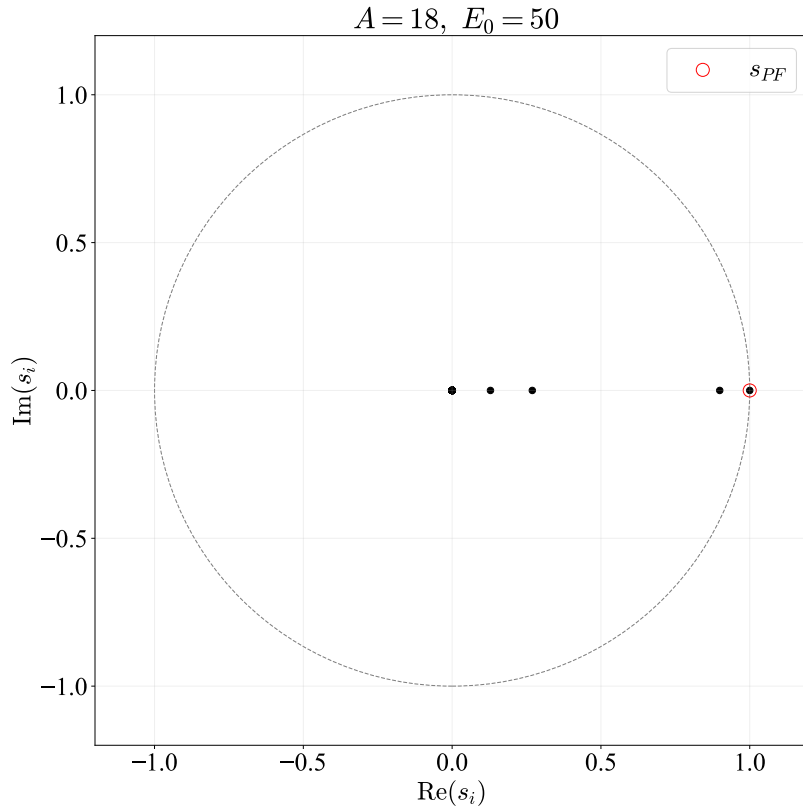


Figure 6.8: Eigenvalues $\{s_i\}_{i=1,\dots,K}$ of \mathbf{T} is shown for the case with fixed points $E_0 = 50, A = 18$. The Perron-Frobenius eigenvalue $s_{PF} = 1$ is highlighted with a red circle. Total $K = 100$ eigenvalues are plotted. The observed number of eigenvalues in the plot appear less than K due to degeneracy and near degeneracy of eigenvalues. Absence of eigenvalues with $|s_i| \approx 1$ implies that the dynamics relaxes to the stationary state quickly. Eigenvalues are real indicating absence of the cyclic modes in the dynamics.

6.4.2 Discussion: preserved energy shell as a heteroclinic connection and invariant distributions

We investigate the properties of the angle map $\Theta_{T,[I_0]}^{FF}$ and corresponding evolution of distributions on the energy shell under fast-forward Floquet driving for two sets of parameters that show qualitatively different types of behaviors. Fig. 6.1 shows the evolution of the energy shell \mathcal{E}_n to \mathcal{E}_{n+1} corresponding to the adiabatic energy $E_0 = 50$ under the evolution by the Hamiltonian H_{FF} for one period $T = 2\tau$, with $\tau = 1.0, A = 14$. The corresponding angle map $\Theta_{T,[I_0]}^{FF}$ is shown in the Fig. 6.2. Similarly the energy shell evolution and the corresponding angle maps for the parameters $A = 18, E_0 = 50$ are shown in Fig. 6.3 and Fig. 6.4. The time integration of the Hamiltonian dynamics are performed with a fourth order symplectic integrator [120]. We see that in the case of $A = 14$ (Fig. 6.2) there is no fixed point in the map $\Theta_{T,[I_0]}^{FF}$, whereas for $A = 18$ (Fig. 6.4), two fixed point θ_a and θ_r are created through a *tangent bifurcation* [73]. θ_a is an attractive fixed point and, θ_r is a repulsive fixed point. Now, if we consider the corresponding two dimensional map $\tilde{\mathcal{M}}_T^{FF}[I_0]$ or equivalently $\mathcal{M}_T^{FF}[I_0]$ for $E_0 = 50$, (and $\lambda(t)$ with $A = 18$ and $\tau = 1.0$) we can see that any randomly sampled point on the energy shell for $E_0 = 50$, will approach the attractive fixed point z_a in the phase space corresponding to the angle variable θ_a , as the number of iterations of the map $n \rightarrow \infty$. Similarly any randomly sampled point on the energy shell $E_0 = 50$ will approach to the the phase space fixed point z_r which corresponds to angle variable θ_r when iterated by the inverse map $\mathcal{M}_T^{FF}[I_0]^{-1}$ when $n \rightarrow \infty$. Hence, the points on the energy shell $E_0 = 50$ here act as the *stable manifold* $W^s(z_a)$ for the fixed point z_a and as an *unstable manifold* $W^u(z_r)$ for the fixed point z_r [73]. Hence the energy shell corresponding to $E_0 = 50$ for H here, has been converted to a *heteroclinic connection* [73], through the applica-

tion of the fast-forward potential U_{FF} . A similar creation of a heteroclinic connection has been discussed in Ref. [121] for a particle on a ring system in the context of an Hamiltonian erasure.

Now, we discuss the evolution of a probability distribution on the energy shell under periodic driving following the theory presented in Secs. 6.3.3 and 6.3.4. We discretized the energy shell into uniform $K = 100$ bins in the angle variable. The transition matrix \mathbf{T} and the evolution of the probability vector \vec{P}_n , for an initial distribution of microcanonical measure (uniform distribution in angle variable), is shown in Fig. 6.5 and Fig. 6.6 for dynamics with no-fixed point ($A = 14$) and with fixed point ($A = 18$) respectively. For $A = 18$, in Fig. 6.6, we see that the distribution \vec{P}_n approaches the invariant distribution \vec{P}_s where only the bin with the attractive fixed point θ_a is populated whereas for $A = 14$, in Fig. 6.5 we see all the bins have some population at the steady state. We also see that for the case with the fixed point $A = 18$, the distribution \vec{P}_n converges to \vec{P}_s rapidly compared to the case without the fixed point $A = 14$. This can be understood by looking at the eigenspectrum of the transition probability matrix \mathbf{T} shown in Fig. 6.7 and Fig. 6.8. For $A = 14$, we find there are many eigenvalues with $|s_i| \approx 1$ (see Fig. 6.7), corresponding to metastable modes that take many iterations to decay, and the complex nature of the eigenvalues implies the cyclic nature of these metastable modes, whereas for $A = 18$ we find that the eigenvalues with non-zero $|s_i|$ have eigenvalues that are real and lie in $(0, 1)$ but not close to 1 (see Fig. 6.8), implying the existence of non-cyclic transient structures [119].

6.5 Appendix: Calculation of the adiabatic energy

For the parameter-dependent Hamiltonian $H(q, p, \lambda)$, the volume enclosed by the energy shell E is given as

$$\Omega(E, \lambda) = \int_{-\infty}^{\infty} \int_{-\infty}^{\infty} dq' dp' \theta [E - H(q', p', \lambda)], \quad (6.37)$$

For an infinitesimal change $\lambda \rightarrow \lambda + \delta\lambda$ and $E \rightarrow E + \delta E$, with the constraint of volume phase space area preservation, $\Omega(E, \lambda) = \Omega(E + \delta E, \lambda + \delta\lambda)$, we can write the cyclic rule for partial derivatives as

$$\left(\frac{\partial E}{\partial \lambda} \right)_{\Omega} = - \frac{(\partial \Omega / \partial \lambda)_E}{(\partial \Omega / \partial E)_{\lambda}} \quad (6.38)$$

Now we introduce the notation $\Sigma(E, \lambda)$ for the energy differential of the phase space area $\Omega(E, \lambda)$ at a fixed λ :

$$\Sigma(E, \lambda) = \left(\frac{\partial \Omega}{\partial E} \right)_{\lambda} = \int_{-\infty}^{\infty} \int_{-\infty}^{\infty} dq' dp' \delta [E - H(q', p', \lambda)] \quad (6.39)$$

Thus we can rewrite Eq. (6.38) as

$$\begin{aligned} \left(\frac{\partial E}{\partial \lambda} \right)_{\Omega} &= - \frac{1}{\Sigma(E, \lambda)} \left[\frac{\partial}{\partial \lambda} \int_{-\infty}^{\infty} \int_{-\infty}^{\infty} dq' dp' \theta [E - H(q', p', \lambda)] \right] \\ &= \frac{1}{\Sigma(E, \lambda)} \int_{-\infty}^{\infty} \int_{-\infty}^{\infty} dq' dp' \delta [E - H(q', p', \lambda)] \left(\frac{\partial H(q', p', \lambda)}{\partial \lambda} \right) \\ &= \left\langle \frac{\partial H(q', p', \lambda)}{\partial \lambda} \right\rangle_{E^{\text{ad}}(\lambda)}^{(\mu)}, \end{aligned} \quad (6.40)$$

where $\langle \dots \rangle_{E^{\text{ad}}(\lambda)}^{(\mu)}$ stands for the microcanonical average on the energy-shell corresponding to the adiabatic energy $E^{\text{ad}}(\lambda)$. Eq. 6.40 can be viewed as a classical analogue of the *Feynman-Hellman theorem* of quantum mechanics. Now if the initial value of λ is λ_0 , and the adiabatic energy is

$E^{\text{ad}}(\lambda_0) = E_0$, we can use the equation above to solve an initial value problem to obtain the adiabatic energy $E^{\text{ad}}(\lambda)$ at any arbitrary λ :

$$E^{\text{ad}}(\lambda) = E_0 + \int_{\lambda_0}^{\lambda} d\lambda' \left\langle \frac{\partial H(q, p, \lambda)}{\partial \lambda} \right\rangle_{E^{\text{ad}}(\lambda')}^{(\mu)}. \quad (6.41)$$

Since we are considering a one-degree-of-freedom system, we can estimate the microcanonical average $\left\langle \frac{\partial H(q', p', \lambda)}{\partial \lambda} \right\rangle_{E^{\text{ad}}(\lambda)}^{(\mu)}$ by calculating the time-average of the observable $\frac{\partial H(q', p', \lambda)}{\partial \lambda}$ by evolving a trajectory [120] for one period, under the frozen Hamiltonian $H(q', p', \lambda) = E^{\text{ad}}(\lambda)$. Now for the double well potential given in Eq. (6.35), we have $\left\langle \frac{\partial H(q', p', \lambda)}{\partial \lambda} \right\rangle_{E^{\text{ad}}(\lambda)}^{(\mu)} = \langle q' \rangle_{E^{\text{ad}}(\lambda)}^{(\mu)}$, and we estimate $E^{\text{ad}}(\lambda + d\lambda)$ by calculating the time average of the position of the particle by evolving a trajectory for every of $E^{\text{ad}}(\lambda)$ and then use an Euler update:

$$E^{\text{ad}}(\lambda + d\lambda) = E^{\text{ad}}(\lambda) + \langle q' \rangle_{E^{\text{ad}}(\lambda)}^{(\mu)} d\lambda \quad (6.42)$$

for λ in the range $[A, -A]$.

6.6 Appendix: Calculation of the flow fields

For the calculation of the flow fields $\tilde{a}(q, \lambda)$ and $\tilde{v}(q, \lambda)$, we use the constructions presented in Ref. [77]. For a given value of λ , we first calculate the $E^{\text{ad}}(\lambda)$ using the method discussed in Appendix 6.5. Once $E^{\text{ad}}(\lambda)$ is obtained, we find the left turning point $q_{\text{ad}}^L(\lambda) = \min_{q'} \{q' | H(q', p', \lambda) = E^{\text{ad}}(\lambda)\}$ for the adiabatic energy shell $H(q, p, \lambda) = E^{\text{ad}}(\lambda)$. Now we

calculate the function

$$S(q, \lambda) = 2 \int_{q_{\text{ad}}^L(\lambda)}^q dq' \sqrt{2(E^{\text{ad}}(\lambda) - U(q', \lambda))} \quad (6.43)$$

for a set of $L + 1$ uniformly spaced points $q = q_k$, where $k = 0, \dots, L$, with $q_0 = q_{\text{ad}}^L(\lambda)$ and $q_L = q_{\text{ad}}^R(\lambda) = \max_{q'} \{q' | H(q', p', \lambda) = E^{\text{ad}}(\lambda)\}$ and for a fixed value of λ . The corresponding values of $S(q, \lambda)$ at these points are given as $S_k = S(q_k, \lambda)$. We now evaluate the function $q(S, \lambda)$ for $M + 1$ uniformly spaced points $\{S_m\}_{m=0, \dots, M}$ where $S_0 = 0$ and $S_M = 2\pi I_0$ by nearest-neighbor interpolation with the data set $\{(S_k, q_k)\}_{k=0, \dots, L}$. We denote the value of $q(S, \lambda)$ for $\{S_m\}$ by $\{\tilde{q}_m\}$. The flow fields at \tilde{q}_m are defined as

$$\tilde{v}(\tilde{q}_m, \lambda) = \frac{d\tilde{q}_m}{d\lambda}, \quad (6.44)$$

$$\tilde{a}(\tilde{q}_m, \lambda) = \frac{d^2\tilde{q}_m}{d\lambda^2} = \frac{\partial \tilde{v}}{\partial q} \tilde{v} + \frac{\partial \tilde{v}}{\partial \lambda}. \quad (6.45)$$

Now we repeat this set of calculations for $N + 1$ values of uniformly spaced points $\lambda = \lambda_n$ which go from $-A$ to A to evaluate \tilde{v} and \tilde{a} over a grid of values (q_m, λ_n) with $m = 0, \dots, M$ and $n = 0, \dots, N$. We then calculate any arbitrary value of \tilde{v} and \tilde{a} for any given (q, λ) by interpolation using these data sets, where we use nearest-neighbor interpolation for the q axis and linear interpolation for the λ axis. For our calculations, we took $L = M = 4999$ and $N = 1999$.

For time integration of the system, we calculate the explicit time-dependent flow field $a(q, t)$ as

$$a(q, t) = \begin{cases} \ddot{\lambda}(t)\tilde{a}(q_{ad}^L(\lambda(t)), \lambda) + \dot{\lambda}(t)\tilde{v}(q_{ad}^L(\lambda(t)), \lambda), & q < q_{ad}^L(\lambda(t)) \\ \ddot{\lambda}(t)\tilde{a}(q, \lambda) + \dot{\lambda}(t)\tilde{v}(q, \lambda), & q \in [q_{ad}^L(\lambda(t)), q_{ad}^R(\lambda(t))] \\ \ddot{\lambda}(t)\tilde{a}(q_{ad}^R(\lambda(t)), \lambda) + \dot{\lambda}(t)\tilde{v}(q_{ad}^R(\lambda(t)), \lambda), & q > q_{ad}^R(\lambda(t)), \end{cases} \quad (6.46)$$

where we have taken the flow fields to be the same as at the boundary turning points when q is outside the energy shell.

6.7 Appendix: Numerical construction of the angle map $\Theta_{T,[I_0]}^{FF}$

To construct the angle map $\Theta_{T,[I_0]}^{FF}$ we generate a set of M points distributed under the *microcanonical measure* for the Hamiltonian $H(q, p, \lambda(0))$ at the energy shell corresponding to energy E_0 . This is done by taking an initial condition on the energy shell $\mathcal{E}(0)$ and evolving it under the frozen Hamiltonian $H(q, p, \lambda(0))$ by a 4th order symplectic integrator [115, 120] while recording the coordinates $z_0^{(j)} \equiv (q_0^{(j)}, p_0^{(j)})$ of the evolving point at times $t_j = (jT/M)$ for $j = 0, \dots, M - 1$. The set $\mathbf{S}_0 = \{z_0^{(j)}\}_{j=0,\dots,M-1}$ are uniformly distributed in the angle variable, and the corresponding angle coordinate for $z_0^{(j)}$ is given as $\theta_0^{(j)} = 2\pi j/M$. Now we evolve the points in the set \mathbf{S}_0 from $t = 0$ to $t = T$ under the time-dependent Hamiltonian $H_{FF}(q, p, \lambda(t))$ using the symplectic integrator to obtain a new set of points $\mathbf{S}_1 = \{z_1^{(j)}\}_{j=0,\dots,M-1}$, where $z_0^{(j)}$ has been mapped to $z_1^{(j)}$ under $\mathcal{M}_{T,[I_0]}^{FF}$. We find the approximate value of the angle coordinate $\theta_1^{(j)}$ by locating the point in S_0 that is closest (in the sense of Euclidean distance in phase space) to the point $z_1^{(j)}$. Say, we find that the point $z_0^{(j*)}$ from \mathbf{S}_0 is closest to the point $z_1^{(j)}$; and $z_0^{(j*)}$ has the corresponding angle coordinate value $\theta_0^{(j*)}$. For large enough M approximate that $z_0^{(j*)}$

and $z_0^{(j^*\pm 1)}$ will be co-linear and we approximate the value of $\theta_1^{(j)}$ by linear interpolation using the points $\{(z_0^{(j*)}, \theta_0^{(j*)}), ((z_0^{(j^*\pm 1)}, \theta_0^{(j^*\pm 1)})\}$. We repeat this calculation to the angle coordinates $\{\theta_1^{(j)}\}$ for all the points in the set \mathbf{S}_1 . Now, we construct the map $\Theta_{T,[I_0]}^{FF}$ numerically by using a smooth spline interpolation from the angle coordinate pairs in the set $\{(\theta_0^{(j)}, \theta_1^{(j)})\}$. Once the smooth map $\Theta_{T,[I_0]}^{FF}$ is obtained, we calculate its derivative function $\partial\Theta_{T,[I_0]}^{FF}$ and also the inverse function θ_f^{-1} numerically.

Chapter 7: Future directions

7.1 Stochastic, quantum and information thermodynamics

In Chapter 2 of this thesis we presented the formalism of feedback-control in continuously monitored systems when the control parameter is obtained from the measurement signal following Ref.[1]. The quantum and discrete stochastic case of the formalism have already been used for different projects related to feedback-cooling of quantum system [122], entanglement generation [123] and thermometry [124]. In general this formalism can be used to study various devices in the context of quantum and nanotechnology where measurement-based feedback control is useful. Studying the corresponding stochastic and quantum thermodynamics of such systems is also an interesting area of research. Investigations of the thermodynamics for systems modeled under the QFPME framework of Ref. [1] on both the trajectory and ensemble-level pictures are required for better applicability of the framework to practical problems in quantum technology. Preliminary work related to the thermodynamics of QFPME can be found in [125]. Investigating the energy contributions arising from each of the terms in the jump trajectory master equation discussed in the Chapter 4 can give us interesting insights about trajectory level quantum thermodynamics. Simulations from the Chapter. 4 (Ref. [3]) can be particularly useful for this.

A connection of Maxwell's demon to quantum error corrections is discussed in Ref. [88]. It will be interesting to see if the ideas related to the Maxwell's demons discussed in this thesis can

also be extended to problems related to quantum error corrections. Another possible research direction could be studying different models of autonomous demons similar to the one discussed in Chapter 5 in both classical and quantum contexts. Investigating quantum versions of autonomous thermodynamic device might lead us to better understanding of how quantum correlations present in an information reservoir can be harnessed for thermodynamic and computational applications.

The simple, two-state model presented in Chapter 3 required a perturbative analysis. Finding similar toy models where QFPME is exactly solvable would also be an interesting project.

The feedback-control master equation for the classical case can be useful for analyzing experimentally relevant information thermodynamic systems similar to the one discussed in Ref. [126].

Classical Hamiltonian systems have been previously investigated in the context of information thermodynamics in Ref. [17, 121]. In Chapter. 6 we explored the evolution of a distribution function of angle variables when a system is being driven by periodically driven classical Hamiltonian system. Studying the change of entropy of the angle variable distribution under Floquet dynamics can be interesting research avenue. Also connecting the ideas from shortcuts to adiabaticity to the inclusive Hamiltonian formalism of information processing [17] is also another potential research direction.

Lastly, investigations on fluctuation theorems and for quantum Maxwell's demons under the measurement-based feedback framework is an active area of research. See Refs.[127, 128] for discussions on thermodynamics of continuous measured quantum systems, which might be useful starting point for further investigations.

7.2 Chemical physics, biological physics and complex systems science

The classical cases (discrete and continuous) of the modelling framework presented in Chapter. 2 can be particularly useful in the context of chemical and biological physics. Biological and artificial molecular motors and chemical reaction networks are often modelled using discrete state dynamics. Studying the effect of feedback-control on such systems with the consideration of different measurement models can be an interesting area of research. Thus the discussions presented in this thesis can be particularly useful for modelling different systems relevant to chemical and biological physics. Relating these models to autonomous demons can give us better understanding of information processing in such systems.

In the fields of ecology, network sciences, finance, system biology or more generally in complex systems sciences interplay of stochasticity, measurement accuracy, and feedback-control play a key role. Investigating different problems from these fields with the modelling frameworks discussed in this thesis can give us fundamental insights about such complex systems. Efficiently modelling the control of high dimensional dynamical systems with possibly chaotic behavior is an active field of research in the field of control systems. Extension of the discussions presented in this thesis to this problem could also be a potential avenue of research. Chapter. 5 is an example of engineering of automated feedback control on a network system to achieve a desired task. Further studies in this avenue will also be interesting [129].

Bibliography

- [1] Björn Annby-Andersson, Faraj Bakhshinezhad, Debankur Bhattacharyya, Guilherme De Sousa, Christopher Jarzynski, Peter Samuelsson, and Patrick P Potts. Quantum fokker-planck master equation for continuous feedback control. *Phys. Rev. Lett.*, 129(5):050401, 2022.
- [2] Debankur Bhattacharyya and Christopher Jarzynski. From a feedback-controlled demon to an information ratchet in a double quantum dot. *Phys. Rev. E*, 106:064101, Dec 2022.
- [3] Björn Annby-Andersson, Debankur Bhattacharyya, Pharnam Bakhshinezhad, Daniel Holst, Guilherme De Sousa, Christopher Jarzynski, Peter Samuelsson, and Patrick P Potts. Maxwell’s demon across the quantum-to-classical transition. *arXiv preprint arXiv:2405.09376*, 2024.
- [4] B. Annby-Andersson, P. Samuelsson, V. F. Maisi, and P. P. Potts. Maxwell’s demon in a double quantum dot with continuous charge detection. *Phys. Rev. B*, 101:165404, 2020.
- [5] A. Rex. Maxwell’s demon—a historical review. *Entropy*, 19(6):240, 2017.
- [6] L Szilard. über die entropieverminderung in einem thermodynamischen system bei eingriffen intelligenter wesen. *Zeitschrift für Physik*, 53(11-12):840–856, 1929.
- [7] Juan MR Parrondo. The szilard engine revisited: Entropy, macroscopic randomness, and symmetry breaking phase transitions. *Chaos: An Interdisciplinary Journal of Nonlinear Science*, 11(3):725–733, 2001.
- [8] J. V. Koski, V. F. Maisi, J. P. Pekola, and D. V. Averin. Experimental realization of a szilard engine with a single electron. *Proceedings of the National Academy of Sciences*, 111(38):13786–13789, 2014.
- [9] R. Landauer. Irreversibility and heat generation in the computing process. *IBM Journal of Research and Development*, 5(3):183–191, 1961.
- [10] R. Landauer. Information is physical. *Physics Today*, 44(5):23–29, 1991.
- [11] M. B. Plenio and V. Vitelli. The physics of forgetting: Landauer’s erasure principle and information theory. *Contemporary Physics*, 42(1):25–60, 2001.

- [12] C.H. Bennett. The thermodynamics of computation—a review. *International Journal of Theoretical Physics*, 21(12):905–940, 1982.
- [13] A. Bérut, A. Arakelyan, A. Petrosyan, S. Ciliberto, R. Dillenschneider, and E. Lutz. Experimental verification of landauer’s principle linking information and thermodynamics. *Nature*, 483(7388):187–189, 2012.
- [14] Y. Jun, M. Gavrilov, and J. Bechhoefer. High-precision test of landauer’s principle in a feedback trap. *Phys. Rev. Letters*, 113(19):190601, 2014.
- [15] D. Mandal and C. Jarzynski. Work and information processing in a solvable model of Maxwell’s demon. *Proceedings of the National Academy of Sciences*, 109(29):11641–11645, 2012.
- [16] Dibyendu Mandal, H. T. Quan, and Christopher Jarzynski. Maxwell’s refrigerator: An exactly solvable model. *Phys. Rev. Lett.*, 111:030602, Jul 2013.
- [17] S. Deffner and C. Jarzynski. Information processing and the second law of thermodynamics: An inclusive, hamiltonian approach. *Phys. Rev. X*, 3:041003, 2013.
- [18] C. H. Bennett. Notes on landauer’s principle, reversible computation, and Maxwell’s demon. *Studies in History and Philosophy of Science Part B: Studies in History and Philosophy of Modern Physics*, 34(3):501–510, 2003.
- [19] Marian Smoluchowski. Experimentell nachweisbare, der üblichen thermodynamik widersprechende molekularphänomene. *Pisma Mariana Smoluchowskiego*, 2(1):226–251, 1927.
- [20] M. Planck, P.J.W. Debye, W. Nernst, M. Smoluchowski, A. Sommerfeld, and H.A. Lorentz. *Vorträge über die kinetische theorie der materie und der elektrizität: gehalten in Göttingen auf einladung der Kommission der Wolfskehlstiftung*. Mathematische Vorlesungen an der Universität Göttingen. B.G. Teubner, 1914.
- [21] P. A. Skordos and W. H. Zurek. Maxwell’s demon, rectifiers, and the second law: Computer simulation of smoluchowski’s trapdoor. *American Journal of Physics*, 60(10):876–882, 1992.
- [22] R.P. Feynman, R.B. Leighton, and M. Sands. *The Feynman Lectures on Physics, Vol. I: The New Millennium Edition: Mainly Mechanics, Radiation, and Heat*. The Feynman Lectures on Physics. Basic Books, 2011.
- [23] Peter Reimann. Brownian motors: noisy transport far from equilibrium. *Physics Reports*, 361(2):57–265, 2002.
- [24] Z. Lu, D. Mandal, and C. Jarzynski. Engineering Maxwell’s demon. *Physics Today*, 67(8):60–61, 2014.
- [25] Z. Lu and C. Jarzynski. A programmable mechanical Maxwell’s demon. *Entropy*, 21(1):65, 2019.

- [26] A. C. Barato and U. Seifert. An autonomous and reversible Maxwell's demon. *EPL*, 101(6):60001, mar 2013.
- [27] A. C. Barato and U. Seifert. Unifying three perspectives on information processing in stochastic thermodynamics. *Phys. Rev. Lett.*, 112:090601, Mar 2014.
- [28] A. C. Barato and U. Seifert. Stochastic thermodynamics with information reservoirs. *Phys. Rev. E*, 90:042150, 2014.
- [29] J. Hoppenau and A. Engel. On the energetics of information exchange. *EPL*, 105(5):50002, 2014.
- [30] Richard E. Spinney, Mikhail Prokopenko, and Dominique Chu. Information ratchets exploiting spatially structured information reservoirs. *Phys. Rev. E*, 98:022124, Aug 2018.
- [31] Pei-Yan Peng and Chang-Kui Duan. A Maxwell demon model connecting information and thermodynamics. *Chinese Phys. Lett.*, 33(8):080501, aug 2016.
- [32] Shubhashis Rana and AM Jayannavar. A multipurpose information engine that can go beyond the carnot limit. *Journal of Statistical Mechanics: Theory and Experiment*, 2016(10):103207, 2016.
- [33] Philipp Strasberg, Gernot Schaller, Tobias Brandes, and Christopher Jarzynski. Second laws for an information driven current through a spin valve. *Phys. Rev. E*, 90:062107, Dec 2014.
- [34] Yuansheng Cao, Zongping Gong, and H. T. Quan. Thermodynamics of information processing based on enzyme kinetics: An exactly solvable model of an information pump. *Phys. Rev. E*, 91:062117, Jun 2015.
- [35] S. Deffner. Information-driven current in a quantum Maxwell demon. *Phys. Rev. E*, 88:062128, 2013.
- [36] Adrian Chapman and Akimasa Miyake. How an autonomous quantum Maxwell demon can harness correlated information. *Phys. Rev. E*, 92:062125, Dec 2015.
- [37] Josey Stevens and Sebastian Deffner. Quantum to classical transition in an information ratchet. *Phys. Rev. E*, 99:042129, Apr 2019.
- [38] Philipp Strasberg, Gernot Schaller, Tobias Brandes, and Massimiliano Esposito. Quantum and information thermodynamics: A unifying framework based on repeated interactions. *Phys. Rev. X*, 7:021003, Apr 2017.
- [39] Alexander B. Boyd, Dibyendu Mandal, and James P. Crutchfield. Identifying functional thermodynamics in autonomous Maxwellian ratchets. *New Journal of Physics*, 18, 2016.
- [40] Alexander B Boyd, Dibyendu Mandal, and James P Crutchfield. Leveraging environmental correlations: The thermodynamics of requisite variety. *Journal of Statistical Physics*, 167(6):1555–1585, 2017.

- [41] Alexander B. Boyd, Dibyendu Mandal, Paul M. Riechers, and James P. Crutchfield. Transient dissipation and structural costs of physical information transduction. *Phys. Rev. Lett.*, 118:220602, Jun 2017.
- [42] Alexander B. Boyd, Dibyendu Mandal, and James P. Crutchfield. Correlation-powered information engines and the thermodynamics of self-correction. *Phys. Rev. E*, 95:012152, Jan 2017.
- [43] Alexander B. Boyd, Dibyendu Mandal, and James P. Crutchfield. Thermodynamics of modularity: Structural costs beyond the landauer bound. *Phys. Rev. X*, 8:031036, Aug 2018.
- [44] Alexandra M. Jurgens and James P. Crutchfield. Functional thermodynamics of Maxwellian ratchets: Constructing and deconstructing patterns, randomizing and derandomizing behaviors. *Phys. Rev. Research*, 2:033334, Aug 2020.
- [45] Neri Merhav. Sequence complexity and work extraction. *Journal of Statistical Mechanics: Theory and Experiment*, 2015(6):P06037, jun 2015.
- [46] Neri Merhav. *Journal of Statistical Mechanics: Theory and Experiment*, 2017(2):023207, feb 2017.
- [47] David H Wolpert. The stochastic thermodynamics of computation. *Journal of Physics A: Mathematical and Theoretical*, 52(19):193001, 2019.
- [48] L. Peliti and S. Pigolotti. *Stochastic Thermodynamics: An Introduction*. Princeton University Press, 2021.
- [49] Udo Seifert. Stochastic thermodynamics, fluctuation theorems and molecular machines. *Rep. Prog. Phys.*, 75(12):126001, nov 2012.
- [50] Massimiliano Esposito and Gernot Schaller. Stochastic thermodynamics for “Maxwell demon” feedbacks. *EPL (Europhysics Letters)*, 99(3):30003, 2012.
- [51] Takahiro Sagawa and Masahito Ueda. Fluctuation theorem with information exchange: Role of correlations in stochastic thermodynamics. *Phys. Rev. Lett.*, 109:180602, Nov 2012.
- [52] Takahiro Sagawa and Masahito Ueda. Nonequilibrium thermodynamics of feedback control. *Phys. Rev. E*, 85:021104, Feb 2012.
- [53] Sourabh Lahiri, Shubhashis Rana, and AM Jayannavar. Fluctuation theorems in the presence of information gain and feedback. *Journal of Physics A: Mathematical and Theoretical*, 45(6):065002, 2012.
- [54] Jordan M. Horowitz and Suriyanarayanan Vaikuntanathan. Nonequilibrium detailed fluctuation theorem for repeated discrete feedback. *Phys. Rev. E*, 82:061120, Dec 2010.
- [55] Patrick P. Potts and Peter Samuelsson. Detailed fluctuation relation for arbitrary measurement and feedback schemes. *Phys. Rev. Lett.*, 121:210603, Nov 2018.

- [56] Qian Zeng and Jin Wang. New fluctuation theorems on Maxwell's demon. *Science Advances*, 7(23):eabf1807, 2021.
- [57] Sosuke Ito and Takahiro Sagawa. Information thermodynamics on causal networks. *Phys. Rev. Lett.*, 111:180603, Oct 2013.
- [58] Naoto Shiraishi, Sosuke Ito, Kyogo Kawaguchi, and Takahiro Sagawa. Role of measurement-feedback separation in autonomous Maxwell's demons. *New Journal of Physics*, 17(4):045012, apr 2015.
- [59] J. M. R. Parrondo, J. M. Horowitz, and T. Sagawa. Thermodynamics of information. *Nature Physics*, 11:131–139, 2015.
- [60] Thitiporn Sangchai, Shaymaa Al Shehimy, Emanuele Penocchio, and Giulio Ragazzon. Artificial molecular ratchets: Tools enabling endergonic processes. *Angewandte Chemie International Edition*, 62(47):e202309501, 2023.
- [61] Howard M. Wiseman and Gerard J. Milburn. *Quantum Measurement and Control*. Cambridge University Press, 2009.
- [62] John Bechhoefer. *Control Theory for Physicists*. Cambridge University Press, 2021.
- [63] Gabriel T. Landi, Michael J. Kewming, Mark T. Mitchison, and Patrick P. Potts. Current fluctuations in open quantum systems: Bridging the gap between quantum continuous measurements and full counting statistics. *PRX Quantum*, 5:020201, Apr 2024.
- [64] Gernot Schaller. *Open quantum systems far from equilibrium*, volume 881. Springer, 2014.
- [65] David Guéry-Odelin, Chris Jarzynski, Carlos A Plata, Antonio Prados, and Emmanuel Trizac. Driving rapidly while remaining in control: classical shortcuts from hamiltonian to stochastic dynamics. *Reports on Progress in Physics*, 86:035902, 2022.
- [66] D. Barker, S. Lehmann, L. Namazi, M. Nilsson, C. Thelander, K. A. Dick, and V. F. Maisi. Individually addressable double quantum dots formed with nanowire polytypes and identified by epitaxial markers. *Applied Physics Letters*, 114(18):183502, 2019.
- [67] H. Risken. *The Fokker-Planck Equation: Methods of Solution and Applications*. Springer Series in Synergetics. Springer Berlin Heidelberg, 2012.
- [68] Andrew J. Daley. Quantum trajectories and open many-body quantum systems. *Adv. Phys.*, 63(2):77–149, 2014.
- [69] J. Schnakenberg. Network theory of microscopic and macroscopic behavior of master equation systems. *Rev. Mod. Phys.*, 48:571–585, Oct 1976.
- [70] I. Percival and D. Richards. *Introduction to Dynamics*. Cambridge University Press, 1982.
- [71] H. Goldstein, C.P. Poole, and J.L. Safko. *Classical Mechanics*. Addison Wesley, 2002.

- [72] S.H. Strogatz. *Nonlinear Dynamics and Chaos: With Applications to Physics, Biology, Chemistry, and Engineering*. CRC Press, 2018.
- [73] Edward Ott. *Chaos in Dynamical Systems*. Cambridge University Press, 2 edition, 2002.
- [74] Björn Annby-Andersson. *A General Formalism for Continuous Feedback Control in Quantum Systems*. Licentiate thesis, , Lund University, August 2022.
- [75] Björn Annby-Andersson. *Continuous measurements of small systems: Feedback control, thermodynamics, entanglement*. Doctoral thesis (compilation) , Lund University, April 2024.
- [76] Holst, Daniel. Continuous Quantum Control of Quantum Dot Systems, 2022. Masters Thesis, Lund University.
- [77] Christopher Jarzynski, Sebastian Deffner, Ayoti Patra, and Yi git Subaş 1. Fast forward to the classical adiabatic invariant. *Phys. Rev. E*, 95:032122, Mar 2017.
- [78] Kurt Jacobs and Daniel A. Steck. A straightforward introduction to continuous quantum measurement. *Contemporary Physics*, 47(5):279–303, 2006.
- [79] K. J. H. Law, A. M. Stuart, and K. C. Zygalakis. Data assimilation: A mathematical introduction, 2015.
- [80] Takahiro Sagawa and Masahito Ueda. Nonequilibrium thermodynamics of feedback control. *Phys. Rev. E*, 85:021104, Feb 2012.
- [81] A. Chantasri, J. Dressel, and A. N. Jordan. Action principle for continuous quantum measurement. *Phys. Rev. A*, 88:042110, Oct 2013.
- [82] Areeya Chantasri and Andrew N. Jordan. Stochastic path-integral formalism for continuous quantum measurement. *Phys. Rev. A*, 92:032125, Sep 2015.
- [83] Harold J. Kushner. On the differential equations satisfied by conditional probability densities of markov processes, with applications. *Journal of the Society for Industrial and Applied Mathematics Series A Control*, 2(1):106–119, 1964.
- [84] Christopher W Wächtler, Philipp Strasberg, Sabine H L Klapp, Gernot Schaller, and Christopher Jarzynski. Stochastic thermodynamics of self-oscillations: the electron shuttle. *New Journal of Physics*, 21(7):073009, jul 2019.
- [85] Andrew M. Smith. *Studies in Nonequilibrium Quantum Thermodynamics*. PhD thesis, 2020.
- [86] Edward Ott. Goodness of ergodic adiabatic invariants. *Phys. Rev. Lett.*, 42:1628–1631, Jun 1979.
- [87] Dibyendu Mandal and Christopher Jarzynski. Analysis of slow transitions between nonequilibrium steady states. *Journal of Statistical Mechanics: Theory and Experiment*, 2016(6):063204, jun 2016.

- [88] M.A. Nielsen and I.L. Chuang. *Quantum Computation and Quantum Information*. Cambridge Series on Information and the Natural Sciences. Cambridge University Press, 2000.
- [89] Jordan M. Horowitz, Takahiro Sagawa, and Juan M. R. Parrondo. Imitating chemical motors with optimal information motors. *Phys. Rev. Lett.*, 111:010602, Jul 2013.
- [90] Niraj Kumar, Christian Van den Broeck, Massimiliano Esposito, and Katja Lindenberg. Thermodynamics of a stochastic twin elevator. *Phys. Rev. E*, 84:051134, Nov 2011.
- [91] *NIST Digital Library of Mathematical Functions*. <https://dlmf.nist.gov/>, Release 1.2.0 of 2024-03-15. F. W. J. Olver, A. B. Olde Daalhuis, D. W. Lozier, B. I. Schneider, R. F. Boisvert, C. W. Clark, B. R. Miller, B. V. Saunders, H. S. Cohl, and M. A. McClain, eds.
- [92] G.B. Arfken, G.B. Arfken, H.J. Weber, and F.E. Harris. *Mathematical Methods for Physicists: A Comprehensive Guide*. Elsevier Science, 2013.
- [93] Eric W. Weisstein. "hermite polynomial." - from mathworld—a wolfram web resource. <https://mathworld.wolfram.com/HermitePolynomial.html>, Visited on 05/31/2024.
- [94] Dmitri V. Averin, Mikko Möttönen, and Jukka P. Pekola. Maxwell's demon based on a single-electron pump. *Phys. Rev. B*, 84:245448, Dec 2011.
- [95] W. G. van der Wiel, S. De Franceschi, J. M. Elzerman, T. Fujisawa, S. Tarucha, and L. P. Kouwenhoven. Electron transport through double quantum dots. *Rev. Mod. Phys.*, 75:1–22, Dec 2002.
- [96] R. Hanson, L. P. Kouwenhoven, J. R. Petta, S. Tarucha, and L. M. K. Vandersypen. Spins in few-electron quantum dots. *Rev. Mod. Phys.*, 79:1217–1265, Oct 2007.
- [97] Mônica A. Cotta. Quantum dots and their applications: What lies ahead? *ACS Applied Nano Materials*, 3(6):4920–4924, 2020.
- [98] Klaus Mølmer, Yvan Castin, and Jean Dalibard. Monte carlo wave-function method in quantum optics. *J. Opt. Soc. Am. B*, 10(3):524–538, Mar 1993.
- [99] B. Misra and E. C. G. Sudarshan. The Zeno's paradox in quantum theory. *Journal of Mathematical Physics*, 18(4):756–763, 04 1977.
- [100] Hsi-Sheng Goan, G. J. Milburn, H. M. Wiseman, and He Bi Sun. Continuous quantum measurement of two coupled quantum dots using a point contact: A quantum trajectory approach. *Phys. Rev. B*, 63:125326, Mar 2001.
- [101] H. M. Wiseman and G. J. Milburn. Quantum theory of field-quadrature measurements. *Phys. Rev. A*, 47:642–662, Jan 1993.
- [102] Michael Bauer, Andre C Barato, and Udo Seifert. Optimized finite-time information machine. *Journal of Statistical Mechanics: Theory and Experiment*, 2014(9):P09010, 2014.

- [103] Naoto Shiraishi, Takumi Matsumoto, and Takahiro Sagawa. Measurement-feedback formalism meets information reservoirs. *New Journal of Physics*, 18(1):013044, 2016.
- [104] Jordan M. Horowitz and Massimiliano Esposito. Thermodynamics with continuous information flow. *Phys. Rev. X*, 4:031015, Jul 2014.
- [105] T L Hill and R M Simmons. Free energy levels and entropy production associated with biochemical kinetic diagrams. *Proceedings of the National Academy of Sciences*, 73(1):95–99, 1976.
- [106] T.L. Hill. *Free Energy Transduction and Biochemical Cycle Kinetics*. Dover Books on Chemistry. Dover Publications, 2013.
- [107] Carl D Meyer. *Matrix analysis and applied linear algebra*, volume 71. Siam, 2000.
- [108] B. Efron and R.J. Tibshirani. *An Introduction to the Bootstrap*. CRC Press, 1994.
- [109] D Hartich, A C Barato, and U Seifert. Stochastic thermodynamics of bipartite systems: transfer entropy inequalities and a Maxwell’s demon interpretation. *Journal of Statistical Mechanics: Theory and Experiment*, 2014(2):P02016, feb 2014.
- [110] Giovanni Diana and Massimiliano Esposito. Mutual entropy production in bipartite systems. *Journal of Statistical Mechanics: Theory and Experiment*, 2014(4):P04010, apr 2014.
- [111] Daniel T. Gillespie. Stochastic simulation of chemical kinetics. *Annual Review of Physical Chemistry*, 58(1):35–55, 2007. PMID: 17037977.
- [112] Daniel T Gillespie. A general method for numerically simulating the stochastic time evolution of coupled chemical reactions. *Journal of Computational Physics*, 22(4):403–434, 1976.
- [113] Daniel T. Gillespie. Exact stochastic simulation of coupled chemical reactions. *The Journal of Physical Chemistry*, 81(25):2340–2361, 1977.
- [114] Ayoti Patra and Christopher Jarzynski. Shortcuts to adiabaticity using flow fields. *New Journal of Physics*, 19(12):125009, 2017.
- [115] A.J. Lichtenberg and M.A. Lieberman. *Regular and Chaotic Dynamics*. Applied Mathematical Sciences. Springer New York, 2013.
- [116] George M Zaslavsky. *Hamiltonian Chaos and Fractional Dynamics*. Oxford University Press, 12 2004.
- [117] Stefan Klus, Péter Koltai, and Christof Schütte. On the numerical approximation of the perron-frobenius and koopman operator. *Journal of Computational Dynamics*, 3(1):51–79, 2016.
- [118] Bernard O Koopman. Hamiltonian systems and transformation in hilbert space. *Proceedings of the National Academy of Sciences*, 17(5):315–318, 1931.

- [119] Eddie Seabrook and Laurenz Wiskott. A Tutorial on the Spectral Theory of Markov Chains. *Neural Computation*, 35(11):1713–1796, 10 2023.
- [120] Etienne Forest and Ronald D. Ruth. Fourth-order symplectic integration. *Physica D: Nonlinear Phenomena*, 43(1):105–117, 1990.
- [121] Roi Holtzman, Geva Arwas, and Oren Raz. Hamiltonian memory: An erasable classical bit. *Phys. Rev. Res.*, 3:013232, Mar 2021.
- [122] Guilherme De Sousa, Pharnam Bakhshinezhad, Björn Annby-Andersson, Peter Samuelsson, Patrick P Potts, and Christopher Jarzynski. Continuous feedback protocols for cooling and trapping a quantum harmonic oscillator. *arXiv preprint arXiv:2404.19047*, 2024.
- [123] Giovanni Francesco Diotallevi, Björn Annby-Andersson, Peter Samuelsson, Armin Tavakoli, and Pharnam Bakhshinezhad. Steady-state entanglement production in a quantum thermal machine with continuous feedback control. *New Journal of Physics*, 26(5):053005, 2024.
- [124] Julia Boeyens, Björn Annby-Andersson, Pharnam Bakhshinezhad, Géraldine Haack, Martí Perarnau-Llobet, Stefan Nimmrichter, Patrick P Potts, and Mohammad Mehboudi. Probe thermometry with continuous measurements. *New Journal of Physics*, 25(12):123009, 2023.
- [125] Jöel Aschwanden. The thermodynamics of continuous feedback control, 2023. Master’s Thesis, University of Basel.
- [126] Tushar K. Saha, Joseph N. E. Lucero, Jannik Ehrich, David A. Sivak, and John Bechhoefer. Bayesian information engine that optimally exploits noisy measurements. *Phys. Rev. Lett.*, 129:130601, Sep 2022.
- [127] Gonzalo Manzano and Roberta Zambrini. Quantum thermodynamics under continuous monitoring: A general framework. *AVS Quantum Science*, 4(2):025302, 05 2022.
- [128] Toshihiro Yada, Nobuyuki Yoshioka, and Takahiro Sagawa. Quantum fluctuation theorem under quantum jumps with continuous measurement and feedback. *Phys. Rev. Lett.*, 128:170601, Apr 2022.
- [129] Raissa M D’Souza, Mario di Bernardo, and Yang-Yu Liu. Controlling complex networks with complex nodes. *Nature Reviews Physics*, 5(4):250–262, 2023.